

Activation of Inert sp^3 C-H, C-O and C-Si Bonds at Cationic Iridium Complexes

By

Scott Matthew Chapp

Dissertation

Submitted to the Faculty of the

Graduate School of Vanderbilt University

in partial fulfillment of the requirements

for the degree of

DOCTOR OF PHILOSOPHY

In

Chemistry

May 14th, 2021

Nashville, Tennessee

Approved:

Nathan D. Schley, Ph.D.

Timothy P. Hanusa, Ph.D.

Janet E. Macdonald, Ph.D.

Sean B. Seymore, Ph.D.

**Copyright © 2021 by Scott Matthew Chapp
All Rights Reserved**

"The best is the enemy of the good"

-Voltaire

-R.H.C

-N.D.S.

ACKNOWLEDGEMENTS

In an attempt to formulate a coherent expression of my immense gratitude to all that have contributed to the success of my graduate career, I must first thank my advisor Nathan Schley. Over the last five and half years, Nathan has been a tremendous mentor and has dedicated countless hours of discussions, suggestions and comedic anecdotes. I would like to thank him for all the time spent training me in X-ray crystallography and for his patience in my early years of crystal growth. His demeanor, approach to chemistry and mentorship is something to aspire towards. I also must thank members of my thesis committee, Tim Hanusa, Janet Macdonald and Sean Seymore for contribution in time and effort. I would also like to thank my undergraduate research advisor, Adam Hill, for his time preparing me for graduate school. His excitement and enthusiasm about inorganic chemistry largely influence my choice to pursue organometallic chemistry.

I must also thank my parents, David and Terri, who have always encouraged me to pursue any and all of my interests. My oldest brothers, Tim and Andrew, for proofreading documents, discussing chemistry and being models of excellence in STEM. My sister, Carolyn, for her love, support and for always being genuinely interested in my research. My other brother, Brian, sister-in-law Hannah, and future sister-in-law Brittany for many hours playing board games.

I am particularly thankful to have joined the Schley lab with fellow founding member Ben Mueller. At the early stages of our graduate careers, we constantly challenged each other to become better synthetic chemists through our NMR identification games or troubleshooting experimental problems. As the years progressed, our hardened optimism and increased skepticism fueled laughter, creativity, pranks and the creation of Capocce. My time in graduate school would have been vastly different without his presence.

It has been a pleasure to work with other members of the Schley group including Caleb Jones, Maggie Jones, Caleb Fast and Griffin Perry, as well as undergraduates Collin Hong, Dan Tong and Lauren Nam. I thank them for helpful comments and suggestions in lab and during group meeting. I am especially grateful to Dr. Yuanyuan Zhang for answering questions and providing advice in my early years in the group. I must also thank current and former members of the Vanderbilt Chemistry department including Ross Koby, Jenna DeSousa, Eric Huseman, Dr. Jeremy Beam, Dr. Mike Turo and Dr. Evan Gizzie for their positive and lasting impacts on my graduate career. Additionally, I would like to acknowledge both Don Stec and Markus Voehler for assistance and troubleshooting NMR issues.

Outside of the chemistry department I must thank the amazing friendships formed through other areas of the Vanderbilt community including: Shannon Melendy, Tyler Jarrett, Analee Benik, Allie Haskew and Mary Brahos. Whether it was through

Sunday night trivia or playing board games, they helped provide an outlet away from lab. Additionally, I must thank Bryce Nagle for his great friendship and unwavering support of my research. In addition to being part of trivia and board game nights, he has been my rock climbing partner for several years and is always a source of positive motivation.

Finally, all of this work would not have been possible without my fiancé and partner, McKenzie Meservey. She bravely moved to Nashville to continue her education in Human Development Counseling and brought an endless supply of laughter, support and positivity. She has been a part of my graduate career from the beginning and has endured my late nights in the lab and drawings on mirrors. She has let me pursue all of my passions and has defined these last five and half years and to that I am forever grateful.

Table of Contents

	Page
DEDICATION.....	iii
ACKNOWLEDGEMENTS.....	iv
LIST OF FIGURES	viii
LIST OF TABLES.....	xii
CHAPTER	
I. INTRODUCTION TO sp^3 BOND ACTIVATION AND FUNCTIONALIZATION	
1.1 Scope of this Work.....	1
1.2 C-H Activation from Alkanes to Ethers.....	2
1.3 C-H Silylation and Olefin Silylation.....	6
1.4 Olefin Oligomerization.....	7
1.5 References.....	10
II. EVIDENCE FOR REVERSIBLE CYCLOMETALATION IN ALKANE DEHYDROGENATION AND C-O BOND CLEAVAGE AT IRIIDIUM BIS(PHOSPHINE) COMPLEXES	
2.1 Introduction.....	14
2.2 Results and Discussion.....	15
2.3 Conclusion.....	22
2.4 Experimental.....	23
2.5 Additional Figures.....	35
2.6 X-Ray Crystallography.....	41
2.7 References.....	53
III. GROUP-TRANSFER REACTIONS OF A CATIONIC IRIIDIUM ALKOXYCARBENE GENERATED BY ETHER DEHYDROGENATION	
3.1 Introduction.....	55
3.2 Results and Discussion.....	56
3.3 Conclusion.....	66
3.4 Experimental.....	66
3.5 Additional Figures.....	76
3.6 X-Ray Crystallography.....	90
3.7 References.....	109
IV. REVERSIBLE $C(sp^3)$ -Si OXIDATIVE ADDITION OF UNSUPPORTED ORGANOSILANES: EFFECTS OF SILICON SUBSTITUENTS ON KINETICS AND THERMODYNAMICS	
4.1 Introduction.....	116
4.2 Results and Discussion.....	118

4.3	Conclusion.....	124
4.4	Experimental.....	125
4.5	Additional Figures.....	143
4.6	X-Ray Crystallography.....	160
4.7	References.....	180
V.	PROGRESS TOWARDS TANDEM OLIGOMERIZATION/HYDROGENATION OF SIMPLE OLEFINS TO BRANCHED ALKANES	
5.1	Introduction.....	184
5.2	Results and Discussion.....	185
5.3	Conclusion.....	190
5.4	Experimental.....	190
5.5	Additional Figures.....	193
5.6	X-Ray Crystallography.....	197
5.7	References.....	206

LIST OF FIGURES

FIGURE	Page
1.1.1. General reaction involving dehydrogenation of an 18 e ⁻ Ir(III) complex with <i>tert</i> -butylethylene (TBE) to generate a reactive 14 e ⁻ Ir(I) complex which can result in C-O, C-H and C-Si bond activation	1
1.1.2. General reaction for tandem oligomerization and hydrogenation of simple olefins to branched alkanes	1
1.2.1. First transition-metal complex observed to activate C-H bonds (left). First homogeneous metal complex to stoichiometrically dehydrogenation an alkane (center). First neutral iridium pincer complex to afford high turnovers numbers for alkane dehydrogenation (right)	2
1.2.2. Potential competing mechanisms that may occur following initial ether C-H activation	3
1.2.3. Representative reaction for catalytic ether dehydrogenation to form vinyl ethers	3
1.2.4. Representative reaction for catalytic hydroaryloxylation to form ethers	4
1.2.5. First examples of intramolecular (left) and intermolecular (right) ether activation to form alkoxy-carbene	4
1.2.6. Possible reactivity of metal carbenes with electrophilic and nucleophilic reagents	5
1.2.7. Molecular orbital diagram of alkoxy-carbenes.....	5
1.2.8. Proposed synthetic cycle for the imination of methyl <i>tert</i> -butyl ether	6
1.3.1. Representative example of <i>sp</i> ² C-H silylation.....	6
1.3.2. Representative example of olefin hydrosilylation.....	7
1.3.3. Proposed mechanism for olefin hydrosilylation and C-H silylation.....	7
1.4.1. Mechanism for dihydrogen activation. Homolytic bond cleavage (1) and heterolytic bond cleavage (3).....	8
1.4.2. General mechanism for ionic hydrogenation.....	9
1.4.3. Graph of carbonyl stretching frequency vs. phosphine cone angle.....	9
1.4.4. Fluoroalkylphosphine-supported iridium complex (left), Fluoroalkylphosphine-supported ruthenium complex (center), tris(3,5-bis(trifluoromethyl)phenyl)phosphine (right)	10
2.1.1. First example of stoichiometric alkane dehydrogenation by a homogeneous metal complex.....	14
2.1.2. Observation of C-O bond cleavage of MTBE upon dehydrogenation of 1 with TBE	15
2.2.1. ORTEPs of 1 (left) and 2 (right)	16
2.2.2. Dehydrogenation of complex 1 with TBE in a mixture of THF/DCM	16
2.2.3. Evidence for reversible cyclometalation of triphenylphosphine	17
2.2.4. Evidence for reversible cyclometalation for the dehydrogenation of cyclopentyl methyl ether	17
2.2.5. Reversibility of cyclometalation in complex 3	17
2.2.6. Isolation of cyclometalated 3-DME	18
2.2.7. ORTEPs of 5 (left) and 3-DME (right) shown at 50% probability. Anions and solvent of crystallization omitted for clarity.....	19
2.2.8. Observation of 3-DCE under original conditions first used for cyclooctane dehydrogenation	19
2.2.9. Evidence for reversible cyclometallation for C-O bond cleavage of MTBE.....	20
2.2.10. Kinetic model for the C-O bond cleavage of MTBE.....	20
2.2.11. Observation of complex 3 in the conversion of 1 to 2 by NMR spectroscopy.....	21
2.2.12. Proposed mechanism for the formation of 2	22
2.2.13. Role of 3 as a masked iridium(I) synthon.....	22
2.4.1. Representative ³¹ P{ ¹ H} NMR of the formation of 2 from 1	27
2.4.2. Kinetics for the cleavage of the C-O bond of MTBE using ³¹ P{ ¹ H} NMR	28
2.4.3. ³¹ P{ ¹ H} spectrum of reaction of 3 with C ₆ D ₆ showing conversion to complex 4	29
2.4.4. ³¹ P{ ¹ H} spectrum of crystals deposited from reaction of 3 with CPME showing conversion to complex 5	30
2.4.5. ³¹ P{ ¹ H} spectrum of reaction of 3 with CPME showing conversion to complexes 5 and 7	31
2.4.6. ³¹ P{ ¹ H} spectrum of reaction of 3 with MTBE showing conversion to complex 2	32
2.4.7. ³¹ P{ ¹ H} spectrum of cyclooctene dehydrogenation by 1 over time showing evidence for formation of 3-DCE prior to complete conversion to complex 6	33
2.4.8. ³¹ P{ ¹ H} spectrum of complex 3-DCE – Generated <i>in situ</i>	34
2.5.1. ¹ H NMR Spectrum of [(PPh ₃) ₂ IrH(C ₄ H ₇)]PF ₆ (2) (500 MHz, CD ₂ Cl ₂)	35
2.5.2. ¹³ C{ ¹ H} NMR Spectra of [(PPh ₃) ₂ IrH(C ₄ H ₇)]PF ₆ (2) (126 MHz, CD ₂ Cl ₂).....	36
2.5.3. ³¹ P{ ¹ H} NMR Spectra of [(PPh ₃) ₂ IrH(C ₄ H ₇)]PF ₆ (2) (202 MHz, CD ₂ Cl ₂)	36

2.5.4.	$^1\text{P}\{^1\text{H}\}$ spectrum of $[(\text{PPh}_3)(\text{PPh}_2\text{C}_6\text{H}_4-)\text{IrH}(\text{THF})_2]\text{PF}_6$ (3) (202 MHz, THF/ CD_2Cl_2) <i>Generated In situ</i>	37
2.5.5.	$^1\text{P}\{^1\text{H}\}$ spectrum of $[(\text{PPh}_3)(\text{PPh}_2\text{C}_6\text{H}_4-)\text{IrH}(\text{THF})_2]\text{PF}_6$ (3) (202 MHz, THF/ CD_2Cl_2). – <i>Isolated</i>	37
2.5.6.	^1H Spectra of $[(\text{PPh}_3)(\text{PPh}_2\text{C}_6\text{H}_4-)\text{IrH}(\text{DME})]\text{PF}_6$ (3-DME) (500 MHz, CD_2Cl_2)	38
2.5.7.	$^{13}\text{C}\{^1\text{H}\}$ NMR Spectra of $[(\text{PPh}_3)(\text{PPh}_2\text{C}_6\text{H}_4-)\text{IrH}(\text{DME})]\text{PF}_6$ (3-DME) (126 MHz, CD_2Cl_2)	38
2.5.8.	$^1\text{P}\{^1\text{H}\}$ NMR Spectra of $[(\text{PPh}_3)(\text{PPh}_2\text{C}_6\text{H}_4-)\text{IrH}(\text{DME})]\text{PF}_6$ (3-DME) (202 MHz, CD_2Cl_2).....	39
2.5.9.	^1H NMR Spectra of $[(\text{PPh}_3)_2\text{IrH}_2(\kappa,\eta^2\text{-MeOC}_5\text{H}_7)]\text{PF}_6$ (5) (500 MHz, CD_2Cl_2)	40
2.5.10.	$^{13}\text{C}\{^1\text{H}\}$ NMR Spectra of $[(\text{PPh}_3)_2\text{IrH}_2(\kappa,\eta^2\text{-MeOC}_5\text{H}_7)]\text{PF}_6$ (5) (126 MHz, CD_2Cl_2)	40
2.5.11.	$^1\text{P}\{^1\text{H}\}$ NMR Spectra of $[(\text{PPh}_3)_2\text{IrH}_2(\kappa,\eta^2\text{-MeOC}_5\text{H}_7)]\text{PF}_6$ (5) (202 MHz, CD_2Cl_2)	41
2.6.1.	ORTEP diagram of 1 with ellipsoids shown at 50%. The anion is omitted for clarity.....	44
2.6.2.	ORTEP diagram of 2 with ellipsoids shown at 50%. The anion is omitted for clarity.....	46
2.6.3.	ORTEP diagram of 3-DME with ellipsoids shown at 50%. The anion is omitted for clarity.....	49
2.6.4.	ORTEP diagram of 5 with ellipsoids shown at 50%. The anion is omitted for clarity.....	52
3.1.1.	Recent ether-derived alkoxy-carbenes	56
3.2.1.	Synthesis of complex 1	57
3.2.2.	Hydrogenation of complex 1 to form 2 followed by dehydrogenation with TBE to form 3	57
3.2.3.	ORTEP diagrams of 1 (left) and 3 (right) shown at 50% probability. Full disorder models are omitted for clarity. Selected bond distances in 3 (Å): Ir=C 1.880(12), Ir-N 2.179(8), O-C _{carbene} 1.342(16)	57
3.2.4.	Dearomatization of complex 3 with KO ^t Bu to form neutral alkoxy-carbene 4	58
3.2.5.	ORTEP diagram of 4 shown at 50% probability. The full disorder model and anion are omitted for clarity. Selected bond distances (Å): Ir=C 1.882(3), Ir-N _{py} 2.096(3). O-C _{carbene} 1.342(4).....	58
3.2.6.	Stoichiometric reaction of complex 3 with adamantyl azide.....	59
3.2.7.	Stoichiometric reaction of complex 4 with adamantyl azide.....	59
3.2.8.	ORTEP diagrams of 6 (left) and 7 (right) shown at 50% probability. Full disorder models are omitted for clarity. S elected bond distances (Å), Complex 6 : Ir-N ₂ 1.915(5), Ir-N _{py} 1.994(5), N≡N 1.105(8). Complex 7 : Ir-N ₂ 1.881(5), Ir-N _{py} 2.053(4), N≡N 1.083(7)	60
3.2.9.	Proposed catalytic cycle for group transfer imination of CPME. Both [2+2] (B) and [2+3] azide-carbene cycloaddition mechanisms have been previously proposed.....	62
3.2.10.	Stoichiometric reaction of complex 3 with phenyl ethyl ketene	63
3.2.11.	ORTEP diagram of 8 shown at 50% probability. The full disorder model and anion are omitted for clarity	63
3.2.12.	Proposal for ketene O-atom transfer.....	64
3.2.13.	Stoichiometric reaction of complex 3 with isobutyl nitrite	64
3.2.14.	ORTEP diagram of 10 shown at 50% probability. The full disorder model and anion are omitted for clarity.....	65
3.5.1.	^1H NMR Spectrum of $[(\text{PNP}(\text{}^i\text{Pr})_4)\text{Ir}(\eta^2\text{-cod})]\text{BAR}_4^{\text{F}}$ (1) (500 MHz, CD_2Cl_2)	76
3.5.2.	^{13}C NMR Spectrum of $[(\text{PNP}(\text{}^i\text{Pr})_4)\text{Ir}(\eta^2\text{-cod})]\text{BAR}_4^{\text{F}}$ (1) (126 MHz, CD_2Cl_2)	77
3.5.3.	^1P NMR Spectrum of $[(\text{PNP}(\text{}^i\text{Pr})_4)\text{Ir}(\eta^2\text{-cod})]\text{BAR}_4^{\text{F}}$ (1) (202 MHz, CD_2Cl_2)	77
3.5.4.	^1H NMR Spectrum of $[(\text{PNP}(\text{}^i\text{Pr})_4)\text{Ir}(\text{H})_2(\text{THF})]\text{BAR}_4^{\text{F}}$ (2) (500 MHz, CD_2Cl_2)	78
3.5.5.	^{13}C NMR Spectrum of $[(\text{PNP}(\text{}^i\text{Pr})_4)\text{Ir}(\text{H})_2(\text{THF})]\text{BAR}_4^{\text{F}}$ (2) (126 MHz, CD_2Cl_2)	78
3.5.6.	^1P NMR Spectrum of $[(\text{PNP}(\text{}^i\text{Pr})_4)\text{Ir}(\text{H})_2(\text{THF})]\text{BAR}_4^{\text{F}}$ (2) (202 MHz, CD_2Cl_2).....	79
3.5.7.	^1H NMR Spectrum of $[(\text{PNP}(\text{}^i\text{Pr})_4)\text{Ir}=\text{CHO}(\text{C}_5\text{H}_9)]\text{BAR}_4^{\text{F}}$ (3) (500 MHz, CD_2Cl_2)	79
3.5.8.	^{13}C NMR Spectrum of $[(\text{PNP}(\text{}^i\text{Pr})_4)\text{Ir}=\text{CHO}(\text{C}_5\text{H}_9)]\text{BAR}_4^{\text{F}}$ (3) (126 MHz, CD_2Cl_2)	80
3.5.9.	^1P NMR Spectrum of $[(\text{PNP}(\text{}^i\text{Pr})_4)\text{Ir}=\text{CHO}(\text{C}_5\text{H}_9)]\text{BAR}_4^{\text{F}}$ (3) (202 MHz, CD_2Cl_2)	80
3.5.10.	^1H NMR Spectrum of $[(\text{PNP}(\text{}^i\text{Pr})_4)\text{Ir}=\text{CHO}(\text{C}_5\text{H}_9)]$ (4) (500 MHz, C_6D_6)	81
3.5.11.	^{13}C NMR Spectrum of $[(\text{PNP}(\text{}^i\text{Pr})_4)\text{Ir}=\text{CHO}(\text{C}_5\text{H}_9)]$ (4) (126 MHz, C_6D_6)	81
3.5.12.	^1P NMR Spectrum of $[(\text{PNP}(\text{}^i\text{Pr})_4)\text{Ir}=\text{CHO}(\text{C}_5\text{H}_9)]$ (4) (202 MHz, C_6D_6)	82
3.5.13.	^1H NMR Spectrum of cyclopentyl N-(adamantyl)formimidate (5) (500 MHz, CDCl_3)	82
3.5.14.	^{13}C NMR Spectrum of cyclopentyl N-(adamantyl)formimidate (5) (126 MHz, CDCl_3)	83
3.5.15.	^1H NMR Spectrum of $[(\text{PNP}(\text{}^i\text{Pr})_4)\text{Ir}(\text{N}_2)]\text{BAR}_4^{\text{F}}$ (6) (500 MHz, CD_2Cl_2)	83
3.5.16.	^{13}C NMR Spectrum of $[(\text{PNP}(\text{}^i\text{Pr})_4)\text{Ir}(\text{N}_2)]\text{BAR}_4^{\text{F}}$ (6) (126 MHz, CD_2Cl_2)	84
3.5.17.	^1P NMR Spectrum of $[(\text{PNP}(\text{}^i\text{Pr})_4)\text{Ir}(\text{N}_2)]\text{BAR}_4^{\text{F}}$ (6) (202 MHz, CD_2Cl_2)	84
3.5.18.	^1H NMR Spectrum of $[(\text{PNP}(\text{}^i\text{Pr})_4)\text{Ir}(\text{N}_2)]$ (7) (500 MHz, C_6D_6)	85
3.5.19.	^{13}C NMR Spectrum of $[(\text{PNP}(\text{}^i\text{Pr})_4)\text{Ir}(\text{N}_2)]$ (7) (126 MHz, C_6D_6)	85

3.5.20.	³¹ P NMR Spectrum of (PNP(ⁱ Pr) ₄)Ir(N ₂) (7) (202 MHz, C ₆ D ₆)	86
3.5.21.	¹ H NMR Spectrum of [(PNP(ⁱ Pr) ₄)Ir=C=C(Ph)(Et)]BAR ^F ₄ (8) (500 MHz, CD ₂ Cl ₂)	86
3.5.22.	¹³ C NMR Spectrum of [(PNP(ⁱ Pr) ₄)Ir=C=C(Ph)(Et)]BAR ^F ₄ (8) (126 MHz, CD ₂ Cl ₂)	87
3.5.23.	³¹ P NMR Spectrum of [(PNP(ⁱ Pr) ₄)Ir=C=C(Ph)(Et)]BAR ^F ₄ (8) (202 MHz, CD ₂ Cl ₂)	87
3.5.24.	¹ H NMR Spectrum of [(PNP(ⁱ Pr) ₄)Ir(CO)]BAR ^F ₄ (9) (500 MHz, CD ₂ Cl ₂)	88
3.5.25.	¹³ C NMR Spectrum of [(PNP(ⁱ Pr) ₄)Ir(CO)]BAR ^F ₄ (9) (126 MHz, CD ₂ Cl ₂)	88
3.5.26.	³¹ P NMR Spectrum of [(PNP(ⁱ Pr) ₄)Ir(CO)]BAR ^F ₄ (9) (202 MHz, CD ₂ Cl ₂)	89
3.5.27.	³¹ P NMR Spectrum of [(PNP(ⁱ Pr) ₄)Ir(NO)[CH(OC ₄ H ₉)(OC ₅ H ₉)]BAR ^F ₄ (10) generated <i>in-situ</i> (162 MHz, CPME)	89
3.6.1.	ORTEP diagram of 1 with ellipsoids shown at 50%. The anion is omitted for clarity.....	93
3.6.2.	ORTEP diagram of 2 with ellipsoids shown at 50%. The anion is omitted for clarity.....	95
3.6.3.	ORTEP diagram of 3 with ellipsoids shown at 50%. The anion is omitted for clarity.....	97
3.6.4.	ORTEP diagram of 4 with ellipsoids shown at 50%	99
3.6.5.	ORTEP diagram of 6 with ellipsoids shown at 50%. The anion is omitted for clarity.....	101
3.6.6.	ORTEP diagram of 7 with ellipsoids shown at 50%	103
3.6.7.	ORTEP diagram of 8 with ellipsoids shown at 50%. The anion is omitted for clarity.....	105
3.6.8.	ORTEP diagram of 9 with ellipsoids shown at 50%. The anion is omitted for clarity.....	107
3.6.9.	ORTEP diagram of 10 with ellipsoids shown at 50%. The anion is omitted for clarity.....	109
4.1.1.	Proposed mechanisms for olefin hydrosilylation and C-H silylation and relationship to this study	116
4.1.2.	Dehydrogenation of complex 1 with TBE in CPME to form complex 2	117
4.1.3.	Dehydrogenation of complex 1 with TBE in methoxytrimethylsilane to form complex 4	118
4.2.1.	Dehydrogenation of complex 1 with TBE in various organosilanes to yield complexes 3-10	119
4.2.2.	ORTEP diagrams of Complexes 3-11 shown at 50% probability. Full disorder models and anions are omitted for clarity	119
4.2.3.	Equilibration of 3 and 8 in 1:1 equimolar SiMe ₄ :SiMe ₃ (CF ₃)	120
4.2.4.	Proposed mechanism for C(sp ³)-Si bond reductive elimination	123
4.4.1.	Kinetics of reductive elimination at 65 °C with HSiEt ₃ : Ln[Ir] versus time. Experiments shown in duplicate.....	137
4.4.2.	Kinetics of reductive elimination at 23 °C with HSiEt ₃ : Ln[Ir] versus time. Experiments shown in duplicate.....	138
4.4.3.	Kinetics of reductive elimination at 65 °C with DSiEt ₃ : Ln[Ir] versus time. Experiments shown in duplicate.....	139
4.4.4.	Kinetics of catalytic hydrosilylation of <i>tert</i> -butylethylene by 1 at 80 °C: Ln[Silane] versus time. Experiments shown in duplicate	140
4.4.5.	Computed thermodynamics of conversion of 3 to 11	141
4.4.6.	Computed relative stabilities of silyl complexes 3-10	143
4.5.1.	¹ H NMR Spectrum of [(PNP(ⁱ Pr) ₄)IrMe(SiMe ₃)]BAR ^F ₄ (3) (500 MHz, CD ₂ Cl ₂)	143
4.5.2.	¹³ C{ ¹ H} NMR Spectrum of [(PNP(ⁱ Pr) ₄)IrMe(SiMe ₃)]BAR ^F ₄ (3) (126 MHz, CD ₂ Cl ₂)	144
4.5.3.	³¹ P{ ¹ H} NMR Spectrum of [(PNP(ⁱ Pr) ₄)IrMe(SiMe ₃)]BAR ^F ₄ (3) (202 MHz, CD ₂ Cl ₂)	144
4.5.4.	¹ H NMR Spectrum of [(PNP(ⁱ Pr) ₄)IrMe(SiMe ₂ (OMe))]BAR ^F ₄ (4) (500 MHz, CD ₂ Cl ₂)	145
4.5.5.	¹³ C{ ¹ H} NMR Spectrum of [(PNP(ⁱ Pr) ₄)IrMe(SiMe ₂ (OMe))]BAR ^F ₄ (4) (126 MHz, CD ₂ Cl ₂)	145
4.5.6.	³¹ P{ ¹ H} NMR Spectrum of [(PNP(ⁱ Pr) ₄)IrMe(SiMe ₂ (OMe))]BAR ^F ₄ (4) (202 MHz, CD ₂ Cl ₂)	146
4.5.7.	¹ H NMR Spectrum of [(PNP(ⁱ Pr) ₄)IrMe(SiMe(OMe) ₂)]BAR ^F ₄ (5) (500 MHz, CD ₂ Cl ₂)	147
4.5.8.	¹³ C{ ¹ H} NMR Spectrum of [(PNP(ⁱ Pr) ₄)IrMe(SiMe(OMe) ₂)]BAR ^F ₄ (5) (126 MHz, CD ₂ Cl ₂)	147
4.5.9.	³¹ P{ ¹ H} NMR Spectrum of [(PNP(ⁱ Pr) ₄)IrMe(SiMe(OMe) ₂)]BAR ^F ₄ (5) (202 MHz, CD ₂ Cl ₂)	148
4.5.10.	¹ H NMR Spectrum of [(PNP(ⁱ Pr) ₄)IrMe(Si(OMe) ₃)]BAR ^F ₄ (6) (500 MHz, CD ₂ Cl ₂)	149
4.5.11.	¹³ C{ ¹ H} NMR Spectrum of [(PNP(ⁱ Pr) ₄)IrMe(Si(OMe) ₃)]BAR ^F ₄ (6) (126 MHz, CD ₂ Cl ₂)	149
4.5.12.	³¹ P{ ¹ H} NMR Spectrum of [(PNP(ⁱ Pr) ₄)IrMe(Si(OMe) ₃)]BAR ^F ₄ (6) (202 MHz, CD ₂ Cl ₂)	150
4.5.13.	¹ H NMR Spectrum of [(PNP(ⁱ Pr) ₄)IrMe(SiMe ₂ (OEt))]BAR ^F ₄ (7) (500 MHz, CD ₂ Cl ₂)	151
4.5.14.	¹³ C{ ¹ H} NMR Spectrum of [(PNP(ⁱ Pr) ₄)IrMe(SiMe ₂ (OEt))]BAR ^F ₄ (7) (126 MHz, CD ₂ Cl ₂)	151
4.5.15.	³¹ P{ ¹ H} NMR Spectrum of [(PNP(ⁱ Pr) ₄)IrMe(SiMe ₂ (OEt))]BAR ^F ₄ (7) (202 MHz, CD ₂ Cl ₂)	152
4.5.16.	¹ H NMR Spectrum of [(PNP(ⁱ Pr) ₄)IrMe(SiMe ₂ (CF ₃))]BAR ^F ₄ (8) (500 MHz, CD ₂ Cl ₂)	153
4.5.17.	¹³ C{ ¹ H} NMR Spectrum of [(PNP(ⁱ Pr) ₄)IrMe(SiMe ₂ (CF ₃))]BAR ^F ₄ (8) (126 MHz, CD ₂ Cl ₂)	153

4.5.18.	$^{31}\text{P}\{^1\text{H}\}$ NMR Spectrum of $[(\text{PNP}(\text{iPr})_4)\text{IrMe}(\text{SiMe}_2(\text{CF}_3))]\text{BAr}^{\text{F}}_4$ (8) (202 MHz, CD_2Cl_2)	154
4.5.19.	^1H NMR Spectrum of $[(\text{PNP}(\text{iPr})_4)\text{IrMe}(\text{SiMe}_2\text{OSiMe}_3)]\text{BAr}^{\text{F}}_4$ (9) (500 MHz, CD_2Cl_2)	155
4.5.20.	$^{13}\text{C}\{^1\text{H}\}$ NMR Spectrum of $[(\text{PNP}(\text{iPr})_4)\text{IrMe}(\text{SiMe}_2\text{OSiMe}_3)]\text{BAr}^{\text{F}}_4$ (9) (126 MHz, CD_2Cl_2)	155
4.5.21.	$^{31}\text{P}\{^1\text{H}\}$ NMR Spectrum of $[(\text{PNP}(\text{iPr})_4)\text{IrMe}(\text{SiMe}_2\text{OSiMe}_3)]\text{BAr}^{\text{F}}_4$ (9) (202 MHz, CD_2Cl_2)	156
4.5.22.	^1H NMR Spectrum of $[(\text{PNP}(\text{iPr})_4)\text{IrMe}(\text{SiMe}_2\text{OSiMe}_2\text{OSiMe}_3)]\text{BAr}^{\text{F}}_4$ (10) (500 MHz, CD_2Cl_2)	157
4.5.23.	$^{13}\text{C}\{^1\text{H}\}$ NMR Spectrum of $[(\text{PNP}(\text{iPr})_4)\text{IrMe}(\text{SiMe}_2\text{OSiMe}_2\text{OSiMe}_3)]\text{BAr}^{\text{F}}_4$ (10) (126 MHz, CD_2Cl_2)	157
4.5.24.	$^{31}\text{P}\{^1\text{H}\}$ NMR Spectrum of $[(\text{PNP}(\text{iPr})_4)\text{IrMe}(\text{SiMe}_2\text{OSiMe}_2\text{OSiMe}_3)]\text{BAr}^{\text{F}}_4$ (10) (202 MHz, CD_2Cl_2)	158
4.5.25.	^1H NMR Spectrum of $[(\text{PNP}(\text{iPr})_4)\text{IrH}(\text{SiEt}_3)]\text{BAr}^{\text{F}}_4$ (11) (500 MHz, CD_2Cl_2)	159
4.5.26.	$^{13}\text{C}\{^1\text{H}\}$ NMR Spectrum $[(\text{PNP}(\text{iPr})_4)\text{IrH}(\text{SiEt}_3)]\text{BAr}^{\text{F}}_4$ (11) (126 MHz, CD_2Cl_2)	159
4.5.27.	$^{31}\text{P}\{^1\text{H}\}$ NMR Spectrum $[(\text{PNP}(\text{iPr})_4)\text{IrH}(\text{SiEt}_3)]\text{BAr}^{\text{F}}_4$ (11) (202 MHz, CD_2Cl_2)	160
4.6.1.	ORTEP diagram of 3 with ellipsoids shown at 50%. The anion is omitted for clarity	164
4.6.2.	ORTEP diagram of 4 with ellipsoids shown at 50%. The anion is omitted for clarity	166
4.6.3.	ORTEP diagram of 5 with ellipsoids shown at 50%. The anion and the full disorder model of the cation is omitted for clarity	168
4.6.4.	ORTEP diagram of 6 with ellipsoids shown at 50%. The anion and the full disorder model of the cation is omitted for clarity	170
4.6.5.	ORTEP diagram of 7 with ellipsoids shown at 50%. The anion and the full disorder model of the cation is omitted for clarity	172
4.6.6.	ORTEP diagram of 8 with ellipsoids shown at 50%. The anion is omitted for clarity	174
4.6.7.	ORTEP diagram of 9 with ellipsoids shown at 50%. The anion is omitted for clarity	176
4.6.8.	ORTEP diagram of 10 with ellipsoids shown at 50%. The anion is omitted for clarity	178
4.6.9.	ORTEP diagram of 11 with ellipsoids shown at 50%. The anion is omitted for clarity	180
5.1.1.	Figure 5.1.1. Lewis base directed α,α -dehydrogenation resulting in 2 and unsuccessful attempts to undergo nucleophilic displacement with CD_3OD to form B	185
5.2.1.	Reaction of $[(\text{cod})\text{IrCl}]_2$ with PAr^{F}_3 , $\text{NaBAr}^{\text{F}}_4$ in DCM	185
5.2.2.	Hydrogenation of 3 in the presence of trace H_2O in 1,2-difluorobenzene	186
5.2.3.	ORTEPs of 4 (left) and 5 (right). Anions, solvent of crystallization and full disorder models omitted for clarity	186
5.2.4.	ORTEPs of 8 (left), 10 (center) and 11 (right). Anions, solvent of crystallization and full disorder models omitted for clarity	186
5.2.5.	Dehydrogenation of 4 with TBE in MTBE	187
5.2.6.	Dehydrogenation of 6 with TBE in MTBE	187
5.2.7.	Reaction of 7 upon addition of triethylamine in MTBE	187
5.2.8.	Dehydrogenation of 4 with isobutene in 1,2-difluorobenzene	188
5.2.9.	Hydrogenation of 3 in diisopropyl ether	188
5.2.10.	Dehydrogenation of 4 with TBE in fluorobenzene	188
5.2.11.	Proposed mechanism for ionic oligomerization/hydrogenation of isobutene to isooctane	189
5.5.1.	Crude ^1H NMR Spectrum of $[(\text{PAr}^{\text{F}}_3)_2\text{IrH}_2(\text{H}_2\text{O})_2]\text{BAr}^{\text{F}}_4$ (4) (500 MHz, CD_2Cl_2)	193
5.5.2.	Crude $^{31}\text{P}\{^1\text{H}\}$ NMR Spectrum of $[(\text{PAr}^{\text{F}}_3)_2\text{IrH}_2(\text{H}_2\text{O})_2]\text{BAr}^{\text{F}}_4$ (4) (202 MHz, CD_2Cl_2)	194
5.5.3.	^1H NMR Spectrum of $[(\text{PPh}_3)_2\text{Ir}(\text{C}_4\text{H}_7)]$ (8) (500 MHz, C_6D_6)	194
5.5.4.	^{13}C NMR Spectrum of $[(\text{PPh}_3)_2\text{Ir}(\text{C}_4\text{H}_7)]$ (8) (126 MHz, C_6D_6)	195
5.5.5.	$^{31}\text{P}\{^1\text{H}\}$ NMR Spectrum of $[(\text{PPh}_3)_2\text{Ir}(\text{C}_4\text{H}_7)]$ (8) (202 MHz, C_6D_6)	195
5.5.6.	Crude ^1H NMR Spectrum (hydride region) of speculated $[(\text{PAr}^{\text{F}}_3)_2\text{IrH}(\text{C}_4\text{H}_7)]\text{BAr}^{\text{F}}_4$ (9) (500 MHz, CD_2Cl_2)	196
5.5.7.	Crude $^{31}\text{P}\{^1\text{H}\}$ NMR Spectrum of $[(\text{PAr}^{\text{F}}_3)_2\text{IrH}(\text{C}_4\text{H}_7)]\text{BAr}^{\text{F}}_4$ (9) (202 MHz, CD_2Cl_2)	196
5.6.1.	ORTEP diagram of 4 with ellipsoids shown at 50%. The anion is omitted for clarity	198
5.6.2.	ORTEP diagram of 5 with ellipsoids shown at 50%	200
5.6.3.	ORTEP diagram of 8 with ellipsoids shown at 50%	202
5.6.4.	ORTEP diagram of 10 with ellipsoids shown at 50%	204
5.6.5.	ORTEP diagram of 11 with ellipsoids shown at 50%. The anion is omitted for clarity	206

LIST OF TABLES

TABLE	Page
2.6.1. Crystal data and structure refinement for Complex 1	43
2.6.2. Crystal data and structure refinement for Complex 2	45
2.6.3. Crystal data and structure refinement for 2-THF	47
2.6.4. Crystal data and structure refinement for 3-DME	48
2.6.5. Crystal data and structure refinement for Complex 4	50
2.6.6. Crystal data and structure refinement for 5	51
3.2.1. Evaluation of Reaction Conditions	60
3.6.1. Crystal data and structure refinement for complex 1	92
3.6.2. Crystal data and structure refinement for complex 2	94
3.6.3. Crystal data and structure refinement for complex 3	96
3.6.4. Crystal data and structure refinement for complex 4	98
3.6.5. Crystal data and structure refinement for complex 6	100
3.6.6. Crystal data and structure refinement for complex 7	102
3.6.7. Crystal data and structure refinement for complex 8	104
3.6.8. Crystal data and structure refinement for complex 9	106
3.6.9. Crystal data and structure refinement for complex 10	108
4.2.1. Experimental and Computed Metrics of Ir Complexes.....	120
4.2.2. Predicted stability of (methyl)iridium silyl complexes	121
4.2.3. Rates of reductive elimination and trapping by HSiEt ₃	123
4.2.4. H/D isotope effect on the rate of reductive elimination and trapping by HSiEt ₃	124
4.6.1. Crystal data and structure refinement for 3	163
4.6.2. Crystal data and structure refinement for 4	165
4.6.3. Crystal data and structure refinement for 5	167
4.6.4. Crystal data and structure refinement for 6	169
4.6.5. Crystal data and structure refinement for 7	171
4.6.6. Crystal data and structure refinement for 8	173
4.6.7. Crystal data and structure refinement for 9	175
4.6.8. Crystal data and structure refinement for 10	177
4.6.9. Crystal data and structure refinement for 11	179
5.2.1. Preliminary pressure optimization of H ₂ :Isobutene for dimerization/hydrogenation of isobutene	190
5.6.1. Crystal data and structure refinement for 4	197
5.6.2. Crystal data and structure refinement for 5	199
5.6.3. Crystal data and structure refinement for 8	201
5.6.4. Crystal data and structure refinement for complex 10	203
5.6.5. Crystal data and structure refinement for 11	205

Chapter I

INTRODUCTION TO sp^3 BOND ACTIVATION AND FUNCTIONALIZATION

1.1 Scope of this work

This dissertation describes research on the activation of inert sp^3 C-H, C-O and C-Si bonds using cationic iridium complexes with the goal of developing new oxidative, catalytic transformations. Chapter 2 outlines a study of intermolecular vs intramolecular C-H activation at an iridium bis(phosphine) complex that was shown to be competent for both alkane dehydrogenation and C-O bond cleavage of alkyl ethers. Chapter 3 describes the formation of an alkoxy-carbene generated via α,α -dehydrogenation (double C-H activation) of cyclopentyl methyl ether at a cationic pincer-supported PNP iridium complex and its reactivity in atom and group-transfer reactions. Chapter 4 explores the unexpected reactivity of a family of methyl silanes towards C(sp^3)-Si activation in the presence of a cationic pincer-supported PNP iridium complex and the effects of silicon substituents on kinetics and thermodynamics. While chapters 2-4 describe different sp^3 bond activations (Chapter 2 C-H/C-O, Chapter 3 C-H, Chapter 4 C-Si) at cationic iridium complexes, all modes of activation are suspected to proceed via a reactive $14 e^-$ Ir(I) complex generated *in-situ* via dehydrogenation with *tert*-butylethylene (**Figure 1.1.1**).

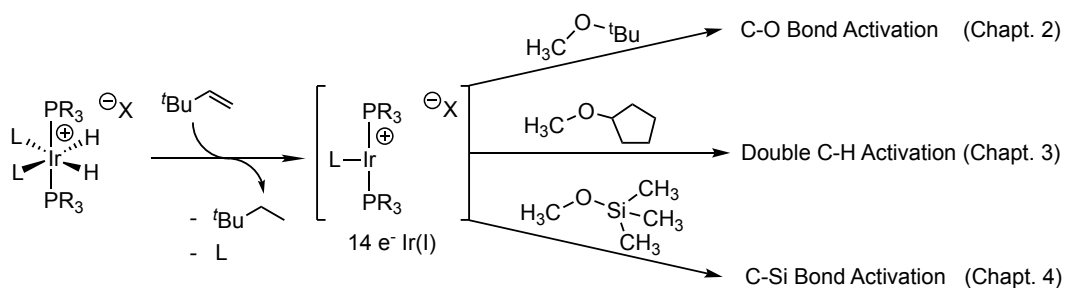


Figure 1.1.1. General reaction involving dehydrogenation of an $18 e^-$ Ir(III) complex with *tert*-butylethylene (TBE) to generate a reactive $14 e^-$ Ir(I) complex which can result in C-O, C-H and C-Si bond activation.

Finally, Chapter 5 details progress towards an acidic iridium bis(phosphine) complex capable of tandem catalytic oligomerization and hydrogenation of simple olefins to branched alkanes (**Figure 1.1.2**).

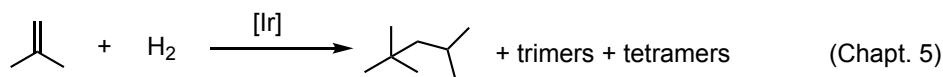


Figure 1.1.2. General reaction for tandem oligomerization and hydrogenation of simple olefins to branched alkanes.

1.2 C-H Activation from Alkanes to Ethers

Green chemistry has become increasingly important over the past several years owing to limited petrochemical resources and society's need for more environmentally friendly processes. As part of this movement, the 12 Principles of Green Chemistry was developed in 1998.¹ The development of catalytic reactions as well as transformations with improved atom economy are central tenets of green chemistry; this dissertation contributes to the development of these components, which will hopefully lead to more environmentally friendly transformations.

The use of transition-metal complexes to catalytically activate and functionalize inert C-H bonds has been a desire since the first observation of benzene C-H activation by Chatt and Davidson's $\text{RuCl}_2(\text{dmpe})_2$ complex in 1965 (**Figure 1.2.1, left**).²

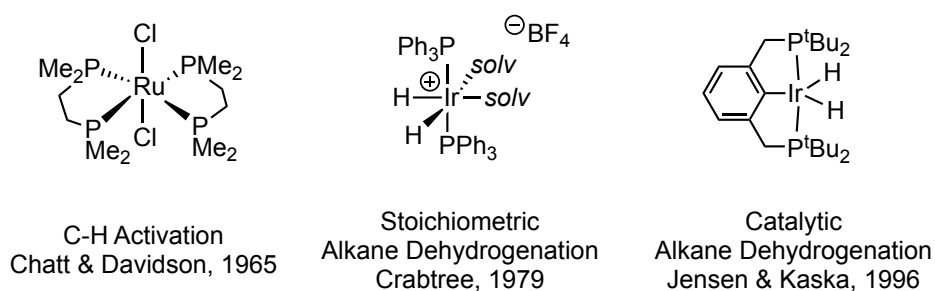


Figure 1.2.1. First transition-metal complex observed to activate C-H bonds (left). First homogeneous metal complex to stoichiometrically dehydrogenation an alkane (center). First neutral iridium pincer complex to afford high turnovers numbers for alkane dehydrogenation (right).

Since then, tremendous progress has been made in the area of alkane dehydrogenation. In 1979 the first example of stoichiometric intermolecular alkane dehydrogenation was demonstrated by the Crabtree group using a cationic bis(phosphine) iridium complex³ (**Figures 1.2.1, center**), a finding that perplexed the organometallic community at the time by highlighting a case where intermolecular C-H activation appeared to be preferred over the corresponding intramolecular activation. Selectivity for inter- versus intramolecular activation continues to challenge organometallic chemists as new methods are developed for C-H activation and functionalization. This topic of intramolecular vs intermolecular selectivity is discussed in more detail in Chapter 2 surrounding the observation of C-O bond cleavage of methyl *tert*-butyl ether.

Despite stoichiometric alkane dehydrogenation having been demonstrated in 1979, an efficient catalytic version of this transformation was not known until 1996 when Jensen and Kaska demonstrated that a thermally stable neutral iridium pincer complex catalyzes the transfer dehydrogenation of cyclooctane at a rate of 12 turnovers/minute.⁴ (**Figure 1.2.1, right**) Since 1996,

effective alkane dehydrogenation catalysts have favored electron-rich pincer iridium complexes, with modern variants showing rates as high as 115 turnovers/minute.⁵

While highly-active catalysts have been developed for alkane dehydrogenation, less research has focused on direct methods towards C-H functionalization of ethers despite their ubiquity among organic compounds. Recent work has identified several late transition-metals, predominantly iridium, capable of ether C-H activation at the α position to give a metal alkoxyalkyl. Depending on the ether substrate and the identity of the metal ion, several competing mechanisms are accessible including vinyl ether formation through β -hydride elimination⁶⁻⁸ (**Figure 1.2.2, eq 1**), C-O bond cleavage via α -alkoxide elimination⁹ (**Figure 1.2.2, eq 2**) or alkoxy-carbene formation through α -hydride elimination (**Figure 1.2.2, eq 3**) (α,α -dehydrogenation).¹⁰⁻¹⁷

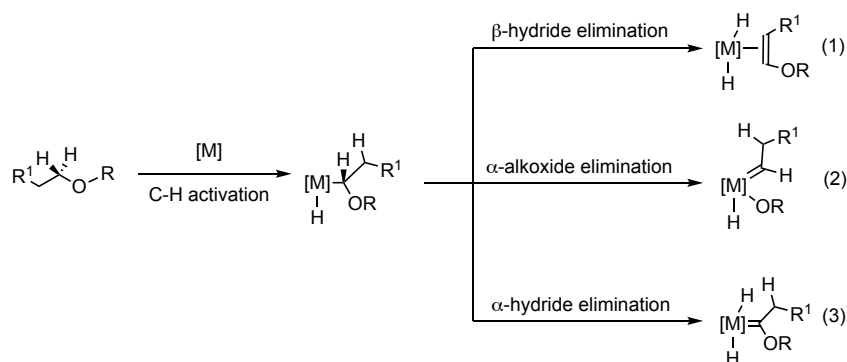


Figure 1.2.2. Potential competing mechanisms that may occur following initial ether C-H activation.

Of these potential products, only vinyl ether formation has been observed under catalytic conditions (**Figure 1.2.3**), while the observation of C-O bond cleavage via α -alkoxide elimination has led to productive catalysis in the thermodynamically favored reverse direction for olefin hydroaryloxylation¹⁸ (**Figure 1.2.4**).

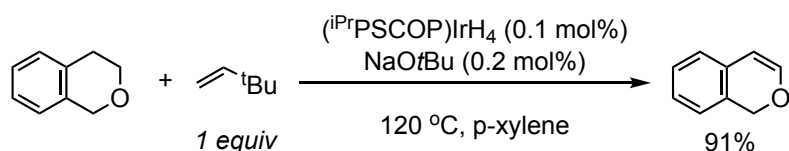


Figure 1.2.3. Representative reaction for catalytic ether dehydrogenation to form vinyl ethers.¹⁹

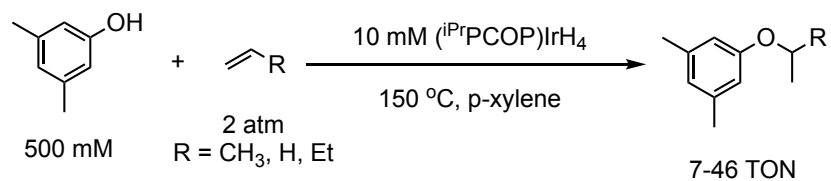


Figure 1.2.4. Representative reaction for catalytic hydroaryloxylation to form ethers.¹⁸

The first observation of ether α,α -dehydrogenation to form an alkoxy carbene was demonstrated by Werner in 1992 in an intramolecular fashion with a phosphinoether (**Figure 1.2.5, left**).²⁰ Later that year, Carmona demonstrated an example of intermolecular alkoxy carbene formation of tetrahydrofuran using an iridium tris(pyrazolyl)borate complex (**Figure 1.2.5, right**).²¹ Since 1992, ether derived alkoxy carbenes have been prepared using Ir, Os, Ru, and Pt.¹⁰⁻¹¹

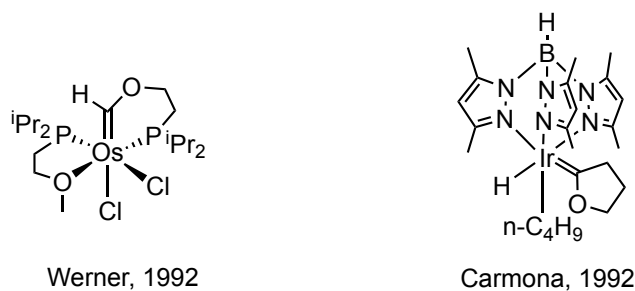


Figure 1.2.5. First examples of intramolecular (left) and intermolecular (right) ether activation to form alkoxy carbenes.

Unlike Schrock carbenes which are nucleophilic at carbon, alkoxy carbenes can include either Fischer carbenes which are electrophilic at carbon or Roper-type carbenes which are nucleophilic at the metal owing to a high-lying, filled d_z^2 orbital^{12,17} (**Figure 1.2.6**). Fischer carbenes have pK_a 's that span a range of ~ 25 units²² and thus suggest a wide range of potential applications, while Roper-type carbenes have been observed to facilitate atom and group-transfer reactions.^{11,12,17} Though both Fischer carbenes and Roper-type carbenes have distinct reactivity, all alkoxy carbenes can function as π -acids owing to the presence of a vacant p-orbital with which backdonation can occur from a metal d_π orbital (**Figure 1.2.7**). In fact, prior to this work, the only example of a catalytic reaction of an ether that proceeded via an alkoxy carbene intermediate was a report by the Grubbs group of a formal synthetic cycle for the imination of methyl *tert*-butyl ether to a formimidate (**Figure 1.2.8**).¹⁷ This reactivity is most consistent with Roper-type alkoxy carbenes and efforts to elucidate and expand this chemistry are described in Chapter 3.

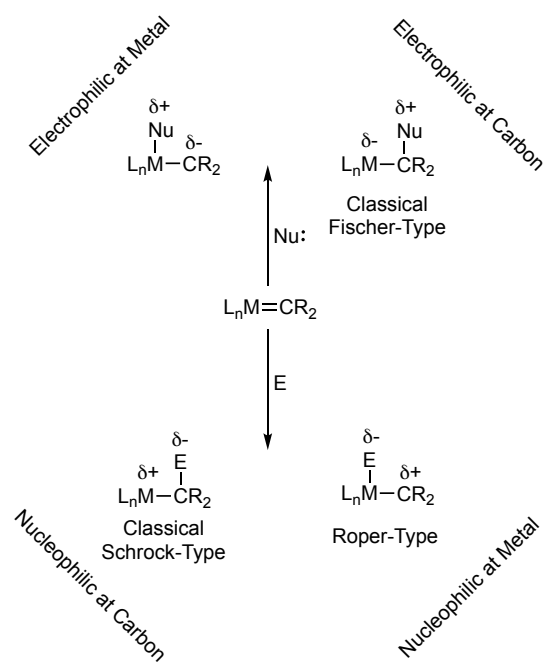


Figure 1.2.6. Possible reactivity of metal carbenes with electrophilic and nucleophilic reagents. Adapted from ²³

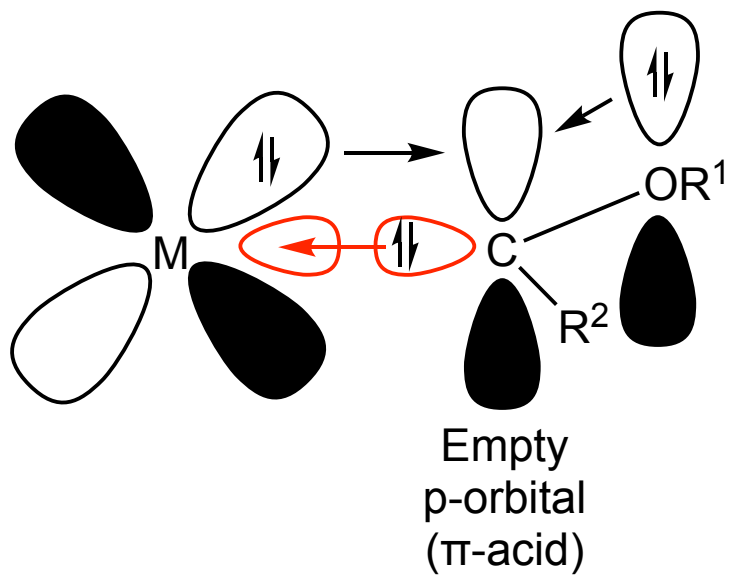


Figure 1.2.7. Molecular orbital diagram of alkoxy carbenes.

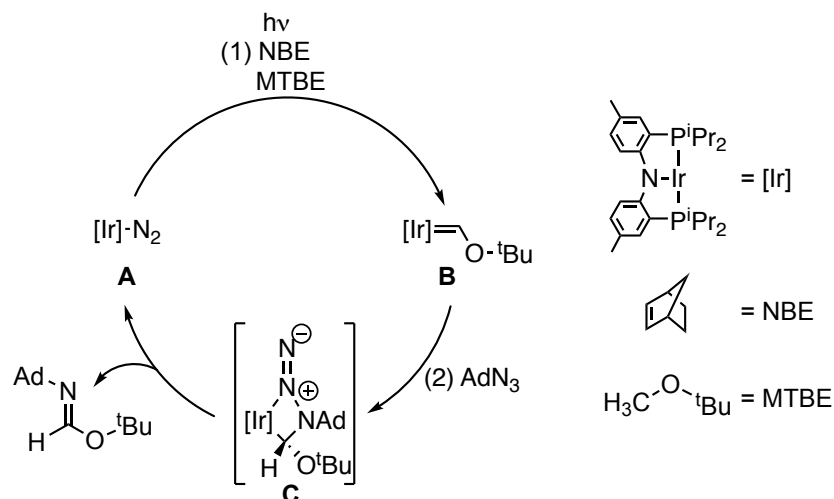


Figure 1.2.8. Proposed synthetic cycle for the imination of methyl *tert*-butyl ether.¹⁷

1.3 C-H Silylation and Olefin Silylation

Though ether activation and functionalization via an alkoxy-carbene intermediate are among many conceivable chemical transformations that could functionalize inert C-H bonds, direct C-H silylation (**Figure 1.3.1**) has been a growing area of interest among organometallic chemists for the synthesis of organosilanes. While traditional syntheses of organosilanes have previously relied on utilizing activated starting materials, including halogenated reagents, organolithiates and Grignard reagents, these methods form stoichiometric amounts of metal salt byproducts and are not considered to be atom-economical. Direct C-H silylation provides the opportunity to access similar products while avoiding stoichiometric byproducts. Pioneering work in this field has been led by the Hartwig group and a recent in-depth review of directed and undirected C-H silylation was reported in 2015.²⁴

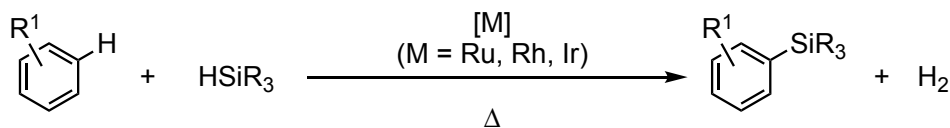


Figure 1.3.1. Representative example of *sp*² C-H silylation.

Alternatively, organosilanes can also be synthesized through olefin hydrosilylation (**Figure 1.3.2**). While this process does not involve the functionalization of an inert C-H bonds, it is still an atom economical process. Olefin hydrosilylation is a more

mature process compared to C-H silylation. Industrial catalytic processes for hydrosilylation rely primarily on Ir²⁵ and Pt catalysts²⁶, with Karstedt's catalyst being most well-known. A review of other transition-metals that catalyze olefin hydrosilylation has been published by Beller.²⁷

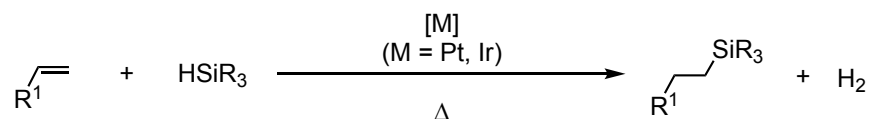


Figure 1.3.2. Representative example of olefin hydrosilylation.

While both C-H silylation and olefin silylation operate via distinct mechanism, both reactions require C-Si reductive elimination prior to product formation (**Figure 1.3.3**). The work presented in Chapter 4 describes studies on C(sp³)-Si reductive elimination from an iridium(III) center and how silicon substituents affect the kinetics and thermodynamics. Information gleaned from these findings has implications for both C-H silylation and olefin silylation.

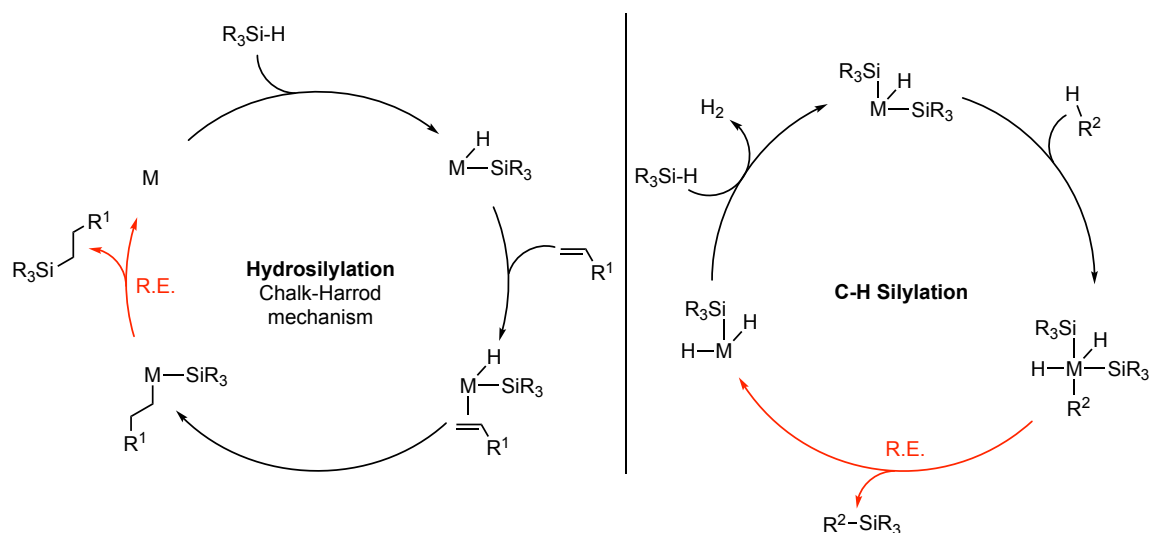


Figure 1.3.3. Proposed mechanism for olefin hydrosilylation²⁶ and C-H silylation²⁸.

1.4 Acidic Metal Complexes

The net ionic charge of organotransition-metal complexes is an important determinant of their reactivity, the work presented in this dissertation has focused on cationic iridium complexes with a central focus to generate less electron-rich metal

ions through the use of non-coordinating anions. By shifting from a neutral complex to a cationic complex, the cationic system has one less electron at the metal making it more acidic when compared to an analogous neutral variant. In fact, many cationic transition-metal complexes bearing non-coordinating anions (specifically triflate) suffer from “Hidden Acid Catalysis”²⁹ whereby trace amounts of strong acids (e.g. triflic acid) are formed and catalyze the reaction. The Hartwig group has specifically demonstrated that triflic acid can catalyze hydroamination and hydroalkoxylation comparable to reactions initiated with metal triflates.³⁰

Though “Hidden Acid Catalysis” is a real concern for determining whether a process is acid catalyzed or metal catalyzed, inclusion of a metal hydrides make this process more challenging. Metal hydrides have been a staple of organometallic chemistry since Hieber’s 1931 claim of $\text{H}_2\text{Fe}(\text{CO})_4$,³¹ which remained a controversial topic until 1950.³² The pK_a of $\text{H}_2\text{Fe}(\text{CO})_4$ is $4.4 = \text{pK}_1$ and $\sim 14 = \text{pK}_2$ in H_2O .³³ Despite their potential acidity, metal hydrides have played a vital role in many catalytic reactions owing to their ability to insert into carbon-carbon and carbon-heteroatom multiple bonds. While metal hydrides can come from a variety of sources, the use of dihydrogen is quite common proceeding through either a stable or transient dihydrogen complex (**Figure 1.4.1**). The first example of an isolable metal dihydrogen complex was published by Kubas³⁴ with Mo and W in 1984 and later in 2003 a highly acidic iridium dihydrogen complex was reported by Heinekey.³⁵

The formation of metal hydrides from dihydrogen can occur via two different mechanisms, homolytic bond cleavage (oxidative addition) (**Figure 1.4.1, eq 1**) and heterolytic bond cleavage (**Figure 1.4.1, eq 3**). Though homolytic bond cleavage is common for many late-transition metals with highly active hydrogenation catalysts, such as Crabtree’s catalyst³⁶, well known to operate via this mechanism, metal complexes capable of heterolytic dihydrogen bond cleavage have resulted in successful platforms for catalytic ionic hydrogenation of carbonyl, ethereal and polyol substrates (**Figure 1.4.2**).³⁷⁻⁴³

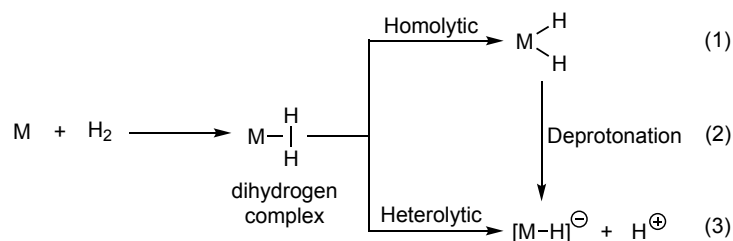


Figure 1.4.1. Mechanism for dihydrogen activation. Homolytic bond cleavage (1) and heterolytic bond cleavage (3).

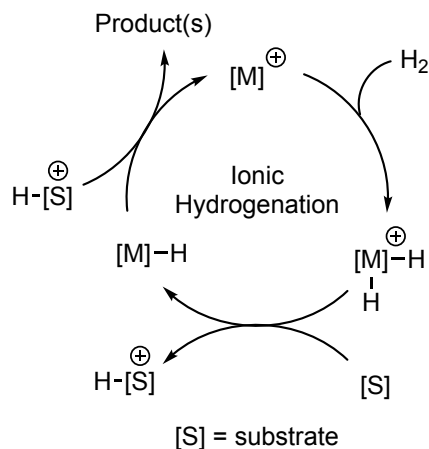


Figure 1.4.2. General mechanism for ionic hydrogenation

Traditionally, metal hydrides are often thought as a source of H^- , however metal hydrides span a hydricity continuum and can act as sources of H^+ depending on the metal and supporting ligand electronics. Just as a cationic metal complexes results in a more acidic metal complex when compared to a neutral variant, any resulting hydrides are more acidic when the anion is too weakly-coordinating to give a neutral species. This enhanced hydride acidity can be compounded by incorporation of other π -acidic ancillary ligands. Carbon monoxide is often considered the quintessential example of a potent π -acid. When bound to a metal, carbon monoxide accepts electron density from a metal d_π orbital into an empty π^* orbital and thus reduces the overall electron density on the metal. The experimental manifestation of this effect has resulted in using carbonyl stretching as a reporter of ligand electron donor power, notably for phosphine ligands (**Figure 1.4.3**).

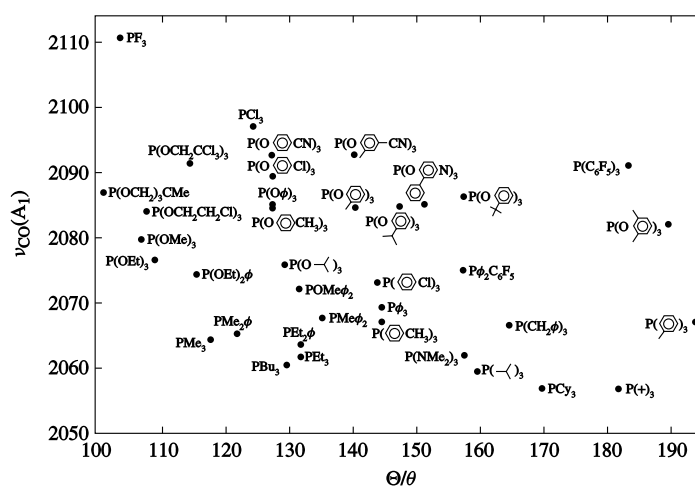


Figure 1.4.3. Graph of carbonyl stretching frequency vs. phosphine cone angle.⁴⁴

While carbon monoxide is a strong π -acceptor and an invaluable tool to evaluate phosphine electronics, phosphines themselves can also be strong π -acceptors in certain cases. Extensive work by the Roddick group has examined a number of π -acidic fluoroalkylphosphines (**Figure 1.4.4, left, center**) which result in highly acidic metal hydrides.⁴⁵⁻⁴⁶ These hydrides are so acidic that deprotonation occurs with unconventional bases such as diethyl ether or acetone.⁴⁶ A large table of observed pK_a values for 179 metal hydrides has been published by Morris and range from -4 to 51.⁴⁷ The work presented in Chapter 5 explores highly acidic cationic iridium complexes supported by electron-poor tris(3,5-bis(trifluoromethyl)phenyl)phosphine (**Figure 1.4.4, right**) for catalytic ionic hydrogenation.

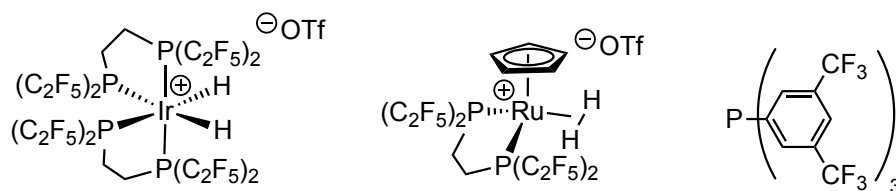


Figure 1.4.4. Fluoroalkylphosphine supported iridium complex (left), Fluoroalkylphosphine supported ruthenium complex (center), tris(3,5-bis(trifluoromethyl)phenyl)phosphine (right)

1.5 References

- (1) Anastas, P. T.; Warner, J. C. *Green Chemistry: Theory and Practice*, Oxford University Press: New York, **1998**, 30.
- (2) Chatt, J and Davidson J. M. The Tautomerism of Arene and Ditertiary Phosphine Complexes of Ruthenium(0), and the Preparation of New Types of Hydrido-Complexes of Ruthenium(II). *J. Chem. Soc.* **1965**, 0, 843-855.
- (3) Crabtree, R. H.; Mihelcic, J. M.; Quirk, J. M. Iridium Complexes in Alkane Dehydrogenation. *J. Am. Chem. Soc.* **1979**, 101(26), 7738-7740.
- (4) Gupta, M.; Hagen, C.; Flesher, R. J.; Kaska, W. C.; Jensen, C. M. A Highly Active Alkane Dehydrogenation Catalyst: Stabilization of Dihydrido Rhodium and Iridium Complexes by a P-C-P Pincer Ligand. *Chem. Commun.*, **1996**, 2083-2084.
- (5) Kumar, A.; Bhatti, T. M.; Goldman, A. S. Dehydrogenation of Alkanes and Aliphatic Groups by Pincer-Ligated Metal Complexes. *Chem. Rev.* **2017**, 12357-12384.
- (6) Lyons, T. W.; Beier, D.; Brookhart, M. Iridium Pincer-Catalyzed Dehydrogenation of Ethers Featuring Ethylene as the Hydrogen Acceptor. *Organometallics*. **2015**, 34(16) 4058-4062.

- (7) Whited, M. T.; Zhu, Y.; Timpa, S. D.; Chen, C. H.; Foxman, B. M.; Ozerov, O. V.; Grubbs, R. H. Probing the C-H Activation of Linear and Cyclic Ethers at (PNP)Ir. *Organometallics*. **2009**, 28(15), 4560–4570.
- (8) Luecke, H. F.; Arndtsen, B. A.; Burger, P.; Bergman, R. G. Synthesis of Fischer Carbene Complexes of Iridium by C-H Bond Activation of Methyl and Cyclic Ethers: Evidence for α -Hydrogen Migration. *J. Am. Chem. Soc.* **1996**, 118 (10), 2517–2518.
- (9) Kundu, S.; Choi, J.; Wang, D. Y.; Choliy, Y.; Emge, T. J.; Krogh-Jespersen, K.; Goldman, A. S. Cleavage of Ether, Ester, and Tosylate C(sp^3)-O Bonds by an Iridium Complex, Initiated by Oxidative Addition of C-H Bonds. Experimental and Computational Studies. *J. Am. Chem. Soc.* **2013**, 135(13), 5127–5143.
- (10) Werner, H. Carbene-Transition Metal Complexes Formed by Double C-H Activation. *Angew. Chem. Int. Ed.* **2010**, 49, 4714–4728.
- (11) Whited, M. T.; Grubbs, R. H. Late Metal Carbene Complexes Generated by Multiple C-H Activations: Examining the Continuum of M=C Bond Reactivity. *Acc. Chem. Res.* **2009**, 42, 10, 1607–1616.
- (12) Whited, M. T.; Grubbs, R. H. Oxygen-Atom Transfer from Carbon Dioxide to a Fischer Carbene at (PNP)Ir. *J. Am. Chem. Soc.* **2008**, 130, 18, 5874–5875.
- (13) Boutry, O.; Gutiérrez, E.; Monge, A.; Nicasio, M. C.; Pérez, P. J.; Carmona, E. Double Carbon-Hydrogen Activation at the α -Carbon of Cyclic Ethers by $\text{Tp}^*\text{Ir}(\text{C}_2\text{H}_4)_2$. *J. Am. Chem. Soc.* **1992**, 114, 7288–7290.
- (14) Gutiérrez-Puebla, E.; Monge, Á.; Nicasio, M. C.; Pérez, P. J.; Poveda, M. L.; Carmona, E. C-H Bond Activation of Benzene and Cyclic Ethers by TpIr^{III} Species. *Chem. A Eur. J.* **1998**, 4(11), 2225–2236.
- (15) Valpuesta, J. E. V.; Álvarez, E.; López-Serrano, J.; Maya, C.; Carmona, E. Reversible Double C-H Bond Activation of Linear and Cyclic Ethers to Form Iridium Carbenes. *Chem. A Eur. J.* **2012**, 18(41), 13149–13159.
- (16) Slugovc, C.; Mereiter, K.; Trofimenko, S.; Carmona, E. Generation of Heteroatom-Substituted Carbene Complexes of Iridium by Double C-H Activation of Ether and Amine Substrates. *Angew. Chemie. Int. Ed.* **2000**, 39 (12), 2158–2160.
- (17) Whited, M. T.; Grubbs, R. H. A Catalytic Cycle for Oxidation of *tert*-Butyl Ether by a Double C-H Activation-Group Transfer Process. *J. Am. Chem. Soc.* **2008**, 130, 49, 16476–16577.
- (18) Haibach, M. C.; Guan, C.; Wang, D. Y.; Li, B.; Lease, N.; Steffens, A. M.; Krogh-Jespersen, K.; Goldman, A. S. Olefin Hydroaryloxylation Catalyzed by Pincer-Iridium Complexes. *J. Am. Chem. Soc.* **2013**, 135, 40, 15062–15070.
- (19) Yao, W.; Zhang, Y.; Jia, X.; Huang, Z. Selective Catalytic Transfer Dehydrogenation of Alkanes and Heterocycles by Iridium Pincer Complex. *Angew. Chem. Int. Ed.* **2014**, 53, 1390–1394.

- (20) Werner, H.; Weber, B.; Nürnberg, O.; Wolf, J. Carbene Osmium Complexes by Double Metalation of Alkoxyalkyl- and Aminoalkylphosphanes. *Angew. Chem. Int Ed.* **1992**, 31, 8, 1025-1027.
- (21) Boutry, O.; Gutiérrez, E.; Monge, A.; Nicasio, M. C.; Pérez, P. J.; Carmona, E. Double Carbon-Hydrogen Activation at the α -Carbon of Cyclic Ethers by $\text{Tp}^*\text{Ir}(\text{C}_2\text{H}_4)_2$. *J. Am. Chem. Soc.* **1992**, 114, 7288-7290.
- (22) Bernasconi, C. F.; Ragains, M. L. Factors that Affect the Kinetic and Thermodynamic Acidities of Fischer Carbene Complexes: New Insights from the Study of the Cationic (methoxymethylcarbene)dicarbonylpentamethylcyclopentadienyl iron $[[\text{Cp}^*(\text{Co})_2\text{Fe}=\text{C}(\text{Ome})\text{Me}]^+]$ in Aqueous Acetonitrile. *J. Organomet. Chem.* **2005**, 690, 5616-5624.
- (23) Gallop, M. A.; Roper, W. R. Carbene and Carbyne Complexes of Ruthenium, Osmium, and Iridium. *Adv. Organomet. Chem.* **1986**, 25, 121-198.
- (24) Cheng, C.; Hartwig, J. F. Catalytic Silylation of Unactivated C-H Bonds. *Chem. Rev.* **2015**, 115, 17, 8946-8975.
- (25) Gao, W.; Ding, S. Progress on Iridium-Catalyzed Hydrosilylation of Alkenes and Alkynes. *Synthesis.* **2020**, 52, 3549-3563.
- (26) Troegel, D.; Stohrer, J. Recent Advances and Actual Challenges in Late Transition Metal Catalyzed Hydrosilylation of Olefins From an Industrial Point of View. *Coord. Chem. Rev.* **2011**, 255, 1440-1459.
- (27) Almeida, L. D.; Wang, H.; Junge, K.; Cui, X.; Beller, M. Recent Advances in Catalytic Hydrosilylation: Developments Beyond Traditional Platinum Catalysts. *Angew. Chem. Int. Ed.* **2021**, 60, 550-565.
- (28) Karmel, C.; Hartwig, J. F. Mechanism of the Iridium-Catalyzed Silylation of Aromatic C-H Bonds. *J. Am. Chem. Soc.* **2020**, 142, 10494-10505.
- (29) Dang, T. T.; Boeck, F.; Hintermann, L. Hidden Brønsted Acid Catalysis: Pathways of Accidental or Deliberate Generation of Triflic Acid from Metal Triflates. *J. Org. Chem.* **2011**, 76, 9353-9361.
- (30) Rosenfeld, D. C.; Shekhar, S.; Takemiya, A.; Utsunomiya, M.; Hartwig, J. F. Hydroamination and Hydroalkoxylation Catalyzed by Triflic Acid. Parallels to Reactions Initiated with Metal Triflates. *Org. Lett.* **2006**, 8, 19, 4179-4182.
- (31) Hieber, W.; Leutert, F. *Naturwissenschaften.* **1931**, 19, 350-361.
- (32) Crabtree, R. H. *The Organometallic Chemistry of Transition Metals*, 6th ed.; Wiley, **2014**, 86.
- (33) Pearson, R. G. The Transition-Metal-Hydrogen Bond. *Chem. Rev.* **1985**, 85, 41-49.
- (34) Kubas, G. J.; Ryan, R. R.; Swanson, B. I.; Vergamini, P. J.; Wasserman, H. J. Characterization of the First Examples of Isolable Molecular Hydrogen Complexes, $\text{M}(\text{CO})_3(\text{PR}_3)_2(\text{H}_2)$ (M = Molybdenum or Tungsten; R = Cy or isopropyl). Evidence for a Side-on Bonded Dihydrogen Ligand. *J. Am. Chem. Soc.* **1984**, 106, 451-452.

- (35) Pons, V.; Heinekey, M. D. An Elogated Dihydrogen Complex of Iridium. *J. Am. Chem. Soc.* **2003**, 125, 8428-8429.
- (36) Crabtree, R. H.; Felkin, H.; Morris, G. E. Cationic Iridium Diolefin Complexes as Alkene Hydrogenation Catalysts and the Isolation of Some Related Hydrido Complexes. *J. Organomet. Chem.* **1977**, 141, 205-215.
- (37) Schlaf, M. Selective Deoxygenation of Sugar Polyols to α,ω -diols and other oxygen content reduced materials—a new challenge to homogeneous ionic hydrogenation and hydrogenolysis catalysis. *Dalton Trans.* **2006**, 4645-4653.
- (38) Eisenstein, O.; Crabtree, R. H. Outer Sphere Hydrogenation Catalysis. *New J. Chem.* **2013**, 37, 21-27.
- (39) Brewster, T. P.; Miller, A. J. M.; Heinekey, M. D.; Goldberg, K. I. Hydrogenation of Carboxylic Acids Catalyzed by Half-Sandwich Complexes of Iridium and Rhodium. *J. Am. Chem. Soc.* **2013**, 135, 43, 16022-16025.
- (40) Brewster, T. P.; Rezayee, N. M.; Culakova, Z.; Sanford, M. S.; Goldberg, K. I. Base-Free Iridium-Catalyzed Hydrogenation of Esters and Lactones. *ACS Catal.* **2016**, 6, 5, 3113-3117.
- (41) Goldberg, J. M.; Goldberg, K. I.; Heinekey, M. D.; Burgess, S. A.; Lao, D. B.; Linehan, J. C. Detection of an Iridium-Dihydrogen Complex: Proposed Intermediate in Ionic Hydrogenation. *J. Am. Chem. Soc.* **2017**, 139, 12638-12646.
- (42) Bullock, M. R.; Voges, M. H. Homogeneous Catalysis with Inexpensive Metals: Ionic Hydrogenation of Ketones with Molybdenum and Tungsten Catalysts. *J. Am. Chem. Soc.* **2000**, 122, 12594-12595.
- (43) Schlaf, M.; Ghosh, P.; Fagan, P. J.; Hauptman, E.; Bullock, M. R. Metal-Catalyzed Selective Deoxygenation of Diols to Alcohols. *Angew. Chem. Int. Ed.* **2001**, 40, 20, 3887-3890.
- (44) Tolman, C. A. Steric Effects of Phosphorus Ligands in Organometallic Chemistry and Homogeneous Catalysis. *Chem. Rev.* **1977**, 77, 3, 313-348.
- (45) Koola, J. D.; Roddick, D. M. Activation of Hydrocarbons by a Ruthenium(II) (Fluoroalkyl)phosphine Hydride Complex. *J. Am. Chem. Soc.* **1991**, 113, 1450-1451.
- (46) Schnabel, C. R.; Roddick, D. M. (Fluoroalkyl)phosphine Hydride Complexes of Iridium. Synthesis and structures of $(dfep)_2IrH$ and $(dfep)_2Ir_2(H)(\mu-H)_2(\mu-O_3SCF_3)$. *Organometallics.* **1993**, 12, 704-711.
- (47) Morris, R. H. Estimating the Acidity of Transition Metal Hydride and Dihydrogen Complexes by Adding Ligand Acidity Constants. *J. Am. Chem. Soc.* **2014**, 136, 1948-1959.

Chapter II

EVIDENCE FOR REVERSIBLE CYCLOMETALATION IN ALKANE DEHYDROGENATION AND C-O BOND CLEAVAGE AT IRIIDIUM BIS(PHOSPHINE) COMPLEXES

Reprinted with permission from Scott M. Chapp and Nathan D. Schley. *Organometallics*. 2017, 36, 4355-4358. Copyright 2017 American Chemical Society.

2.1 Introduction

The cleavage of C-H bonds by oxidative addition to homogeneous transition metal complexes has emerged as a strategy of significant importance for the activation of otherwise inert organic substrates towards catalytic functionalization. Early reports of stoichiometric alkane dehydrogenation at cationic iridium(III) complexes laid the groundwork for extensive research in catalytic alkane dehydrogenation at pincer-supported neutral iridium complexes. Efficient alkane dehydrogenation catalysts based on this work now play a key role in catalytic alkane metathesis systems.¹⁻² In 1979 the Crabtree group reported that cationic bis(phosphine) iridium complexes of the type $[(\text{PR}_3)_2\text{IrH}_2(\text{solv})_2]^+\text{X}^-$ ($\text{solv} = \text{acetone}$, $\text{X} = \text{BF}_4$) reacted in stoichiometric fashion with certain alkanes leading to stable iridium(I) olefin or iridium(III) polyenyl products (**Figure 2.1.1, eq 1**).³ These observations are considered to be the first example of alkane dehydrogenation by homogeneous transition metal complexes, and were immensely important to the nascent field of C-H activation.

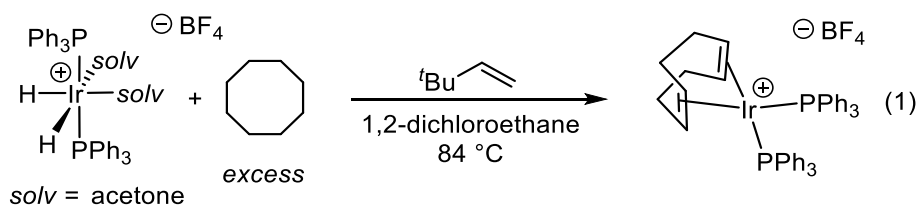


Figure 2.1.1. First example of stoichiometric alkane dehydrogenation by a homogeneous metal complex

The observed selectivity for intermolecular C-H activation over intramolecular cyclometalation of the phosphine ligand was a unique feature of the Crabtree system that proved perplexing at the time.⁴ One hypothesis considered that cyclometalation might occur reversibly prior to intermolecular alkane activation.⁵ Evidence for competing, irreversible cyclometalation of triphenylphosphine in Bergman's seminal demonstration of direct C-H oxidative addition of alkanes at

Cp*Ir complexes^{6,7} ultimately led to the hypothesis that cyclometalation in the Crabtree system was disfavored for steric reasons.⁴ Although this family of cationic complexes has not been shown to effect efficient *catalytic* alkane dehydrogenation,⁸ key results from these initial reports including the finding that tert-butyl ethylene (TBE) is an unusually effective hydrogen acceptor, remain critical to modern embodiments of alkane dehydrogenation catalysts.^{9,10}

Our research group has been examining the α,α -dehydrogenation of ethers to the corresponding alkoxy-carbenes, and has demonstrated the facile and reversible sequential C-H bond cleavage of pendant ethers to give the corresponding alkoxy-carbenes at cationic iridium centers.¹¹ As part of our exploration of intermolecular ether activation we have been investigating analogous complexes to those used in Crabtree's initial report with the hypothesis that the known α,β -dehydrogenation behavior with alkanes would translate to reactivity in the α,α -dehydrogenation of ethers.^{3,12-13} We now report the unexpected ability of the cationic complex $[(PPh_3)_2IrH_2(THF)_2]PF_6$ (**1**) to cleave the C-O bond in methyl tert-butyl ether (MTBE) on dehydrogenation as well as the observation, isolation, and crystallographic characterization of a product resulting from intramolecular cyclometalation of the phosphine ligand. Though not previously observed, this same cyclometalated complex was suggested to form reversibly¹³ from the 1979 report on alkane dehydrogenation³ at cationic iridium centers.³ The isolation of this species allows us to shed light on a key mechanistic question surrounding selectivity for intermolecular versus intramolecular C-H activation in this class of complexes.

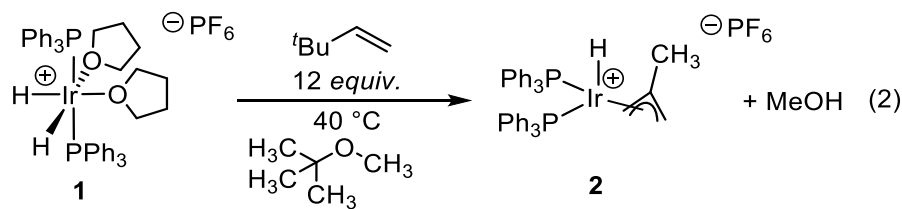


Figure 2.1.2. Observation of C-O bond cleavage of MTBE upon dehydrogenation of **1** with TBE

2.2 Results and Discussion

Drawing on conditions used for the dehydrogenation of alkanes by cationic iridium complexes,¹⁰ the reactivity of complex **1** with MTBE in dichloromethane was investigated in the presence of TBE as a hydrogen acceptor. Instead of alkoxy-carbene formation as is observed in other iridium systems,^{14,15} the dehydrogenation of complex **1** in the presence of

excess MTBE rapidly gives a new monohydride complex which we have characterized as the iridium(III) methallyl complex $[(\text{PPh}_3)_2\text{IrH}(\eta^3\text{-C}_4\text{H}_7)]\text{PF}_6$ (**2**). (**Figure 2.2.1**) The methallyl ligand in **2** arises from C-O bond cleavage of the tert-butyl group in MTBE, with the byproduct MeOH being detectable by GC-FID. Complex **2** can be prepared independently by the treatment of **1** with isobutene, which presumably serves as both substrate and H_2 acceptor.

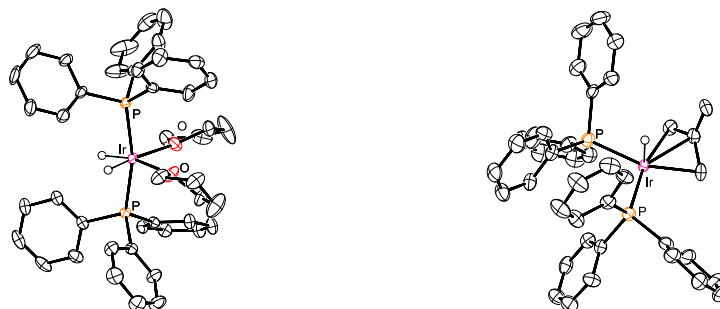


Figure 2.2.1. ORTEPs of **1** (left) and **2** (right). Anions, solvent of crystallization and full disorder models omitted for clarity

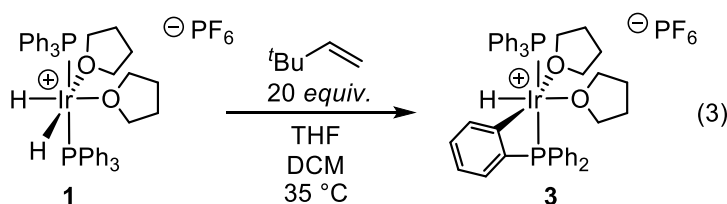


Figure 2.2.2. Dehydrogenation of complex **1** with TBE in a mixture of THF/DCM

Dehydrogenation of **1** in the absence of MTBE gives rise to a new monohydride product at -26.6 ppm coupled to two inequivalent phosphines (**Figure 2.2.2, eq 3**). We initially assigned this product as complex **3** on the basis of an upfield-shifted ^{31}P NMR resonance at -41.9 ppm indicative of a small phosphorus-containing ring obtained by ortho cyclometalation.¹⁶ The iridium analogue of Wilkinson's complex is famously unstable with respect to cyclometalation,¹⁷ and a number of related cyclometalated iridium PPh_3 complexes are known.¹⁸⁻²² The formation of a cyclometalated complex resulting from dehydrogenation of **1** to give $[(\text{PPh}_3)(\text{PPh}_2\text{C}_6\text{H}_4)\text{IrH}(\text{solv})_2]^+$ (**3**) would be a plausible competing reaction in the known alkane dehydrogenation chemistry of $[(\text{PPh}_3)_2\text{IrH}_2(\text{solv})_2]^+\text{X}^-$, indeed the Crabtree group commented on this possibility:

“Either cyclometalation is reversible, or it does not occur at all. Possibly the bis(phosphine) system is insufficiently bulky to promote cyclometalation; we have certainly never seen evidence for it.”¹³

Isolation of **3** allows for this hypothesis to be tested for the first time. Dissolution of **3** in benzene rapidly gives the iridium(I) arene complex $[(\eta^6\text{-benzene})\text{Ir}(\text{PPh}_3)_2]\text{PF}_6$ (**4**) (Figure 2.2.3, eq 4). Dehydrogenation of $[(\text{PPh}_3)_2\text{IrH}_2(\text{acetone})_2]^+$ with TBE in benzene solvent is known to give this product directly.²³ We find the comparable dehydrogenation of **1** to **4** in neat benzene occurs without evidence for the formation of **3** in detectable concentrations. The formation of **4** from **3** requires reductive elimination of the cyclometalated moiety, demonstrating that cyclometalation is indeed reversible as Crabtree previously postulated. In this manner **3** reacts as a cationic iridium(I) synthon, with reversible reductive elimination providing access to an unsaturated iridium(I) intermediate, likely $[(\text{PPh}_3)_2\text{Ir}(\text{solv})]\text{PF}_6$ or an equivalent complex.

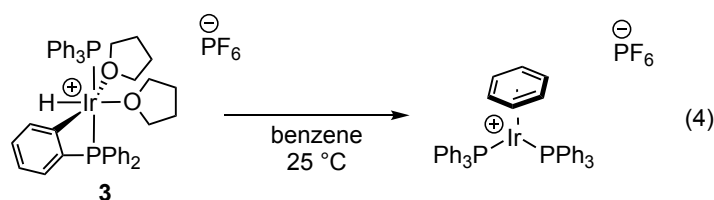


Figure 2.2.3. Evidence for reversible cyclometalation of triphenylphosphine

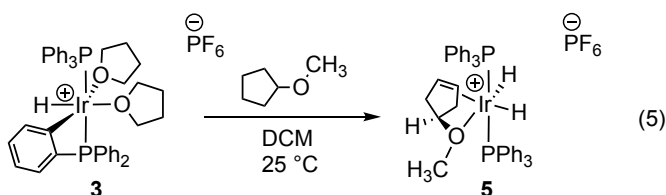


Figure 2.2.4. Evidence for reversible cyclometalation for the dehydrogenation of cyclopentyl methyl ether

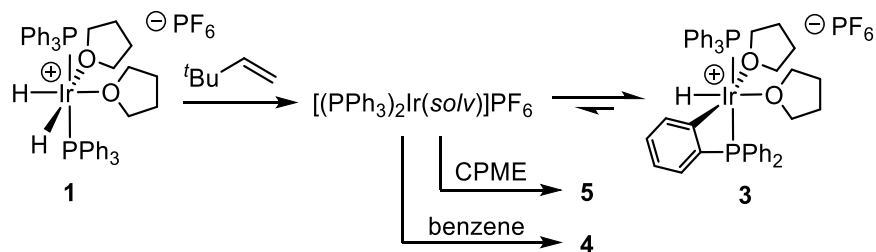


Figure 2.2.5. Reversibility of cyclometalation in complex 3

In the interest of establishing the relevance of the cyclometalated complex **3** to alkane dehydrogenation we undertook a stoichiometric test of its alkane dehydrogenation ability in the absence of a hydrogen acceptor. Complex **3** rapidly dehydrogenates cyclopentyl methyl ether (CPME) to give complex **5** as a major product by ^1H NMR spectroscopy. (**Figure 2.2.4, eq 5**) Complex **5** is a rare olefin dihydride complex that can also be prepared directly from **1** by reaction with one equivalent of TBE in cyclopentyl methyl ether. The observed selectivity for the 3,4-dehydro product is quite unusual, as ether dehydrogenation typically gives alkoxy-carbene or vinyl ether products.²⁴ The generation of **5** from **3** in the absence of an external hydrogen acceptor demonstrates the ability of **3** to dehydrogenate alkane functionality. Furthermore, owing to the reversibility of cyclometalation in this system, kinetic selectivity for intermolecular alkane C-H activation is not a requirement for access to thermodynamic products resulting from intermolecular reactions (**Figure 2.2.5**).

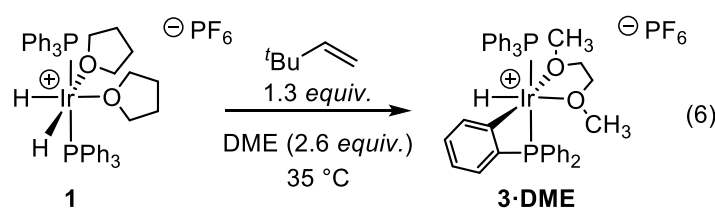


Figure 2.2.6. Isolation of cyclometalated **3·DME**

The instability of complex **3** has frustrated our efforts to obtain pure crystalline samples, however generation of **3** in the presence of 2.6 equivalents of 1,2-dimethoxyethane gives the corresponding DME adduct **3·DME** which can readily be obtained in crystalline form (**Figure 2.2.6, eq 6**). The solid state structure of **3·DME** (**Figure 2.2.7, right**) shows an acute C-Ir-P angle formed by cyclometalation of an ortho C-H bond of $68.4(1)^\circ$ and provides an unambiguous assignment of compound **3**. Complex **3·DME** still reacts with benzene to give **4**, but this reaction proceeds at a significantly slower rate than for **3**. In the absence of DME, the bis(THF) adduct **3** degrades slowly on standing in THF/DCM mixtures and decomposes within seconds in dichloromethane in the absence of excess THF. These observations can be accommodated by assuming that reductive elimination in **3** to give a reactive iridium(I) fragment occurs through a 5-coordinate species accessible via solvent dissociation.

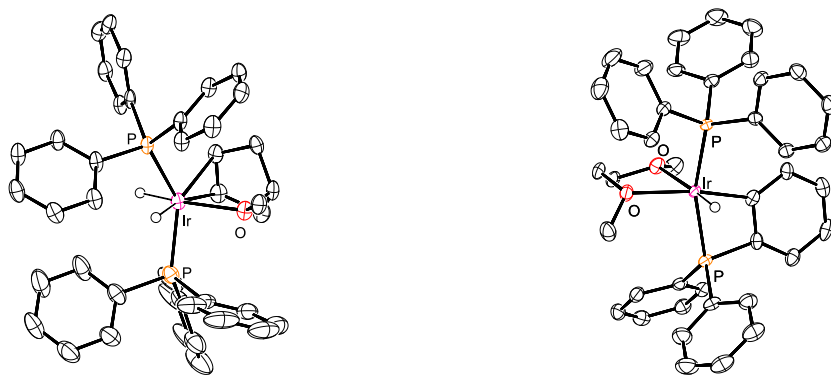


Figure 2.2.7. ORTEPs of **5** (left) and **3·DME** (right) shown at 50% probability. Anions and solvent of crystallization omitted for clarity.

Although **3** is formed on dehydrogenation of **1** in the absence of substrate and is competent in stoichiometric alkane dehydrogenation, the instability of **3** in the absence of an excess of a coordinating solvent seems to argue against **3** being a major species in solution under the conditions for alkane dehydrogenation employed by Crabtree.¹³ (**Figure 2.1.1, eq 1**) However, we have been able to detect the formation of complex **3·DCE** as a major component under these conditions, suggesting that 1,2-dichloroethane is sufficiently coordinating²⁵ to prevent the rapid decomposition observed in CD_2Cl_2 . Conversion of **1** to **3·DCE** occurs at room temperature, with subsequent heating to reflux giving $[(\text{cod})\text{Ir}(\text{PPh}_3)_2]\text{PF}_6$ (**6**) as previously reported (**Figure 2.2.8, eq 7**).¹³ This observation provides strong evidence for competing cyclometalation as a kinetic product prior to alkane dehydrogenation.

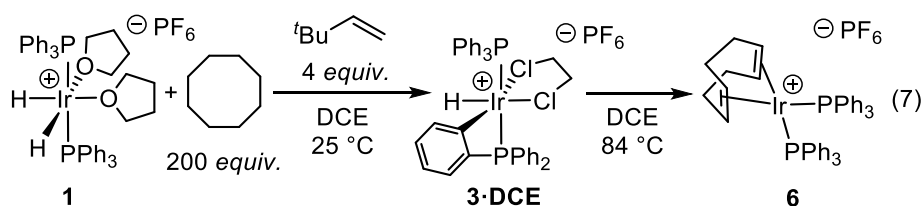


Figure 2.2.8. Observation of **3·DCE** under original conditions first used for cyclooctane dehydrogenation

Having established that complex **3** is capable of alkane dehydrogenation, we have investigated whether **3** also maintains reactivity in the C-O bond cleavage chemistry that gives rise to the allyl complex **2**. Treatment of solutions of **3** with

MTBE rapidly gives the methallyl complex **2** in the absence of added hydrogen acceptor, providing evidence that **3** is competent for stoichiometric MTBE C-O bond cleavage (**Figure 2.2.9, eq 8**).

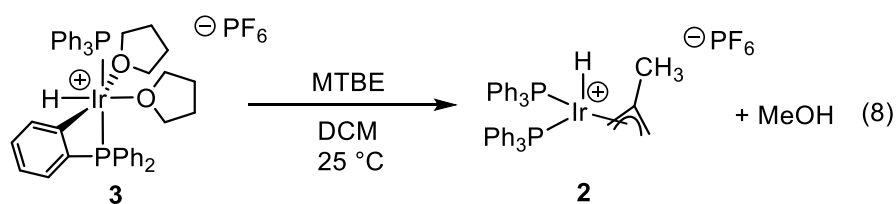


Figure 2.2.9. Evidence for reversible cyclometalation for C-O bond cleavage of MTBE

When solutions of **1**, MTBE, and TBE are monitored by $^{31}\text{P}\{^1\text{H}\}$ NMR spectroscopy, complex **3** is observed during the formation of **2**, reaching a maximal concentration at roughly 50% conversion with respect to **1**. (**Figure 2.2.11**) Kinetic analyses of this transformation under pseudo first-order conditions can be fit to two consecutive irreversible steps **1** \rightarrow **3** \rightarrow **2**. Kinetic analyses of this transformation under pseudo-first-order conditions can be fit to a model assuming dehydrogenation of **1** gives the reactive intermediate **A** in equilibrium with complex **3** (**Figure 2.2.10**). A second irreversible step converts **A** to the product **2**. Although **A** is not observed, its plausible identity is the three-coordinate complex $[(\text{PPh}_3)_2\text{Ir}(\text{sol})]\text{PF}_6$, where the last site is occupied either by the solvent or by TBE.¹³

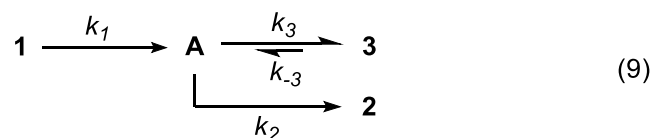


Figure 2.2.10. Kinetic model for the C-O bond cleavage of MTBE

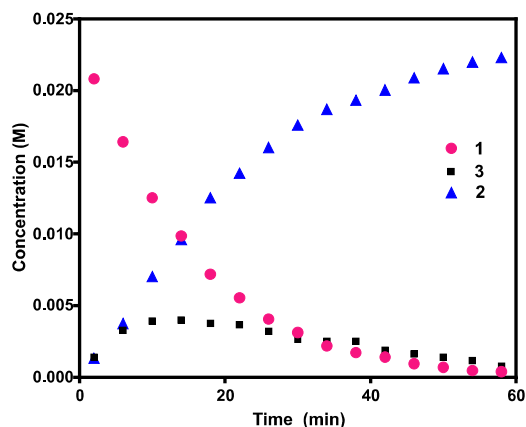


Figure 2.2.11. Observation of complex **3** in the conversion of **1** to **2** by NMR spectroscopy.²⁶

MTBE degradation by complexes of iridium has been previously observed, but typically occurs without concomitant allyl formation. The Grubbs group has shown that thermolysis of an MTBE-derived iridium alkoxycarbene results in formation of the corresponding metal carbonyl.^{14,27} They have proposed a mechanism involving isobutene elimination from an alkoxycarbene intermediate to give an iridium σ -formyl which decomposes by carbonyl deinsertion.¹⁴ Although a related mechanism may be operative in the formation of complex **2**, no evidence for metal carbonyl formation is observed, and methanol is detected as the major C₁ product of MTBE cleavage. This difference in selectivity is significant since carbonyls are potent π -acidic ligands and their binding to electron-rich metal centers can be associated with a loss of reactivity. The absence of carbonyl formation in this system leaves open significant opportunities for catalysis involving MTBE-derived allyls.

A plausible mechanism for MTBE cleavage by **1** is given in **Figure 2.2.12**. Initial dehydrogenation of **1** likely gives the transient species $[(PPh_3)_2Ir(THF)]PF_6$ (**A**) which is in equilibrium with **3** via reversible cyclometalation. MTBE C-H activation is proposed to occur at the *tert*-butyl group to give intermediate **B**. Subsequent β -alkoxide elimination would give intermediate **C** after which sequential reductive elimination of methanol followed by oxidative addition of the η^2 -isobutene provides complex **2**. A related mechanism is proposed to be operative in the C-O bond cleavage of ethoxybenzene to give a η^2 -ethylene product by a PCP-Ir pincer complex reported by Goldman,²⁸ and in an associated catalytic example.²⁹

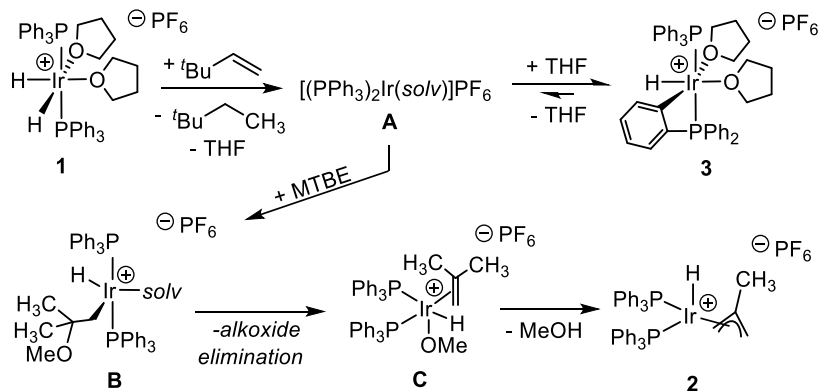


Figure 2.2.12. Proposed mechanism for the formation of **2**

2.3 Conclusion

In light of the ability of **3** to react with alkanes and MTBE (*vide supra*), its stability in ethereal solvent appears kinetic in nature. The observed C-O bond cleavage chemistry with MTBE demonstrates an unusual mode of ether activation which presumably competes with α,α -dehydrogenation at the methoxy position to give the alkoxy carbene. As we have recently demonstrated that alkoxy carbene formation can be completely reversible at cationic bis(phosphine) iridium complexes at room temperature,¹¹ the transient formation of an MTBE-derived alkoxy carbene prior to C-O bond scission cannot be ruled out.

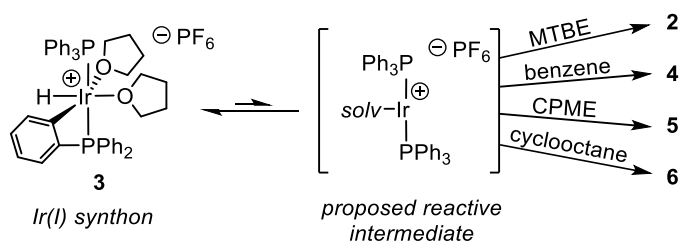


Figure 2.2.13. Role of **3** as a masked iridium(I) synthon.

Controlling the selectivity for intermolecular C-H bonds over intramolecular ligand C-H bonds has been a key challenge of C-H activation chemistry since the earliest examples. We have shown that the previously observed selectivity of cationic bis(phosphine) iridium complexes for intermolecular C-H activation is not a kinetic phenomenon. Instead, these

complexes rapidly undergo dehydrogenation-induced intramolecular cyclometalation. Unlike in the well-known Cp*Ir case, this cyclometalation event is reversible, masking a reactive iridium(I) fragment that is presumably responsible for the observed reactivity with alkane functionality (**Figure 2.2.13**). Our observation that cyclometalation can precede intermolecular cyclooctane dehydrogenation under previously reported conditions supports a role for this cyclometalated complex as an off-path species and a competing kinetic product in the first example of alkane dehydrogenation by a homogeneous transition-metal complex.

2.4 Experimental

General Considerations. All manipulations were carried out using standard vacuum, Schlenk, cannula, or glovebox techniques under N₂ unless otherwise specified. Tetrahydrofuran, dichloromethane, pentane, and diethyl ether were degassed with argon and dried over activated alumina using a solvent purification system. Benzene, MTBE, DME, and CPME were degassed with nitrogen and stored over activated 4Å molecular sieves.

Spectroscopy. ¹H, ¹³C and ³¹P NMR spectra were recorded on Bruker NMR spectrometers at ambient temperature unless otherwise noted. ¹H and ¹³C chemical shifts are referenced to residual solvent signals; ³¹P chemical shifts are referenced to an external H₃PO₄ standard.

X-ray Crystallography. X-ray crystallographic data were collected on a Rigaku Oxford Diffraction Supernova diffractometer. Crystal samples were handled under immersion oil and quickly transferred to a cold nitrogen stream.

Elemental Analysis. Elemental analyses of complexes **2** and **3·DME** are of the bulk samples for which yields are reported. No additional purification operations are carried out prior to packaging for analysis. Elemental analyses were performed at the University of Rochester CENTC Elemental Analysis Facility.

Preparation of [(PPh₃)₂IrH₂(THF)₂]PF₆ (1**).** Complex **1** was prepared according to a previously published procedure for the BF₄ salt.⁵

Preparation of [(PPh₃)₂IrH(C₄H₇)]PF₆ (2**) from isobutene.** A 20 mL scintillation vial was charged with complex **1** (0.1106 g, 0.11 mmol) and 1.5 mL of dichloromethane and sealed with a PTFE-lined septum cap. The solution was cooled to 0 °C and isobutene was bubbled through the solution for 5 minutes causing an immediate color change from colorless to yellow. The solution was reduced to dryness under vacuum and the resulting yellow solid washed with 5 mL of pentane and then dried under vacuum to give complex **2** (0.0975 g, 97%). Single crystals of **2** were obtained by layering a saturated THF solution with diethyl ether at room temperature. Anal. Calcd. For C₄₀H₃₈F₆IrP₃: C, 52.34; H, 4.17. Found: C, 52.20; H, 4.15.

¹H NMR (500 MHz, CD₂Cl₂): δ -38.66 (br, 1H, IrH), 2.16 (br, 2H, CH_{anti}), 2.19 (s, 3H, CH₃), 3.46 (br, 2H, CH_{syn}), 7.15-7.19 (m, 12H, Ar), 7.27-7.30 (m, 12H, Ar), 7.38-7.41 (m, 6H, Ar)

³¹P{¹H} NMR (202 MHz, CD₂Cl₂): δ 15.85 (br), -143.09 (sep, ¹J_{P-F} = 712.0 Hz)

¹³C{¹H} NMR (126 MHz, CD₂Cl₂): δ 27.24, 63.65, 125.01, 129.12 (d, 11.2 Hz), 131.32, 132.75 (d, 53.9 Hz), 133.50 (d, 11.5 Hz)

Preparation of [(PPh₃)₂IrH(C₄H₇)]PF₆ (2**) from MTBE.** A 20 mL scintillation vial was charged with complex **1** (0.3807 g, 0.377 mmol), 5 mL of MTBE, and *tert*-butylethylene (0.58 mL, 4.5 mmol). The vial was sealed with a PTFE-lined septum cap and heated with vigorous stirring for 3 hours at 40 °C. The supernatant was decanted under nitrogen and the solid dried under to give complex **2** (0.3123 g, 90%).

Preparation of [(PPh₃)(PPh₂C₆H₄-)IrH(THF)₂]]PF₆ (3**).** A 20 mL scintillation vial was charged with complex **1** (0.0304 g, 0.030 mmol), 0.15 mL of CH₂Cl₂, 0.45 mL of tetrahydrofuran, followed by *tert*-butylethylene (76.5 μL, 0.60 mmol). The vial was sealed with a PTFE-lined cap and then stirred for 2 h at 35 °C. Excess pentane (*ca* 5 ml) was added to give a precipitate which was separated by removal of the supernatant with a pipette. The residue was dried under vacuum to give an impure off-white solid (0.0260 g). The resulting solid decomposes slowly on standing at room temperature.

Note: The sensitivity of this complex limits the purity of the isolable solid. After isolation, the components can be estimated by ³¹P{¹H} spectroscopy in a 1:1 mixture of THF-*d*₈/CD₂Cl₂. Complex **3** is observed in a 5:1 ratio with an unidentified product which appears only after addition of pentane (δ 25.22 (s)).

^1H NMR (500 MHz, 1:1 THF- d_8 /CD $_2$ Cl $_2$): δ -26.90 (t, 1H, IrH, 15.06 Hz) 1.55 (m, 4H, OCH $_2$ CH $_2$), 3.34 (m, 4H, OCH $_2$). A complete assignment could not be made.

$^{31}\text{P}\{^1\text{H}\}$ NMR (202 MHz, 1:1 THF- d_8 /CD $_2$ Cl $_2$): δ 22.90 (dd, $^2\text{J}_{\text{P-P}}$ 365.2 Hz, $^2\text{J}_{\text{P-H}}$ 14.6 Hz), -41.86 (dd, $^2\text{J}_{\text{P-P}}$ 365.0 Hz, $^2\text{J}_{\text{P-H}}$ 14.6 Hz), -141.46 (sep, $^1\text{J}_{\text{P-F}}$ = 710.3 Hz)

$^{13}\text{C}\{^1\text{H}\}$ NMR (126 MHz, 1:1 THF- d_8 /CD $_2$ Cl $_2$): δ 27.09(s, OCH $_2$ CH $_2$), 70.91(s, OCH $_2$). A complete assignment could not be made.

Preparation of [(PPh $_3$)(PPh $_2$ C $_6$ H $_4$ -)IrH(DME)]PF $_6$ (3-DME). A 20 mL scintillation vial was charged with complex **1** (0.0402 g, 0.040 mmol), 1 mL of dichloromethane, dimethoxyethane (11 μL , 0.11 mmol), and *tert*-butylethylene (7.0 μL , 0.055 mmol). The vial was sealed with a PTFE-lined cap and then stirred for 17 h at 35 $^\circ\text{C}$. Excess pentane (*ca* 5 ml) was added to give a precipitate which was separated by removal of the supernatant with a pipette. The residue was dried under vacuum, then taken up in 2 mL of pentane and evaporated to dryness three times to yield an off-white solid. (0.0365 g, 96%). Single crystals of **3-DME** were obtained by layering a saturated dichloromethane solution with pentane at room temperature. Anal. Calcd. For C $_{40}$ H $_{40}$ F $_6$ IrO $_2$ P $_3$: C, 50.47; H, 4.24. Found: C, 50.19; H, 3.94.

^1H NMR (500 MHz, CD $_2$ Cl $_2$): δ -26.63 (dd, 1H, IrH, $^2\text{J}_{\text{P-H}}$ 12.6 Hz, $^2\text{J}_{\text{P-H}}$ 17.4 Hz), 2.93 (s, 3H, OCH $_3$), 2.96-3.01 (m, 1H, OCH $_2$ CH $_2$ O), 3.18 (m, 2H, OCH $_2$ CH $_2$ O), 3.30 (m, 1H, OCH $_2$ CH $_2$ O), 3.40 (s, 3H OCH $_3$) 6.41 (dd, 1H, 5.1 Hz, 6.6 Hz, CH $_{\text{Ar}}$), 6.89 (t, 1H, 7.5 Hz, CH $_{\text{Ar}}$), 7.01 (t, 1H, 5.8 Hz, CH $_{\text{Ar}}$), 7.13-7.26 (m, 4H, CH $_{\text{Ar}}$), 7.45-7.65 (m, 20H, CH $_{\text{Ar}}$) 7.99 (dd, 2H, 6.5 Hz, CH $_{\text{Ar}}$)

$^{31}\text{P}\{^1\text{H}\}$ NMR (202 MHz, CD $_2$ Cl $_2$): δ 19.05 (dd, $^2\text{J}_{\text{P-P}}$ 359.7 Hz, $^2\text{J}_{\text{P-H}}$ 10.2 Hz), -40.82 (dd, $^2\text{J}_{\text{P-P}}$ 359.7 Hz, $^2\text{J}_{\text{P-H}}$ 8.3 Hz), -143.29 (sep, $^1\text{J}_{\text{P-F}}$ = 710.2 Hz)

$^{13}\text{C}\{^1\text{H}\}$ NMR (126 MHz, CD $_2$ Cl $_2$): δ 61.92, 69.43, 74.43, 75.49, 124.12 (d, 9.3 Hz), 128.65, 129.17 (d, 10.1 Hz), 129.64 (d, 11.0 Hz), 130.02 (d, 9.9 Hz), 130.66 (d, 2.6 Hz), 130.81 (d, 2.6 Hz), 131.21 (d, 2.4 Hz), 131.58 (d, 2.2 Hz) 131.70 (d, 2.4 Hz), 132.16 (d, 2.4 Hz) 132.57 (d, 10.7 Hz), 134.19 (dd, 12.5 Hz, 2.3 Hz), 134.41 (d, $^2\text{J}_{\text{C-P}}$ 10.7 Hz), 137.13 (dd, 16.3 Hz, 4.9 Hz) 148.58 (d, 51.6 Hz)

[(PPh $_3$) $_2$ Ir(η^6 -benzene)]PF $_6$ (**4**). The synthesis and characterization of complex **4** as the SbF $_6$ salt has been reported.²³

Preparation of [(PPh₃)₂IrH₂(κ,η²-MeOC₅H₇)]PF₆ (5**).** A 4 mL scintillation vial was charged with complex **1** (0.0390 g, 0.039 mmol), dichloromethane (0.20 mL) and cyclopentyl methyl ether (0.40 mL). *tert*-butylethylene (5.0 μL, 0.039 mmol) was then added and the vial sealed with a PTFE-lined cap. The reaction was allowed to stand at room temperature for 23 hours, after which colorless crystals had deposited. The supernatant was removed by pipette and the crystals washed with three 1 mL portions of pentane. The crystals were dried under vacuum to yield the crystalline product **5** as a CPME solvate (0.0226 g, 54% as the solvate **5** + CPME).

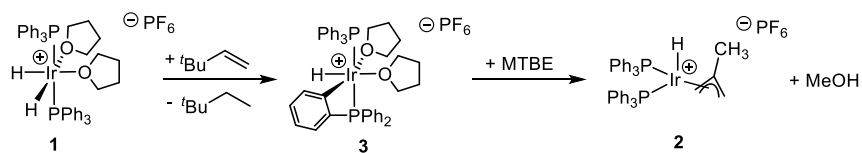
¹H NMR (500 MHz, CD₂Cl₂): δ -30.99 (td, 1H, IrH, ²J_{P,H} = 18.2 Hz, ²J_{H-H} = 6.42 Hz), -9.75 (td, 1H, IrH, ²J_{P,H} 19.1 Hz, ²J_{H-H} 7.31 Hz), 1.50-1.59 (m, 4H, CHCH₂) 2.71 (s, 3H, OCH₃), 3.10 (s, 1H, OCH), 3.93 (s, 2H, CH=CH), 7.43-7.57 (m, 30H Ar)

³¹P{¹H} NMR (202 MHz, CD₂Cl₂): δ 11.73 (m), -143.29 (sep, ¹J_{P-F} = 710.6 Hz)

¹³C{¹H} NMR (126 MHz, CD₂Cl₂): δ 37.74, 63.03, 76.49, 82.89, 129.16 (t, 5.1 Hz), 131.56, 133.28 (t, 29.0 Hz), 134.07 (t, 5.6 Hz)

Representative Procedure:

In the glove box, a J. Young-style NMR tube was charged with a solution of **1** (0.015 g, 0.015 mmol) and MTBE (177 μL, 1.5 mmol) in 0.40 mL of a 3:1 THF/CD₂Cl₂ solution. The solution was frozen solid in a liquid nitrogen-cooled cold well and *tert*-butylethylene (57 μL, 0.45 mmol) was added. The tube was sealed and then thawed and inverted immediately prior to analysis by NMR.



Conditions: [MTBE] = 2.3 M [TBE] = 0.70 M, [1]₀ = 0.023 M

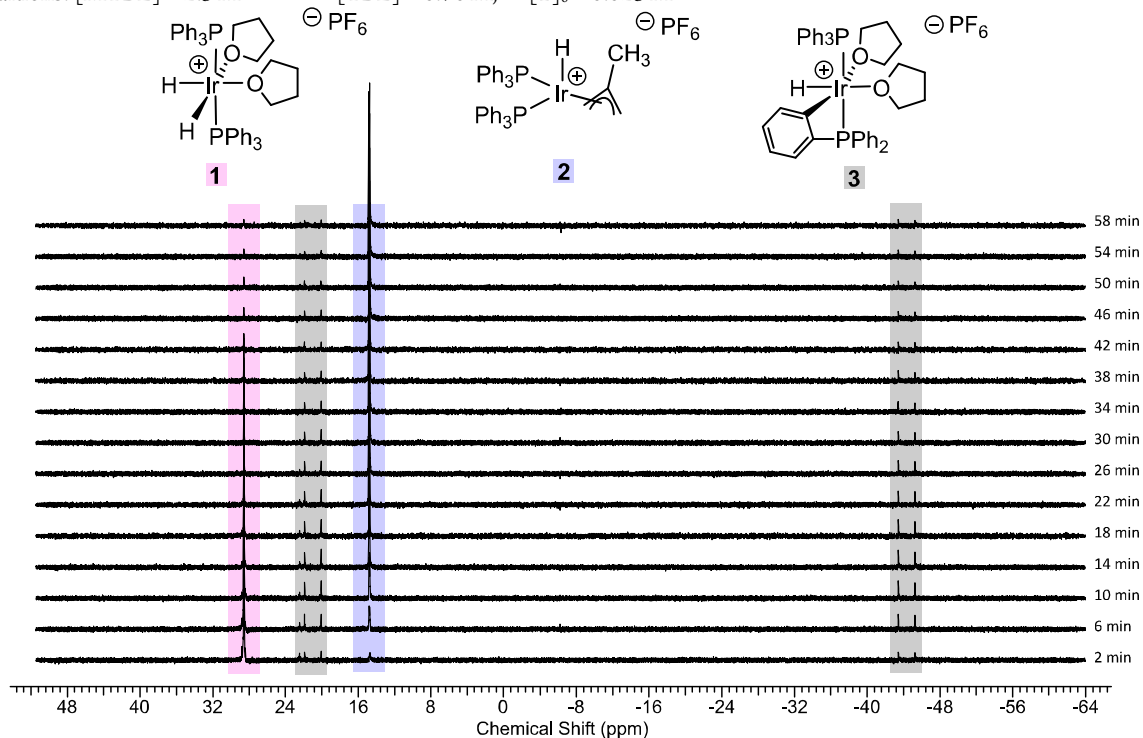


Figure 2.4.1. Representative $^{31}\text{P}\{^1\text{H}\}$ NMR of the formation of **2** from **1**.

Kinetic Modeling of the formation of **2** from **1**.

Figure S2. Fit of concentration data to a model assuming pseudo-first order kinetics for all steps: $\mathbf{1} \rightarrow \mathbf{A} \rightarrow \mathbf{2}$; $\mathbf{A} \rightleftharpoons \mathbf{3}$. Error bars were obtained from kinetic experiments in triplicate. Solid lines represent predictions based on the model using refined parameters. Parameter refinement of the pseudo rate constants against experimental data was done with COPASI.³⁰ The pseudo rate constants k_2 and k_3 were found to be strongly correlated and thus their values cannot be precisely predicted. The ratio k_3/k_2 can however be determined by systematic variation of each parameter during fitting.

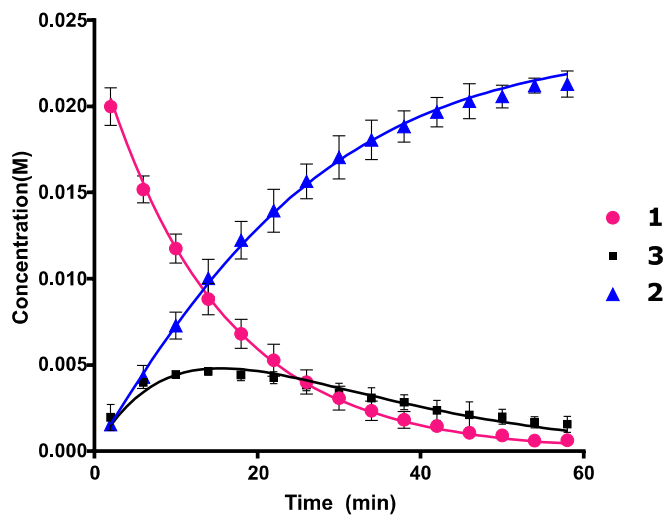
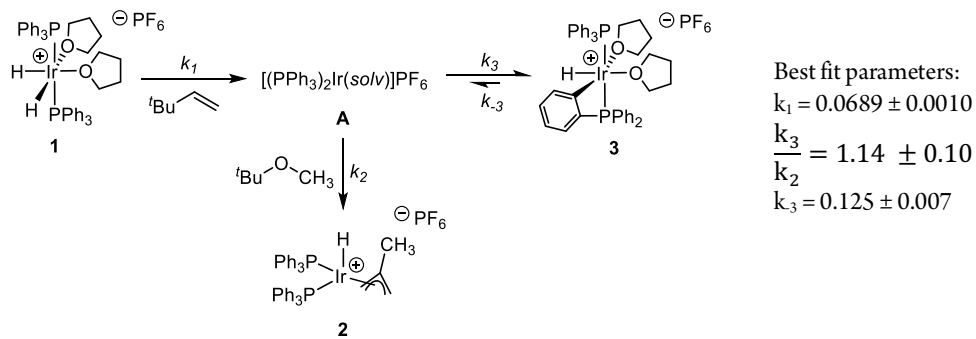


Figure 2.4.2 Kinetics for the cleavage of the C-O bond of MTBE using $^{31}\text{P}\{^1\text{H}\}$ NMR

Formation of the arene complex $[(\text{PPh}_3)_2\text{Ir}(\eta^6\text{-benzene})]\text{PF}_6$ (**4**). A 20 mL scintillation vial was charged with complex **1** (0.0056g, 0.0056mmol), 0.1 mL CD_2Cl_2 , 0.4 mL tetrahydrofuran, followed by *tert*-butylethylene (15 μL , 0.12 mmol). The solution was transferred to a J. Young NMR tube and sealed. The reaction was heated at 35 °C for 2 h, during which time the formation of **3** could be observed by $^{31}\text{P}\{^1\text{H}\}$ spectroscopy. The reaction was then precipitated with 5 mL pentane and the solvent removed by pipette. The residue was dried under vacuum to yield crude **3** as an off-white solid. Addition of 0.6 mL of C_6D_6 gave an orange solution. Complex **4** was identified as the major product by comparison to previously reported spectra.²³

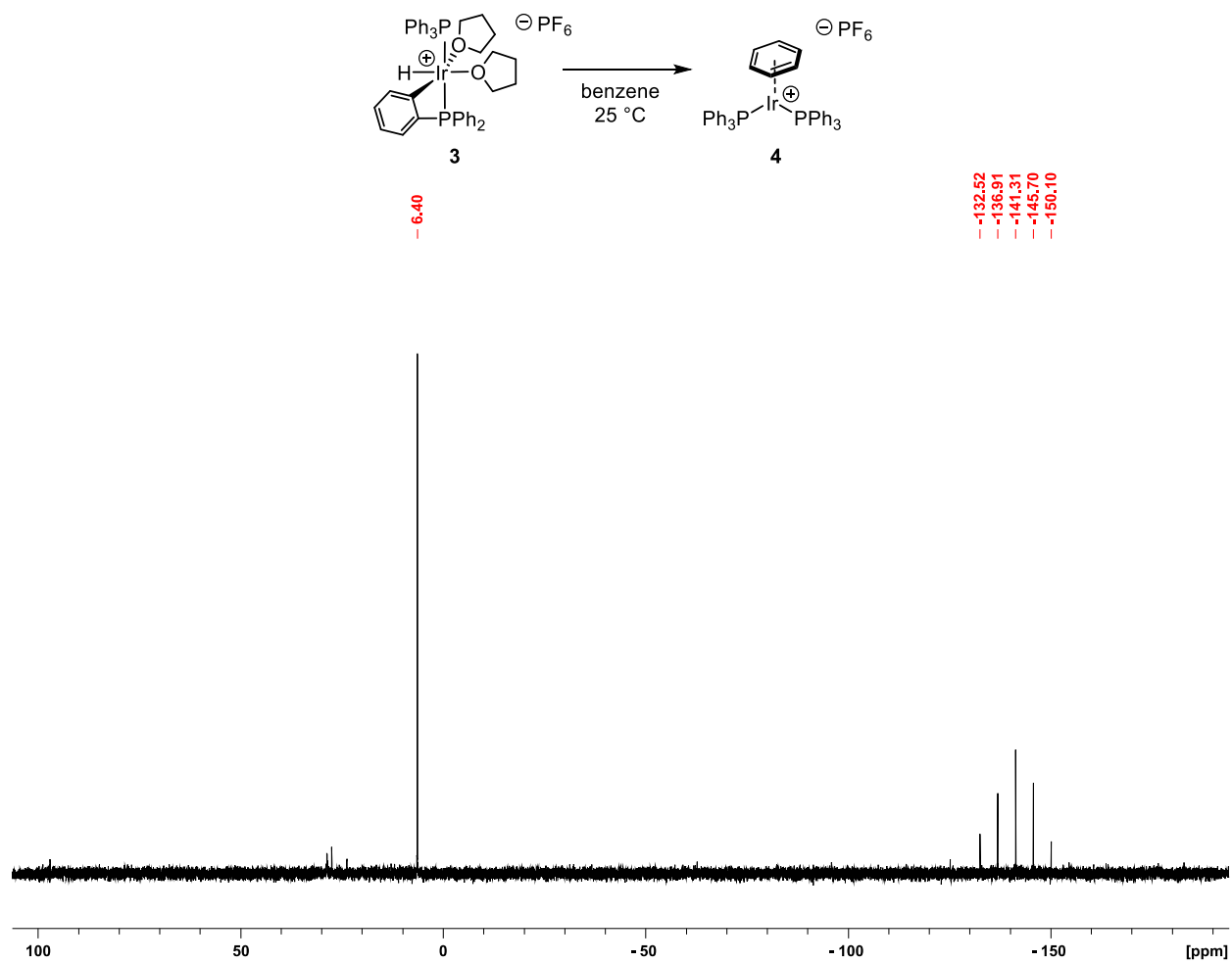


Figure 2.4.3. $^{31}\text{P}\{^1\text{H}\}$ spectrum of reaction of **3** with C_6D_6 showing conversion to complex **4**.

Complex 3 with cyclopentyl methyl ether to form complex 5.

Method A.

A 20 mL scintillation vial was charged with complex **1** (0.0103 g, 0.010 mmol), 0.1 mL of CD_2Cl_2 , 0.5 mL of tetrahydrofuran, followed by *tert*-butylethylene (26 μL , 0.20 mmol). The solution was transferred to a J. Young NMR tube and sealed. The reaction was heated at 35 °C for 2 h, precipitated with 5 mL pentane and the solvent removed by pipette. The residue was dried under vacuum to yield crude **3** as an off-white solid. Addition of cyclopentyl methyl ether (0.5 mL) and 0.10 mL of CD_2Cl_2 gave a solution which rapidly deposited pale orange crystals of **5**, which were separated by filtration.

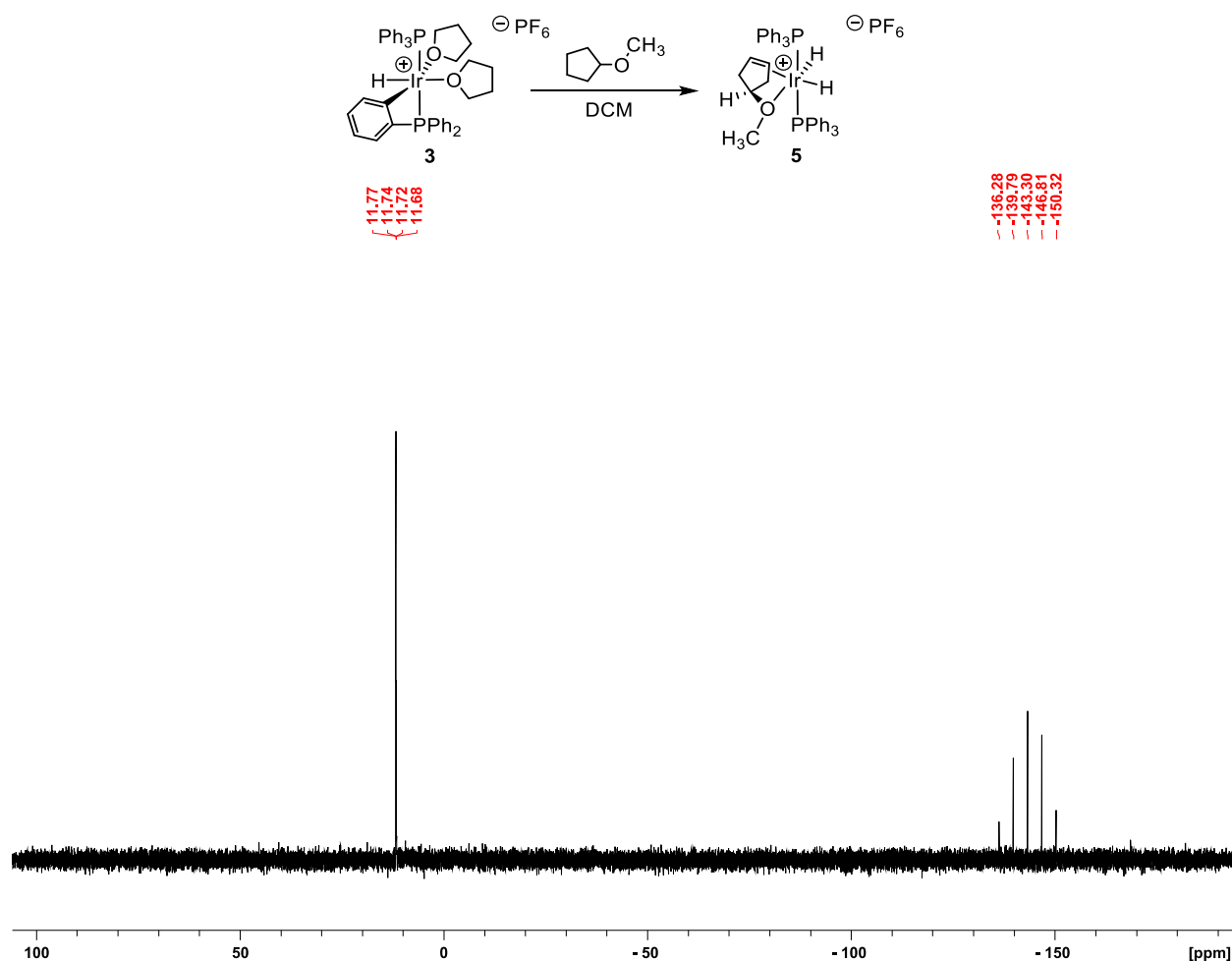


Figure 2.4.4. $^{31}\text{P}\{^1\text{H}\}$ spectrum of crystals deposited from reaction of **3** with CPME showing conversion to complex **5**.

Method B.

A.J. Young NMR tube was charged with crude complex **3** (0.0046 g). Addition of 0.40 mL cyclopentyl methyl ether and 0.20 ml of CD₂Cl₂ gave a solution which when analyzed after 2 h at room temperature, contains a mixture of complexes **5** and **7**. Complexes **5** and **7** were identified by comparison of the ³¹P{¹H} spectra to authentic samples.

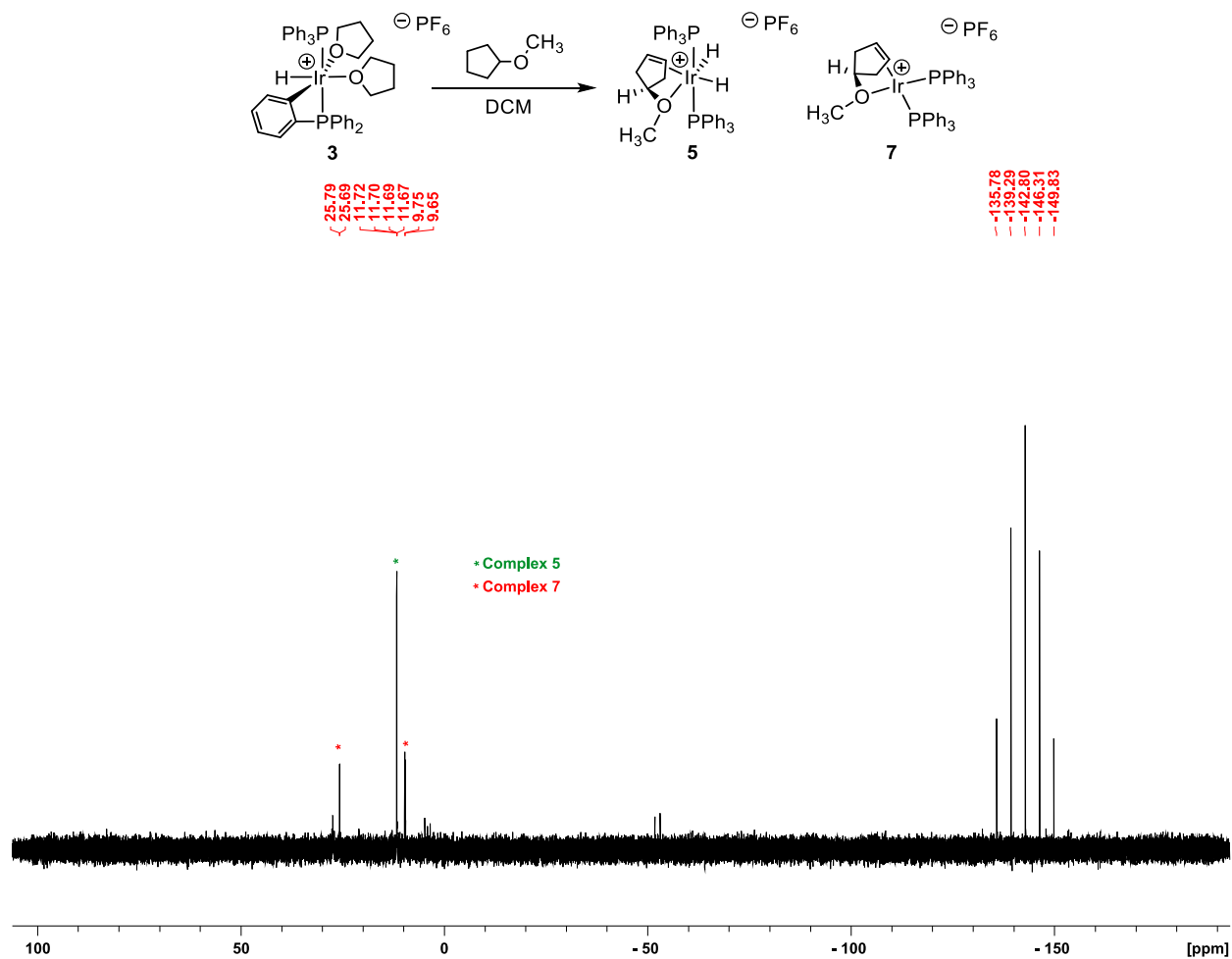


Figure 2.4.5. ³¹P{¹H} spectrum of reaction of **3** with CPME showing conversion to complexes **5** and **7**.

Complex 3 with methyl *tert*-butylether. A J. Young NMR tube was charged with crude complex **3** (0.0055 g, 0.0055 mmol). Addition of 0.40 mL of methyl *tert*-butylether and 0.20 mL CD₂Cl₂ gave a solution that was allowed to stand for 30 min at room temperature. Complex **2** was identified as the major product by ³¹P{¹H} spectroscopy by comparison to authentic samples.

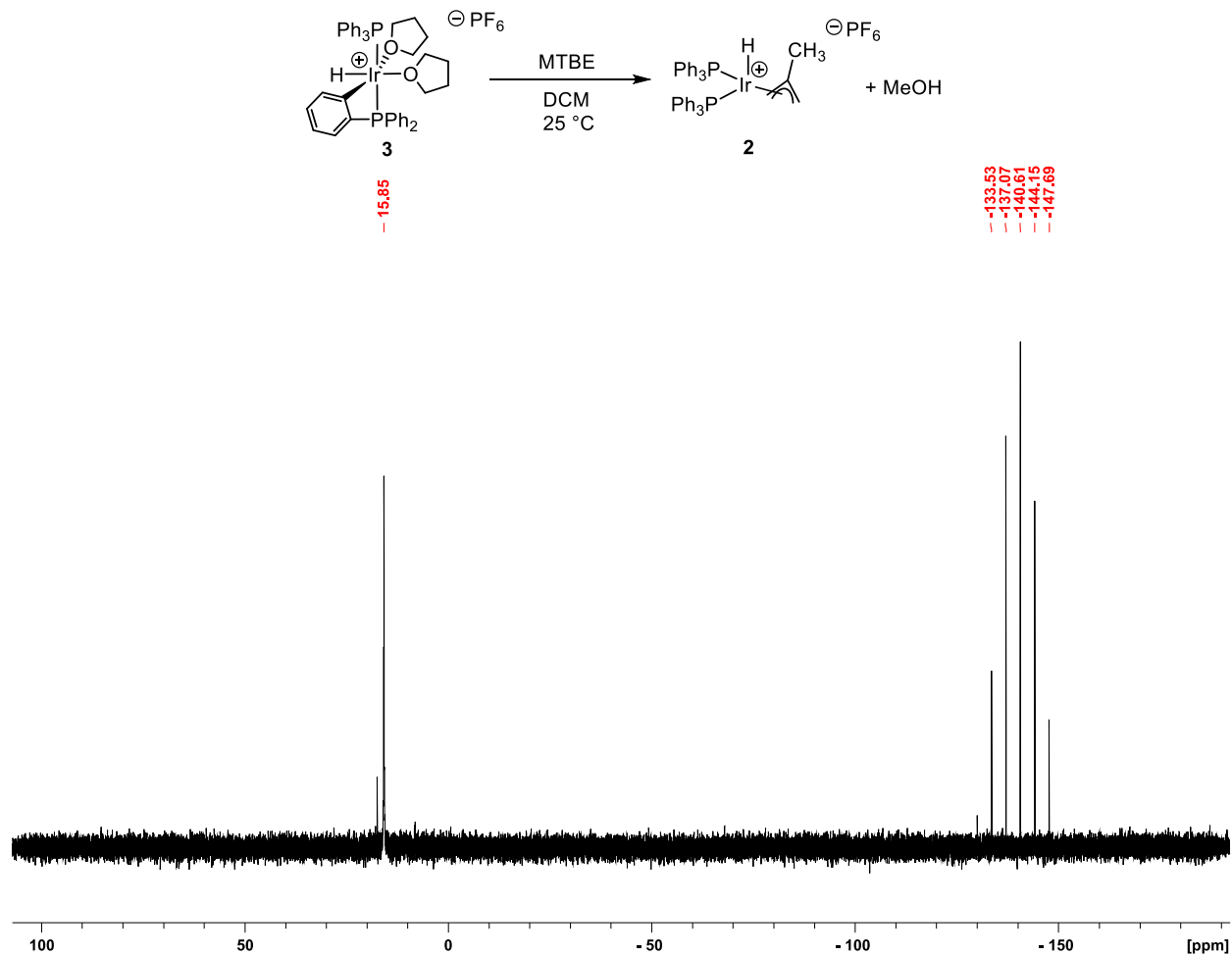


Figure 2.4.6. ³¹P{¹H} spectrum of reaction of **3** with MTBE showing conversion to complex **2**.

Observation of 3 in cyclooctane dehydrogenation. A 20 mL scintillation vial was charged with complex **1** (0.0108 g, 0.0107 mmol), 0.05 mL CD₂Cl₂, 0.3 mL 1,2-dichloroethane, 0.33 mL cyclooctane, followed by *tert*-butylethylene (5 μL, 0.04 mmol). The mixture was stirred at room temperature 20 minutes, then transferred to a J. Young NMR tube. Analysis by ³¹P{¹H} NMR spectroscopy after 2 hr at room temperature shows formation of complex **3** and the product [(cod)Ir(PPh₃)₂]PF₆. The sealed tube was then heated in an 84 °C oil bath for 1 hour, which led to complete conversion to the product of cyclooctane dehydrogenation. The identity of the signal assigned as [(cod)Ir(PPh₃)₂]PF₆ (**6**) was verified by doping with an authentic sample.

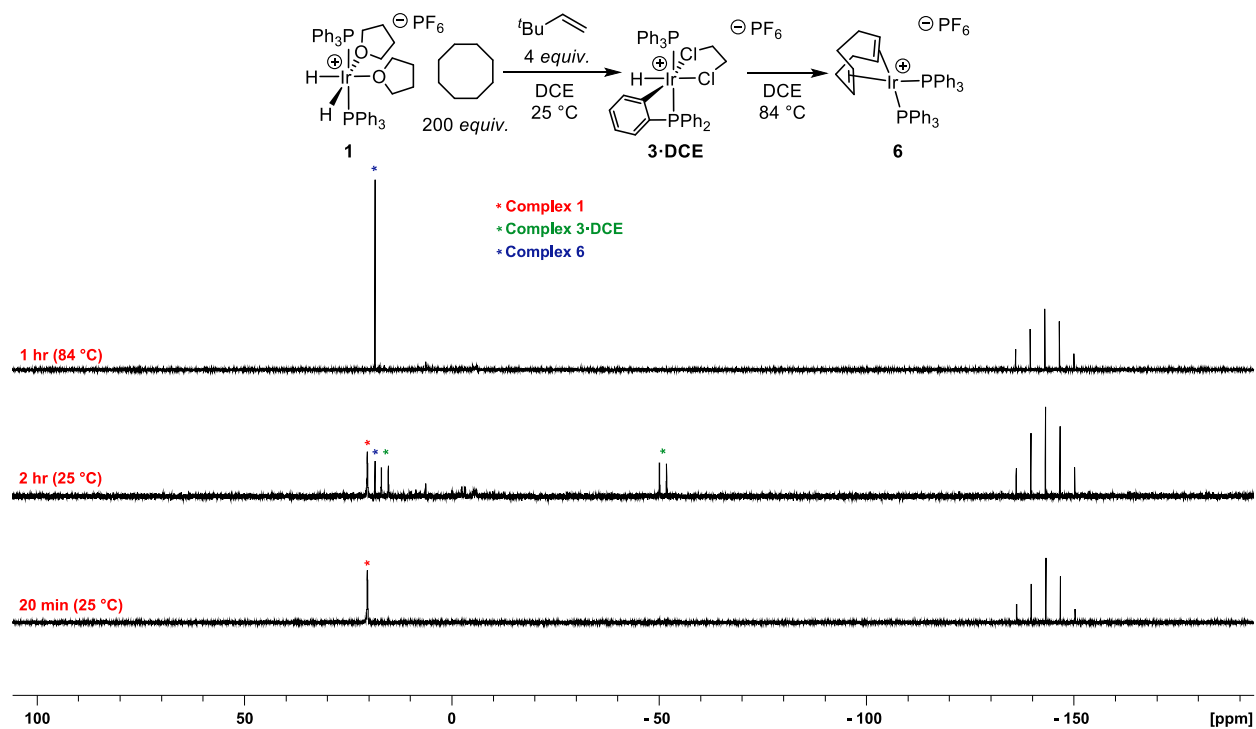


Figure 2.4.7. ³¹P{¹H} spectrum of cyclooctene dehydrogenation by **1** over time showing evidence for formation of **3**·DCE prior to complete conversion to complex **6**.

Observation of Complex 3-DCE generated *in-situ*. A J. Young NMR tube was charged with **1** (0.0102 g, 0.01mmol), 0.50 mL of DCE, 0.10 mL CD₂Cl₂ and *tert*-butylethylene (26 μL, 0.20 mmol). The solution was shaken and allowed to stand for 30 min at room temperature. Analysis by ³¹P{¹H} spectroscopy shows conversion to **3-DCE**.

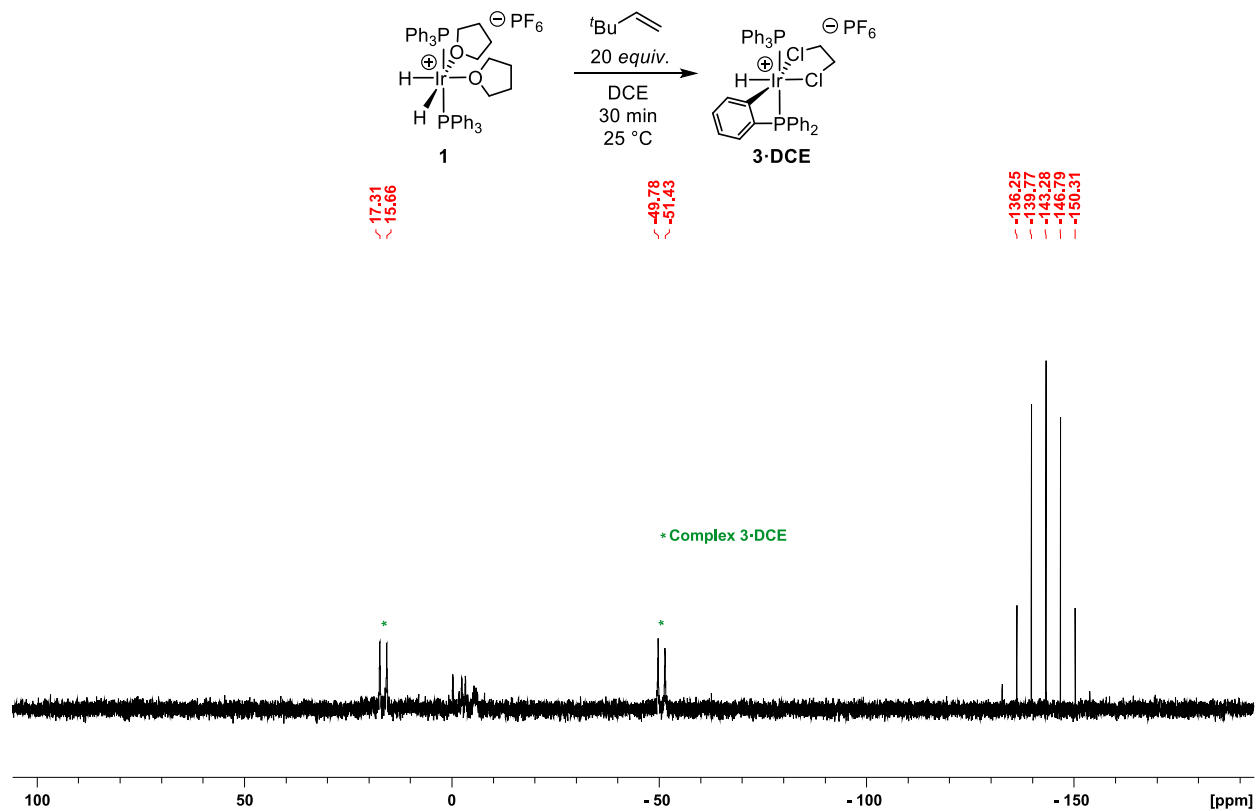


Figure 2.4.8. ³¹P{¹H} spectrum of complex **3-DCE** – Generated *in situ*

2.5 Additional Figures

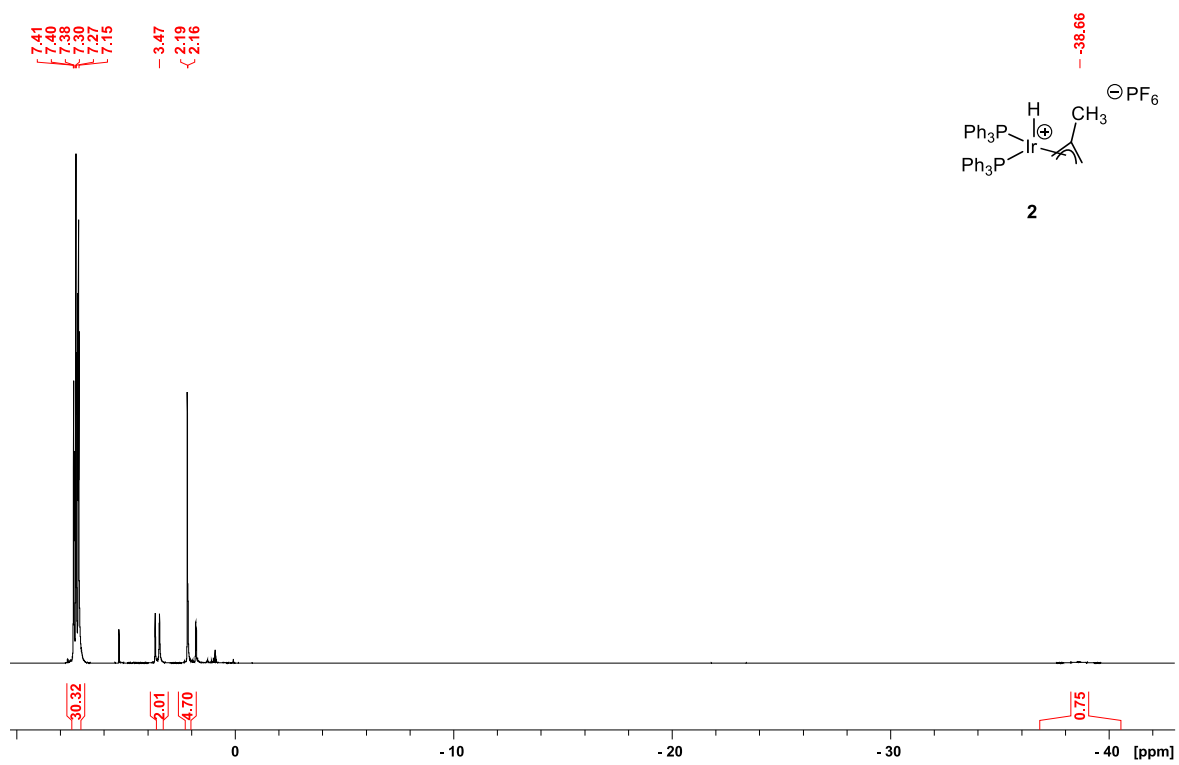


Figure 2.5.1. ^1H NMR Spectrum of $[(\text{PPh}_3)_2\text{IrH}(\text{C}_4\text{H}_7)]\text{PF}_6$ (**2**) (500 MHz, CD_2Cl_2).

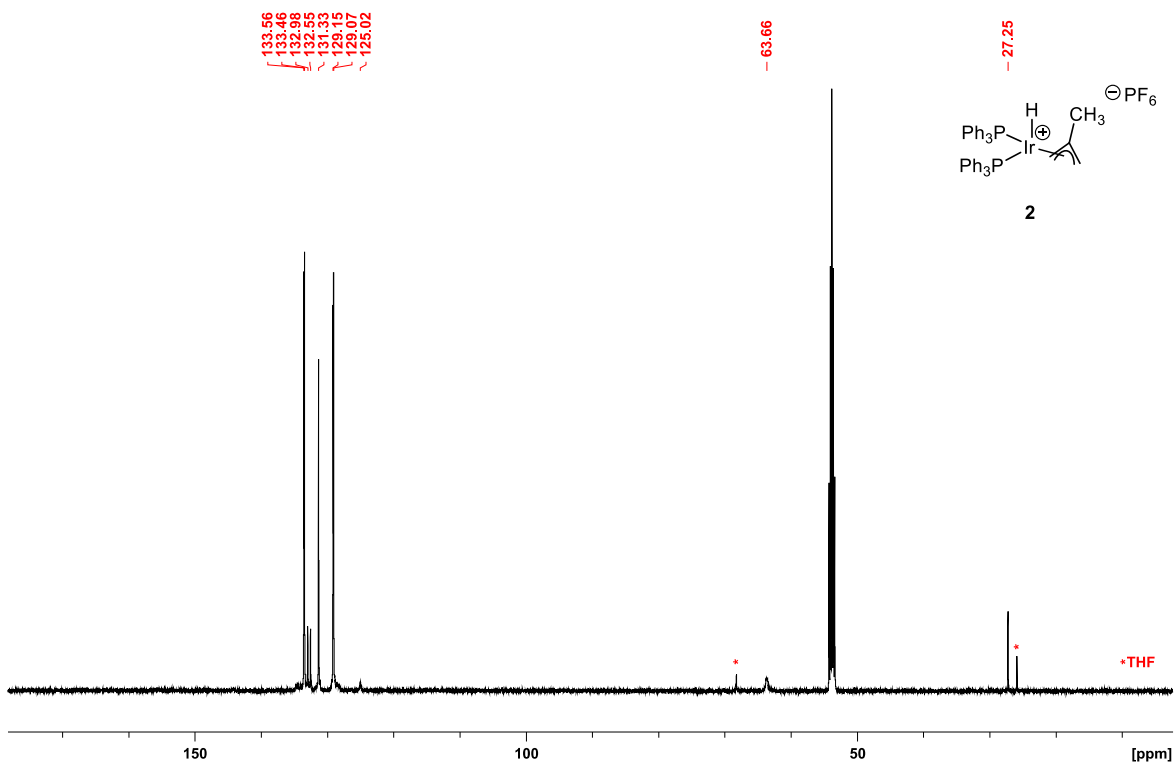


Figure 2.5.2. $^{13}C\{^1H\}$ NMR Spectra of $[(PPh_3)_2IrH(C_4H_7)]PF_6$ (**2**) (126 MHz, CD_2Cl_2).

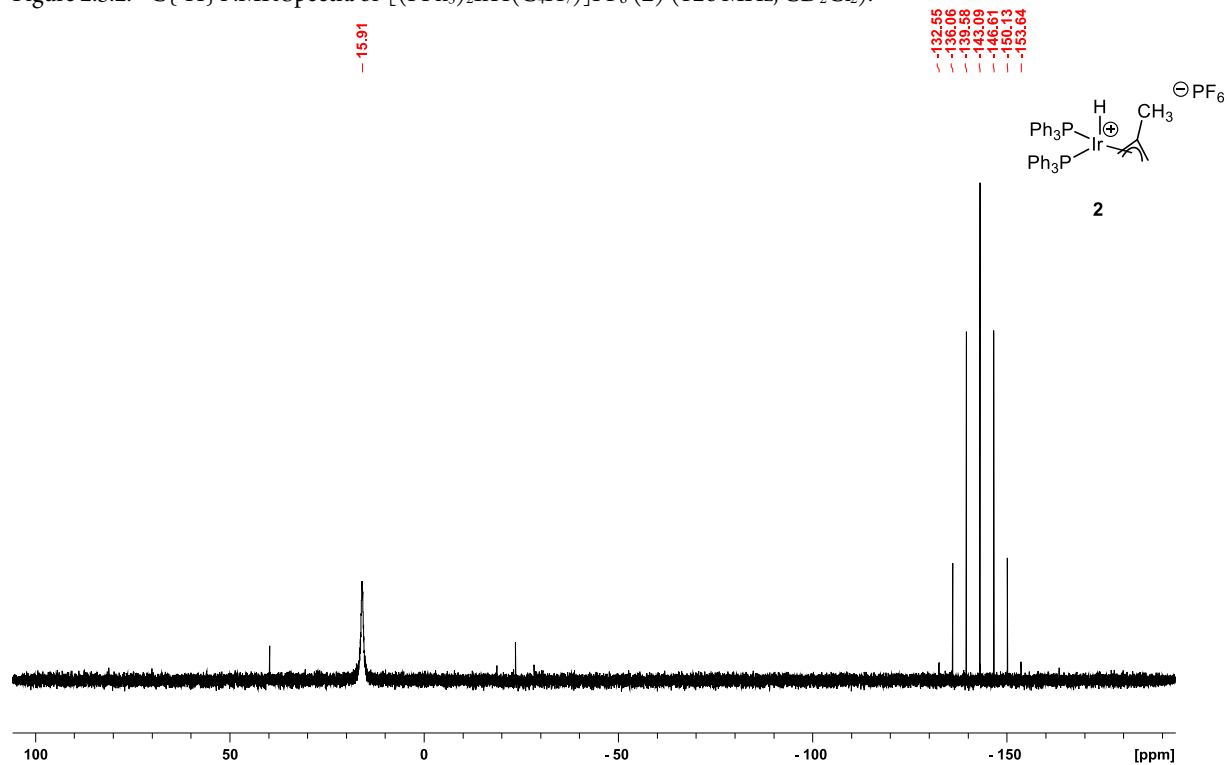


Figure 2.5.3. $^{31}P\{^1H\}$ NMR Spectra of $[(PPh_3)_2IrH(C_4H_7)]PF_6$ (**2**) (202 MHz, CD_2Cl_2).

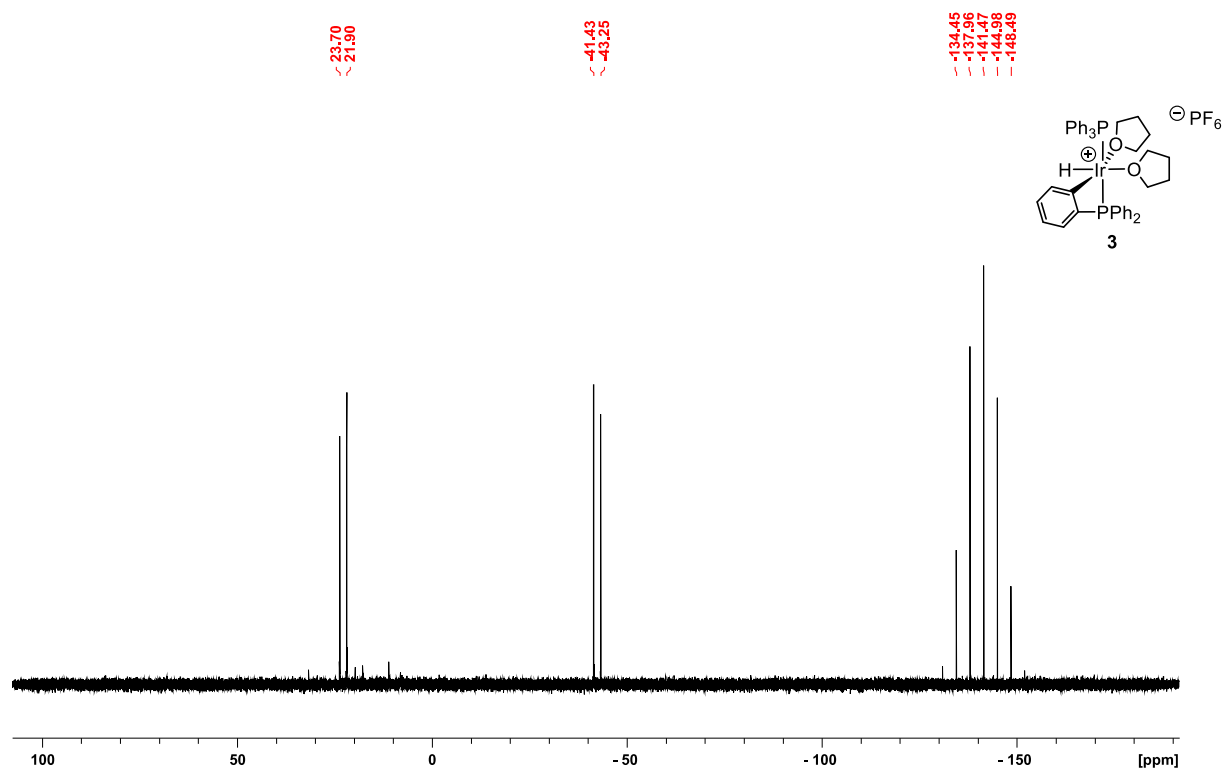


Figure 2.5.4. $^{31}\text{P}\{^1\text{H}\}$ spectrum of $[(\text{PPh}_3)(\text{PPh}_2\text{C}_6\text{H}_4-)\text{IrH}(\text{THF})_2]\text{PF}_6$ (**3**) (202 MHz, THF/ CD_2Cl_2).

Generated In situ

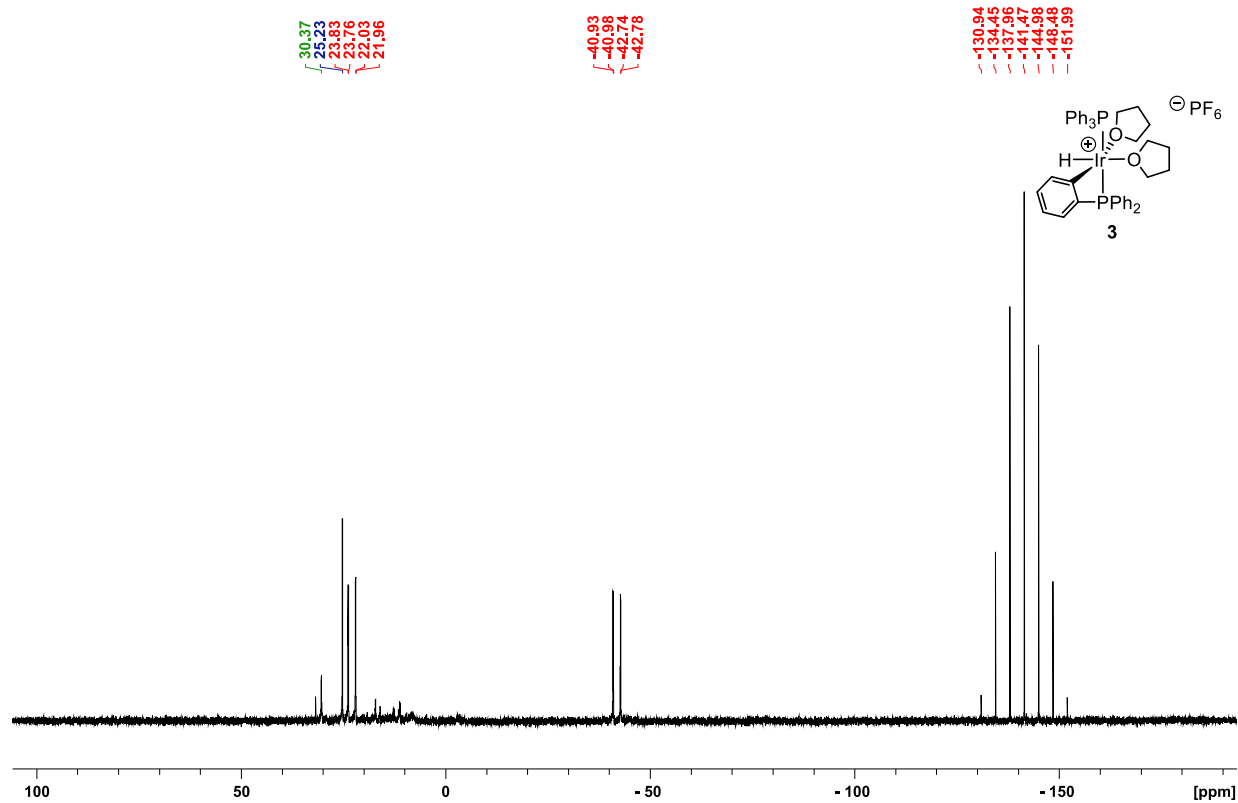


Figure 2.5.5. $^{31}\text{P}\{^1\text{H}\}$ spectrum of $[(\text{PPh}_3)(\text{PPh}_2\text{C}_6\text{H}_4-)\text{IrH}(\text{THF})_2]\text{PF}_6$ (**3**) (202 MHz, THF/ CD_2Cl_2). – Isolated

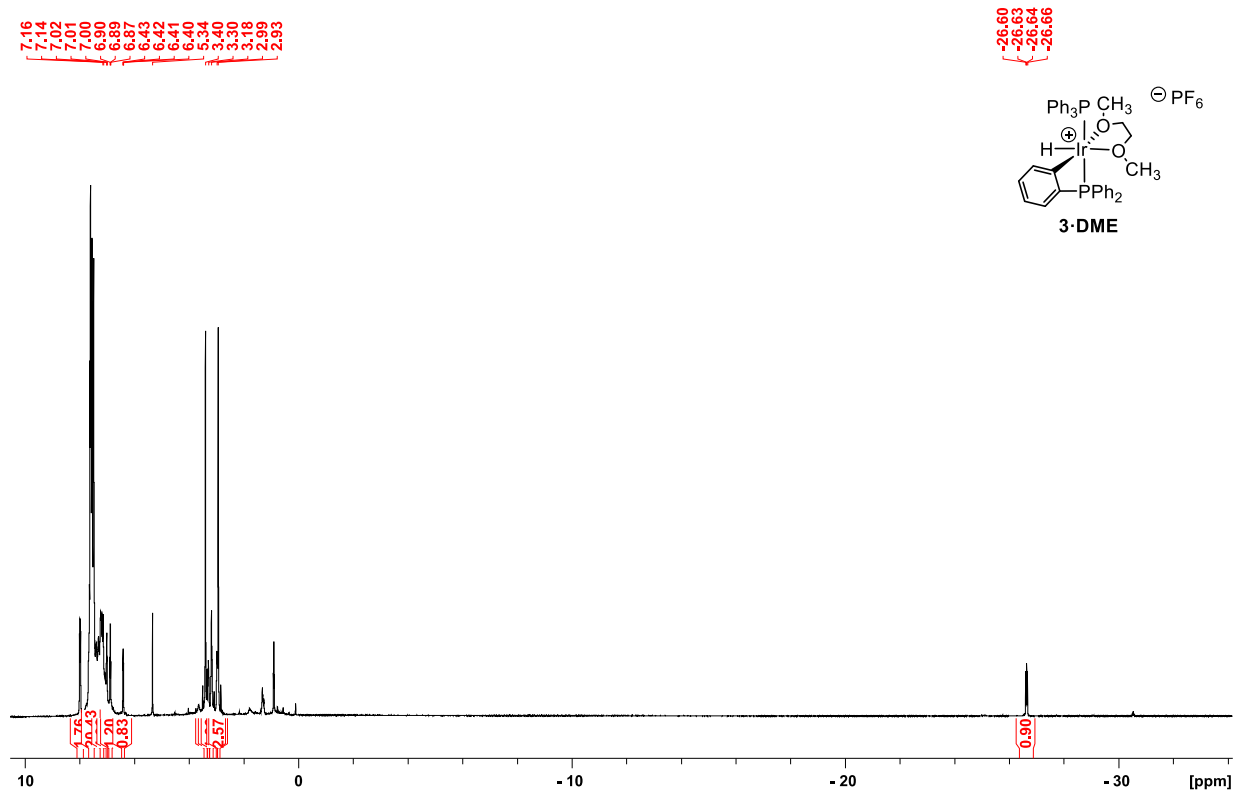


Figure 2.5.6. ¹H Spectra of [(PPh₃)(PPh₂C₆H₄-)IrH(DME)]PF₆ (**3-DME**) (500 MHz, CD₂Cl₂).

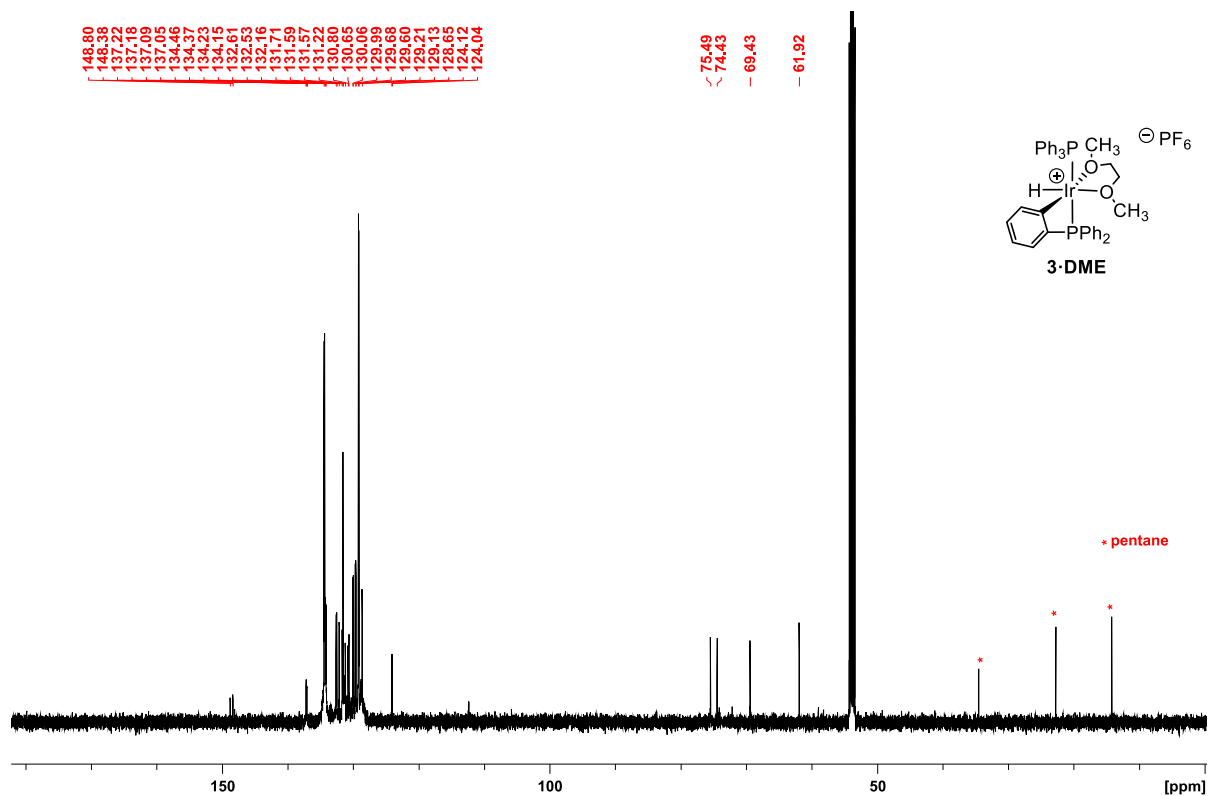


Figure 2.5.7. ¹³C{¹H} NMR Spectra of [(PPh₃)(PPh₂C₆H₄-)IrH(DME)]PF₆ (**3-DME**) (126 MHz, CD₂Cl₂).

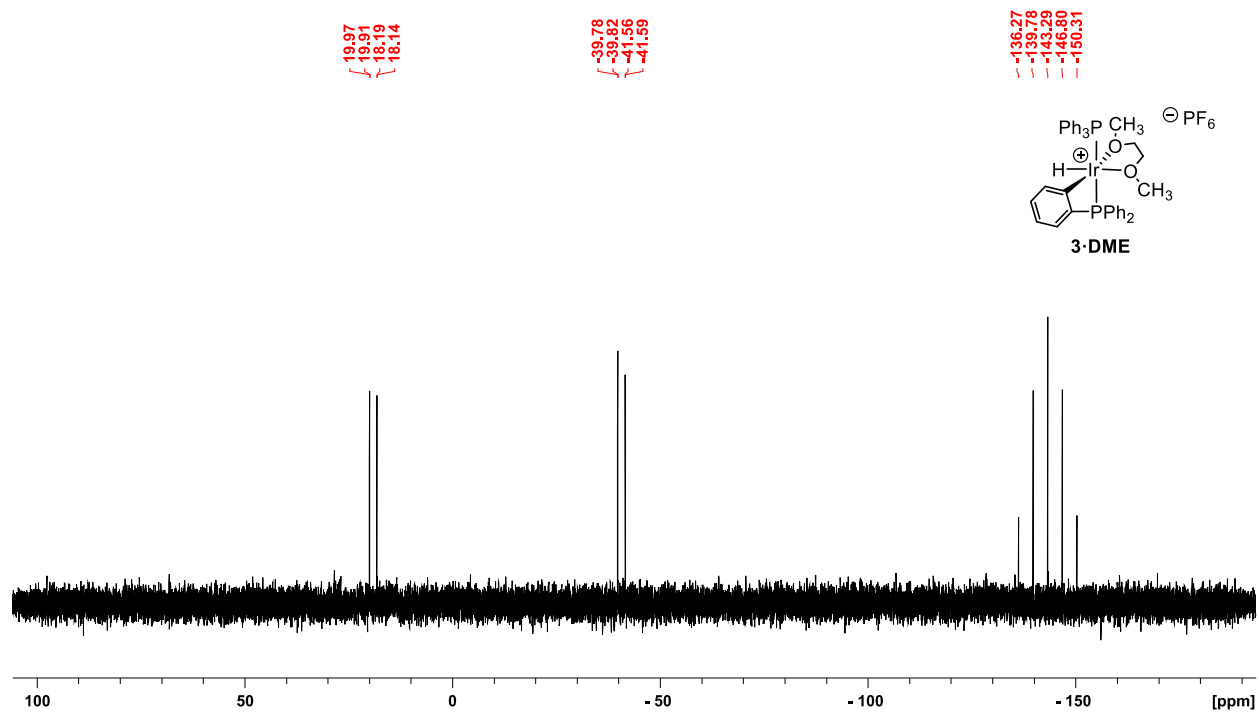


Figure 2.5.8. $^{31}\text{P}\{^1\text{H}\}$ NMR Spectra of $[(\text{PPh}_3)(\text{PPh}_2\text{C}_6\text{H}_4-)\text{IrH}(\text{DME})]\text{PF}_6$ (**3-DME**) (202 MHz, CD_2Cl_2).

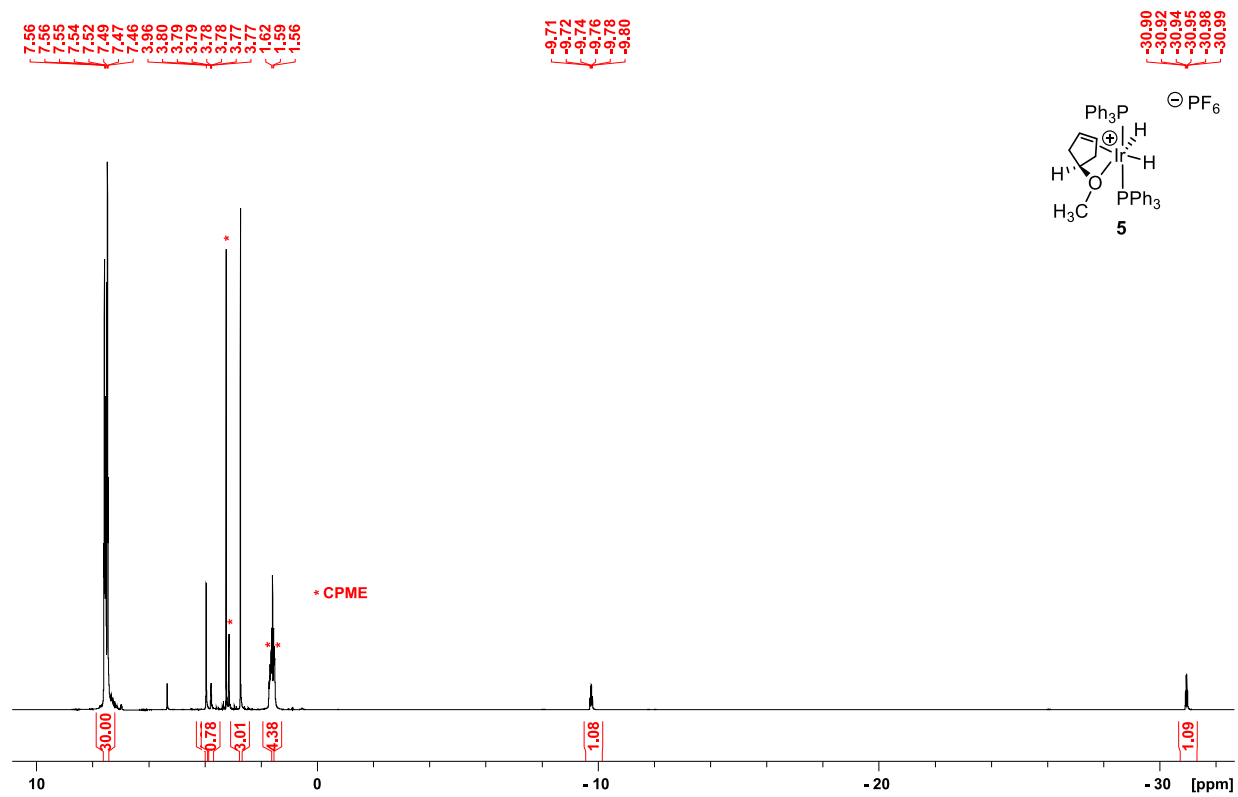


Figure 2.5.9. 1H NMR Spectra of $[(PPh_3)_2IrH_2(\kappa, \eta^2-MeOC_3H_7)]PF_6$ (**5**) (500 MHz, CD_2Cl_2).

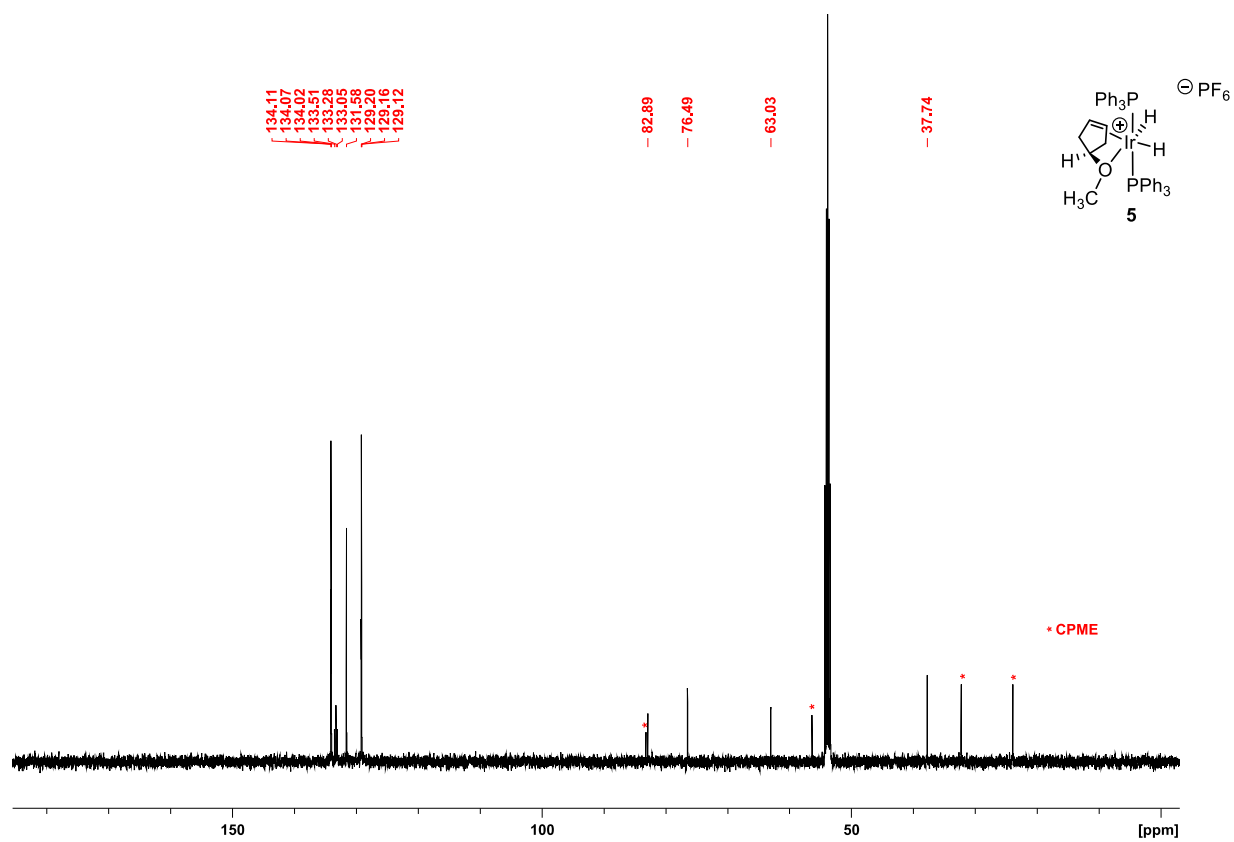


Figure 2.5.10. $^{13}C\{^1H\}$ NMR Spectra of $[(PPh_3)_2IrH_2(\kappa, \eta^2-MeOC_3H_7)]PF_6$ (**5**) (126 MHz, CD_2Cl_2).

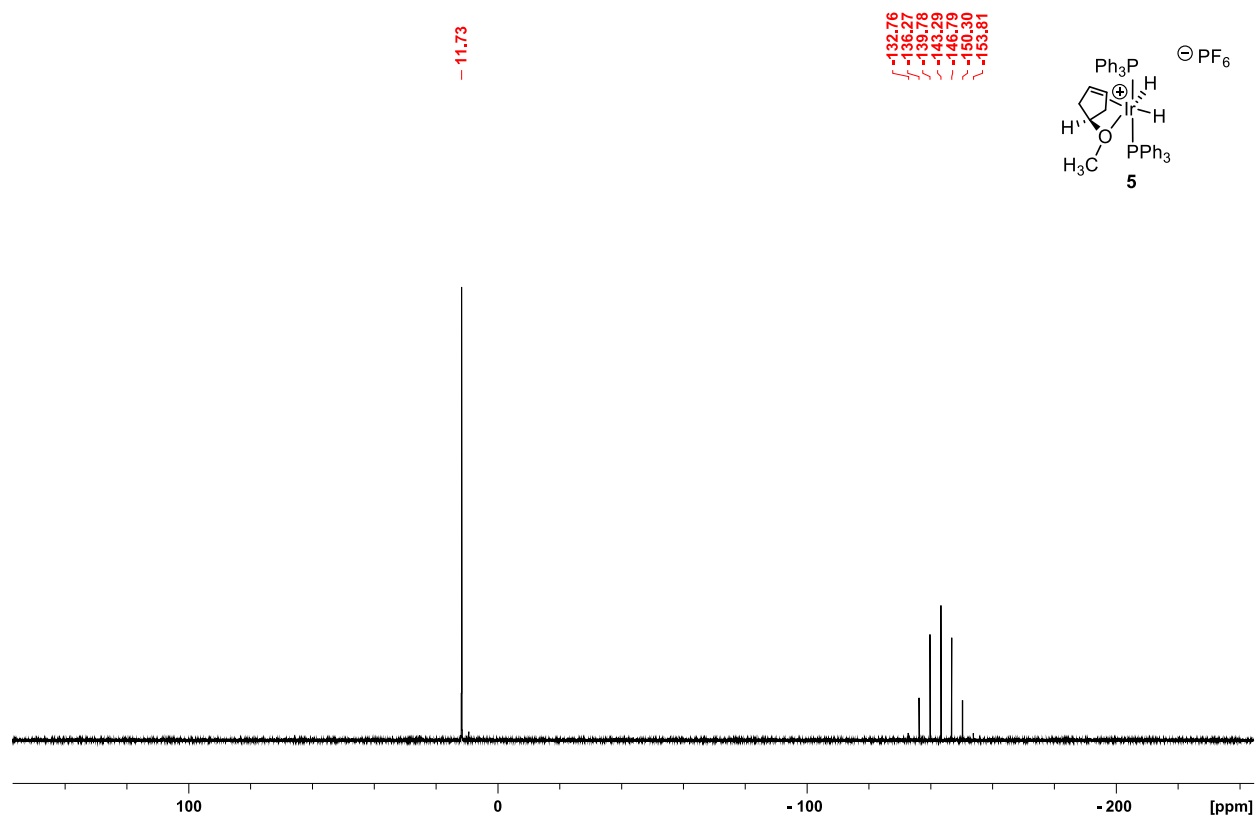


Figure 2.5.11. $^{31}\text{P}\{^1\text{H}\}$ NMR Spectra of $[(\text{PPh}_3)_2\text{IrH}_2(\kappa,\eta^2\text{-MeOC}_5\text{H}_7)]\text{PF}_6$ (**5**) (202 MHz, CD_2Cl_2).

2.6 X-Ray Crystallography

Details of crystallographic refinement for complexes 1, 2, 2-THF, 3-DME, 4 and 5.

Complex 1

THF disorder was modeled with appropriate similarity restraints. Metal hydrides were placed at idealized positions and refined with restraints.

Complex 2

Disorder in the iridium atom and allyl was modeled with appropriate similarity restraints. The metal hydride on the Ir atom of high occupancy was located in the difference map and refined with a thermal parameter fixed to ride on the parent metal atom. The hydride on the Ir atom of low occupancy was added in an idealized position and its thermal parameter was fixed to ride on the parent metal atom.

Complex **2**•THF

This adduct was obtained when **2** was crystalized from THF. Metal hydrides were located in the difference map and refined with a M-H distance restraint and with thermal parameters fixed to ride on the parent metal atom.

Complex **3**•DME

Metal hydride was located in the difference map and refined without restraint. Its thermal parameter was fixed to ride on the parent Ir atom.

Complex **4**

The structure was refined without restraint.

Complex **5**

The metal hydrides were located in the difference map and refined with a M-H bond restraint and thermal parameters fixed to ride on the parent metal atom. The disordered dichloromethane molecule was modeled with similarity restraints placed on the C-Cl bonds.

Table 2.6.1. Crystal data and structure refinement for Complex 1.

Identification code	01	
Empirical formula	$C_{50}H_{60}F_6IrO_{3.50}P_3$	
Formula weight	1116.09	
Temperature	100 K	
Wavelength	0.71073 Å	
Crystal system	Orthorhombic	
Space group	Iba2	
Unit cell dimensions	a = 22.2028(3) Å	$\alpha = 90^\circ$
	b = 19.9227(2) Å	$\beta = 90^\circ$
	c = 21.6313(3) Å	$\gamma = 90^\circ$
Volume	9568.4(2) Å ³	
Z	8	
Density (calculated)	1.550 Mg/m ³	
Absorption coefficient	2.957 mm ⁻¹	
F(000)	4512	
Crystal size	0.183 x 0.162 x 0.101 mm ³	
Theta range for data collection	2.936 to 30.268°.	
Index ranges	-29 ≤ h ≤ 29, -28 ≤ k ≤ 27, -18 ≤ l ≤ 30	
Reflections collected	31741	
Independent reflections	9923 [R(int) = 0.0233]	
Completeness to theta = 25.242°	99.7 %	
Absorption correction	Gaussian	
Max. and min. transmission	1.000 and 0.723	
Refinement method	Full-matrix least-squares on F ²	
Data / restraints / parameters	9923 / 39 / 618	
Goodness-of-fit on F ²	1.020	
Final R indices [I > 2σ(I)]	R1 = 0.0242, wR2 = 0.0564	
R indices (all data)	R1 = 0.0269, wR2 = 0.0580	
Absolute structure parameter	-0.022(3)	
Largest diff. peak and hole	1.142 and -0.829 e/Å ⁻³	

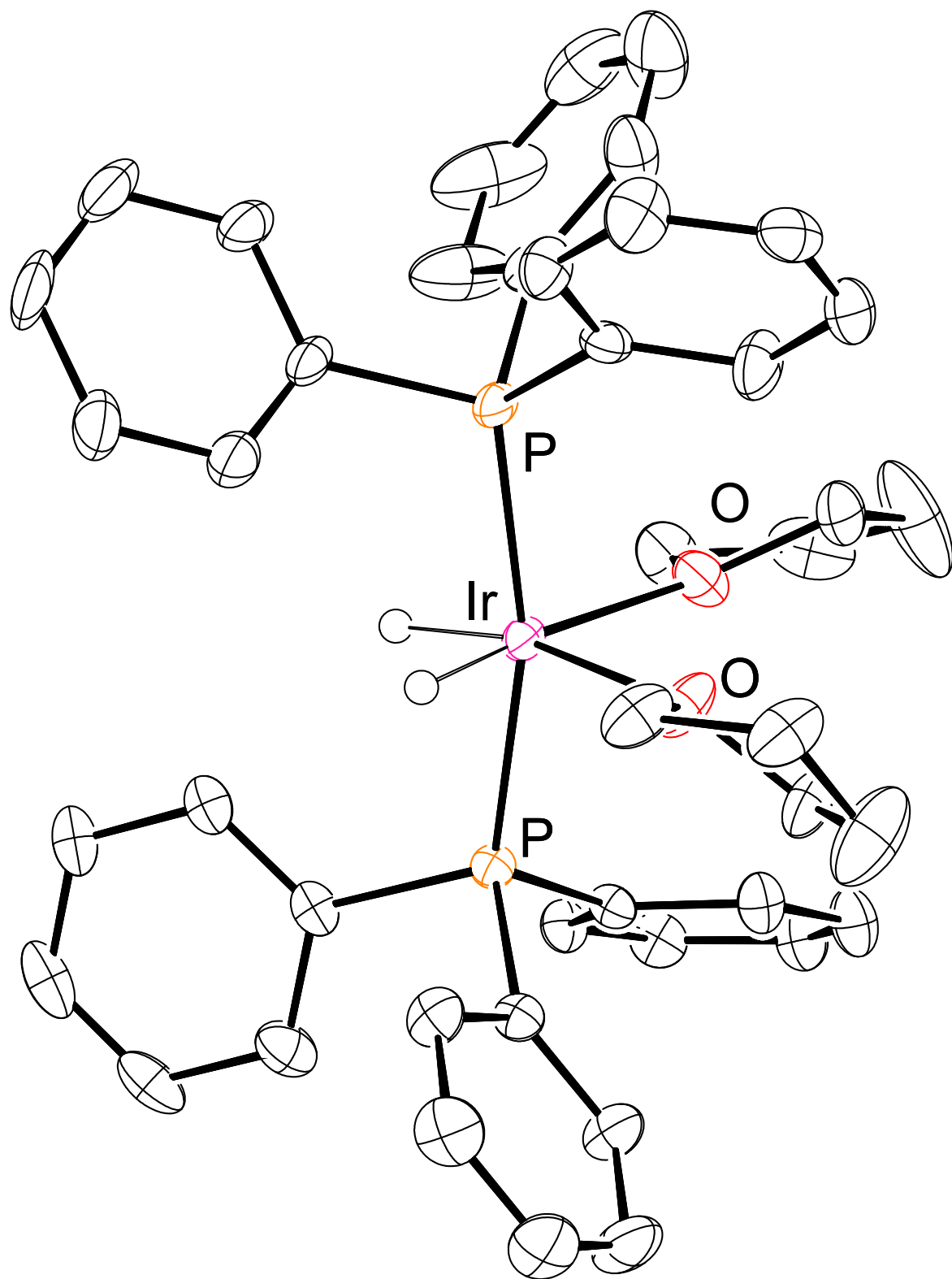


Figure 2.6.1. ORTEP diagram of **1** with ellipsoids shown at 50%. The anion is omitted for clarity.

Table 2.6.2. Crystal data and structure refinement for Complex 2.

Identification code	02	
Empirical formula	$C_{40}H_{38}F_6IrP_3$	
Formula weight	917.81	
Temperature	100 K	
Wavelength	0.71073 Å	
Crystal system	Orthorhombic	
Space group	$Pna2_1$	
Unit cell dimensions	$a = 19.4179(8)$ Å	$\alpha = 90^\circ$
	$b = 11.2723(4)$ Å	$\beta = 90^\circ$
	$c = 16.8144(8)$ Å	$\gamma = 90^\circ$
Volume	$3680.4(3)$ Å ³	
Z	4	
Density (calculated)	1.656 Mg/m ³	
Absorption coefficient	3.817 mm ⁻¹	
F(000)	1816	
Crystal size	$0.086 \times 0.082 \times 0.062$ mm ³	
Theta range for data collection	3.022 to 30.208° .	
Index ranges	$-26 \leq h \leq 27$, $-14 \leq k \leq 15$, $-21 \leq l \leq 18$	
Reflections collected	31483	
Independent reflections	9165 [R(int) = 0.0597]	
Completeness to theta = 26.000°	99.8 %	
Absorption correction	Analytical	
Max. and min. transmission	0.832 and 0.759	
Refinement method	Full-matrix least-squares on F ²	
Data / restraints / parameters	9165 / 111 / 504	
Goodness-of-fit on F ²	1.024	
Final R indices [I > 2σ(I)]	R1 = 0.0458, wR2 = 0.1001	
R indices (all data)	R1 = 0.0637, wR2 = 0.1097	
Absolute structure parameter	-0.009(6)	
Largest diff. peak and hole	2.231 and -1.722 e/Å ⁻³	

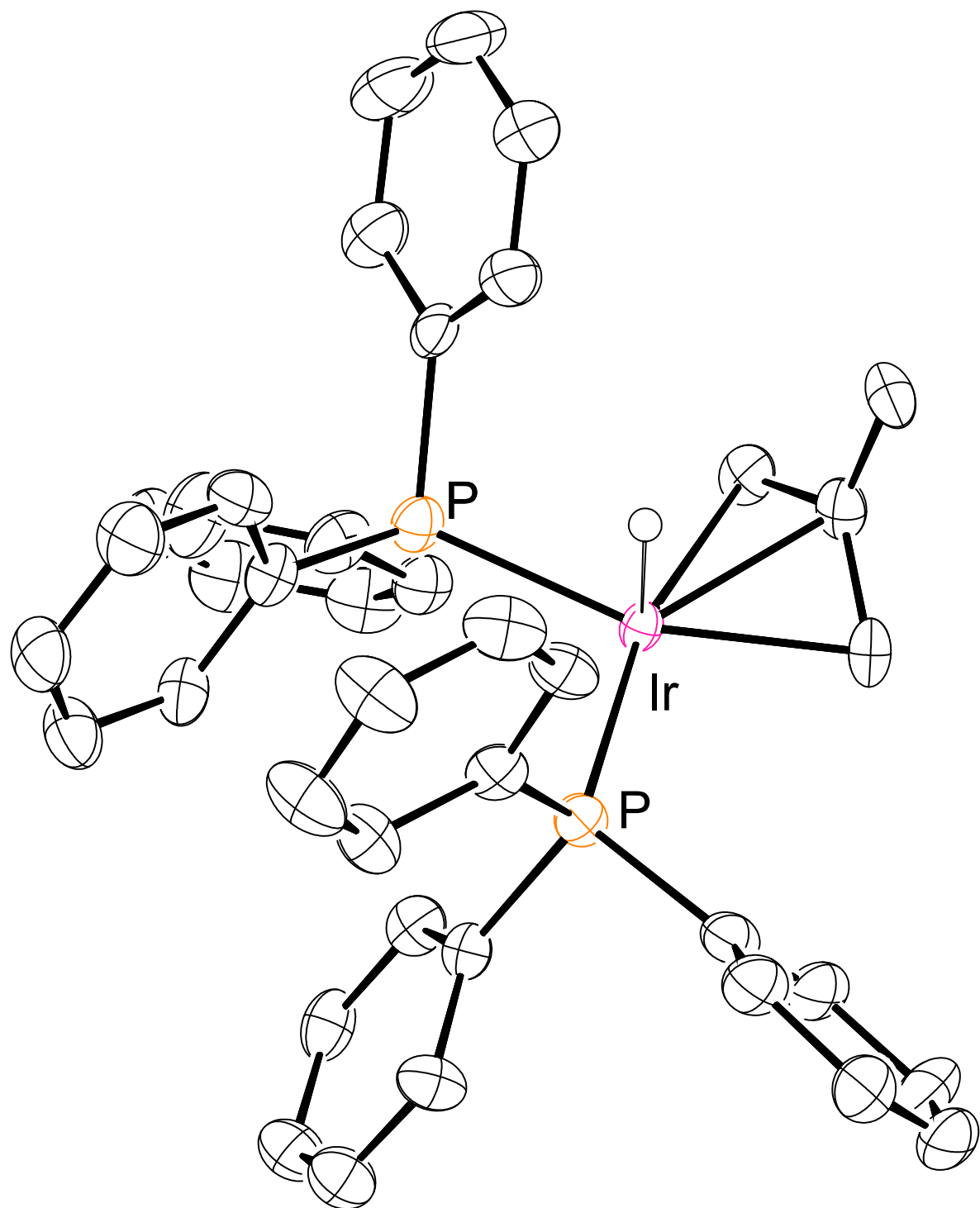


Figure 2.6.2. ORTEP diagram of **2** with ellipsoids shown at 50%. The anion is omitted for clarity.

Table 2.6.3. Crystal data and structure refinement for **2-THF**.

Identification code	02-THF	
Empirical formula	C ₄₆ H ₃₀ F ₆ IrO _{1.50} P ₃	
Formula weight	1025.97	
Temperature	100 K	
Wavelength	0.71073 Å	
Crystal system	Triclinic	
Space group	P-1	
Unit cell dimensions	a = 10.9524(2) Å	α = 78.1399(16)°
	b = 18.8750(3) Å	β = 88.2692(15)°
	c = 21.2762(4) Å	γ = 80.2988(15)°
Volume	4242.88(14) Å ³	
Z	4	
Density (calculated)	1.606 Mg/m ³	
Absorption coefficient	3.323 mm ⁻¹	
F(000)	2056	
Crystal size	0.196 x 0.13 x 0.123 mm ³	
Theta range for data collection	3.040 to 30.324°.	
Index ranges	-15 ≤ h ≤ 15, -26 ≤ k ≤ 26, -29 ≤ l ≤ 29	
Reflections collected	82359	
Independent reflections	22681 [R(int) = 0.0381]	
Completeness to theta = 26.000°	99.8 %	
Absorption correction	Gaussian	
Max. and min. transmission	1.000 and 0.629	
Refinement method	Full-matrix least-squares on F ²	
Data / restraints / parameters	22681 / 8 / 1054	
Goodness-of-fit on F ²	1.099	
Final R indices [I > 2σ(I)]	R1 = 0.0392, wR2 = 0.0827	
R indices (all data)	R1 = 0.0512, wR2 = 0.0876	
Largest diff. peak and hole	2.233 and -1.364 e/Å ⁻³	

Table 2.6.4. Crystal data and structure refinement for **3-DME**.

Identification code	04-DME	
Empirical formula	C ₄₀ H ₄₀ F ₆ IrO ₂ P ₃	
Formula weight	951.83	
Temperature	100.0(2) K	
Wavelength	1.54184 Å	
Crystal system	Monoclinic	
Space group	P 1 21/n 1	
Unit cell dimensions	a = 9.39324(13) Å	α = 90°
	b = 18.6566(3) Å	β = 95.5852(12)°
	c = 21.7876(3) Å	γ = 90°
Volume	3800.05(10) Å ³	
Z	4	
Density (calculated)	1.664 Mg/m ³	
Absorption coefficient	8.553 mm ⁻¹	
F(000)	1888	
Crystal size	0.08 x 0.023 x 0.013 mm ³	
Theta range for data collection	3.125 to 73.409°.	
Index ranges	-11 ≤ h ≤ 11, -22 ≤ k ≤ 22, -26 ≤ l ≤ 27	
Reflections collected	36529	
Independent reflections	7525 [R(int) = 0.0437]	
Completeness to theta = 67.684°	100.0 %	
Absorption correction	Gaussian	
Max. and min. transmission	0.925 and 0.592	
Refinement method	Full-matrix least-squares on F ²	
Data / restraints / parameters	7525 / 0 / 474	
Goodness-of-fit on F ²	1.017	
Final R indices [I > 2σ(I)]	R1 = 0.0292, wR2 = 0.0683	
R indices (all data)	R1 = 0.0366, wR2 = 0.0720	
Largest diff. peak and hole	1.249 and -1.064 e/Å ⁻³	

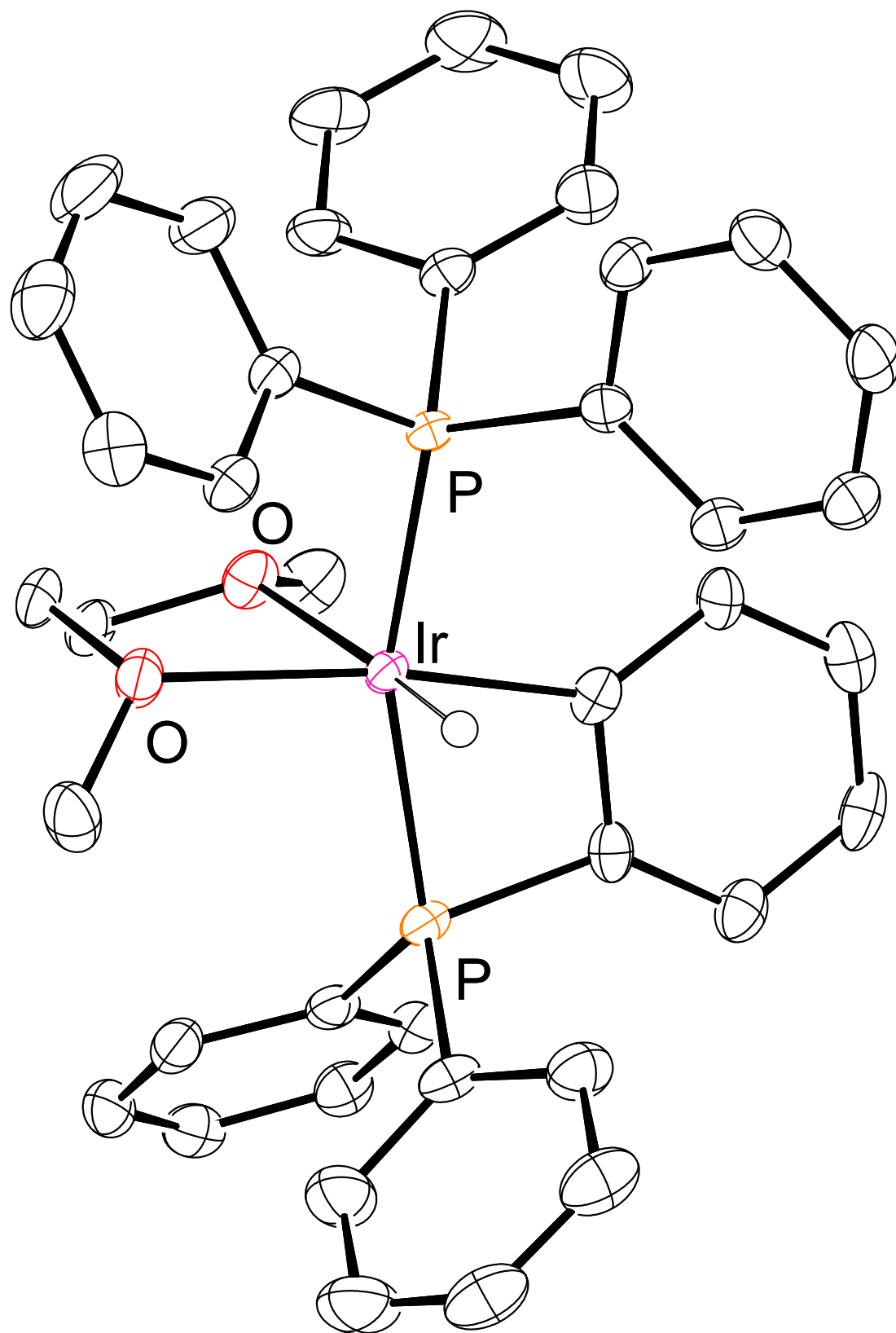


Figure 2.6.3. ORTEP diagram of 3-DME with ellipsoids shown at 50%. The anion is omitted for clarity.

Table 2.6.5. Crystal data and structure refinement for Complex 4.

Identification code	05	
Empirical formula	$C_{50}H_{32}F_6IrO_2P_3$	
Formula weight	1084.02	
Temperature	100 K	
Wavelength	0.71073 Å	
Crystal system	Triclinic	
Space group	P-1	
Unit cell dimensions	a = 11.42708(19) Å	$\alpha = 77.3551(19)^\circ$
	b = 11.7193(2) Å	$\beta = 76.4459(18)^\circ$
	c = 17.9221(4) Å	$\gamma = 73.6314(17)^\circ$
Volume	2208.39(9) Å ³	
Z	2	
Density (calculated)	1.630 Mg/m ³	
Absorption coefficient	3.198 mm ⁻¹	
F(000)	1088	
Crystal size	0.142 x 0.098 x 0.018 mm ³	
Theta range for data collection	2.938 to 30.221°.	
Index ranges	-15 ≤ h ≤ 16, -16 ≤ k ≤ 16, -25 ≤ l ≤ 24	
Reflections collected	53910	
Independent reflections	11862 [R(int) = 0.0380]	
Completeness to theta = 26.000°	99.8 %	
Absorption correction	Gaussian	
Max. and min. transmission	1.000 and 0.601	
Refinement method	Full-matrix least-squares on F ²	
Data / restraints / parameters	11862 / 0 / 559	
Goodness-of-fit on F ²	1.060	
Final R indices [I > 2σ(I)]	R1 = 0.0250, wR2 = 0.0523	
R indices (all data)	R1 = 0.0291, wR2 = 0.0538	
Largest diff. peak and hole	1.727 and -1.337 e/Å ⁻³	

Table 2.6.6. Crystal data and structure refinement for **5**.

Identification code	06	
Empirical formula	$C_{43}H_{44}Cl_2F_6IrOP_3$	
Formula weight	1046.79	
Temperature	100.0(2) K	
Wavelength	1.54184 Å	
Crystal system	Monoclinic	
Space group	$P2_1/c$	
Unit cell dimensions	$a = 21.3198(3)$ Å	$\alpha = 90^\circ$
	$b = 11.9139(2)$ Å	$\beta = 93.3313(12)^\circ$
	$c = 16.0929(2)$ Å	$\gamma = 90^\circ$
Volume	$4080.71(11)$ Å ³	
Z	4	
Density (calculated)	1.704 Mg/m ³	
Absorption coefficient	9.185 mm ⁻¹	
F(000)	2080	
Crystal size	$0.18 \times 0.125 \times 0.005$ mm ³	
Theta range for data collection	4.154 to 73.539° .	
Index ranges	$-25 \leq h \leq 26$, $-14 \leq k \leq 14$, $-14 \leq l \leq 18$	
Reflections collected	32737	
Independent reflections	8027 [R(int) = 0.0512]	
Completeness to theta = 67.684°	99.3 %	
Absorption correction	Gaussian	
Max. and min. transmission	1.000 and 0.280	
Refinement method	Full-matrix least-squares on F ²	
Data / restraints / parameters	8027 / 8 / 531	
Goodness-of-fit on F ²	1.025	
Final R indices [I > 2sigma(I)]	R1 = 0.0376, wR2 = 0.0888	
R indices (all data)	R1 = 0.0443, wR2 = 0.0937	
Largest diff. peak and hole	1.725 and -1.158 e/Å ⁻³	

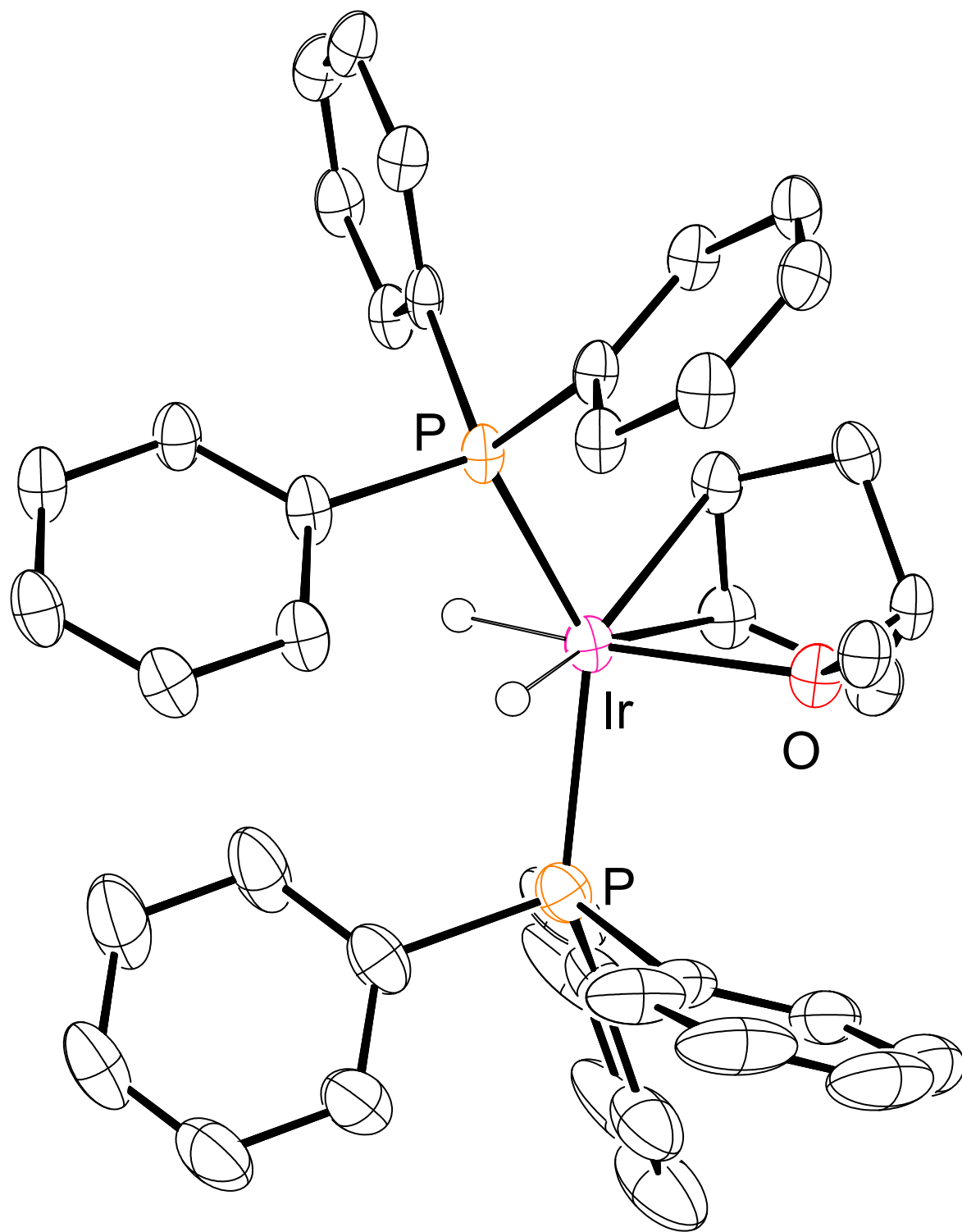


Figure 2.6.4. ORTEP diagram of **5** with ellipsoids shown at 50%. The anion is omitted for clarity.

2.7 REFERENCES

- (1) Haibach, M. C.; Kundu, S.; Brookhart, M.; Goldman, A. S., *Acc. Chem. Res.* **2012**, *45* (6), 947-958.
- (2) Choi, J.; MacArthur, A. H. R.; Brookhart, M.; Goldman, A. S., *Chem. Rev.* **2011**, *111* (3), 1761-1779.
- (3) Crabtree, R. H.; Mihelcic, J. M.; Quirk, J. M., *J. Am. Chem. Soc.* **1979**, *101* (26), 7738-7740.
- (4) Crabtree, R. H., *Chem. Rev.* **1985**, *85* (4), 245-269.
- (5) Crabtree, R. H.; Demou, P. C.; Eden, D.; Mihelcic, J. M.; Parnell, C. A.; Quirk, J. M.; Morris, G. E., *J. Am. Chem. Soc.* **1982**, *104* (25), 6994-7001.
- (6) Janowicz, A. H.; Bergman, R. G., *J. Am. Chem. Soc.* **1982**, *104* (1), 352-354.
- (7) Janowicz, A. H.; Bergman, R. G., *J. Am. Chem. Soc.* **1983**, *105* (12), 3929-3939.
- (8) Catalysis is observed in certain cases in the presence of a base, which is suggestive of catalysis through neutral intermediates. See reference 12 for one example.
- (9) Choi, J.; Goldman, A. S., Ir-Catalyzed Functionalization of C–H Bonds. In *Iridium Catalysis*, Andersson, P. G., Ed. Springer Berlin Heidelberg: Berlin, Heidelberg, 2011; pp 139-167.
- (10) Findlater, M.; Choi, J.; Goldman, A. S.; Brookhart, M., Alkane Dehydrogenation. In *Alkane C-H Activation by Single-Site Metal Catalysis*, Pérez, P. J., Ed. Springer Netherlands: Dordrecht, 2012; pp 113-141.
- (11) Zhang, Y.; Schley, N. D., *Chem. Commun.* **2017**, *53* (13), 2130-2133.
- (12) Burk, M. J.; Crabtree, R. H.; Parnell, C. P.; Uriarte, R. J., *Organometallics* **1984**, *3* (5), 816-817.
- (13) Crabtree, R. H.; Mellea, M. F.; Mihelcic, J. M.; Quirk, J. M., *J. Am. Chem. Soc.* **1982**, *104* (1), 107-113.
- (14) Romero, P. E.; Whited, M. T.; Grubbs, R. H., *Organometallics* **2008**, *27* (14), 3422-3429.
- (15) Luecke, H. F.; Arndtsen, B. A.; Burger, P.; Bergman, R. G., *J. Am. Chem. Soc.* **1996**, *118* (10), 2517-2518.
- (16) Pregosin, P. S., *NMR in Organometallic Chemistry*. Wiley-VCH: Weinheim, 2012; p 474.
- (17) Bennett, M. A.; Milner, D. L., *Chem. Commun.* **1967**, (12), 581-582.
- (18) Del Piero, G.; Perego, G.; Zazzetta, A.; Cesari, M., *Cryst. Struct. Commun.* **1974**, *3* (4), 725-9.
- (19) Longato, B.; Morandini, F.; Bresadola, S., *J. Organomet. Chem.* **1975**, *88* (1), C7-C8.
- (20) Mohr, F.; Privér, S. H.; Bhargava, S. K.; Bennett, M. A., *Coord. Chem. Rev.* **2006**, *250* (15–16), 1851-1888.
- (21) Feldman, J. D.; Peters, J. C.; Tilley, T. D., *Organometallics* **2002**, *21* (20), 4050-4064.
- (22) Geoffroy, G. L.; Pierantozzi, R., *J. Am. Chem. Soc.* **1976**, *98* (25), 8054-8059.

- (23) Crabtree, R. H.; Parnell, C. P., *Organometallics* **1985**, *4* (3), 519-523.
- (24) West, N. M.; White, P. S.; Templeton, J. L., *J. Am. Chem. Soc.* **2007**, *129* (41), 12372-12373.
- (25) Moxham, G. L.; Brayshaw, S. K.; Weller, A. S., *Dalton Trans.* **2007**, (18), 1759-1761.
- (26) For details of the conditions see § 2.4 Experimental
- (27) Whited, M. T.; Grubbs, R. H., *J. Am. Chem. Soc.* **2008**, *130* (18), 5874-5875.
- (28) Choi, J.; Choliy, Y.; Zhang, X.; Emge, T. J.; Krogh-Jespersen, K.; Goldman, A. S., *J. Am. Chem. Soc.* **2009**, *131* (43), 15627-15629.
- (29) Haibach, M. C.; Lease, N.; Goldman, A. S., *Angew. Chem. Int. Ed.* **2014**, *53* (38), 10160-10163.
- (30) Hoops, S.; Sahle, S.; Gauges, R.; Lee, C.; Pahle, J.; Simus, N.; Singhal, M.; Xu, L.; Mendes, P.; Kummer, U., *Bioinformatics* **2006**, *22* (24), 3067-3074.

Chapter III

GROUP-TRANSFER REACTION OF A CATIONIC IRIDIUM ALKOXYCARBENE GENERATED BY ETHER DEHYDROGENATION

Reprinted with permission from Scott M. Chapp and Nathan D. Schley. *Inorg. Chem.* 2020, 59, 7143-7149. Copyright 2020 American Chemical Society.

3.1 Introduction

The selective activation and functionalization of inert C-H bonds by homogeneous metal complexes has been an area of significant interest since pioneering studies on alkane C-H oxidative addition and alkane dehydrogenation.¹⁻⁴ These foundational stoichiometric systems led the way to early examples of catalytic alkane transfer dehydrogenation.⁵⁻⁹ Further development of alkane dehydrogenation over the intervening decades has revealed design criteria that favor neutral, electron-rich and thermally-stable pincer iridium complexes analogous to those initially applied to alkane dehydrogenation by Kaska and Jensen in 1996.¹⁰⁻¹⁴

In contrast to the large body of work on alkane dehydrogenation, the dehydrogenation of compounds bearing heteroatom functionality has seen considerably less attention. Jensen and Kaska reported the transfer dehydrogenation of THF to a mixture of furan and dihydrofurans¹⁵ and Goldman has reported the α,β -dehydrogenation of alkyl amines.¹⁶⁻¹⁷ More recently, Brookhart¹⁸ and Huang¹⁹ demonstrated that neutral PCP pincer-supported iridium complexes catalyze the transfer dehydrogenation of alkyl ethers to vinyl ether products. The α,β -dehydrogenation of amines and ethers is complicated by competing α,α -dehydrogenation to give aminocarbene and alkoxy carbene complexes respectively. The formation of iridium alkoxy carbene complexes via ether dehydrogenation and their reactivity has been studied extensively both by Carmona and by Whited and Grubbs.²⁰⁻²¹ Grubbs' work demonstrated that neutral iridium alkoxy carbenes undergo group-transfer reactions with heterocumulenes and certain 1,3-dipolar reagents including CO₂, phenyl isocyanate and adamantyl azide (Ad-N₃). These transformations were proposed to occur via initial [2+2] cyclization to give a 4-membered iridacyclic intermediate. This reactivity is distinct from that of canonical group 6 alkoxy carbenes, and argues for a significant role for the high-lying, filled d_{z²} orbital responsible for the M=CH(OR) π -backbonding interaction.²²

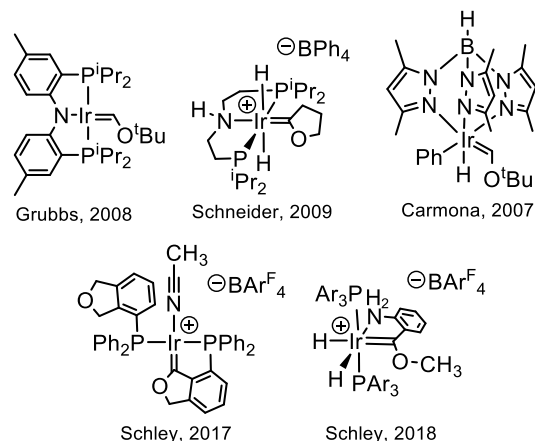


Figure 3.1.1. Recent ether-derived alkoxy-carbenes.

In this context our group has been exploring the chemistry of *cationic* bis(phosphine)iridium alkoxy-carbene complexes with the aim of developing systems with reduced metal-alkoxy-carbene backbonding and enhanced electrophilicity relative to neutral variants. Prior to our studies, a single example of THF dehydrogenation to give a cationic iridium alkoxy-carbene over a period of days had been reported by Schneider (**Figure 3.1.1**).²³ We have since demonstrated facile formation of cationic alkoxy-carbene complexes via ether dehydrogenation in Lewis base-directed intra- and intermolecular examples, with evidence for reversible α -hydride insertion and C-O bond cleavage reactions in certain cases.²⁴⁻²⁵ Despite the body of work on the generation of alkoxy-carbene complexes via ether dehydrogenation, few stoichiometric transformations and only a single catalytic reaction have been reported.^{21, 26-27} We now report the synthesis of a cationic pincer-supported Ir(I) alkoxy-carbene complex generated by α,α -dehydrogenation of cyclopentyl methyl ether (CPME) and demonstrate its reactivity in atom- and group-transfer reactions with an alkyl azide, a ketene and an alkyl nitrite. This complex serves as a catalyst in ether imination, showing that cationic iridium complexes are sufficiently competent at ether dehydrogenation to support catalytic transformations.

3.2 Results and Discussion

Treatment of commercially-available $[(\text{cod})_2\text{Ir}]\text{BARF}_4$ with 2,6-bis((diisopropylphosphino)methyl)pyridine (**L1**) gives complex **1** (**Figure 3.2.1, eq 1**) which undergoes hydrogenation to an iridium dihydride complex **2** (**Figure 3.2.2, eq 2**). Dehydrogenation of **2** with *tert*-butylethylene in CPME yields a product with a single $^{31}\text{P}\{^1\text{H}\}$ NMR signal and a broad,

downfield-shifted ^1H resonance at 13.5 ppm. This signal is in the range expected for an alkoxymethylidene $\text{Ir}=\text{CHOR}$ resonance,²⁸⁻³⁰ which along with the appearance of a $^{13}\text{C}\{^1\text{H}\}$ resonance at 234.7 ppm led us to assign the product as cationic alkoxycarbene complex **3**, a site of CPME activation distinct from the 3,4-dehydrogenation observed in a related non-pincer complex.³¹ Numerous attempts at confirmation of this assignment through X-ray crystallography ultimately led to a structure solution for **3** from samples crystallizing as 3-component merohedral twins in the P2_1 space group (**Figure 3.2.2, right**). The unambiguous characterization of **3** represents one of only a few cationic iridium alkoxycarbene complexes generated by ether dehydrogenation.^{23-25,32}

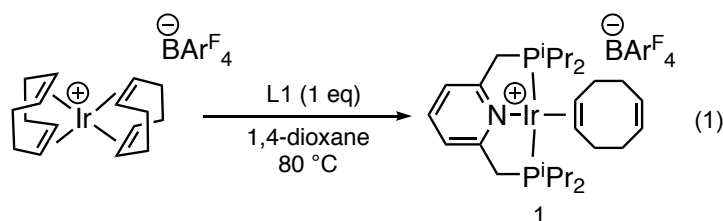


Figure 3.2.1. Synthesis of complex **1**

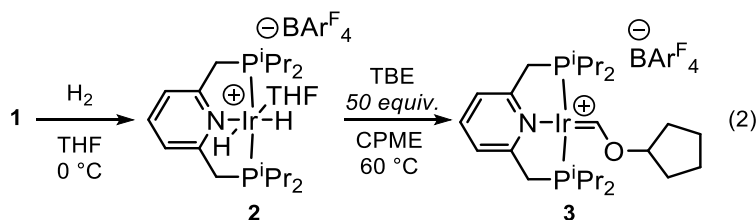


Figure 3.2.2. Hydrogenation of complex **1** to form **2** followed by dehydrogenation with TBE to form **3**

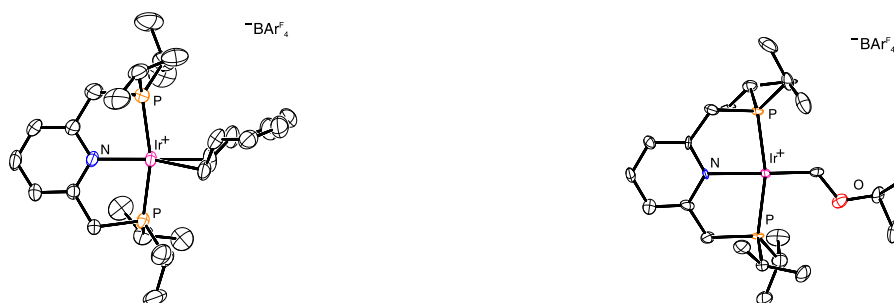


Figure 3.2.3. ORTEP diagrams of **1** (left) and **3** (right) shown at 50% probability. Full disorder models are omitted for clarity. Selected bond distances in **3** (Å): $\text{Ir}=\text{C}$ 1.880(12), $\text{Ir}-\text{N}$ 2.179(8), $\text{O}-\text{C}_{\text{carbene}}$ 1.342(16)

Work by Milstein has shown that metal-bound bis(phosphinomethyl)pyridines like **L1** can undergo deprotonation at the α -phosphino methylene position to give a formally monoanionic PNP ligand.³³ Treatment of **3** with potassium *tert*-butoxide gives the neutral alkoxy carbene complex **4** (**Figure 3.2.4, eq 3**), which can be distinguished by a shift of the Ir=CHOR ¹³C resonance from 234.7 to 221.5 ppm. The bond metrical parameters obtained from the crystal structure of **4** show significant Kekulé distortion of the pyridine moiety and contraction of one exocyclic C-C bond consistent with those observed in other systems (**Figure 3.2.5**).³⁴⁻³⁵ The Ir=C_{carbene} bond length in **4** is 1.881(3) Å, which is indistinguishable from the bond length of 1.880(12) Å in **3** and similar to that of a neutral (PNP)Ir(I) alkoxy carbene complexes reported by Grubbs (1.884(4) Å)³⁰ as well as a cationic iridium(I) alkoxy carbene (1.912(4) Å) we have previously reported.²⁴ Thus the iridium carbene bond length in **3** and **4** appear insensitive to the net ionic charge. In contrast, these values are shorter than those observed for a cationic iridium(III) alkoxy carbene reported by Schneider (1.938(3) Å)²³ as well as a trio of cationic iridium(III) alkoxybenzylidenes we have previously reported (1.997(3), 1.997(8) and 2.001(2)).²⁴⁻²⁵ These observations suggest that iridium alkoxy carbene bond lengths are most sensitive to the formal oxidation state.

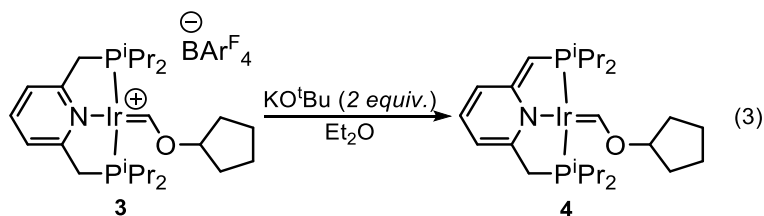


Figure 3.2.4. Dearomatization of complex **3** with KO^tBu to form neutral alkoxy carbene **4**

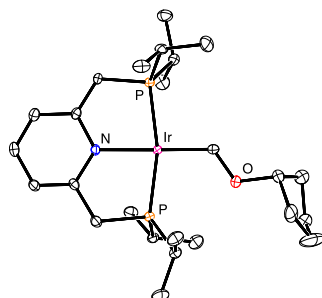


Figure 3.2.5. ORTEP diagram of **4** shown at 50% probability. The full disorder model and anion are omitted for clarity. Selected bond distances (Å): Ir=C 1.882(3), Ir-N_{py} 2.096(3), O-C_{carbene} 1.342(4).

The structural similarity of complex **4** to the family of neutral PNP(Ir) alkoxy-carbenes prepared by Whited and Grubbs via ether dehydrogenation encouraged a closer comparison of the two systems. In particular, we were interested in whether the reactivity of the neutral complex **4** towards alkyl azides would match that observed by Grubbs for the analogous complex shown in **Figure 3.1.1**. Additionally, cationic derivative **3** could be compared directly to **4** in order to ascertain whether the net ionic charge modulates the reactivity of alkoxy-carbenes towards group-transfer reactions.

Indeed, both complexes **3** and **4** react rapidly with Ad-N₃ at room temperature to give N-adamantyl formimidate **5** and the corresponding Ir-N₂ complexes **6** and **7** respectively (**Figure 3.2.6, eq 4**; **Figure 3.2.7, eq 5**). N₂ binding can be confirmed by analysis of their infrared spectra, which show an Ir-N₂ band at 2141 cm⁻¹ for **6** and 2076 cm⁻¹ for complex **7**. For comparison, a neutral (PNP)IrN₂ complex reported by Grubbs absorbs at 2067 cm⁻¹, demonstrating a clear decrease in Ir-N₂ backbonding for the cationic variant **6**. The assignment of **6** and **7** was confirmed by single crystal X-ray diffraction of both species (**Figure 3.2.8**) and by conversion of **6** to **7** on treatment with potassium *tert*-butoxide.

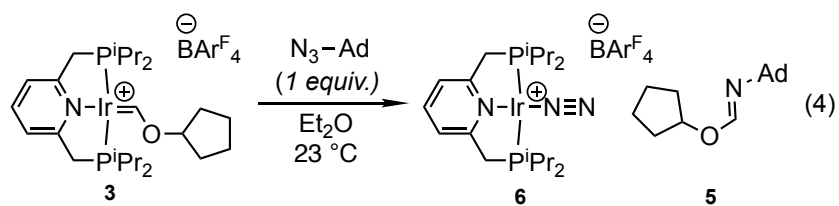


Figure 3.2.6. Stoichiometric reaction of complex **3** with adamantyl azide

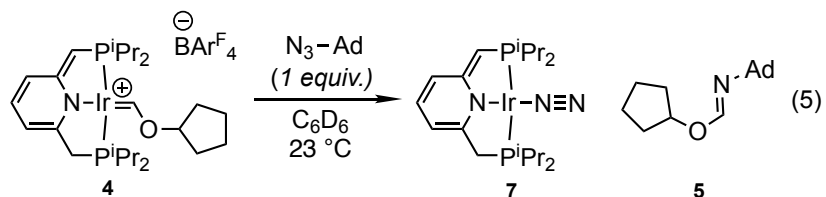


Figure 3.2.7. Stoichiometric reaction of complex **4** with adamantyl azide

An analogous azide-alkoxy-carbene group-transfer reaction has been used previously as part of a synthetic cycle for the imination of ethers to formimidates. The incompatibility of the system with excess azide reagent initially precluded the development of a true catalytic reaction, but through stepwise addition under photolysis, 4 turnovers could be obtained over

several days.²⁶ These conditions were subsequently improved through the slow addition of Ad-N₃ over 30 hours, leading to a catalytic system capable of 10 turnovers.^{21,27}

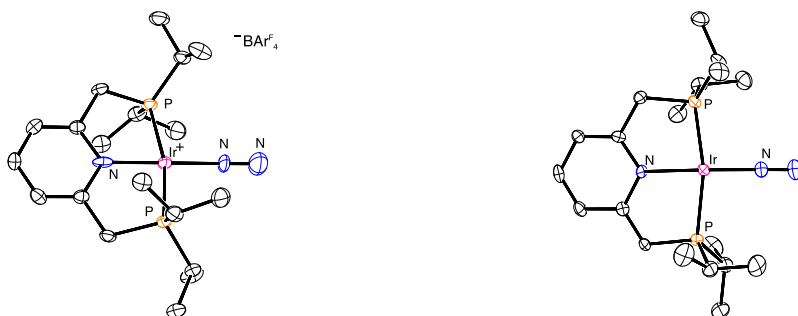


Figure 3.2.8. ORTEP diagrams of **6** (left) and **7** (right) shown at 50% probability. Full disorder models are omitted for clarity. Selected bond distances (Å), Complex **6**: Ir-N₂ 1.915(5), Ir-N_{py} 1.994(5), N≡N 1.105(8). Complex **7**: Ir-N₂ 1.881(5), Ir-N_{py} 2.053(4), N≡N 1.083(7).

Table 3.2.1. Evaluation of Reaction Conditions

Entry	Catalyst (mol %)	Temp. (°C)	Time (hr.)	Light source	Yield ^a
1	3 (10%)	23	22	blue	0.4%
2	3 (10%)	90	22	none	0.8%
3	3 (10%)	90	22	blue	83% ^b
4	3 (5%)	90	22	blue	39% ^b
5	3 (10%)	80	22	blue	70% ^b
6	4 (10%)	90	22	blue	29% ^b
7	3 (10%)	90	1	blue	68% ^b
8	1 (10%)	90	22	blue	84% ^b

^a NMR yield. ^b Average of two experiments.

By comparison, cationic complex **3** serves as a competent catalyst for the group-transfer imination of CPME under batch conditions without requirement for slow azide addition. Under optimized conditions under blue light irradiation we observe 8.3 turnovers to give 83% yield of formimidate **5** (Table 3.2.1, entry 3). The majority of turnovers occur within the first hour (Table 3.2.1, entry 7), demonstrating rapid catalysis without the sensitivity to excess azide observed in the neutral

Grubbs system. In a series of experiments we found that **3** reacts productively with Ad-N₃ to give **5** at 23 °C, but that a reaction temperature of 90 °C under blue light irradiation is required for productive catalysis. When a catalytic reaction is examined in the dark by ³¹P{¹H} NMR after exposure to blue light at 90 °C for 5 or 15 minutes, complex **6** appears to be the major metal-containing species in solution. This observation supports a role for light in N₂ dissociation and is consistent with **6** being on-path intermediate in catalysis (**Figure 3.2.9**). Although **3** closely matches the total turnover number achieved by the Grubbs system, the tolerance of batch conditions rather than a requirement for azide slow addition is a marked improvement. In contrast, the neutral complex **4** achieves only 2.9 turnovers under comparable batch conditions (**Table 3.2.1, entry 6**). The neutral N₂ complex **7** shows sensitivity to excess Ad-N₃, degrading to several unidentified species over minutes to hours under irradiation. In the case of the catalysis by the cationic complex **3**, total turnover numbers appear to be limited by catalyst degradation, as ³¹P{¹H} NMR analyses show numerous unidentified products after cessation of catalysis.

The success of complex **3** as an ether imination catalyst inspired us to examine the precursor, complex **1** for the same transformation. Dissociation of 1,5-cyclooctadiene would provide access to a three coordinate 14 e⁻ Ir(I) fragment **A** (**Figure 3.2.9**) analogous to those proposed as reactive intermediates in both α-C-H activation of CPME and C-H activation of alkanes.^{12-14,23,36} Under our optimized conditions complex **1** shows comparable activity to **3** with 8.3 TON (83%) (**Table 3.2.1, entry 8**). This observation should simplify future reaction development since derivatives of ligands related to **L1** can be accessed in one step from commercially available iridium starting materials. Indeed the ^tBu analogue of **1** has been previously reported.³⁷

A proposed mechanism for catalytic CPME imination by **3** is given in **Figure 3.2.9**. Reaction of **3** with Ad-N₃ could proceed via either initial [2+2]²⁶ (**B**) or [2+3]³⁸ cycloaddition, after which extrusion of formimidate **5** would give N₂ complex **6**. Light-promoted dissociation of dinitrogen would give the 14 e⁻ Ir(I) fragment **A**, which is likely the species responsible for CPME activation to regenerate **3**.

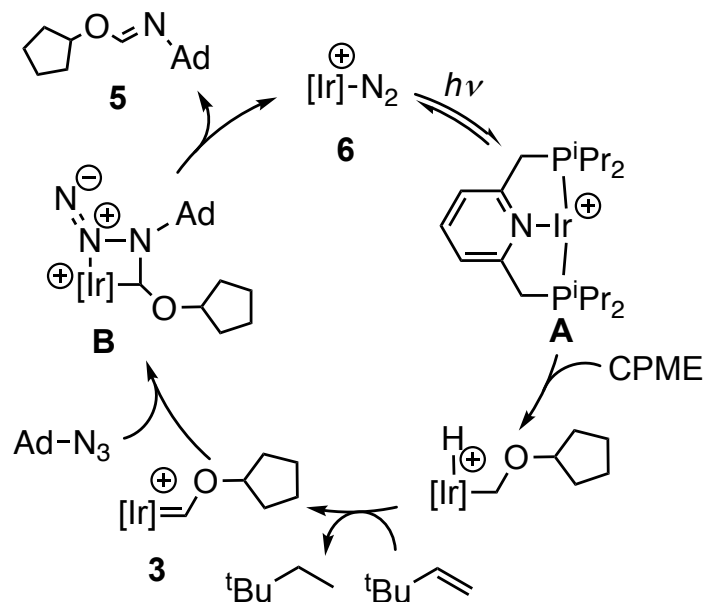


Figure 3.2.9. Proposed catalytic cycle for group transfer imination of CPME. Both $[2+2]^{26}$ (B) and $[2+3]^{38}$ azide-carbene cycloaddition mechanisms have been previously proposed.

In total, the stoichiometric reactivity of alkoxy-carbene complexes **3** and **4** with Ad-N_3 closely mirrors observations made by Whited and Grubbs. In our case, complex **3** was found to serve as a catalyst for group transfer imination of CPME without requirement for portionwise or slow addition of azide, while the neutral complex **4** appears to share the Grubbs system's reported sensitivity to excess azide.²⁶

As complexes of square planar d^8 metal ions, **3** and **4** bear a filled high-lying d_z^2 orbital which has been implicated in so-called Roper-type carbene chemistry of which group-transfer reactions of azides represent one example.^{21-22, 39-40} Other electrophiles including CO_2 , carbonyl sulfide, and phenyl isocyanate have been demonstrated to give formate esters, thioformates and formimidates, respectively.^{22, 30} We suspected that other substrates might undergo similar group-transfer reactions via what has been proposed as an initial $[2+2]$ cycloaddition²² to alkoxy-carbene **3**, and identified diazoalkanes, ketenes and alkyl nitrites as possible candidates for C-C or C-O bond-forming chemistry. Just as alkyl azides are observed to transfer a formal nitrene equivalent, we hypothesized that diazoalkanes and alkyl aryl ketenes⁴¹⁻⁴⁵ might serve as carbene equivalents to give the products of formal carbene-carbene cross-coupling.

Surprisingly, complex **3** is largely unreactive towards either one equivalent or an excess of trimethylsilyldiazomethane at room temperature. While elevated temperatures or irradiation with blue light did lead to partial consumption of **3**, the N_2 adduct **6** is observed only in trace quantities and no organic product of carbene transfer was detectable. In contrast, treatment

of **3** with 25 equivalents of phenyl ethyl ketene gives cyclopentyl formate and two new iridium-containing species in a ratio of 95:5 by $^{31}\text{P}\{^1\text{H}\}$ NMR (**Figure 3.2.10, eq 6**).

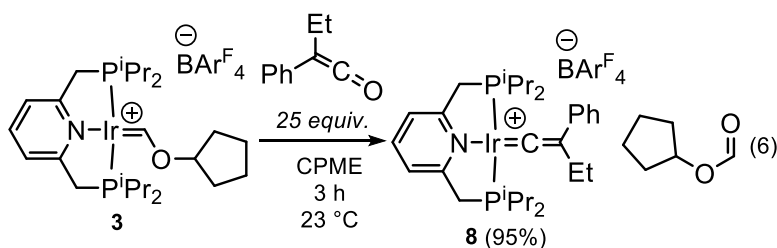


Figure 3.2.10. Stoichiometric reaction of complex **3** with phenyl ethyl ketene

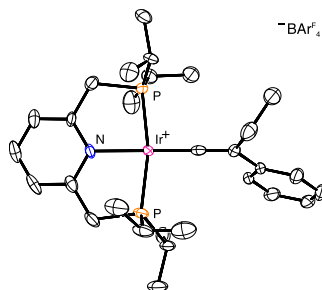


Figure 3.2.11. ORTEP diagram of **8** shown at 50% probability. The full disorder model and anion are omitted for clarity.

We have characterized the minor product as the Ir(I)-CO complex **9** by doping with an authentic sample of **9** generated independently⁴⁶ (see § 3.4 Experimental). The major product was separable by crystallization and found to be the unexpected cationic iridium vinylidene complex **8** (**Figure 3.2.11**). Thus, phenyl ethyl ketene appears to serve as an oxygen atom donor rather than a carbene equivalent. This outcome is interesting when considered alongside the reported reactivity of phenyl isocyanate with a related neutral alkoxycarbene,³⁰ which serves as a nitrene source despite the electronic similarity of ketenes and isocyanates.⁴⁷ Ketenes undergo thermal [2+2] reactions with a variety of substrates including simple olefins, but such reactivity engages the C=C fragment of the ketene moiety.⁴⁸ In our case the observed group transfer reaction of phenyl ethyl ketene likely requires that initial [2+2] cycloaddition occur via the C=O fragment, implicating the pair of stepwise or concerted, asynchronous nucleophilic additions shown in **Figure 3.2.12** rather than a concerted, synchronous [2+2] process. A closely-related mechanism has been proposed for a series of oxygen atom transfer reactions of an isolable niobocene ketene

complex,⁴⁹⁻⁵⁰ demonstrating the O-nucleophilicity of α -metalloketenes. The structure of a (diphenylketene- κ^2 O,C¹)iridium(I) complex reported by Grotjahn is also consistent with this proposal, though O-atom transfer from a diphenylketene- κ^2 C¹,C² adduct may also be possible.⁵¹

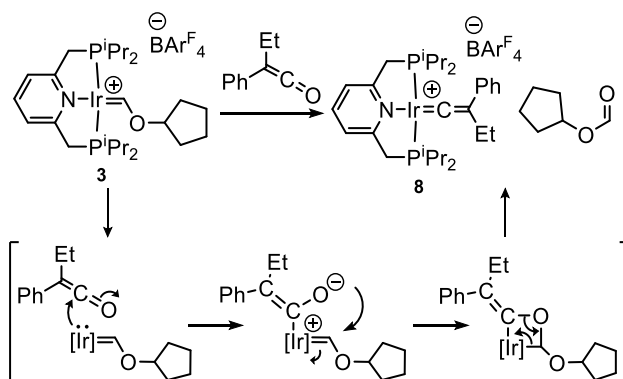


Figure 3.2.12. Proposal for ketene O-atom transfer

Previous studies by Whited and Grubbs were limited to group- or atom-transfer reactions of heterocumulenes, but the possibility that **3** might be capable of non-concerted group transfer reactions encouraged us to explore other electrophiles. One promising reagent – isobutyl nitrite, was found to react with **3** to give a single new complex with a major ³¹P{¹H} NMR signal in 92% yield at 34 ppm. We have characterized this species as the iridium dialkoxyalkyl nitrosyl complex **10** resulting from formal alkoxide group-transfer and scission of the N-O bond. Transition metal dialkoxyalkyls are proposed as tetrahedral intermediates in the alkoxide exchange of alkoxy-carbene complexes, however there is only a single report of a transition metal dialkoxyalkyl complex in the Cambridge Crystallographic Database. In that case, nucleophilic attack of NaMn(CO)₅ on di(phenoxy)chloromethane gave the corresponding manganese diphenoxyalkyl,⁵² making **10** the only isolable dialkoxyalkyl generated by alkoxide transfer to an alkoxy-carbene.

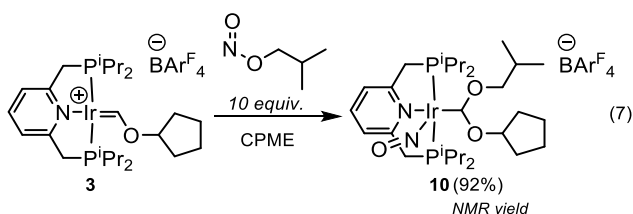


Figure 3.2.13. Stoichiometric reaction of complex **3** with isobutyl nitrite

The solid-state structure of **10** shows a square pyramidal complex containing a bent nitrosyl with an Ir-N-O angle of $123.0(5)^\circ$ and a vacant site *trans* to the nitrosyl ligand, an arrangement shared by all other reported bent, 5-coordinate iridium nitrosyls.⁵³⁻⁵⁸ Though we have been successful in characterizing **10** in the solid state by both single-crystal X-ray diffraction (**Figure 3.2.14**) and elemental analysis, the instability of **10** in solution has precluded the collection of high quality ^1H and $^{13}\text{C}\{^1\text{H}\}$ NMR data. Nonetheless, the dialkoxyalkyl ^1H resonance can be identified as a triplet occurring at 7.18 ppm with $^3J_{\text{HP}} = 4.7$ Hz, which collapses to a broad singlet on ^{31}P decoupling. This is in good agreement with the reported manganese dialkoxyalkyl which resonates at 7.38 ppm. There is no reported ^{13}C chemical shift for the manganese dialkoxyalkyl, however an HSQC experiment with **10** shows a correlation with a ^{13}C resonance at 94.2 ppm, which aligns well with an iridium hydroxyaminoalkyl reported to resonate at 96.9 ppm.⁵⁹

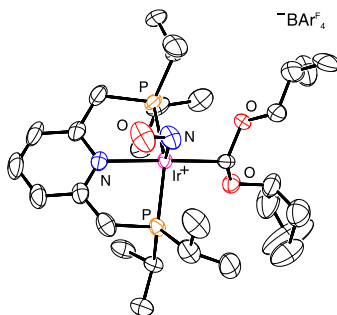


Figure 3.2.14. ORTEP diagram of **10** shown at 50% probability. The full disorder model and anion are omitted for clarity.

The conversion of **3** to **10** presumably occurs via initial binding of Ir to the electrophilic N atom of isobutyl nitrite. This binding mode has been inferred previously on the basis of IR and NMR data at complexes of Ru⁶⁰ and Ir⁶¹ and shown in a single crystallographically characterized example on Pd.⁶² Subsequent alkoxide transfer to the alkoxy carbene would give **10**. A related reverse reaction, the formation of an N-coordinated alkyl nitrite via alkoxide attack at a metal nitrosyl, has been previously observed at Ir.⁶¹

3.3 Conclusion

In summary, we report the synthesis of cationic and neutral $\text{PNP}(\text{iPr})_4$ iridium alkoxycarbene complexes via transfer dehydrogenation of CPME. Both alkoxycarbene complexes react with Ad-N_3 to form the corresponding Ir-N_2 complex and a formimidate resulting from formal nitrene transfer to the alkoxycarbene. This reactivity mirrors observations by Whited and Grubbs on a related neutral iridium alkoxycarbene system. We have translated this stoichiometric reactivity to catalysis in both the cationic and neutral alkoxycarbene cases, however the cationic complex **3** shows superior performance. Under optimized batch conditions **3** displays 7 TON within the first hour, comparing favorably against the previously reported system which requires slow addition of azide over more than 24 hours for comparable turnover numbers. The precursor complex $[(\text{PNP}(\text{iPr})_4)\text{Ir}(\eta^2\text{-cod})]\text{BAR}^{\text{F}}_4$ (**1**) is also found to serve as an active catalyst with similar performance.

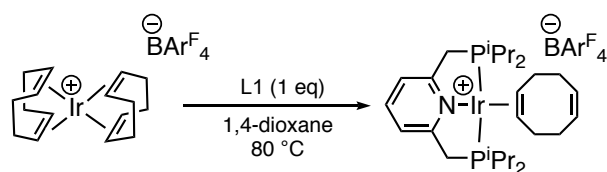
In addition, we have further expanded the scope of reagents which undergo atom or group-transfer reactions with iridium alkoxycarbenes to include phenyl ethyl ketene and isobutyl nitrite. These experiments have led to the isolation of a ketene-derived iridium vinylidene complex and the first late transition metal dialkoxyalkyl complex to be structurally characterized. The reactivity of **3** with phenyl ethyl ketene and isobutyl nitrite is suggestive of a stepwise, initial [2+2] cycloaddition rather than a concerted process. These results add to our understanding of alkoxycarbene complexes of d^8 metal ions and show promise for future development for new functionalization reactions of ethers that proceed through alkoxycarbene intermediates.

3.4 Experimental

General Considerations. All manipulations were carried out using standard vacuum, Schlenk, cannula, or glovebox techniques under N_2 unless otherwise specified. Tetrahydrofuran, dichloromethane, pentane, and diethyl ether were degassed with argon and dried over activated alumina using a solvent purification system. 1,4-dioxane and CPME were degassed with nitrogen and stored over activated 4Å molecular sieves. 1-azidoadamantane, potassium *tert*-butoxide and isobutyl nitrite were purchased from commercial suppliers and used as received. 3,3-dimethyl-1-butene (*tert*-butylethylene) sourced from a commercial supplier was found to be contaminated with Me_2S , which could be removed by stirring over CuBr followed by distillation. **L1**,⁶³ ($\text{NaBAR}^{\text{F}}_4$),⁶⁴⁻⁶⁵ $[\text{cod}_2\text{Ir}]\text{BAR}^{\text{F}}_4$,⁶⁶ and phenyl ethyl ketene⁶⁷⁻⁶⁸ were prepared by published procedures.

Spectroscopy. ^1H , $^{13}\text{C}\{^1\text{H}\}$ and $^{31}\text{P}\{^1\text{H}\}$ NMR spectra were recorded on Bruker NMR spectrometers at ambient temperature unless otherwise noted. ^1H and ^{13}C chemical shifts are referenced to residual solvent signals; ^{31}P chemical shifts are referenced to an external H_3PO_4 standard.

Elemental Analysis. Elemental analyses of complexes **1**, **2**, **3**, **4**, **6**, **8**, **9** and **10** are of the bulk samples for which yields are reported. No additional purification operations are carried out prior to packaging for analysis. Elemental analyses were performed at the University of Rochester CENTC Elemental Analysis Facility.

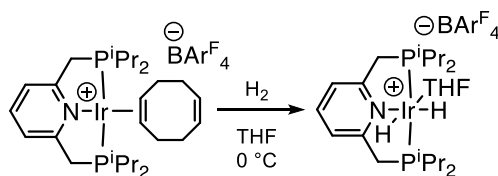


Preparation of $[(\text{PNP}(\text{iPr})_4)\text{Ir}(\eta^2\text{-cod})]\text{BARF}_4$ (1**).** In an inert atmosphere glove box, a 20 mL scintillation vial was charged with $[\text{cod}_2\text{Ir}]\text{BARF}_4$ (0.3003 g, 0.24 mmol), 3.5 mL of 1,4-dioxane followed by $\text{PNP}(\text{iPr})_4$ (**L1**) (0.0819 g, 0.24 mmol) and sealed with a PTFE-lined septum cap. The solution was heated at $80\text{ }^\circ\text{C}$ for 1 hr, allowed to cool to room temperature, and layered with 1 mL of pentane. After standing for 2 hours red crystals had deposited. The solution was layered with 3 additional mL of pentane and allowed to stand overnight. The supernatant was decanted via a pipette and the crystals dried under vacuum. The crystals were then treated with 1 mL diethyl ether followed by dropwise addition of 1 mL pentane while gently swirling the suspension. The supernatant was decanted via pipette and the resulting red crystals were washed with 2 mL of a 1:1 mixture of diethyl ether and pentane. The crystals were then mechanically ground with a spatula and dried under vacuum to give complex **1** as a red solid. Yield: 0.3097 g (82%). Single crystals of **1** were obtained by layering a saturated solution of diethyl ether with pentane at room temperature. Anal. Calcd. For $\text{C}_{59}\text{H}_{59}\text{B}_1\text{F}_{24}\text{IrN}_1\text{P}_2$: C, 47.15; H, 3.96; N, 0.93. Found: C, 46.994; H, 3.730; N, 0.822.

^1H NMR (500 MHz, CD_2Cl_2): δ 1.09-1.16 (m, 12H, PCHCH_3), 1.19-1.25 (m, 12H, PCHCH_3), 1.50-1.65 (m, 4H, CH_2), 1.96-2.08 (m, 2H, CH_2), 2.28-2.39 (m, 6H, PCH and CH_2), 3.42-3.53 (m, 4H, PCH_2), 3.68 (br m, 1H, CH-CH_2), 4.80-4.82 (br m, 1H, CH-CH_2), 5.47-5.51 (br m, 1H, CH-CH_2), 6.05 (d, 1H, CH-CH_2 , $^3J_{\text{H-H}} = 11.8$ Hz), 7.51 (d, 2H, $\text{py-H}_{3,5}$, $^3J_{\text{H-H}} = 7.9$ Hz), 7.55 (br s, 4H, CH of BARF_4), 7.72 (br s, 8H, CH of BARF_4), 7.87 (t, 1H, py-H_4 , $^3J_{\text{H-H}} = 7.7$ Hz)

$^{31}\text{P}\{^1\text{H}\}$ NMR (202 MHz, CD_2Cl_2): δ 36.2 (br s)

$^{13}\text{C}\{^1\text{H}\}$ NMR (125 MHz, CD_2Cl_2): δ 17.82 (s, $\text{PCH}(\text{CH}_3)_2$), 17.85 (s, $\text{PCH}(\text{CH}_3)_2$), 19.14 (s, $\text{PCH}(\text{CH}_3)_2$), 19.72 (s, $\text{PCH}(\text{CH}_3)_2$), 22.94 (s, $\text{CH}-\text{CH}_2-\text{CH}_2$), 24.67 (t, $\text{PCH}(\text{CH}_3)_2$, $^1\text{J}_{\text{C-P}} = 10.5$ Hz), 25.29 (t, $\text{PCH}(\text{CH}_3)_2$, $^1\text{J}_{\text{C-P}} = 10.5$ Hz), 30.28 (s, $\text{CH}-\text{CH}_2-\text{CH}_2$), 30.43 (s, $\text{CH}-\text{CH}_2-\text{CH}_2$), 35.36 (s, $\text{CH}-\text{CH}_2-\text{CH}_2$), 37.43 (t, PCH_2 , $^1\text{J}_{\text{C-P}} = 11.9$ Hz), 53.03 (s, $\text{CH}=\text{CH}$), 56.08 (s, $\text{CH}=\text{CH}$), 117.90 (t, CH of BAR^{F}_4 , $^3\text{J}_{\text{C-F}} = 3.7$ Hz), 121.08 (t, py-C3,5 , $^3\text{J}_{\text{C-P}} = 4.5$ Hz), 125.02 (q, CF_3 of BAR^{F}_4 , $^1\text{J}_{\text{C-F}} = 272.2$ Hz), 129.32 (q, C of BAR^{F}_4 , $^2\text{J}_{\text{C-F}} = 31.9$ Hz), 130.14 (s, $\text{CH}=\text{CH}$), 130.55 (s, $\text{CH}=\text{CH}$), 135.23 (s, CH of BAR^{F}_4), 140.76 (s, py-C4), 162.19 (q, B-C , $^1\text{J}_{\text{C-B}} = 49.9$ Hz), 165.94 (t, py-C2,6 , $\text{J}_{\text{C-P}} = 3.6$ Hz)

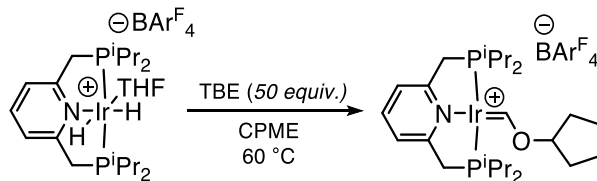


Preparation of $[(\text{PNP}(\text{Pr})_4)\text{Ir}(\text{H})_2(\text{THF})]\text{BAR}^{\text{F}}_4$ (2**).** In an inert atmosphere glove box, a 20 mL scintillation vial was charged with complex **1** (0.3472 g, 0.23 mmol) and 3 mL of tetrahydrofuran and sealed with a PTFE-lined septum cap. The solution was cooled to 0 °C and hydrogen was bubbled through the solution for 30 minutes causing a color change from red to yellow. After 30 minutes, 10 mL of pentane was added and hydrogen bubbling was continued at 0 °C for 5 minutes. At this point the solution was reduced to dryness under vacuum to give a pale yellow foam. This residue was triturated with 5 mL pentane followed by evaporation under vacuum. This process was repeated two additional times to give an off-white solid. This solid was washed with three 5 mL portions of pentane and then dried under vacuum to yield complex **2** as an off-white solid. Yield: 0.3233 g (95%). Single crystals of **2** were obtained by layering a saturated solution of diethyl ether with pentane at room temperature. Anal. Calcd. For $\text{C}_{55}\text{H}_{57}\text{B}_1\text{F}_{24}\text{IrN}_1\text{O}_1\text{P}_2$: C, 44.97; H, 3.91; N, 0.95. Found: C, 44.538; H, 3.576; N, 0.736.

^1H NMR (400 MHz, CD_2Cl_2): δ -22.57 (br s, 2H, IrH), 1.07-1.13 (m, 12H, PCHCH_3), 1.20-1.26 (m, 12H, PCHCH_3), 1.81 (m, 4H, OCH_2CH_2), 2.29 (m, 4H, PCH), 3.66 (m, 4H, OCH_2), 3.72 (t, 4H, PCH_2 , $\text{J}_{\text{P-H}} = 3.9$ Hz), 7.41 (d, 2H, py-H3,5 , $^3\text{J}_{\text{H-H}} = 7.8$ Hz), 7.55 (br s, 4H, CH of BAR^{F}_4), 7.71 (br s, 10H, CH of BAR^{F}_4 and py-H4)

$^{31}\text{P}\{^1\text{H}\}$ NMR (162 MHz, CD_2Cl_2): δ 45.9 (br s)

$^{13}\text{C}\{^1\text{H}\}$ NMR (101 MHz, CD_2Cl_2): δ 18.99 (s, $\text{PCH}(\text{CH}_3)_2$), 19.61 (s, $\text{PCH}(\text{CH}_3)_2$), 26.08 (s, OCH_2CH_2), 26.17 (t, $\text{PCH}(\text{CH}_3)_2$, $^1\text{J}_{\text{C-P}} = 15.3$ Hz), 43.74 (t, PCH_2 , $^1\text{J}_{\text{C-P}} = 15.3$ Hz), 70.65 (s, OCH_2), 117.87 (t, CH of BAR^{F}_4 , $^3\text{J}_{\text{C-F}} = 3.7$ Hz), 121.29 (t, py-C3,5 , $^3\text{J}_{\text{C-P}} = 4.7$ Hz), 125.00 (q, CF_3 of BAR^{F}_4 , $^1\text{J}_{\text{C-F}} = 272.3$ Hz), 129.27 (q, C of BAR^{F}_4 , $^2\text{J}_{\text{C-F}} = 31.1$ Hz), 135.20 (s, CH of BAR^{F}_4), 138.66 (s, py-C4), 162.16 (q, B-C , $^1\text{J}_{\text{C-B}} = 49.9$ Hz), 163.51 (t, py-C2,6 , $\text{J}_{\text{C-P}} = 3.6$ Hz)

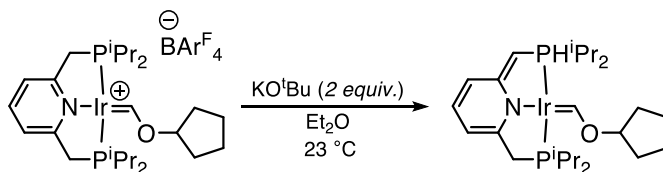


Preparation of [(PNP(ⁱPr)₄)Ir=CHO(C₅H₉)]BArF₄ (3**).** In an inert-atmosphere glove box, a 20 mL scintillation vial was charged with complex **2** (0.1001 g, 0.068 mmol), cyclopentyl methyl ether (2 mL), *tert*-butylethylene (0.43 mL, 3.4 mmol) and sealed with a PTFE-lined septum cap. The reaction was heated at 60 °C for 1.5 hr, changing color from yellow-orange to deep green. The reaction was cooled to room temperature and the solvent removed under vacuum. 5 mL pentane was added and the suspension was dried under vacuum. This process was repeated two additional times. The resulting green solid was washed with three, 5 mL portions of pentane and dried under vacuum to yield complex **3** as a green solid. Yield: 0.0982 g (97%). Single crystals of **3** were obtained by layering a saturated solution of CD₂Cl₂ with pentane at room temperature. Anal. Calcd. For C₅₇H₅₇B₁F₂₄IrN₁O₁P₂: C, 45.86; H, 3.85; N, 0.94. Found: C, 45.553; H, 3.433; N, 0.800.

¹H NMR (500 MHz, CD₂Cl₂): δ 1.07-1.11 (m, 12H, PCH(CH₃)₂), 1.25-1.30 (m, 12H, PCH(CH₃)₂), 1.65-1.96 (m, 8H, CH₂), 2.48 (m, 4H, PCH), 3.66 (t, 4H, PCH₂, J_{P-H} = 3.8 Hz), 4.44 (br s, 1H, OCH), 7.48 (d, 2H, py-H3,5, ³J_{H-H} = 7.8 Hz), 7.55 (br s, 4H, CH of BArF₄), 7.71 (br s, 9H, CH of BArF₄ and py-H4), 13.49 (br s, 1H, Ir=CH)

³¹P{¹H} NMR (202 MHz, CD₂Cl₂): δ 51.3 (s)

¹³C{¹H} NMR (125 MHz, CD₂Cl₂): δ 18.09 (s, PCH(CH₃)₂), 19.13 (s, PCH(CH₃)₂), 23.98 (s, CH₂), 25.37 (t, PCH(CH₃)₂, ¹J_{C-P} = 15.0 Hz), 33.65 (s, CH₂), 37.76 (t, PCH₂, ¹J_{C-P} = 12.0 Hz), 96.60 (s, O-CH-(CH₂)₂), 117.87 (s, CH of BArF₄), 121.06 (t, py-C3,5, ³J_{C-P} = 4.4 Hz), 125.00 (q, CF₃ of BArF₄, ¹J_{C-F} = 272.4 Hz), 129.29 (q, C of BArF₄, ²J_{C-F} = 31.4 Hz), 135.20 (s, CH of BArF₄), 140.59 (s, py-C4), 162.16 (q, B-C, ¹J_{C-B} = 49.9 Hz), 166.21 (s, py-C2,6), 234.78 (s, Ir=CH)



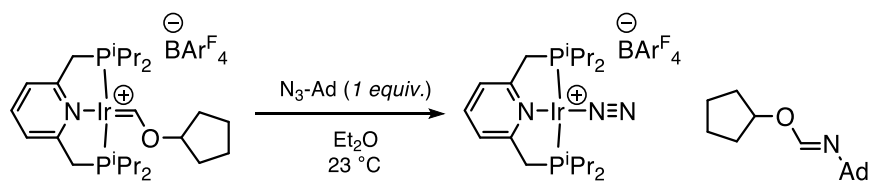
Preparation of [(PNP(ⁱPr)₄)Ir=CHO(C₅H₉)] (4**).** In an inert-atmosphere glove box, a 20 mL scintillation vial was charged with

complex **3** (0.2979 g, 0.20 mmol), potassium *tert*-butoxide (0.0454 g, 0.40 mmol), and 3.5 mL of diethyl ether in order and was sealed with a PTFE-lined septum cap. Addition of diethyl ether gave an immediate color change to dark purple. The reaction was allowed to stand for 30 min at room temperature at which point the solvent was removed under vacuum. The residue was extracted with five, 2 mL portions of pentane and filtered. The combined extracts were dried under vacuum to give a purple solid. This solid was extracted a second time with five, 2 mL portions of pentane and filtered. The filtrate was dried under vacuum to yield complex **4** as a dark purple solid. Yield: 0.1045 g (83%). Single crystals of **4** were obtained by slow evaporation of a saturated pentane solution at room temperature. Anal. Calcd. For C₂₅H₄₄IrN₁O₁P₂: C, 47.75; H, 7.05; N, 2.23. Found: C, 48.071; H, 7.136; N, 1.919.

¹H NMR (500 MHz, C₆D₆): δ 0.98 (dd, 6H, PCH(CH₃)₂), ³J_{H-P} = 13.1 Hz, ³J_{H-H} = 6.9 Hz), 1.21 (dd, 6H, PCH(CH₃)₂), ³J_{H-P} = 16.3 Hz, ³J_{H-H} = 7.2 Hz), 1.30-1.46 (m, 16H, PCH(CH₃)₂ and CH₂ and CH₂), 1.60 (m, 2H, CH₂), 1.73 (m, 2H, CH₂), 2.11 (m, 2H, PCH), 2.37 (m, 2H, PCH), 2.69 (d, 2H, PCH₂, ²J_{H-P} = 9.2 Hz), 3.81 (sept, 1H, O-CH-(CH₂)₂, J_{H-H} = 2.9 Hz), 3.98 (dd, 1H, P-CH=C, ⁴J_{H-P} = 2.4 Hz, ²J_{H-P} = 3.7 Hz), 5.46 (d, 1H, py-H3 or H5, J_{H-H} = 6.3 Hz), 6.40 (m, 1H, py-H4), 6.47 (d, 1H, py-H3 or H5, J_{H-H} = 8.9 Hz), 13.55 (dd, 1H, Ir=CH, ³J_{H-P} = 3.09 Hz, ³J_{H-P} = 11.4 Hz)

³¹P{¹H} NMR (202 MHz, C₆D₆): δ 38.0 (d, ²J_{P-P} = 311.0 Hz), 47.9 (d, ²J_{P-P} = 311.0 Hz)

¹³C{¹H} NMR (125 MHz, C₆D₆): δ 18.10 (s, PCH(CH₃)₂), 18.35 (s, PCH(CH₃)₂), 19.43 (d, PCH(CH₃)₂, ²J_{C-P} = 5.8 Hz), 20.41 (d, PCH(CH₃)₂, ²J_{C-P} = 5.4 Hz), 23.94 (s, CH₂), 25.02 (d, PCH(CH₃)₂, ¹J_{C-P} = 24.4 Hz), 26.03 (d, PCH(CH₃)₂, ¹J_{C-P} = 30.9 Hz), 33.45 (s, CH₂), 36.81 (d, PCH₂, ¹J_{C-P} = 24.4 Hz), 69.31 (d, PCH=C, ¹J_{C-P} = 58.7 Hz), 91.81 (s, O-CH-(CH₂)₂), 97.50 (d, py-C3 or C5, ³J_{C-P} = 10.4 Hz), 114.46 (d, py-C3 or C5, ³J_{C-P} = 16.9 Hz), 132.32 (s, py-C4), 161.79 (t, py-C2 or C6, J_{C-P} = 5.0 Hz), 161.79 (dd, py-C2 or C6, J_{C-P} = 5.0 Hz, J_{C-P} = 17.4 Hz), 221.57 (m, Ir=C)



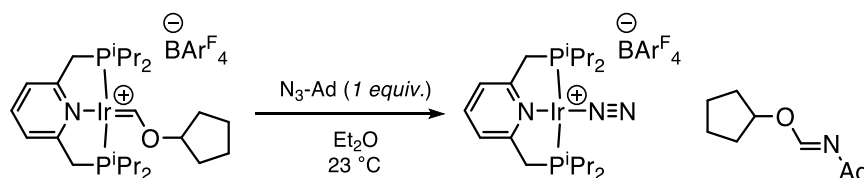
Preparation of cyclopentyl N-(adamantyl)formimidate (5). In an inert-atmosphere glove box, a 40 mL scintillation vial wrapped with aluminum foil was charged with complex **3** (0.3013g, 0.20 mmol) and 28.0 mL of diethyl ether. A solution of 1-azidoadamantane (0.0361 g, 0.20 mmol) in 2.0 mL diethyl ether was added and the reaction was allowed to stand at room temperature for 21 hrs. At this point the solvent was removed under vacuum to yield a bright orange residue. The product was

extracted with three, 5 mL portions of pentane and filtered. The combined extracts were then dried under vacuum to give a yellow residue which was then extracted with five, 1 mL portions of pentane. The combined extracts were filtered through a 0.45 μm PTFE syringe filter and were evaporated under vacuum to give **5** as a yellow oil. Yield: 0.0286 g (57%).

^1H NMR (500 MHz, CDCl_3): 1.59-1.80 (m, 20H), 2.07 (br s, 3H, Ad-CH), 5.00 (m, 1H, O-CH(C_4H_8)), 7.45 (s, 1H, N=CH)

$^{13}\text{C}\{^1\text{H}\}$ NMR (125 MHz, CDCl_3): 23.63 (s, CH_2), 29.80 (s, CH), 29.94 (s, CH), 32.84 (s, CH_2), 36.05 (s, CH_2), 36.69 (s, CH_2), 41.66 (s, CH_2), 44.43 (s, CH_2), 53.37 (s, N-C-(CH_2)₃), 77.79 (s, O-CH-(CH_2)₂), 151.47 (s, N=CH-O)

HRMS (ACPI/Orbitrap) m/z $[\text{M}+\text{H}]^+$ calcd for $\text{C}_{16}\text{H}_{25}\text{NOH}^+$: 248.2009, found: 248.2009.



Preparation of $[(\text{PNP}(\text{iPr})_4)\text{Ir}(\text{N}_2)]\text{BAr}^{\text{F}}_4$ (6**).** In an inert-atmosphere glove box a 20 mL scintillation vial was charged with complex **3** (0.1002g, 0.067 mmol) and 8 mL of diethyl ether. A solution of 1-azidoadamantane (0.0121 g, 0.068 mmol) in 2 mL diethyl ether was added and the vial sealed with a PTFE-lined septum cap. After 21 hours at room temperature the solvent was removed under vacuum. The resulting bright orange residue was treated with 5 mL pentane and then scraped with a spatula to give a suspension. The supernatant was decanted using a pipette and the residue washed with three, 5 mL portions of pentane. The resulting material was dried under vacuum to give complex **7** as a bright orange solid. Yield: 0.0945 g (99%). Single crystals of **7** were obtained by layering a saturated diethyl ether solution with pentane at room temperature. Anal. Calcd. For $\text{C}_{51}\text{H}_{47}\text{B}_1\text{F}_4\text{IrN}_3\text{P}_2$: C, 43.05; H, 3.33; N, 2.95. Found: C, 43.547; H, 3.403; N, 2.391.

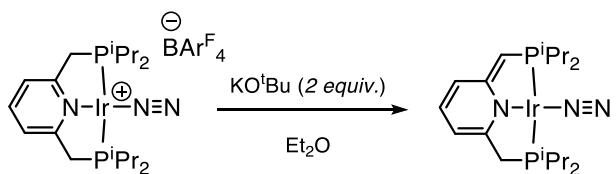
IR (ATR-FTIR): $\nu(\text{N}_2)$ 2141 cm^{-1}

^1H NMR (500 MHz, CD_2Cl_2): δ 1.16-1.21 (m, 12H, $\text{PCH}(\text{CH}_3)_2$), 1.30-1.35 (m, 12H, $\text{PCH}(\text{CH}_3)_2$), 2.44-2.52 (m, 4H, PCH), 3.47 (t, 4H, PCH_2 , $^2\text{J}_{\text{H-P}} = 4.1$ Hz), 7.38 (d, 2H, py-H3,5, $^3\text{J}_{\text{H-H}} = 7.9$ Hz), 7.55 (br s, 4H, CH of BAr^{F}_4), 7.72 (br s, 8H, CH of BAr^{F}_4), 7.77 (t, 1H, py-H4, $^3\text{J}_{\text{H-H}} = 7.9$ Hz)

$^{31}\text{P}\{^1\text{H}\}$ NMR (202 MHz, CD_2Cl_2): δ 54.5 (s)

$^{13}\text{C}\{^1\text{H}\}$ NMR (125 MHz, CD_2Cl_2): δ 18.08 (s, $\text{PCH}(\text{CH}_3)_2$), 18.95 (s, $\text{PCH}(\text{CH}_3)_2$), 25.54 (t, $\text{PCH}(\text{CH}_3)_2$, $^1\text{J}_{\text{C-P}} = 15.0$ Hz), 35.57

(t, PCH₂, ¹J_{C-P} = 125.4 Hz), 117.89 (pentet, CH of BAr^F₄), 122.11 (t, py-C3,5, ³J_{C-P} = 5.2 Hz), 125.02 (q, CF₃ of BAr^F₄, ¹J_{C-F} = 272.4 Hz), 129.30 (qq, C of BAr^F₄, J_{C-F} = 31.4 Hz, J_{C-F} = 2.8 Hz), 135.22 (s, CH of BAr^F₄), 139.32 (s, py-C4), 162.18 (q, B-C, ¹J_{C-B} = 49.9 Hz), 167.01 (t, py-C2,6 ³J_{C-P} = 5.4 Hz)



Preparation of (PNP(ⁱPr)₄)Ir(N₂) (7). In an inert-atmosphere glove box a 20 mL scintillation vial wrapped with aluminium foil was charged with complex **6** (0.5002 g, 0.35 mmol), potassium *tert*-butoxide (0.0475 g, 0.42 mmol), 4.0 mL of diethyl ether and sealed with a PTFE-lined septum cap. The resulting red solution was allowed to stand at room temperature for 1 h and 45 min, at which point the solvent was removed under vacuum to give a red solid. The red solid was extracted with twenty five, 2 mL portions of pentane and the combined extracts filtered and dried under vacuum to give complex **7** as a transferrable, red solid. Yield: 0.1954 g (99%). Single crystals of **7** were obtained by slow evaporation of pentane at room temperature. Suitable elemental analysis could not be obtained.

Preparation of (PNP(ⁱPr)₄)Ir(N₂) (7) generated *in situ* from complex **4.** (eqn. 5)

In an inert-atmosphere glove box a 4 mL scintillation vial was charged with complex **4** (0.0101 g, 0.016 mmol), 1-azidoadamantane (0.0029 g, 0.016 mmol), 0.60 mL C₆D₆ and the solution transferred to a J. Young NMR tube. Analysis of the ³¹P{¹H} and ¹H spectra of the solution matched that of complex **7**.

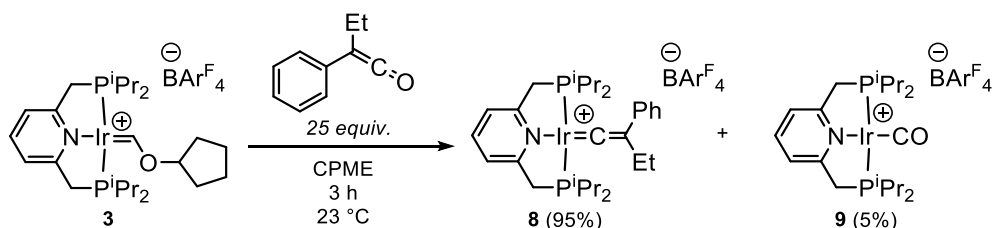
IR (ATR-FTIR): ν(N₂) 2076 cm⁻¹

¹H NMR (500 MHz, C₆D₆): δ 0.87 (dd, 6H, PCH(CH₃)₂, ³J_{H-P} = 13.8 Hz, ³J_{H-H} = 6.9 Hz), 1.06 (dd, 6H, PCH(CH₃)₂, ³J_{H-P} = 16.3 Hz, ³J_{H-H} = 7.1 Hz), 1.27 (dd, 6H, PCH(CH₃)₂, ³J_{H-P} = 14.0 Hz, ³J_{H-H} = 6.9 Hz), 1.40 (dd, 6H, PCH(CH₃)₂, ³J_{H-P} = 16.1 Hz, ³J_{H-H} = 7.1 Hz), 1.77 (m, 2H, PCH(CH₃)₂), 2.21 (m, 2H, PCH(CH₃)₂), 2.46 (d, 2H, PCH₂, ²J_{H-P} = 9.8 Hz), 3.81 (t, 1H, PCH, J_{H-P} = 3.4 Hz), 3.37 (d, 1H, py-H, ³J_{H-H} = 6.0 Hz), 6.33-6.39 (m, 2 H py-H)

³¹P{¹H} NMR (202 MHz, C₆D₆): δ 44.5 (d, ²J_{P-P} = 276.4 Hz), 50.3 (d, ²J_{P-P} = 276.8 Hz)

¹³C{¹H} NMR (125 MHz, C₆D₆): δ 17.99 (s, PCH(CH₃)₂), 18.38 (s, PCH(CH₃)₂), 18.89 (d, PCH(CH₃)₂, ²J_{C-P} = 4.4 Hz), 19.58 (d, PCH(CH₃)₂, ²J_{C-P} = 4.4 Hz), 25.02 (dd, PCH(CH₃)₂, ¹J_{C-P} = 26.2 Hz, ³J_{C-P} = 1.7 Hz), 27.05 (dd, PCH(CH₃)₂, ¹J_{C-P} = 33.1 Hz, ³J_{C-P}

= 1.5 Hz), 34.62 (d, PCH₂, ¹J_{C-P} = 25.5 Hz), 63.08 (d, PCH, ¹J_{C-P} = 61.0 Hz), 97.99 (d, py-C3 or C5, ²J_{C-P} = 11.80), 114.28 (d, py-C3 or C5, ²J_{C-P} = 18.40), 131.33 (s, py-C4), 161.23 (t, py-C2 or C6, ²J_{C-P} = 5.7 Hz), 176.40 (dd, py-C2 or C6, J_{C-P} = 18.4 Hz, J_{C-P} = 6.0 Hz)



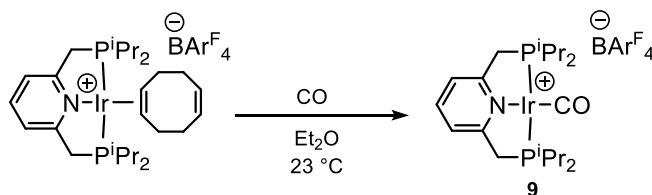
Preparation of [(PNP(ⁱPr)₄)Ir=C=C(Ph)(Et)]BAR^F₄ (8**).** In an inert-atmosphere glove box a 20 mL scintillation vial was charged with complex **3** (0.0990 g, 0.066 mmol), 2.0 mL of CPME followed by phenyl ethyl ketene (226 μ L, 1.7 mmol). The reaction was allowed to stand at room temperature for 3 hours, at which point the solvent was removed under vacuum to give a blue residue. The crude material was washed with 10 mL pentane followed by three, 3 mL portions of pentane and was dried under vacuum. The resulting blue solid was then dissolved in a minimum of diethyl ether (*ca.* 1 mL) which was carefully layered with pentane in two, 9 mL portions. After several days, blue crystals deposited. The supernatant was then decanted and the crystals washed with three, 3 mL portions of pentane to give **10**. Yield: 0.0720 g (71%) (*ca.* 95% purity by ³¹P{¹H}) ³¹P{¹H} NMR in CD₂Cl₂ shows two species in a 95:5 ratio with **8** being the major product. The impurity at 61.4 ppm corresponds to complex **9** which was confirmed by independent synthesis. Single crystals of **8** were obtained directly from the separated pentane washings after standing at room temperature. Alternatively, single crystals could be obtained by layering a saturated tetrahydrofuran solution with pentane followed by storage at -35 °C. Anal. Calcd. For C₆₁H₅₇B₁F₂₄IrN₁P₂ (**8**, 95%) and C₅₂H₄₇B₁F₂₄IrN₁O₁P₂ (**9**, 5%): C, 47.85; H, 3.75; N, 0.92. Found: C, 47.955; H, 3.671; N, 0.812. [Anal. Calcd for **8**: C₆₁H₅₇B₁F₂₄IrN₁P₂: C, 48.04; H, 3.77; N, 0.92.]

¹H NMR (500 MHz, CD₂Cl₂): δ 1.09 (t, 3H, CH₃, ³J_{H-H} = 7.4 Hz), 1.17-1.26 (m, 24H, PCH(CH₃)₂), 2.44 (m, 12H, PCH(CH₃)₂), 2.78 (q, 2H, CH₂, ³J_{H-H} = 7.3 Hz), 3.87 (t, 4H, PCH₂, ²J_{H-P} = 4.0 Hz), 7.02 (t, 1H, Ar-H, J_{H-H} = 7.2 Hz) 7.22-7.30 (m, 4H, Ar-H), 7.55-7.58 (br m, 6H, CH of BAR^F₄ and py-H), 7.72 (br s, 8H, CH of BAR^F₄) 7.80 (t, 1H, py-H, ³J_{H-H} = 7.8 Hz)

³¹P{¹H} NMR (202 MHz, CD₂Cl₂): δ 45.5 (s)

¹³C{¹H} NMR (125 MHz, CD₂Cl₂): δ 8.51 (s, CH₂), 15.31 (s, CH₃), 18.33 (s, PCH(CH₃)₂), 18.98 (s, PCH(CH₃)₂), 25.90 (t, PCH(CH₃)₂, ¹J_{C-P} = 15.2 Hz), 37.67 (t, PCH₂, ¹J_{C-P} = 12.2 Hz), 117.92 (pentent, CH of BAR^F₄), 121.79 (t, py-C3,5, ³J_{C-P} = 4.5 Hz),

122.10 (s, Ar-C), 123.71 (t, C=C, $^3J_{C-P} = 3.4$ Hz), 125.05 (q, CF_3 of BAR^F_4 , $^1J_{C-F} = 272.0$ Hz), 126.13 (s, Ar-CH) 126.31 (s, Ar-CH), 128.79 (s, Ar-CH), 129.33 (qq, C of BAR^F_4 , $J_{C-F} = 31.4$ Hz), 135.24 (s, CH of BAR^F_4), 142.25 (s, py-C4), 162.17 (q, B-C, $^1J_{C-B} = 50.0$ Hz), 167.01 (t, py-C2,6, $^3J_{C-P} = 4.5$ Hz), 298.34 (t, Ir=C, $^2J_{C-P} = 10.6$ Hz)



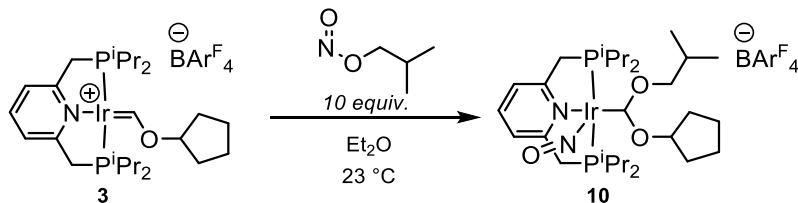
Preparation of $[(PNP(^iPr)_4)Ir(CO)]BAR^F_4$ (9**).** In an inert-atmosphere glove box a 20 mL scintillation vial was charged with complex **1** (0.0262 g, 0.017 mmol), 2.0 mL of diethyl ether and the vial sealed with a PTFE-lined septum cap. Carbon monoxide was then bubbled through the solution for 2 minutes at room temperature, causing a color change from red to yellow. The solvent was then removed under vacuum to give a yellow residue. The solid was washed with three, 5 mL portions of pentane and dried under vacuum. The residue was scraped with a spatula and then washed with an additional three, 5 mL portions of pentane. The material was dried under vacuum to give **10** as a yellow solid. Yield: 0.0238 g (95%). Single crystals of **9** were obtained by layering a saturated diethyl ether solution with pentane at room temperature. Anal. Calcd. For $C_{52}H_{47}B_1F_{24}IrN_1O_1P_2$: C, 43.89; H, 3.33; N, 0.98. Found: C, 44.275; H, 3.171; N, 0.813.

IR (ATR-FTIR): $\nu(\text{CO})$ 1986 cm^{-1}

^1H NMR (500 MHz, CD_2Cl_2): δ 1.18 (m, 12H, $\text{PCH}(\text{CH}_3)_2$), 1.30 (m, 12H, $\text{PCH}(\text{CH}_3)_2$), 2.51 (m, 4H, $\text{PCH}(\text{CH}_3)_2$), 3.72 (t, 4H, PCH_2 , $^2J_{\text{H-P}} = 4.1$ Hz), 7.53-7.55 (br m, 6H, CH of BAR^F_4 and py-H), 7.71 (br s, 8H, CH of BAR^F_4) 7.88 (t, 1H, py-H, $^3J_{\text{H-H}} = 7.8$ Hz)

$^{31}\text{P}\{^1\text{H}\}$ NMR (202 MHz, CD_2Cl_2): δ 61.4 (s)

$^{13}\text{C}\{^1\text{H}\}$ NMR (125 MHz, CD_2Cl_2): δ 18.29 (s, $\text{PCH}(\text{CH}_3)_2$), 19.19 (s, $\text{PCH}(\text{CH}_3)_2$), 26.31 (t, $\text{PCH}(\text{CH}_3)_2$, $^1J_{C-P} = 15.9$ Hz), 36.67 (t, PCH_2 , $^1J_{C-P} = 12.6$ Hz), 117.89 (pentet, CH of BAR^F_4), 122.24 (t, py-C3,5, $^3J_{C-P} = 5.0$ Hz), 125.01 (q, CF_3 of BAR^F_4 , $^1J_{C-F} = 272.6$ Hz), 129.30 (q, C of BAR^F_4 , $J_{C-F} = 31.3$ Hz) 135.21 (s, CH of BAR^F_4), 141.22 (s, py-C4), 162.16 (q, B-C, $^1J_{C-B} = 50.3$ Hz), 166.36 (t, py-C2,6 $^3J_{C-P} = 5.3$ Hz) 180.43 (t, Ir-CO, $^2J_{C-P} = 8.6$ Hz)



Preparation of $[(\text{PNP}(\text{}^i\text{Pr})_4)\text{Ir}(\text{NO})[\text{CH}(\text{O}^i\text{Bu})(\text{OC}_5\text{H}_9)] \text{BAr}^{\text{F}_4}$ (10**).** In an inert-atmosphere glove box a 20 mL scintillation vial was charged with complex **3** (0.0508 g, 0.033 mmol), 2.0 mL of diethyl ether followed by isobutyl nitrite (4.0 μL , 0.033 mmol). The reaction was allowed to stand at room temperature for 30 min, during which time it changed color from dark green to orange. The solvent was then removed under vacuum to yield a yellow/orange residue. The residue was washed with five, 2 mL portions of pentane and dried under vacuum. The resulting solid was mechanically ground with a spatula and then washed with another five, 2 mL portions of pentane to give the crude product as a pale orange solid. Yield: 0.0465 g (*ca.* 78% purity). Analysis of the crude product obtained as above by $^{31}\text{P}\{^1\text{H}\}$ NMR in $\text{THF-}d_8$ shows two species in a 78:22 ratio with **10** being the major product. The major impurity corresponds to an unidentified species with a signal at 52.3 ppm that appears to form during the concentration steps in the procedure above. Complex **10** decomposes in a few hours on standing at room temperature in solution or over a period of weeks in the solid state. Anal. Calcd. For $\text{C}_{61}\text{H}_{66}\text{B}_1\text{F}_{24}\text{IrN}_2\text{O}_3\text{P}_2$: C, 45.90; H, 4.17; N, 1.76. Found: C, 45.675; H, 3.891; N, 1.564.

^1H NMR (Partial, 500 MHz, $\text{THF-}d_8$): δ 7.18 (t, 1H, ($\text{Ir-CH}(\text{O}^i\text{Bu})(\text{OC}_5\text{H}_9)$), $^3J_{\text{H-P}} = 4.7$ Hz)

$^{31}\text{P}\{^1\text{H}\}$ NMR (202 MHz, $\text{THF-}d_8$): δ 34.1 (s, complex **10**, 78%), 52.3 (s, unidentified impurity, 22%)

$^{31}\text{P}\{^1\text{H}\}$ NMR (202 MHz, CPME): δ 33.9 (s, complex **10**, generated *in situ*)

$^{13}\text{C}\{^1\text{H}\}$ NMR (Partial, 125 MHz, $\text{THF-}d_8$): δ 88.7 ($\text{Ir-CH}(\text{O}^i\text{Bu})(\text{OC}_5\text{H}_9)$)

Representative Procedures for Catalytic Group Transfer. In an inert-atmosphere glove box a 4 mL borosilicate scintillation vial was charged with 2.0 mL of CPME, 100 μL of a 34 mM CPME solution of iridium catalyst (Complex **1**, **3**, or **4** - See Table 1 entries 3, 6, and 7 respectively) followed by 100 μL of 340 mM stock solution of 1-azidoadamantane in CPME. Neat *tert*-butylethylene (22.0 μL , 0.17 mmol) was then added and the reaction sealed with a PTFE-lined cap. The reaction was heated to the corresponding temperature and irradiated with blue light* for 22 hours. The solvent was then removed by rotary evaporation and the residue taken up in 0.60 mL CDCl_3 . A 5.0 μL aliquot of pyridine was added as an internal standard and the resulting solution was analyzed by ^1H

NMR. NMR yields were determined by comparison of the product resonance at 5.0 ppm (m, 1H, O-CH(C₄H₈)) to the internal standard.

*A Kessil H150-Blue 34W LED lamp was used as the blue light source ($\lambda_{\text{max}} = 420, 460 \text{ nm}$)

Representative Procedures for the Detection of Cyclopentyl Formate. In an inert-atmosphere glove box a 20 mL scintillation vial was charged with complex **3** (0.0204 g, 0.013 mmol), 2.0 mL of diethyl ether followed by phenyl ethyl ketene (2.0 μL , 0.015 mmol). The vessel was sealed and allowed to stand at room temperature for 72 hr. The solvent was then removed under gentle vacuum and the resulting residue dissolved in 0.60 mL CDCl₃ and transferred to a J. Young NMR tube. The formation of cyclopentyl formate was confirmed by comparison of the crude ¹H NMR spectra to that reported for cyclopentyl formate.⁶⁹

3.5 Additional Figures

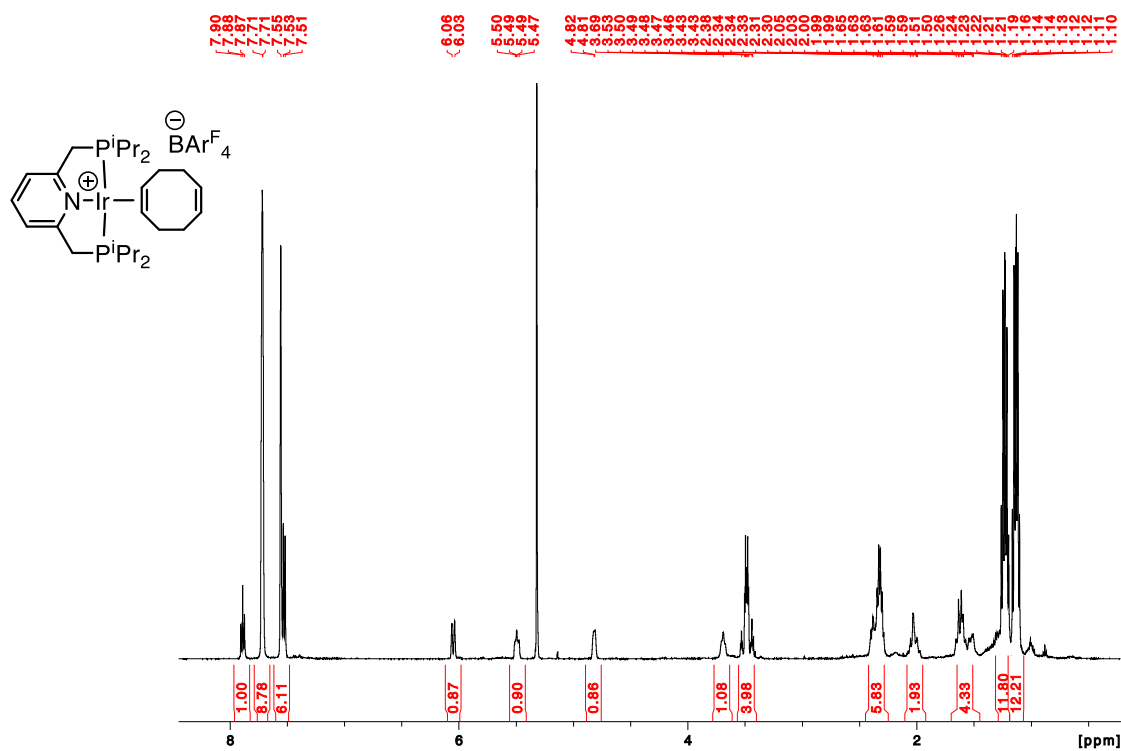


Figure 3.5.1. ¹H NMR Spectrum of [(PNP(ⁱPr)₄Ir(η²-cod)]BARF₄ (**1**) (500 MHz, CD₂Cl₂).

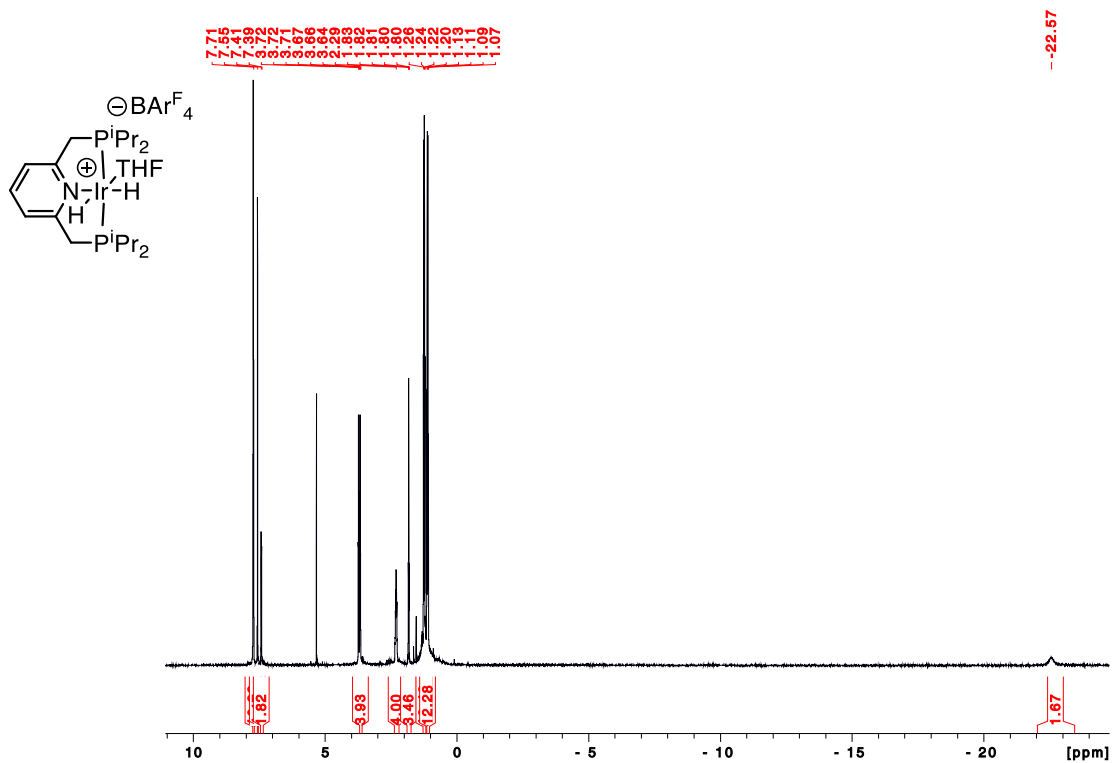


Figure 3.5.4. ^1H NMR Spectrum of $[(\text{PNP}(\text{Pr})_4\text{Ir}(\text{H})_2(\text{THF}))]\text{BARF}_4$ (2) (500 MHz, CD_2Cl_2).

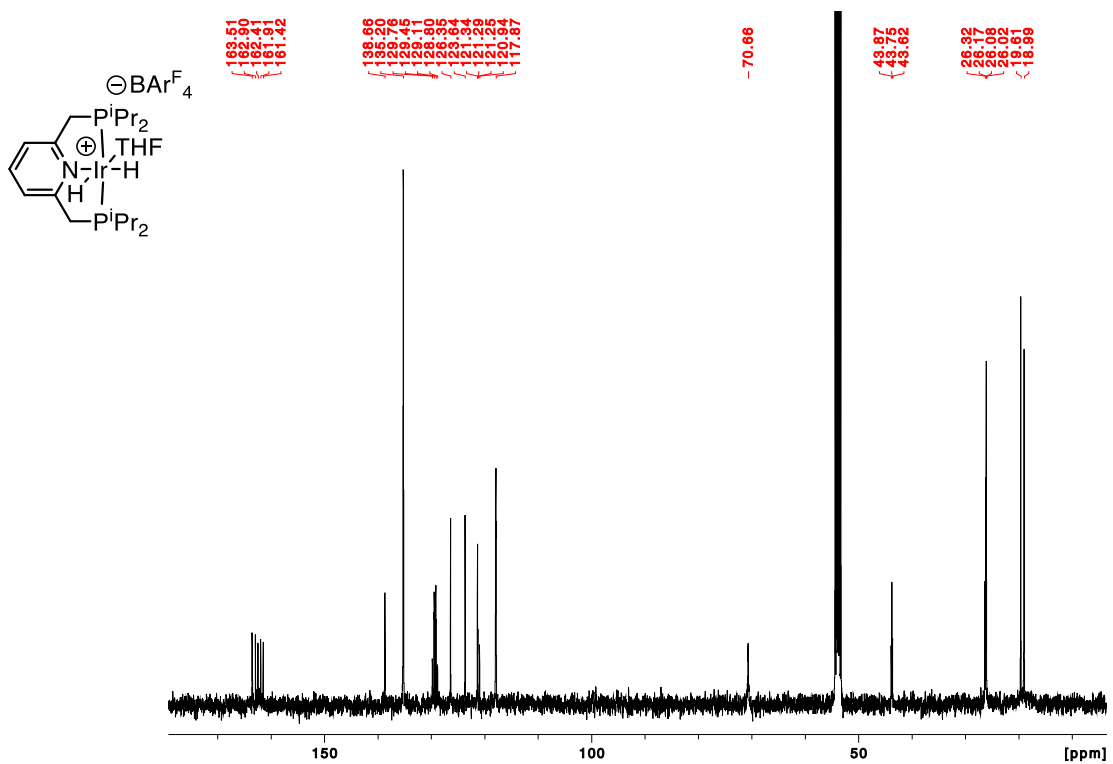


Figure 3.5.5. ^{13}C NMR Spectrum of $[(\text{PNP}(\text{Pr})_4\text{Ir}(\text{H})_2(\text{THF}))]\text{BARF}_4$ (2) (126 MHz, CD_2Cl_2).

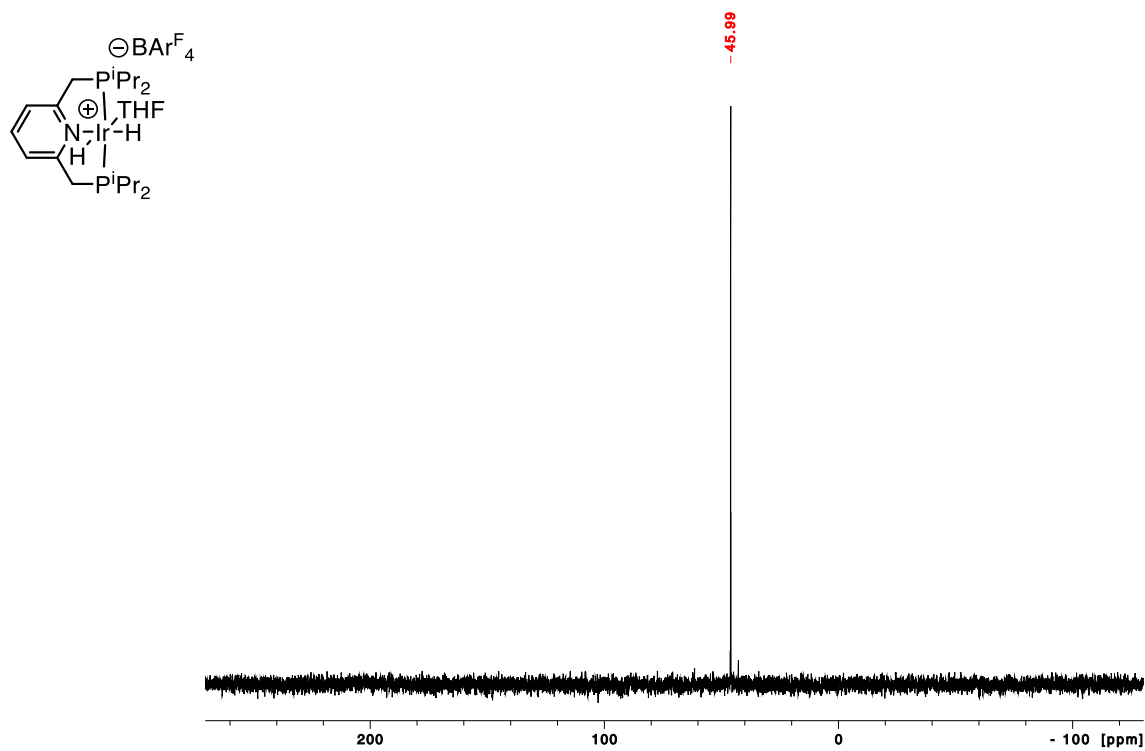


Figure 3.5.6. ^{31}P NMR Spectrum of $[(\text{PNP}(\text{Pr})_4)\text{Ir}(\text{H})_2(\text{THF})]\text{BARF}_4$ (2) (202 MHz, CD_2Cl_2).

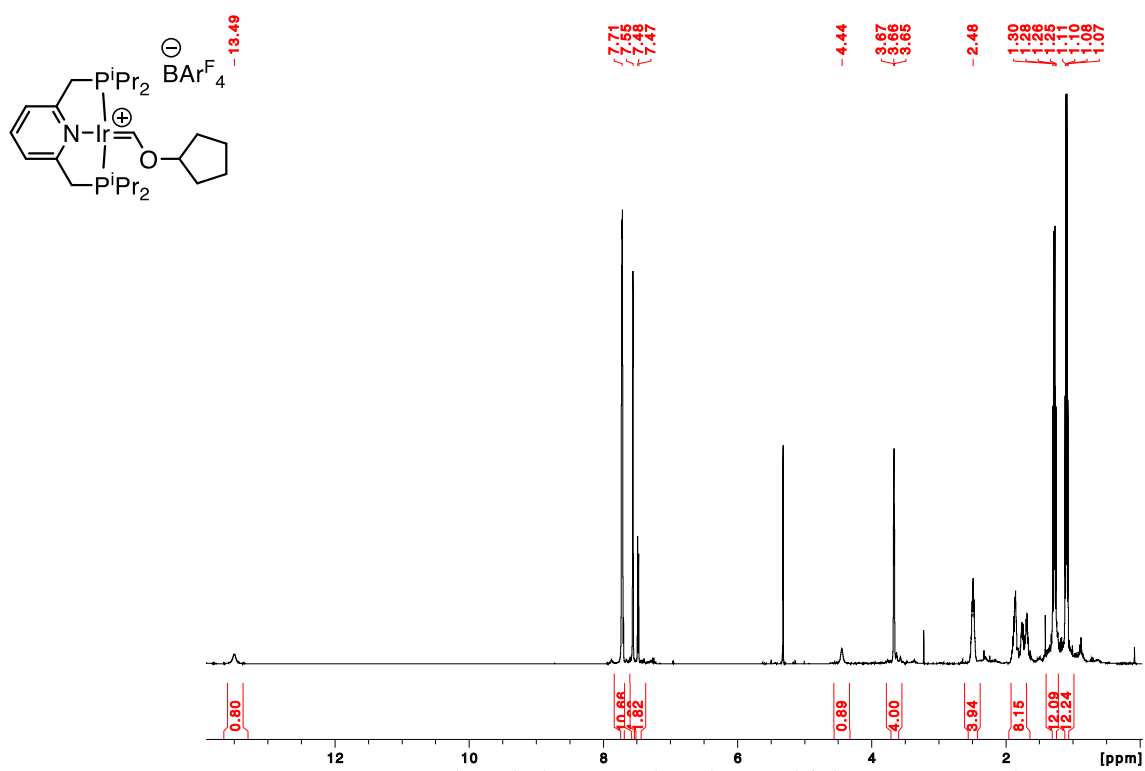


Figure 3.5.7. ^1H NMR Spectrum of $[(\text{PNP}(\text{Pr})_4)\text{Ir}=\text{CHO}(\text{C}_5\text{H}_9)]\text{BARF}_4$ (3) (500 MHz, CD_2Cl_2).

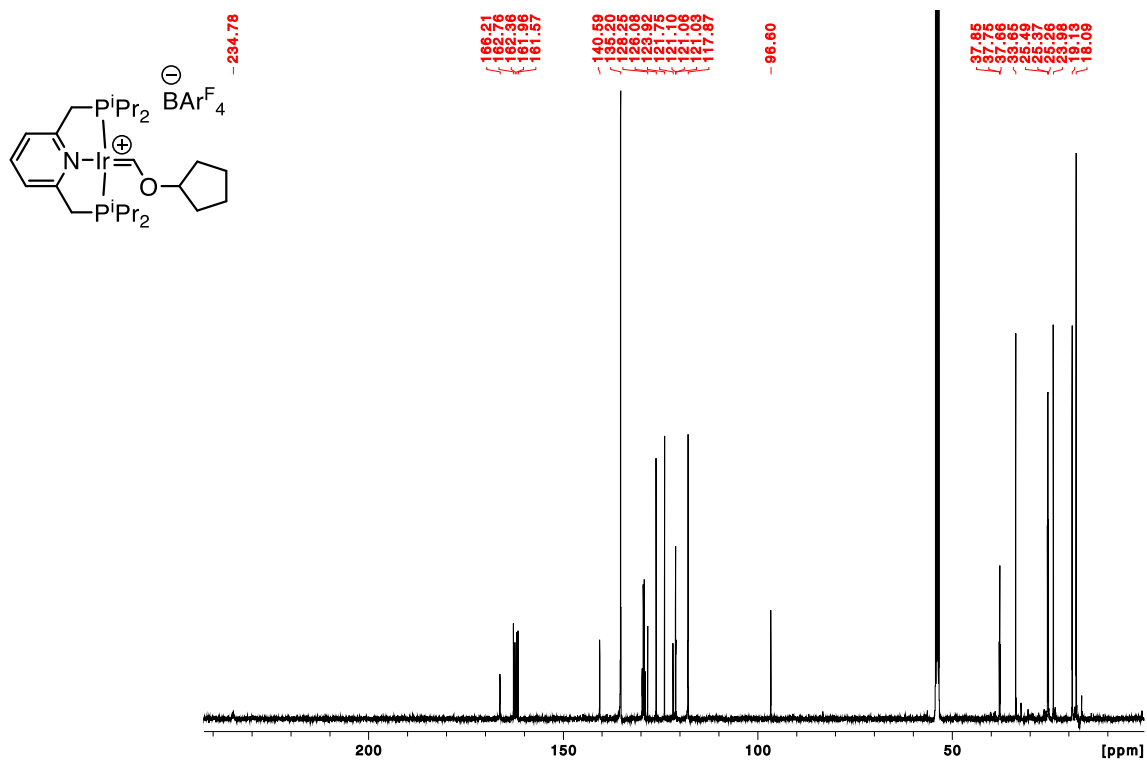


Figure 3.5.8. ^{13}C NMR Spectrum of $[(\text{PNP}(\text{}^i\text{Pr})_4\text{Ir}=\text{CHO}(\text{C}_5\text{H}_9))\text{BARF}_4^-]$ (3) (126 MHz, CD_2Cl_2).

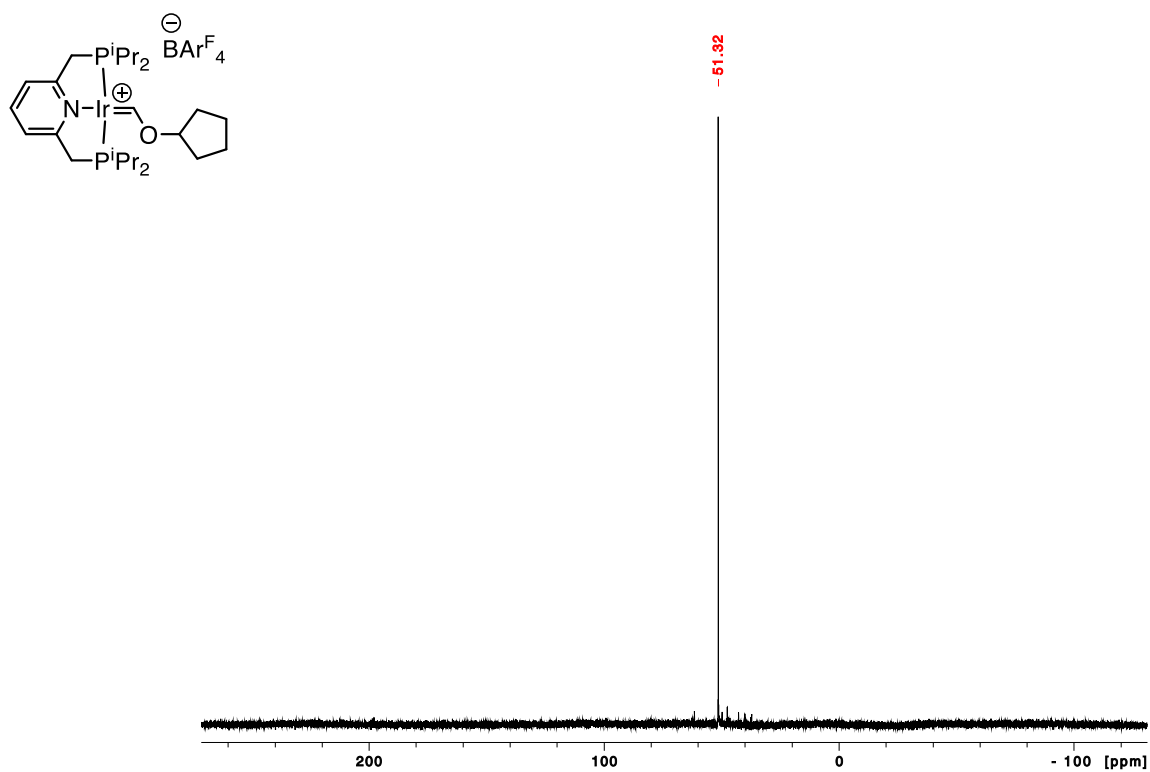


Figure 3.5.9. ^{31}P NMR Spectrum of $[(\text{PNP}(\text{}^i\text{Pr})_4\text{Ir}=\text{CHO}(\text{C}_5\text{H}_9))\text{BARF}_4^-]$ (3) (202 MHz, CD_2Cl_2).

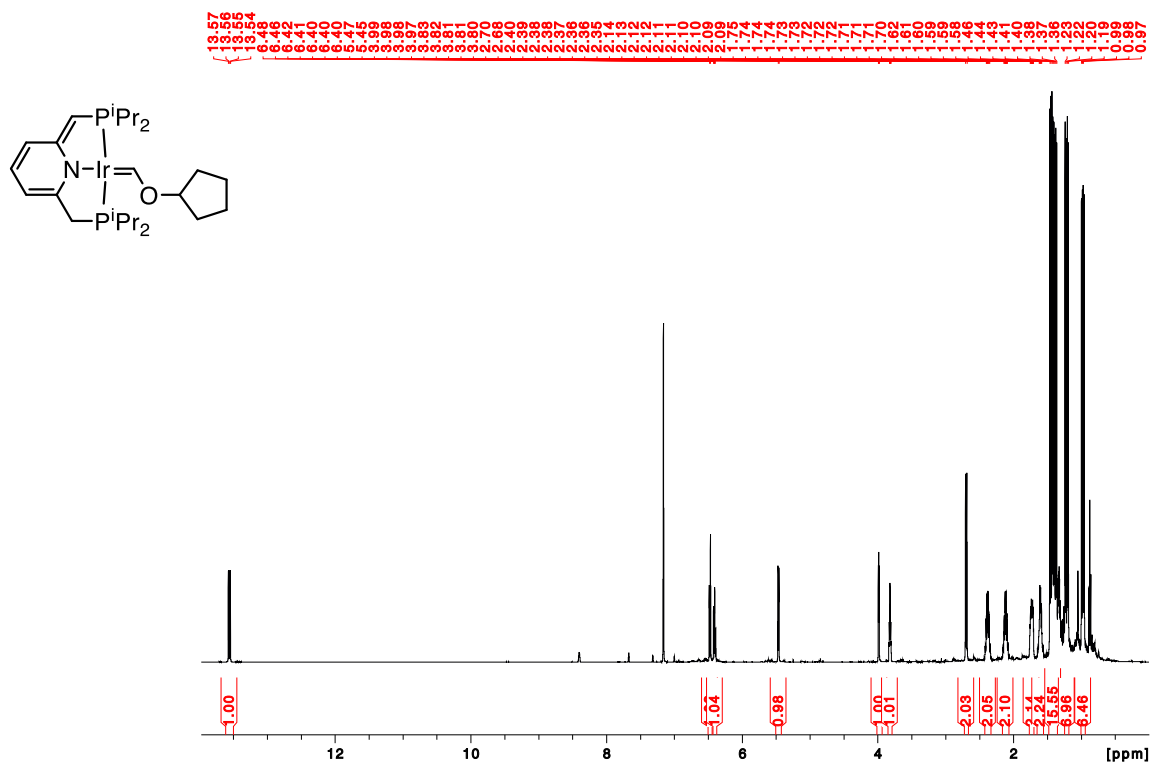


Figure 3.5.10. ^1H NMR Spectrum of $[\text{PNP}(\text{iPr})_4\text{Ir}=\text{CHO}(\text{C}_5\text{H}_9)]$ (4) (500 MHz, C_6D_6).

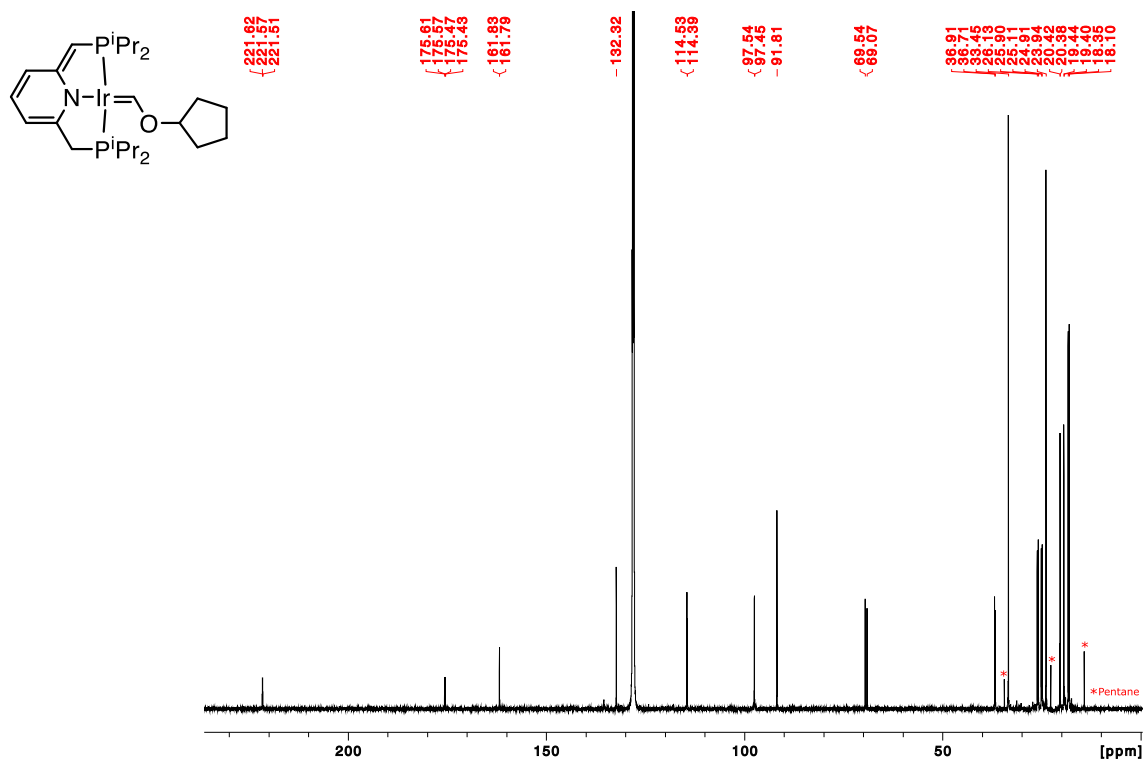


Figure 3.5.11. ^{13}C NMR Spectrum of $[\text{PNP}(\text{iPr})_4\text{Ir}=\text{CHO}(\text{C}_5\text{H}_9)]$ (4) (126 MHz, C_6D_6).

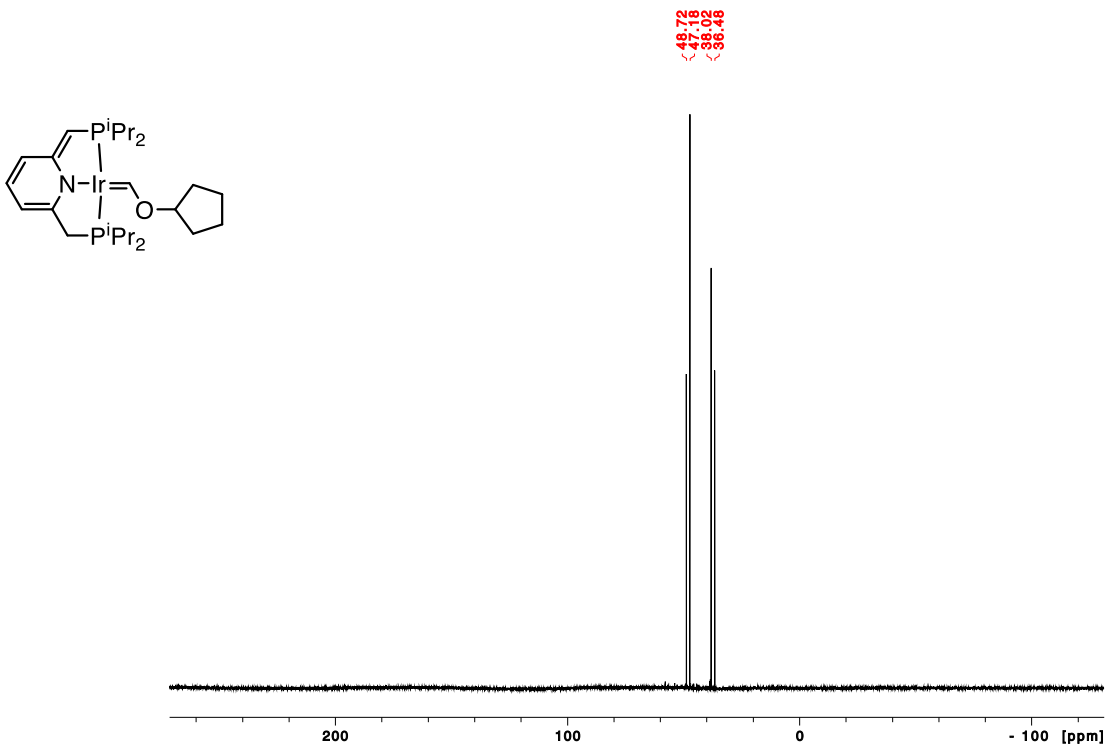


Figure 3.5.12. ^{31}P NMR Spectrum of $[\text{PNP}(\text{}^1\text{Pr})_4\text{Ir}=\text{CHO}(\text{C}_5\text{H}_9)]$ (4) (202 MHz, C_6D_6).

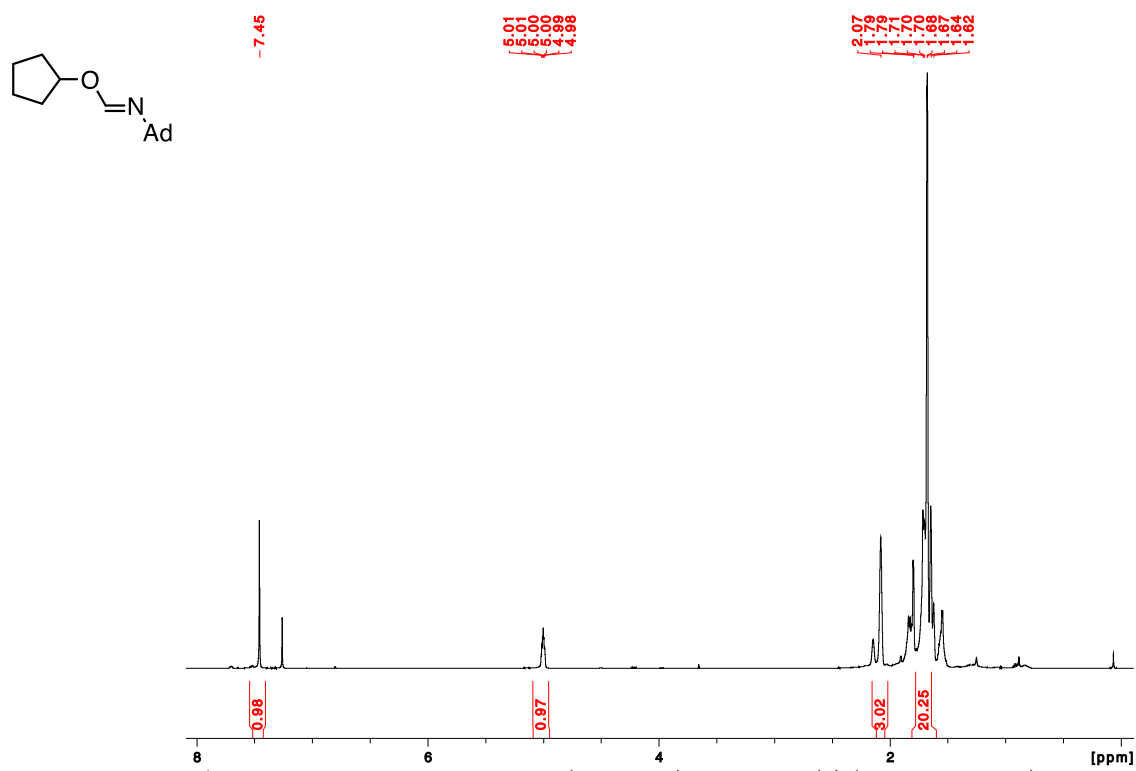


Figure 3.5.13. ^1H NMR Spectrum of cyclopentyl N-(adamantyl)formimidate (5) (500 MHz, CDCl_3).

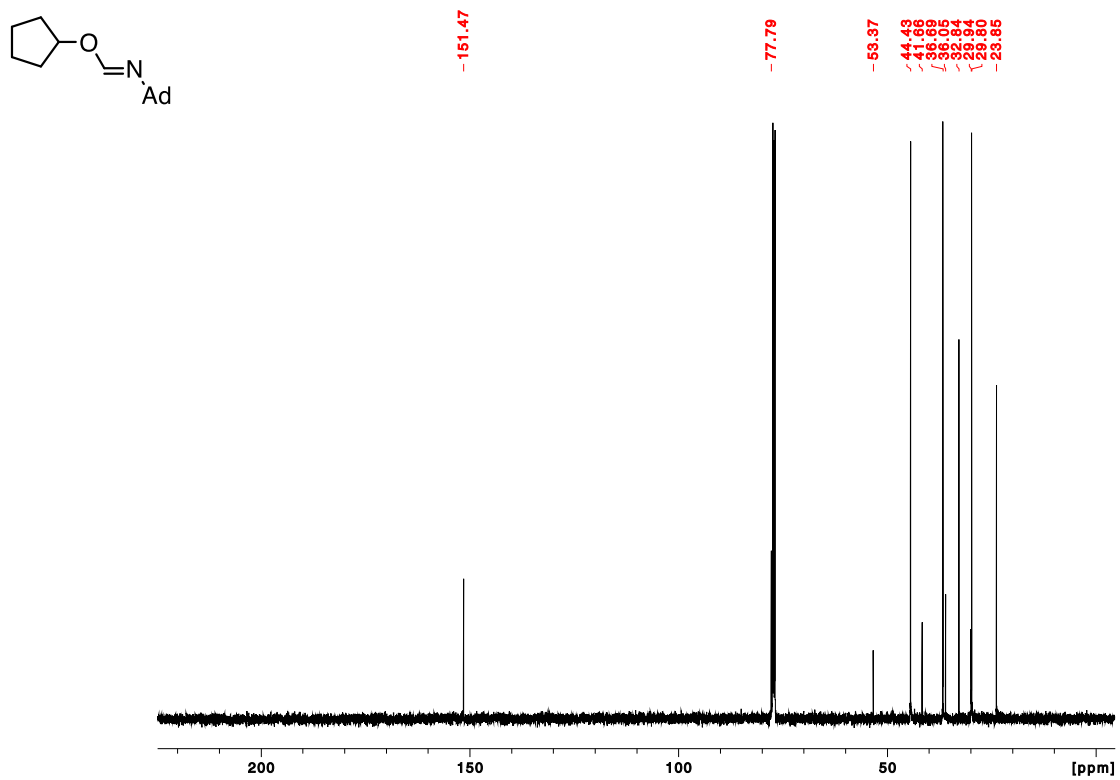


Figure 3.5.14. ^{13}C NMR Spectrum of cyclopentyl N-(adamantyl)formimidate (**5**) (126 MHz, CDCl_3).

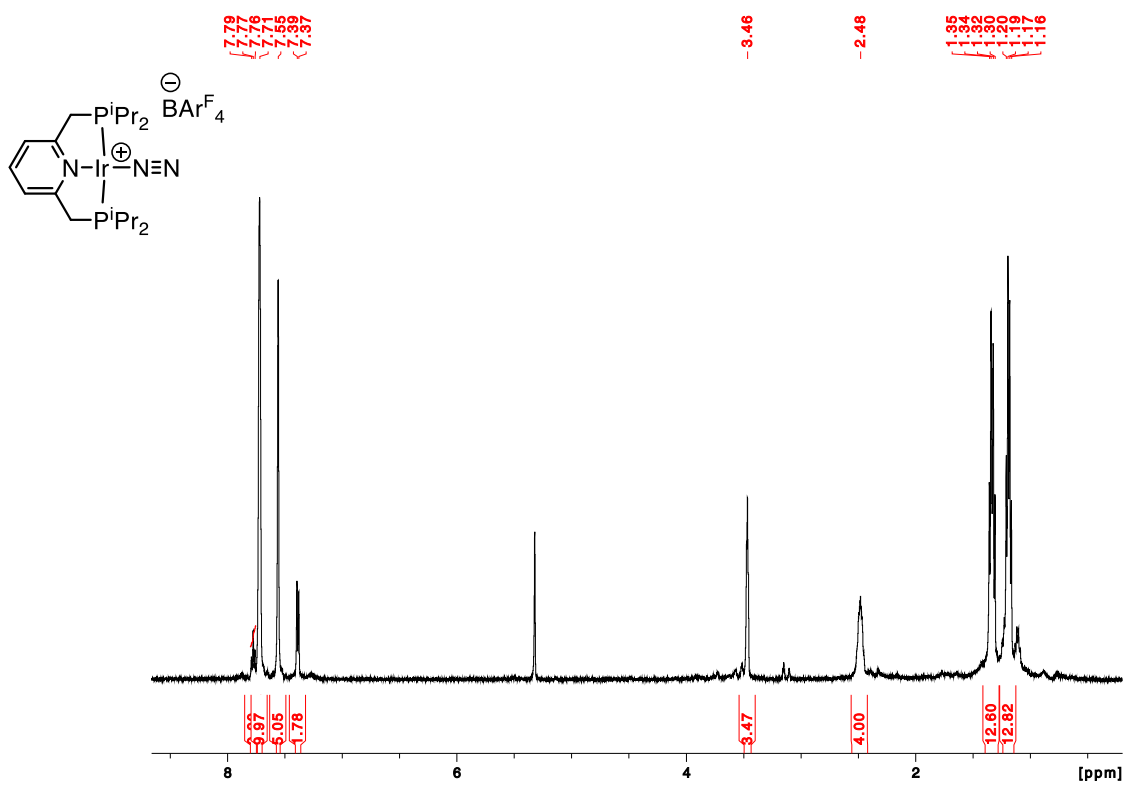


Figure 3.5.15. ^1H NMR Spectrum of $[(\text{PNP}(\text{Pr})_4)\text{Ir}(\text{N}_2)]\text{BARF}_4$ (**6**) (500 MHz, CD_2Cl_2).

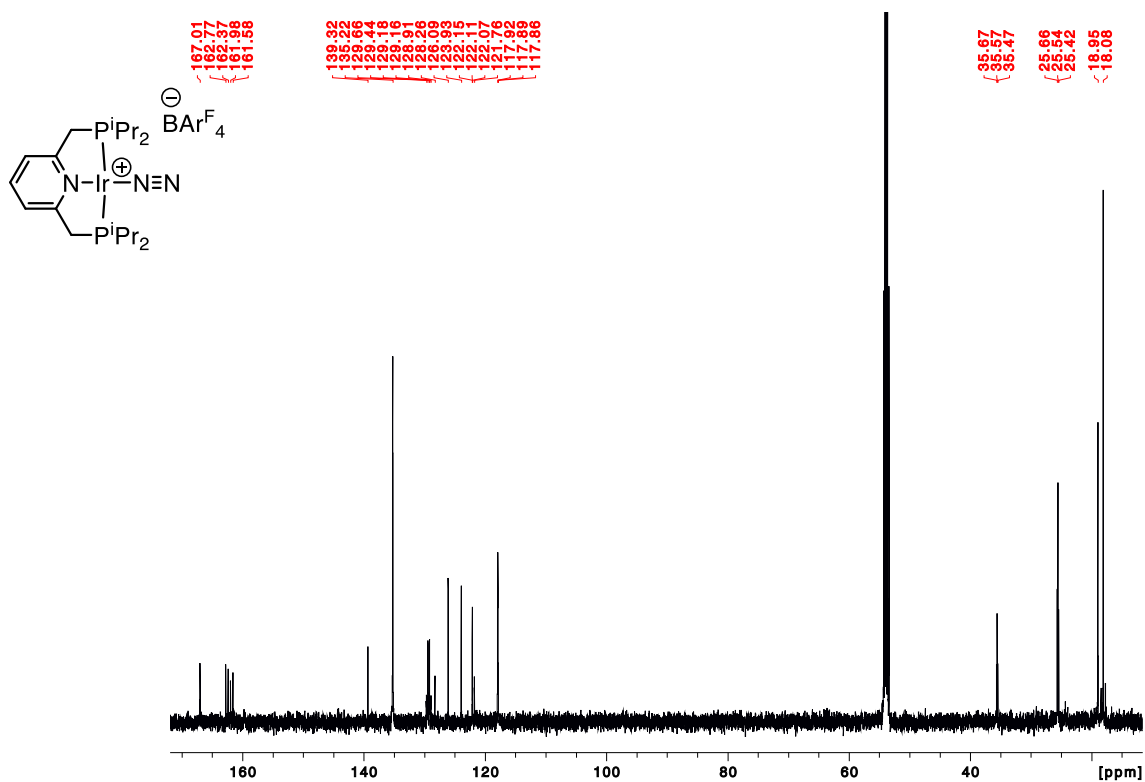


Figure 3.5.16. ^{13}C NMR Spectrum of $[(\text{PNP}(\text{iPr})_4)\text{Ir}(\text{N}_2)]\text{BARF}_4$ (6) (126 MHz, CD_2Cl_2).

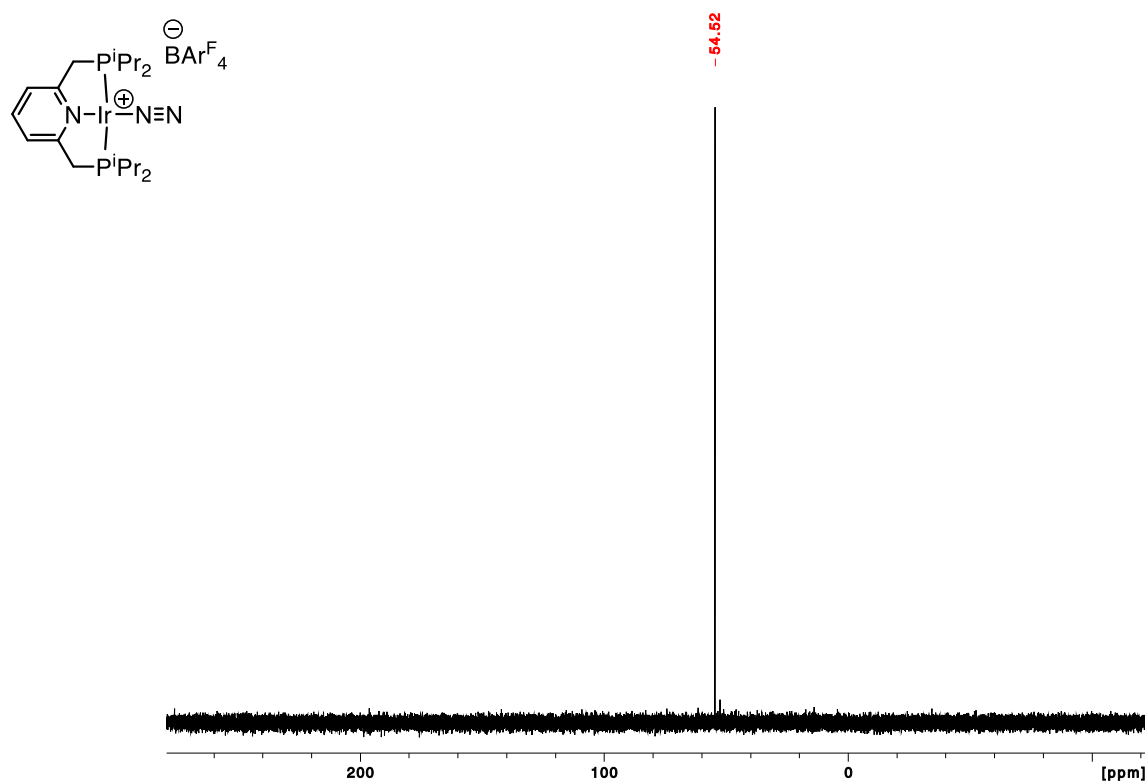


Figure 3.5.17. ^{31}P NMR Spectrum of $[(\text{PNP}(\text{iPr})_4)\text{Ir}(\text{N}_2)]\text{BARF}_4$ (6) (202 MHz, CD_2Cl_2).

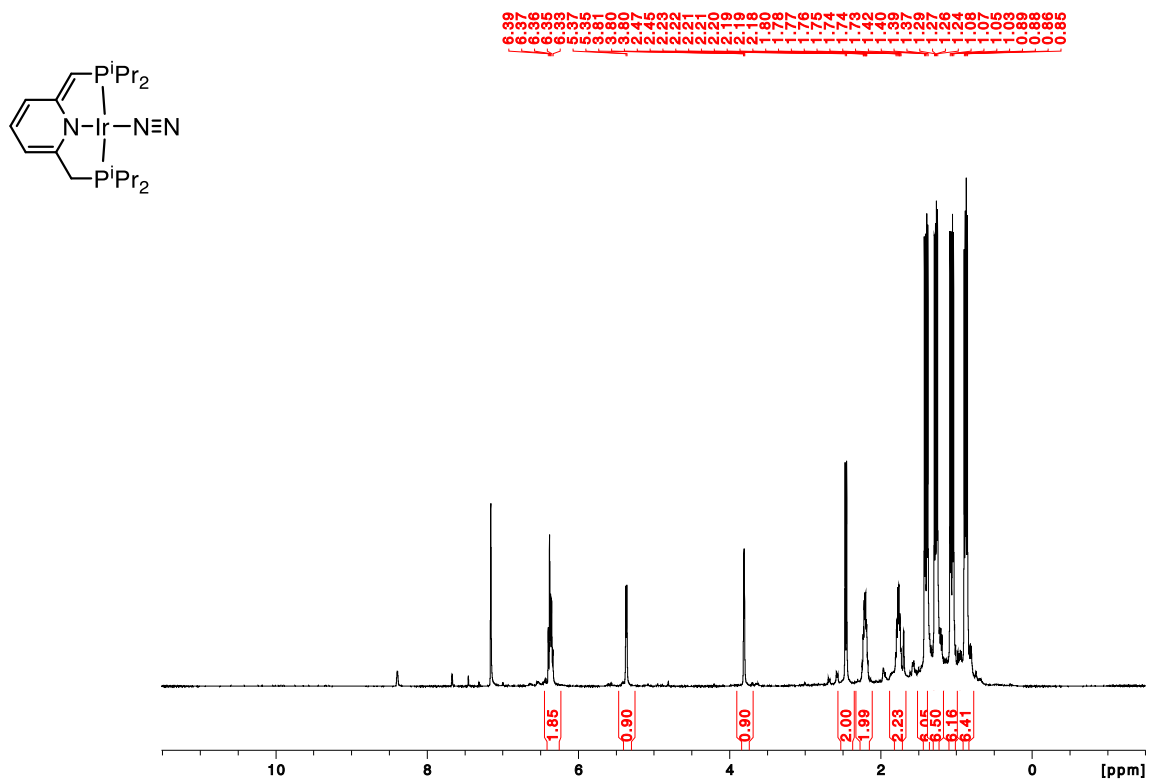


Figure 3.5.18. ^1H NMR Spectrum of $(\text{PNP}(^i\text{Pr})_4)\text{Ir}(\text{N}_2)$ (**7**) (500 MHz, C_6D_6).

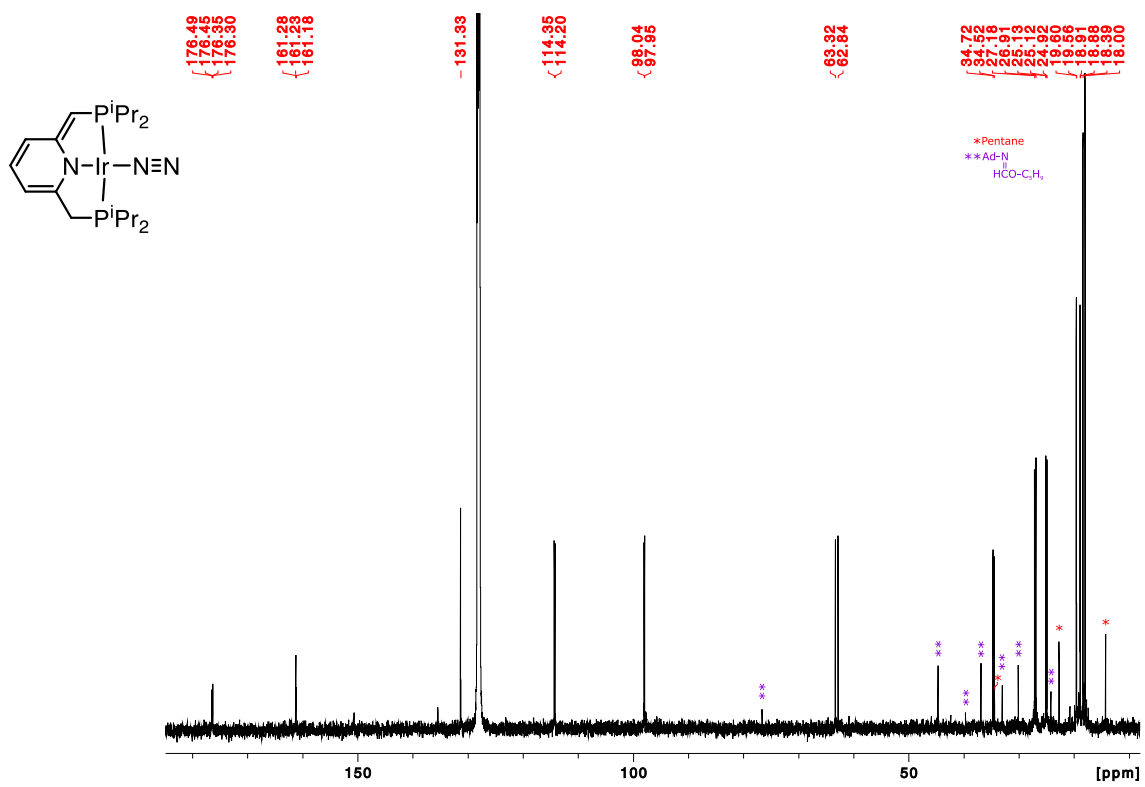


Figure 3.5.19. ^{13}C NMR Spectrum of $(\text{PNP}(^i\text{Pr})_4)\text{Ir}(\text{N}_2)$ (**7**) (126 MHz, C_6D_6).

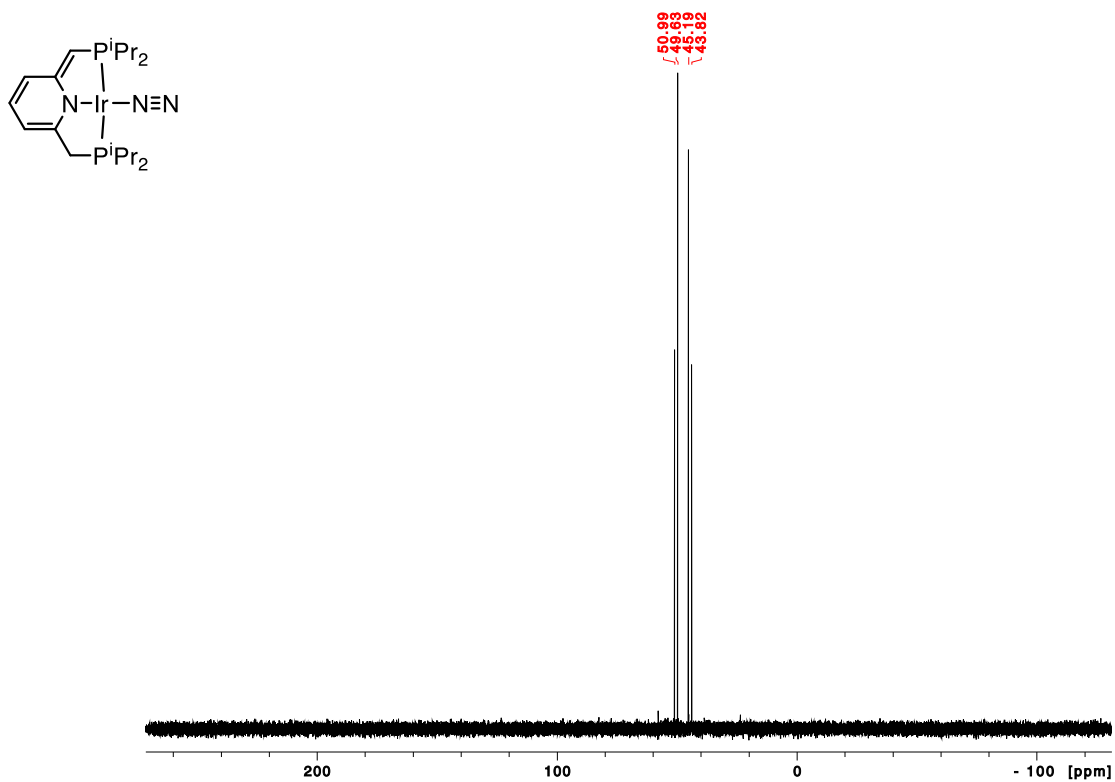


Figure 3.5.20. ^{31}P NMR Spectrum of $(\text{PNP}(\text{iPr})_4)\text{Ir}(\text{N}_2)$ (7) (202 MHz, C_6D_6).

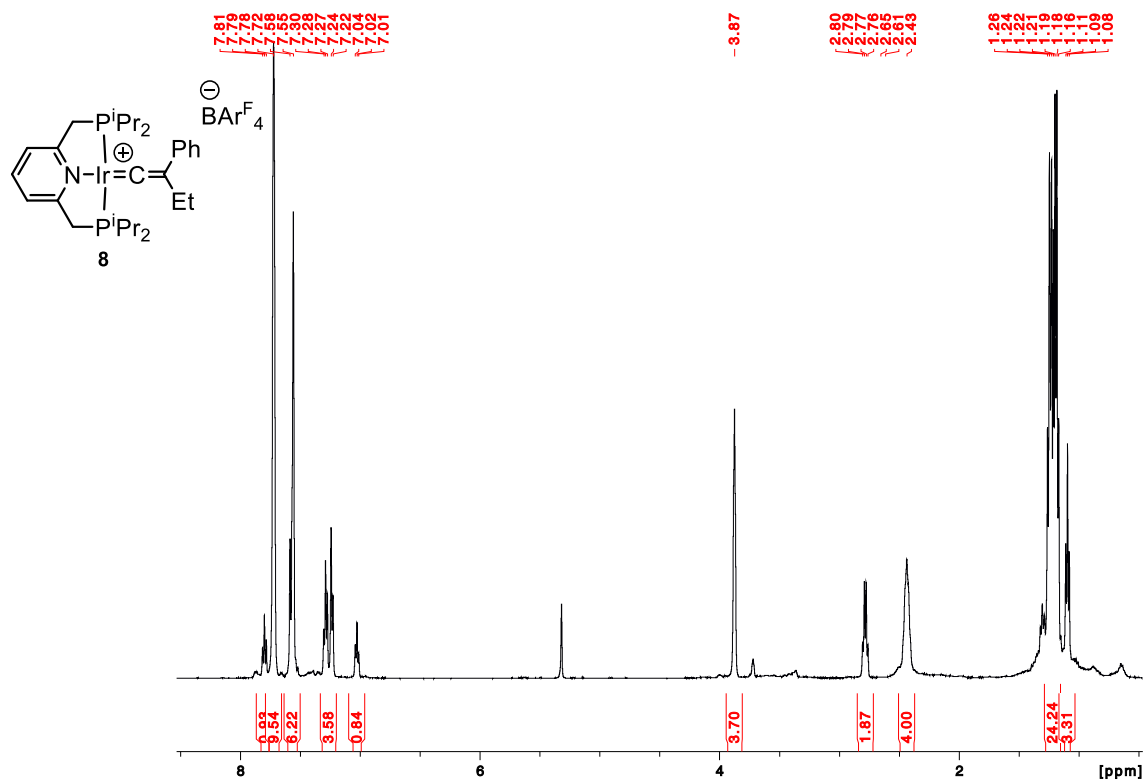


Figure 3.5.21. ^1H NMR Spectrum of $[(\text{PNP}(\text{iPr})_4)\text{Ir}=\text{C}=\text{C}(\text{Ph})(\text{Et})]\text{BARF}_4$ (8) (500 MHz, CD_2Cl_2).

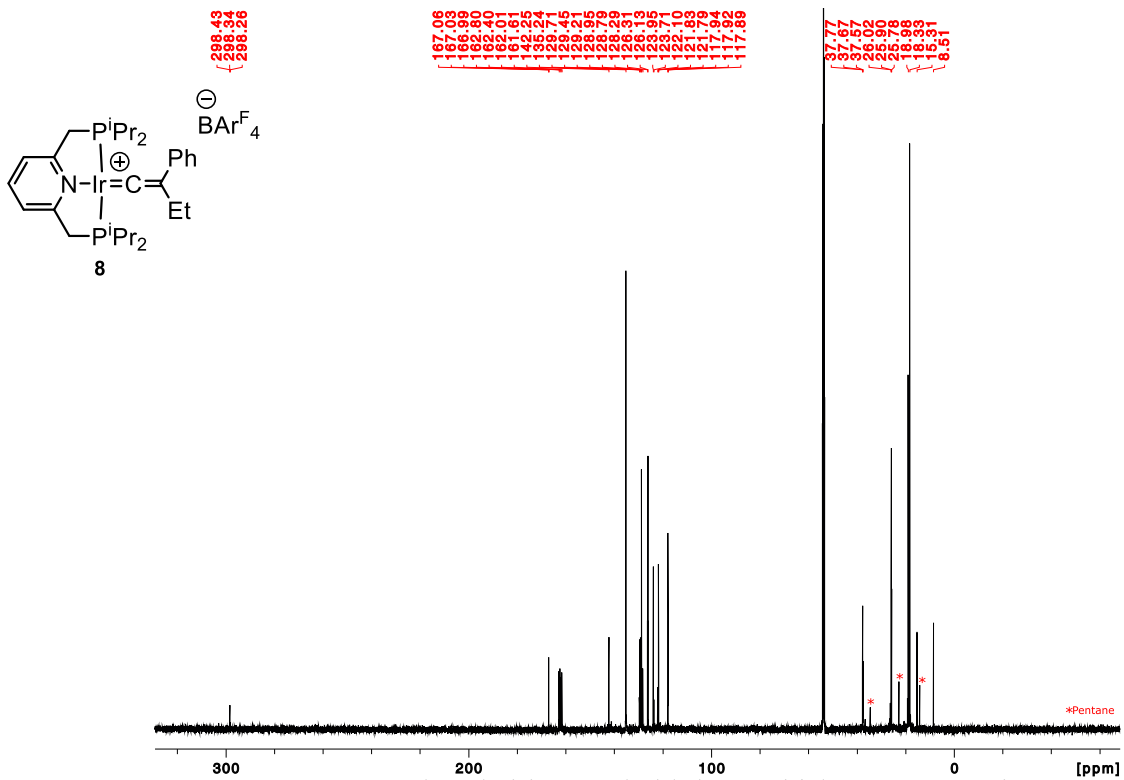


Figure 3.5.22. ¹³C NMR Spectrum of [(PNP(ⁱPr)₄)Ir=C=C(Ph)(Et)]BAR₄^F (8) (126 MHz, CD₂Cl₂).

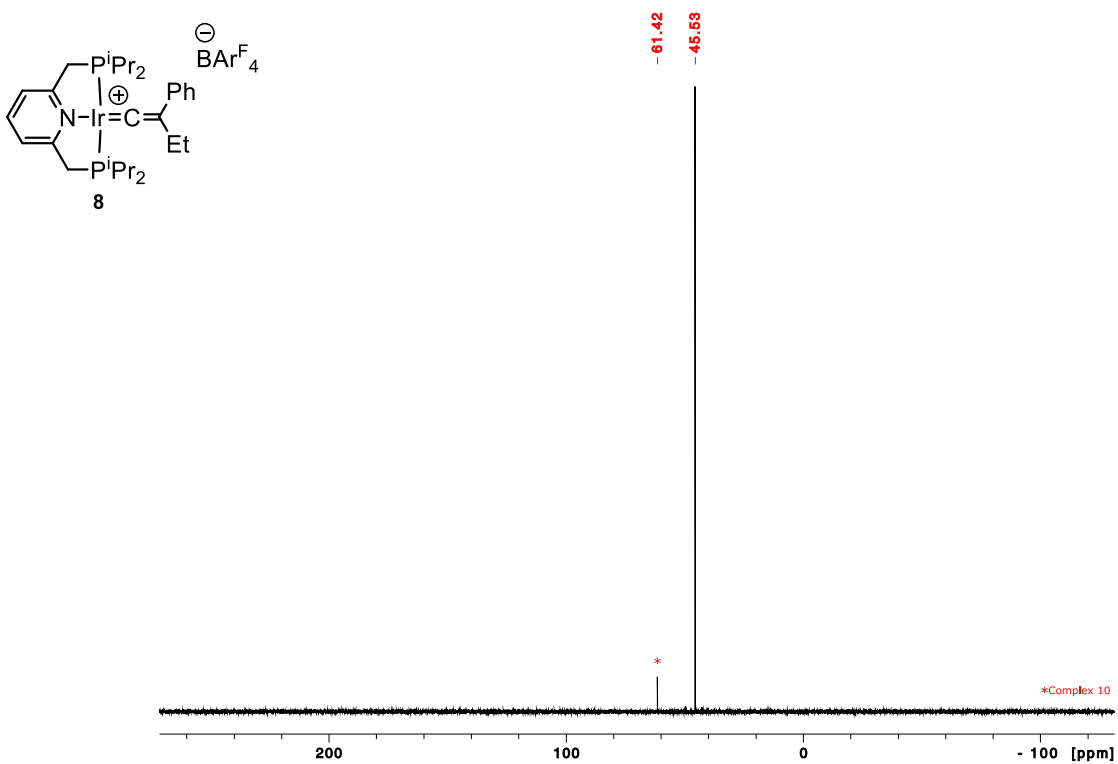


Figure 3.5.23. ³¹P NMR Spectrum of [(PNP(ⁱPr)₄)Ir=C=C(Ph)(Et)]BAR₄^F (8) (202 MHz, CD₂Cl₂).

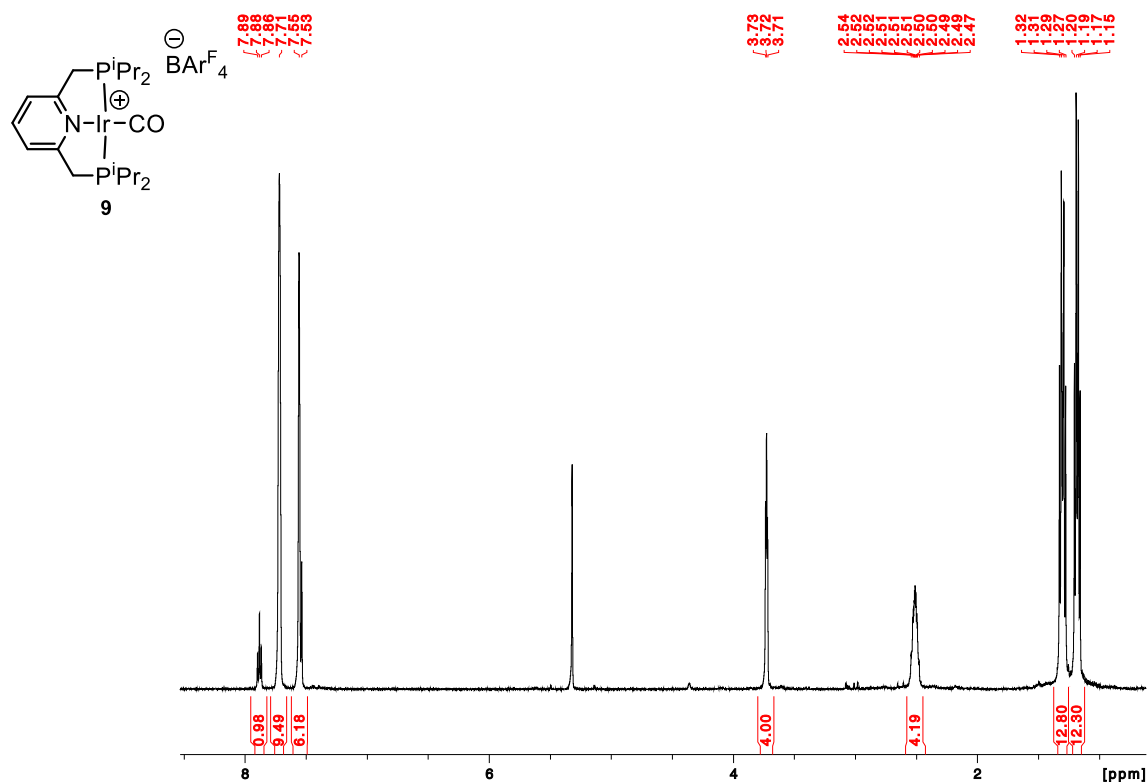


Figure 3.5.24. 1H NMR Spectrum of $[(PNP(iPr)_4)Ir(CO)]BARF_4$ (**9**) (500 MHz, CD_2Cl_2).

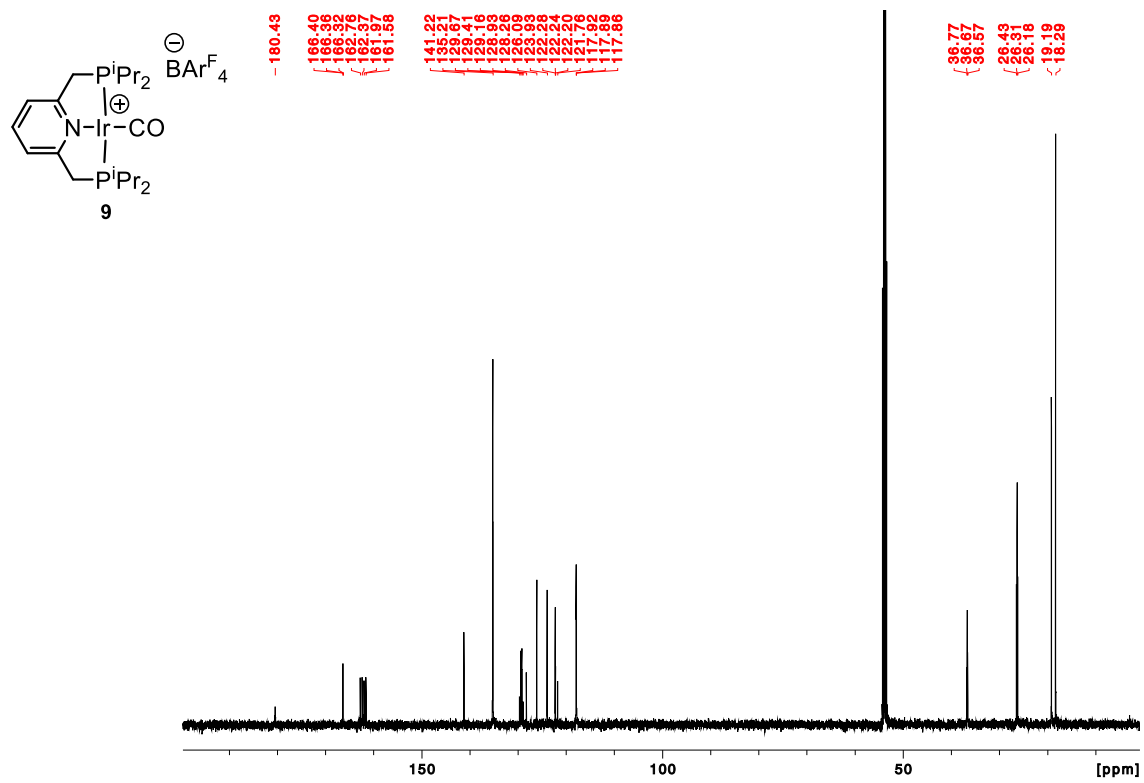


Figure 3.5.25. ^{13}C NMR Spectrum of $[(PNP(iPr)_4)Ir(CO)]BARF_4$ (**9**) (126 MHz, CD_2Cl_2).

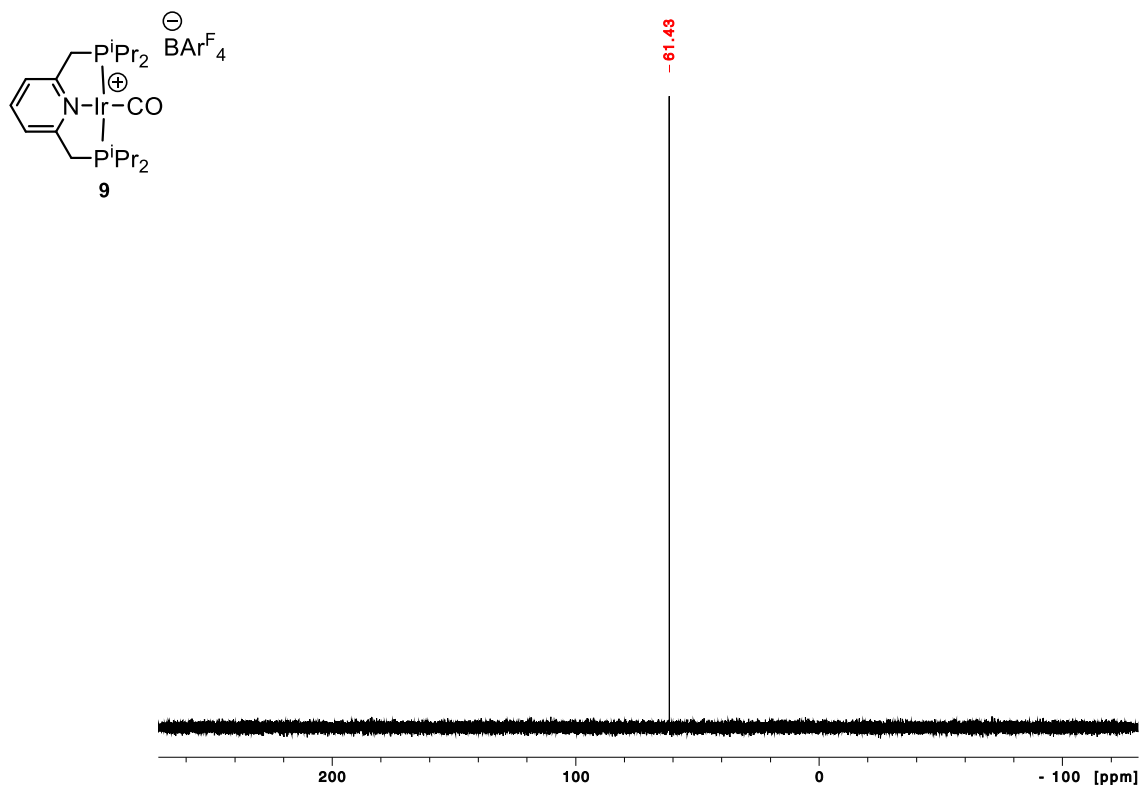


Figure 3.5.26. ^{31}P NMR Spectrum of $[(PNP(^iPr)_4)Ir(CO)]BArF_4$ (**9**) (202 MHz, CD_2Cl_2).

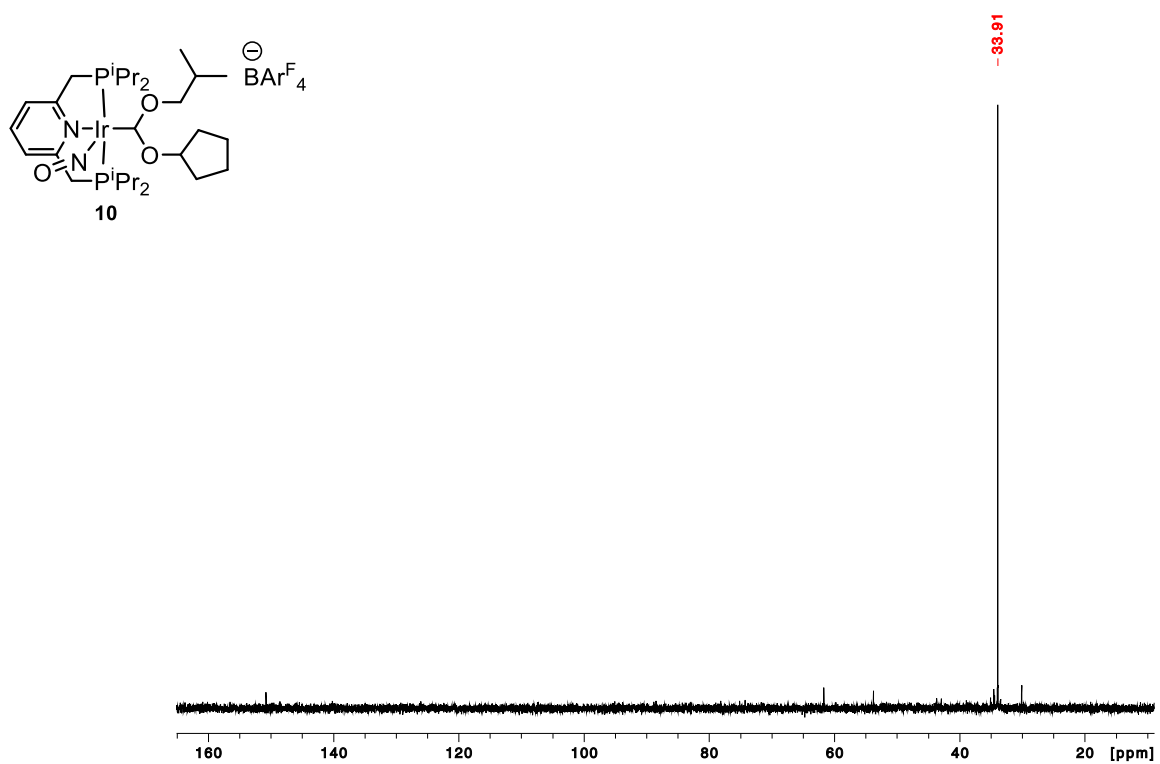


Figure 3.5.27. ^{31}P NMR Spectrum of $[(PNP(^iPr)_4)Ir(NO)[CH(OC_4H_9)(OC_5H_9)]]BArF_4$ (**10**) generated *in-situ* (162 MHz, CPME).

3.6 X-Ray Crystallography

Details of crystallographic refinement

General Methods. A suitable crystal of each sample was selected for analysis and mounted in a polyimide loop. Crystal samples were handled under immersion oil and quickly transferred to a cold nitrogen stream. All measurements were made on a Rigaku Oxford Diffraction Supernova Eos CCD with filtered Cu-K α or Mo-K α radiation at a temperature of 100 K. Using Olex2,⁷⁰ the structure was solved with the ShelXT structure solution program using Direct Methods and refined with the ShelXL refinement package⁷¹ using Least Squares minimization.

Complex 1

Disordered trifluoromethyl groups on the anion were modeled over two positions with similarity restraints placed on C-F and C-C bond distances and disordered atom thermal parameters. The disordered olefin ligand was modeled over two positions with similarity restraints placed on C-C bond distances and atom thermal parameters. The four carbon atoms that make up the unbound olefin in the diene were further restrained to lie in a single plane to ensure a sensible olefin geometry.

Complex 2

Disordered trifluoromethyl and isopropyl groups were modeled over two positions with similarity restraints placed on disordered atom thermal parameters, and C-C and C-F bonds. The metal hydrides were located in the difference map and refined with a strong Ir-H bond restraint. Their thermal parameters were fixed to ride on the parent Ir atom.

Complex 3

All crystals examined from multiple batches of this compound presented with apparently tetragonal symmetry, however no reasonable structural solutions could be found. The structure was solved as a twinned monoclinic sample in the P2₁ space group. The merohedral twin components were generated using the TWINROTMAT routine in PLATON and the occupancy of the twin components were refined. A similarity restraint was applied to the atom thermal parameters for N1, Ir1, and C1. Disorder in a trifluoromethyl group and an isopropyl group was modeled over two positions with similarity restraints applied to the bond lengths and atom thermal parameters of disordered atoms.

Complex 4

The model was refined without restraint.

Complex 6

The model was refined without restraint.

Complex 7

The model was refined without restraint.

Complex 8

Disordered trifluoromethyl groups were modeled over two positions with similarity restraints placed on C-F bond distances and atom thermal parameters. Disordered pentane molecules were modeled over two positions with similarity restraints placed on C-C bond distances and atom thermal parameters. Disorder in the isopropyl groups was modeled over two positions with similarity restraints placed on C-C and C-P bond distances and atom thermal parameters.

Complex 9

Extensive two site disorder in the iridium cation and the BAr^{F}_4 anion presented a challenge. Design of the model required extensive similarity restraints placed on both atom thermal parameters and bond lengths, but many of these could be removed to give a less-restrained but still stable model for the final cycles of refinement. The final disorder model uses a single global similarity restraint placed on the thermal parameters of nearby atoms.

Complex 10

The metal ion position is disordered with a minor population present in the κ^2 -form (bound to both the oxygen and carbon atom of the dialkoxyalkyl ligand). This disorder was modeled with similarity restraints placed on Ir-N, Ir-P and N-O distances as well as restraints on non-bonded contacts necessary to model the very low population positions of the nitrosyl. The metal atom thermal parameters were constrained to be equal. Disorder in the trifluoromethyl groups of the anion was modeled with similarity restraints placed on C-C and C-F bond distances and atom thermal parameters.

Table 3.6.1. Crystal data and structure refinement for complex 1.

Identification code	complex_1	
Empirical formula	C ₅₉ H ₃₈ BF ₂₄ IrNP ₂	
Formula weight	1502.01	
Temperature	100.01(10) K	
Wavelength	0.71073 Å	
Crystal system	Monoclinic	
Space group	C 1 2/c 1	
Unit cell dimensions	a = 18.9369(2) Å	α = 90°
	b = 17.8826(2) Å	β = 91.1277(11)°
	c = 36.1583(5) Å	γ = 90°
Volume	12242.3(3) Å ³	
Z	8	
Density (calculated)	1.630 Mg/m ³	
Absorption coefficient	2.346 mm ⁻¹	
F(000)	5976	
Crystal size	0.197 x 0.11 x 0.108 mm ³	
Theta range for data collection	2.253 to 30.388°.	
Index ranges	-26<=h<=26, -24<=k<=23, -49<=l<=51	
Reflections collected	77693	
Independent reflections	16556 [R(int) = 0.0610]	
Completeness to theta = 25.242°	99.9 %	
Absorption correction	Gaussian	
Max. and min. transmission	1.000 and 0.700	
Refinement method	Full-matrix least-squares on F ²	
Data / restraints / parameters	16556 / 1624 / 1063	
Goodness-of-fit on F ²	1.097	
Final R indices [I>2sigma(I)]	R1 = 0.0623, wR2 = 0.1246	
R indices (all data)	R1 = 0.0862, wR2 = 0.1345	
Absolute structure parameter	0.637(5)	
Extinction coefficient	n/a	
Largest diff. peak and hole	2.692 and -1.235 e/Å ⁻³	

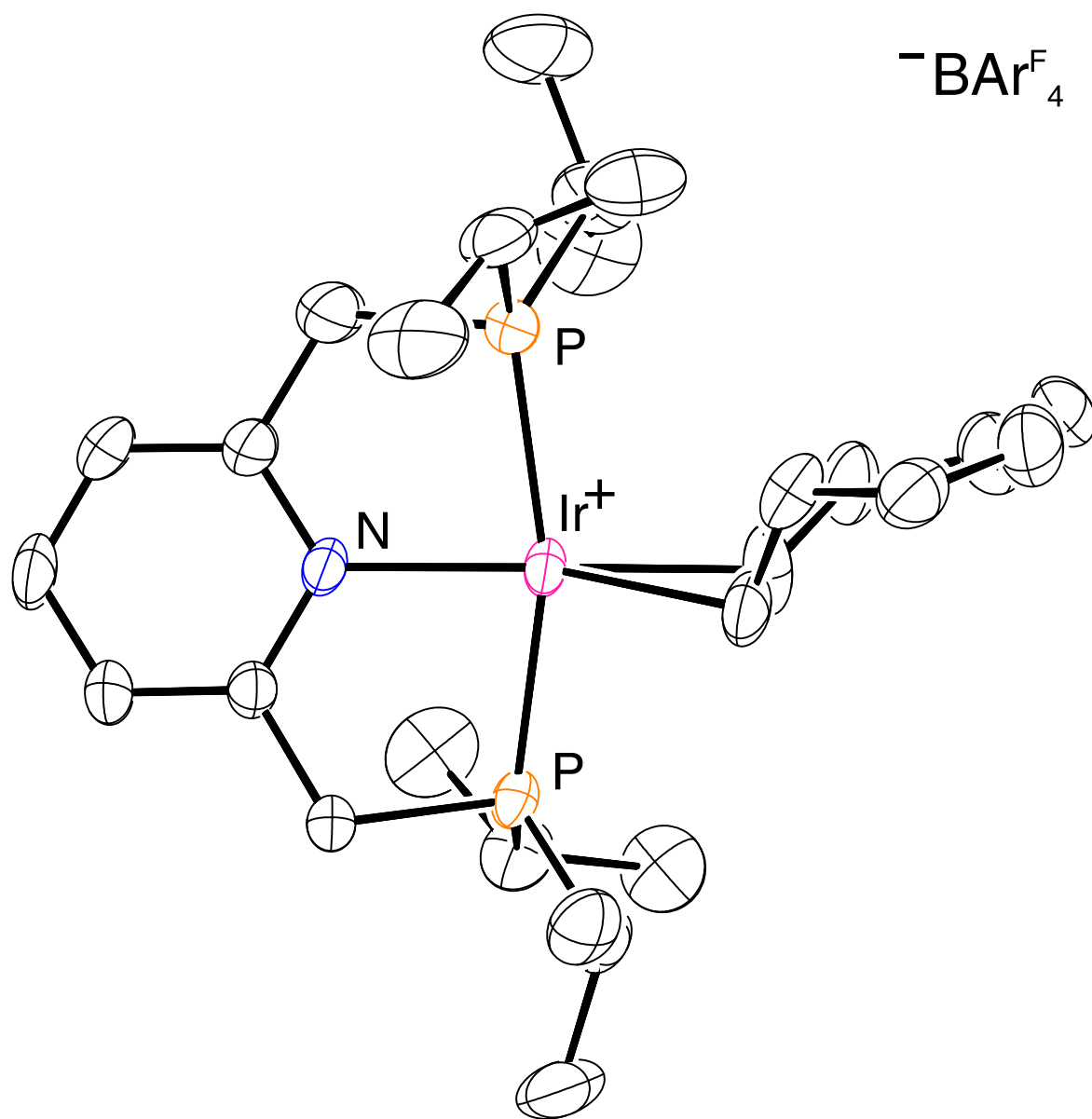


Figure 3.6.1. ORTEP diagram of **1** with ellipsoids shown at 50%. The anion is omitted for clarity.

Table 3.6.2. Crystal data and structure refinement for complex **2**.

Identification code	complex_2	
Empirical formula	C ₅₅ H ₃₇ BF ₂₄ IrNOP ₂	
Formula weight	1468.96	
Temperature	100.00(10) K	
Wavelength	1.54184 Å	
Crystal system	Triclinic	
Space group	P-1	
Unit cell dimensions	a = 12.9943(3) Å	α = 98.649(2)°
	b = 13.1678(3) Å	β = 105.522(2)°
	c = 18.6857(3) Å	γ = 95.873(2)°
Volume	3011.29(11) Å ³	
Z	2	
Density (calculated)	1.620 Mg/m ³	
Absorption coefficient	5.819 mm ⁻¹	
F(000)	1460	
Crystal size	0.174 x 0.059 x 0.042 mm ³	
Theta range for data collection	2.497 to 73.487°.	
Index ranges	-16 ≤ h ≤ 15, -13 ≤ k ≤ 16, -23 ≤ l ≤ 23	
Reflections collected	57602	
Independent reflections	11955 [R(int) = 0.0498]	
Completeness to theta = 67.684°	100.0 %	
Absorption correction	Gaussian	
Max. and min. transmission	0.967 and 0.517	
Refinement method	Full-matrix least-squares on F ²	
Data / restraints / parameters	11955 / 204 / 867	
Goodness-of-fit on F ²	1.049	
Final R indices [I > 2σ(I)]	R1 = 0.0574, wR2 = 0.1486	
R indices (all data)	R1 = 0.0642, wR2 = 0.1541	
Absolute structure parameter	0.637(5)	
Extinction coefficient	n/a	
Largest diff. peak and hole	3.137 and -1.084 e/Å ⁻³	

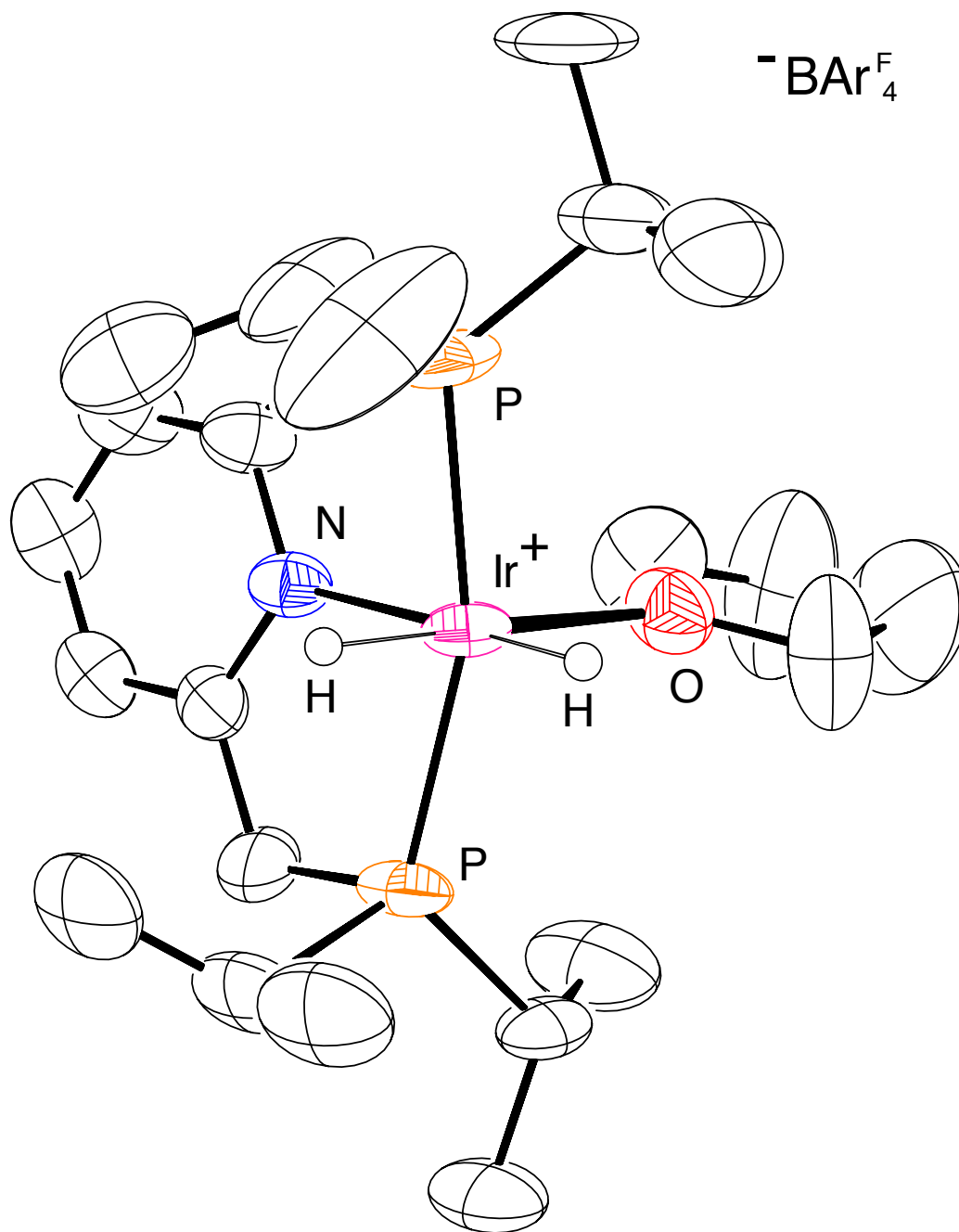


Figure 3.6.2. ORTEP diagram of **2** with ellipsoids shown at 50%. The anion is omitted for clarity.

Table 3.6.3. Crystal data and structure refinement for complex 3.

Identification code	complex_3	
Empirical formula	C ₅₇ H ₅₇ BF ₂₄ IrNOP ₂	
Formula weight	1492.98	
Temperature	100.00(10) K	
Wavelength	1.54184 Å	
Crystal system	Monoclinic	
Space group	P 1 21 1	
Unit cell dimensions	a = 13.28988(15) Å	α = 90°
	b = 17.31748(16) Å	β = 90.0034(9)°
	c = 13.29572(13) Å	γ = 90°
Volume	3059.97(5) Å ³	
Z	2	
Density (calculated)	1.620 Mg/m ³	
Absorption coefficient	5.738 mm ⁻¹	
F(000)	1484	
Crystal size	0.134 x 0.04 x 0.029 mm ³	
Theta range for data collection	3.324 to 73.350°.	
Index ranges	-16 ≤ h ≤ 16, -21 ≤ k ≤ 21, -16 ≤ l ≤ 16	
Reflections collected	11157	
Completeness to theta = 67.684°	100.0 %	
Absorption correction	Gaussian	
Max. and min. transmission	0.900 and 0.562	
Refinement method	Full-matrix least-squares on F ²	
Data / restraints / parameters	11157 / 203 / 861	
Goodness-of-fit on F ²	1.039	
Final R indices [I > 2σ(I)]	R1 = 0.0421, wR2 = 0.1092	
R indices (all data)	R1 = 0.0425, wR2 = 0.1096	
Absolute structure parameter	0.637(5)	
Extinction coefficient	n/a	
Largest diff. peak and hole	1.422 and -1.358 e/Å ⁻³	

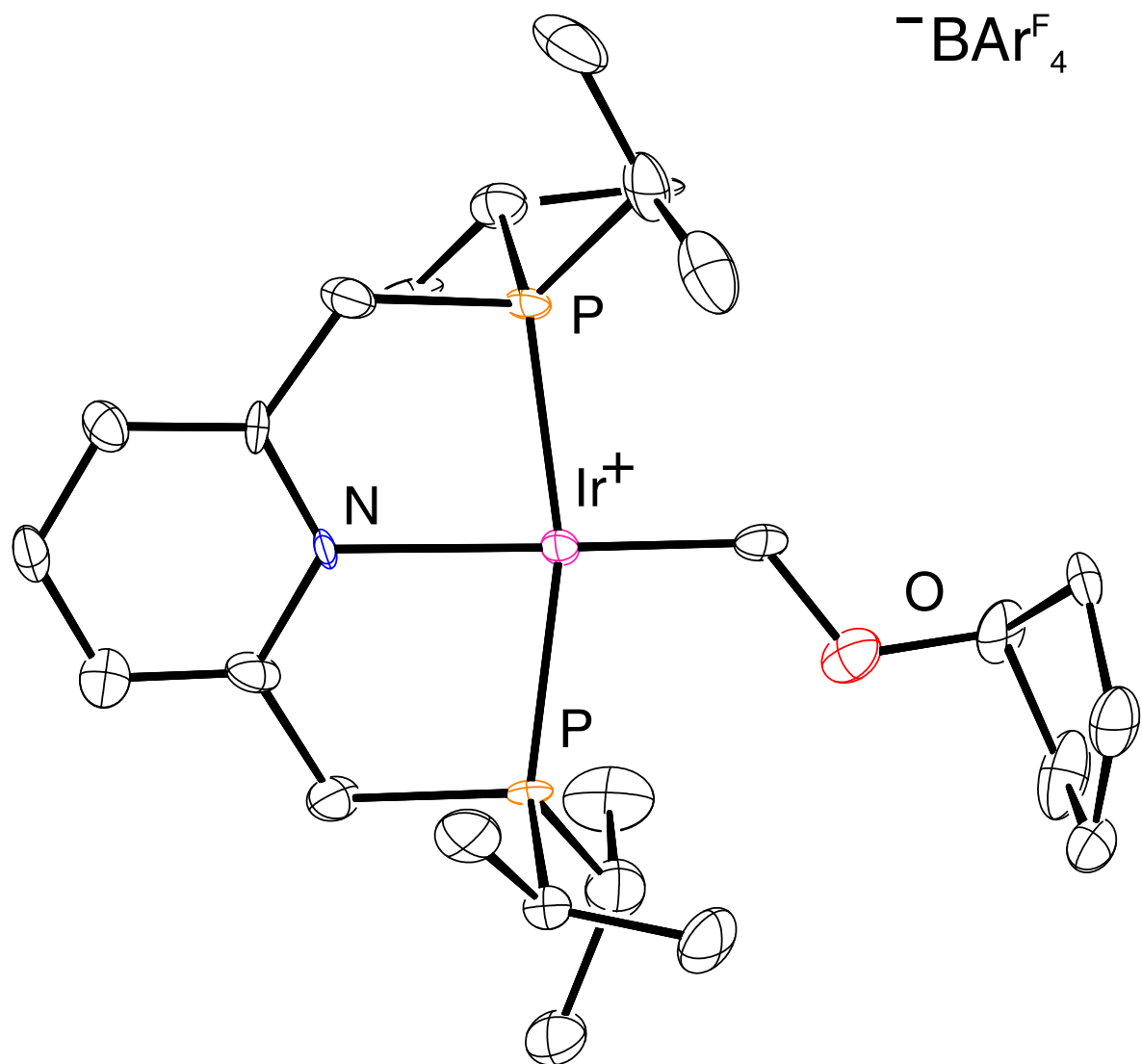


Figure 3.6.3. ORTEP diagram of **3** with ellipsoids shown at 50%. The anion is omitted for clarity.

Table 3.6.4. Crystal data and structure refinement for complex 4.

Identification code	complex_4	
Empirical formula	C ₂₃ H ₄₄ IrNOP ₂	
Formula weight	628.75	
Temperature	99.98(17) K	
Wavelength	0.71073 Å	
Crystal system	Monoclinic	
Space group	P 1 21/n 1	
Unit cell dimensions	a = 12.2736(5) Å	α = 90°
	b = 16.6947(4) Å	β = 110.835(5)°
	c = 13.7692(5) Å	γ = 90°
Volume	2636.87(19) Å ³	
Z	4	
Density (calculated)	1.584 Mg/m ³	
Absorption coefficient	5.201 mm ⁻¹	
F(000)	1264	
Crystal size	0.291 x 0.031 x 0.018 mm ³	
Theta range for data collection	2.269 to 30.350°.	
Index ranges	-16 ≤ h ≤ 16, -21 ≤ k ≤ 23, -18 ≤ l ≤ 18	
Reflections collected	33134	
Independent reflections	7178 [R(int) = 0.0648]	
Completeness to theta = 25.242°	99.9 %	
Absorption correction	Gaussian	
Max. and min. transmission	1.000 and 0.399	
Refinement method	Full-matrix least-squares on F ²	
Data / restraints / parameters	7178 / 0 / 279	
Goodness-of-fit on F ²	1.014	
Final R indices [I > 2σ(I)]	R1 = 0.0333, wR2 = 0.0562	
R indices (all data)	R1 = 0.0481, wR2 = 0.0598	
Extinction coefficient	n/a	
Largest diff. peak and hole	1.700 and -1.103 e/Å ⁻³	

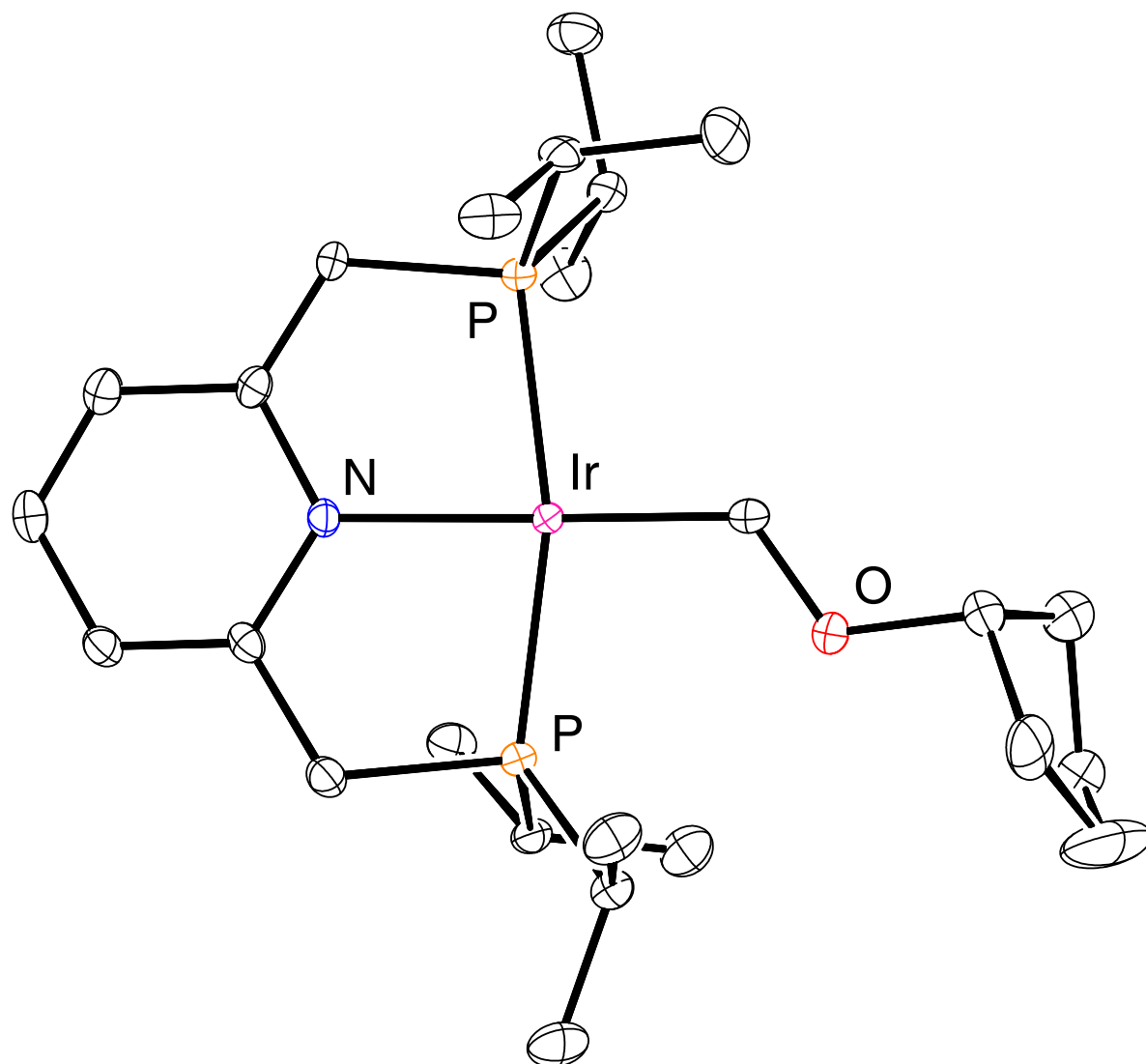


Figure 3.6.4. ORTEP diagram of 4 with ellipsoids shown at 50%.

Table 3.6.5. Crystal data and structure refinement for complex 6.

Identification code	complex_6	
Empirical formula	C ₅₁ H ₄₇ BF ₂₄ IrN ₃ P ₂	
Formula weight	1422.86	
Temperature	99.99(10) K	
Wavelength	0.71073 Å	
Crystal system	Monoclinic	
Space group	C 1 2/c 1	
Unit cell dimensions	a = 18.9915(6) Å	α = 90°
	b = 17.3847(5) Å	β = 93.060(3)°
	c = 17.1142(5) Å	γ = 90°
Volume	5642.4(3) Å ³	
Z	4	
Density (calculated)	1.675 Mg/m ³	
Absorption coefficient	2.541 mm ⁻¹	
F(000)	2808	
Crystal size	0.267 x 0.198 x 0.03 mm ³	
Theta range for data collection	2.384 to 28.279°.	
Index ranges	-25 ≤ h ≤ 25, -22 ≤ k ≤ 23, -22 ≤ l ≤ 22	
Reflections collected	32856	
Independent reflections	6947 [R(int) = 0.0646]	
Completeness to theta = 25.242°	99.9 %	
Absorption correction	Semi-empirical from equivalents	
Max. and min. transmission	1.00000 and 0.36965	
Refinement method	Full-matrix least-squares on F ²	
Data / restraints / parameters	6947 / 0 / 377	
Goodness-of-fit on F ²	1.077	
Final R indices [I > 2σ(I)]	R1 = 0.0438, wR2 = 0.1025	
R indices (all data)	R1 = 0.0579, wR2 = 0.1094	
Extinction coefficient	n/a	
Largest diff. peak and hole	3.179 and -1.579 e/Å ⁻³	

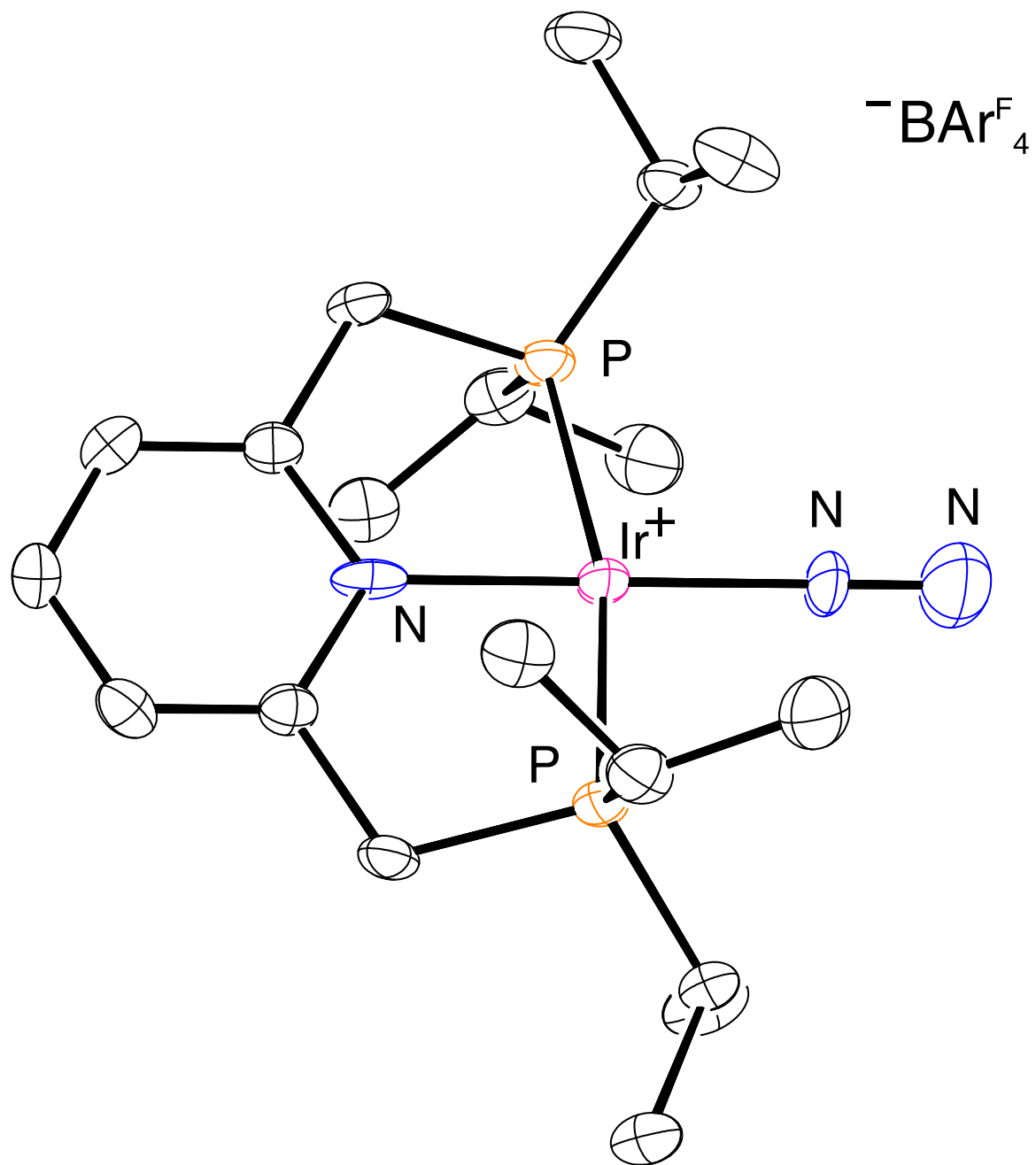


Figure 3.6.5. ORTEP diagram of **6** with ellipsoids shown at 50%. The anion is omitted for clarity.

Table 3.6.6. Crystal data and structure refinement for complex 7.

Identification code	complex_7	
Empirical formula	C ₁₉ H ₃₄ IrN ₃ P ₂	
Formula weight	558.63	
Temperature	100.01(10) K	
Wavelength	0.71073 Å	
Crystal system	Monoclinic	
Space group	P 1 21/n 1	
Unit cell dimensions	a = 11.1898(4) Å	α = 90°
	b = 13.6854(5) Å	β = 97.389(4)°
	c = 28.9997(12) Å	γ = 90°
Volume	4404.1(3) Å ³	
Z	8	
Density (calculated)	1.685 Mg/m ³	
Absorption coefficient	6.216 mm ⁻¹	
F(000)	2208	
Crystal size	0.202 x 0.127 x 0.058 mm ³	
Theta range for data collection	2.363 to 27.550°.	
Index ranges	-14 ≤ h ≤ 13, -17 ≤ k ≤ 16, -37 ≤ l ≤ 37	
Reflections collected	47060	
Independent reflections	10125 [R(int) = 0.0933]	
Completeness to theta = 25.242°	99.9 %	
Absorption correction	Gaussian	
Max. and min. transmission	1.000 and 0.382	
Refinement method	Full-matrix least-squares on F ²	
Data / restraints / parameters	10125 / 0 / 467	
Goodness-of-fit on F ²	1.036	
Final R indices [I > 2σ(I)]	R1 = 0.0450, wR2 = 0.0794	
R indices (all data)	R1 = 0.0649, wR2 = 0.0871	
Extinction coefficient	n/a	
Largest diff. peak and hole	1.400 and -1.417 e/Å ⁻³	

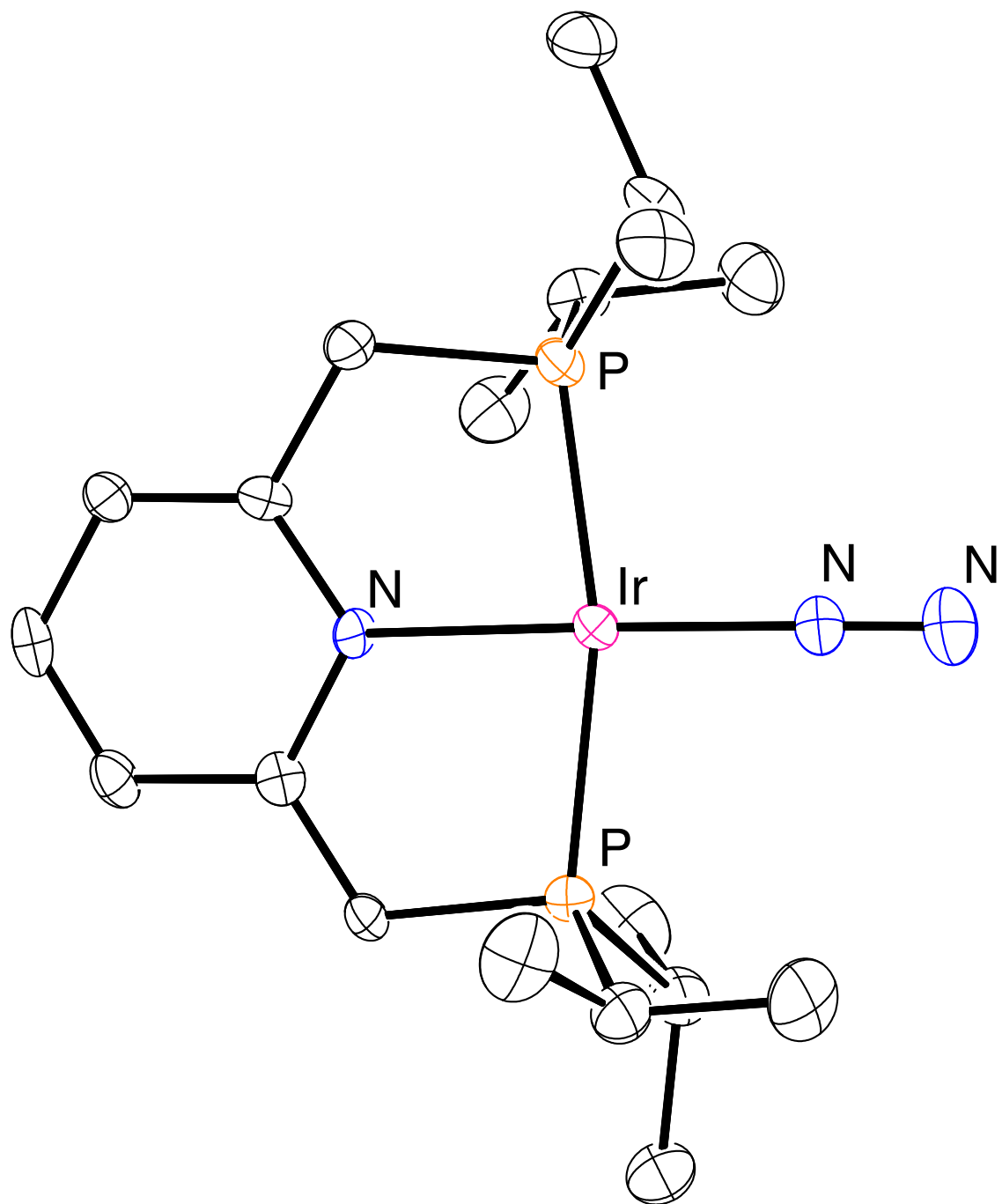


Figure 3.6.6. ORTEP diagram of 7 with ellipsoids shown at 50%.

Table 3.6.7. Crystal data and structure refinement for complex 8.

Identification code	complex_8	
Empirical formula	$C_{61}H_{57}BF_{24}IrNP_2 \cdot 2(C_5H_{12})$	
Formula weight	1669.31	
Temperature	99.99(10) K	
Wavelength	0.71073 Å	
Crystal system	Triclinic	
Space group	P-1	
Unit cell dimensions	a = 12.4998(6) Å	$\alpha = 87.152(5)^\circ$
	b = 17.0461(8) Å	$\beta = 82.587(5)^\circ$
	c = 17.8435(12) Å	$\gamma = 76.616(4)^\circ$
Volume	3667.0(3) Å ³	
Z	2	
Density (calculated)	1.512 Mg/m ³	
Absorption coefficient	1.966 mm ⁻¹	
F(000)	1684	
Crystal size	0.457 x 0.16 x 0.022 mm ³	
Theta range for data collection	2.303 to 26.372°.	
Index ranges	-15 ≤ h ≤ 15, -21 ≤ k ≤ 21, -22 ≤ l ≤ 22	
Reflections collected	59347	
Independent reflections	15014 [R(int) = 0.0875]	
Completeness to theta = 25.242°	99.9 %	
Absorption correction	Gaussian	
Max. and min. transmission	1.000 and 0.218	
Refinement method	Full-matrix least-squares on F ²	
Data / restraints / parameters	15014 / 680 / 1143	
Goodness-of-fit on F ²	1.016	
Final R indices [I > 2σ(I)]	R1 = 0.0454, wR2 = 0.0939	
R indices (all data)	R1 = 0.0634, wR2 = 0.1027	
Extinction coefficient	n/a	
Largest diff. peak and hole	1.490 and -1.609 e/Å ⁻³	

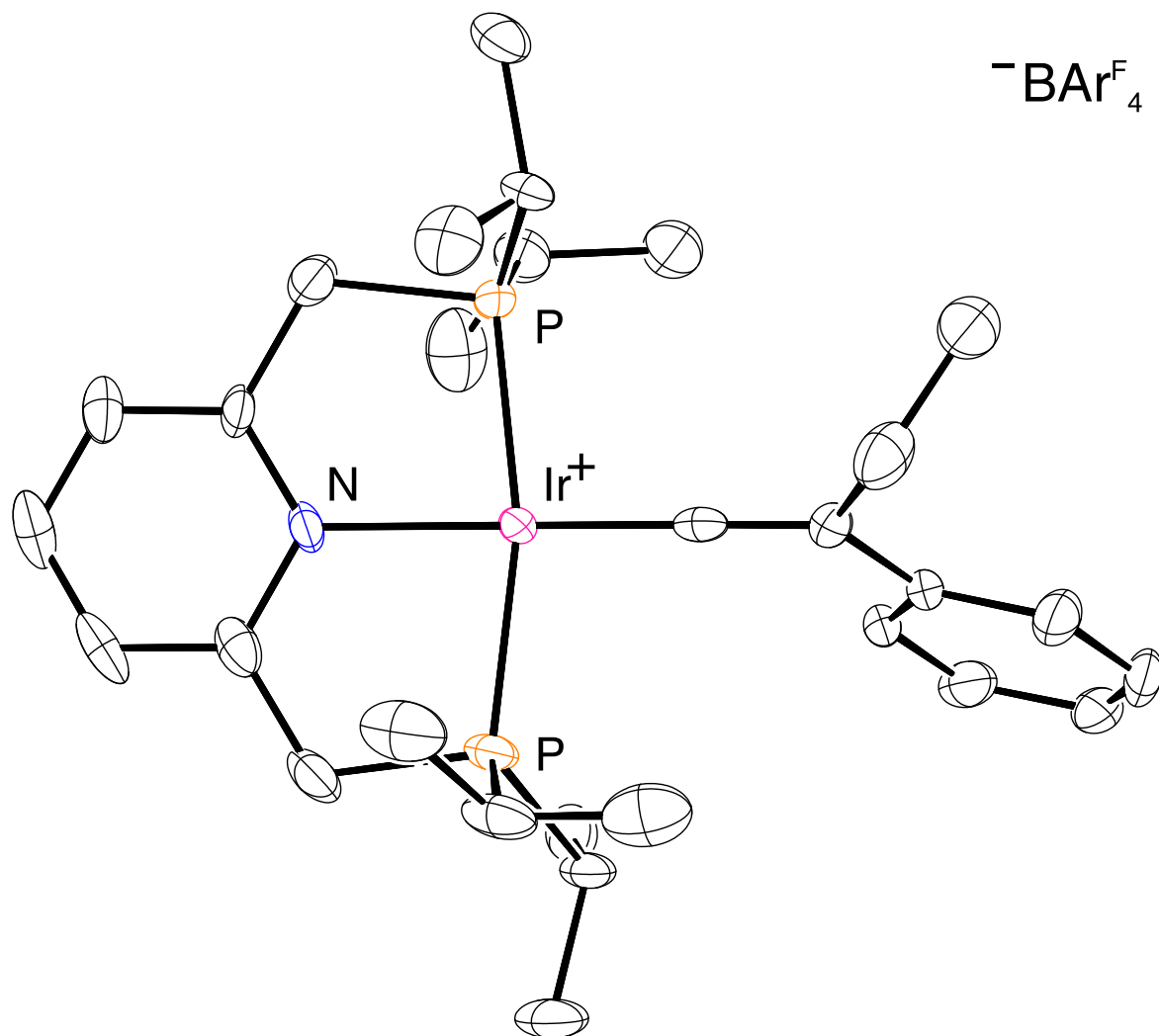


Figure 3.6.7. ORTEP diagram of **8** with ellipsoids shown at 50%. The anion is omitted for clarity.

Table 3.6.8. Crystal data and structure refinement for complex **9**.

Identification code	complex_9	
Empirical formula	C ₅₂ H ₄₇ BF ₂₄ IrNOP ₂	
Formula weight	1422.85	
Temperature	100.00(10) K	
Wavelength	1.54184 Å	
Crystal system	Monoclinic	
Space group	P 1 21/c 1	
Unit cell dimensions	a = 12.3950(2) Å	α = 90.0°
	b = 12.08210(10) Å	β = 95.6180(10)°
	c = 38.1863(4) Å	γ = 90.0°
Volume	5691.22(12) Å ³	
Z	4	
Density (calculated)	1.661 Mg/m ³	
Absorption coefficient	6.138 mm ⁻¹	
F(000)	2808	
Crystal size	0.16 x 0.114 x 0.054 mm ³	
Theta range for data collection	2.325 to 73.503°.	
Index ranges	-15 ≤ h ≤ 15, -14 ≤ k ≤ 9, -46 ≤ l ≤ 47	
Reflections collected	55865	
Independent reflections	11317 [R(int) = 0.0303]	
Completeness to theta = 67.684°	100.0 %	
Absorption correction	Gaussian	
Max. and min. transmission	0.884 and 0.479	
Refinement method	Full-matrix least-squares on F ²	
Data / restraints / parameters	11317 / 1980 / 1287	
Goodness-of-fit on F ²	1.113	
Final R indices [I > 2σ(I)]	R1 = 0.0419, wR2 = 0.0787	
R indices (all data)	R1 = 0.0460, wR2 = 0.0800	
Extinction coefficient	n/a	
Largest diff. peak and hole	2.205 and -1.921 e/Å ⁻³	

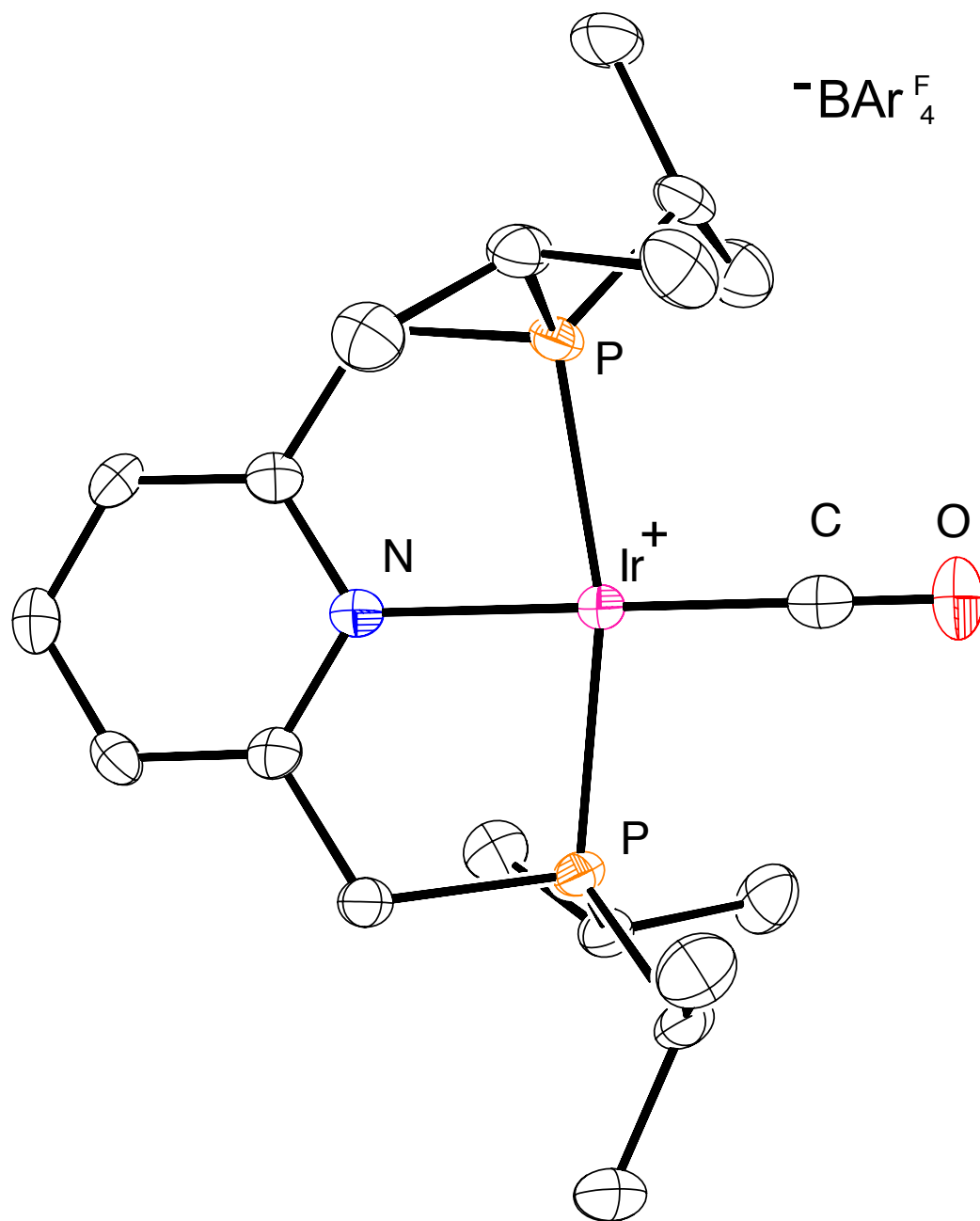


Figure 3.6.8. ORTEP diagram of **9** with ellipsoids shown at 50%. The anion is omitted for clarity.

Table 3.6.9. Crystal data and structure refinement for complex **10**.

Identification code	complex_10	
Empirical formula	C ₆₁ H ₆₆ BF ₂₄ IrN ₂ O ₃ P ₂	
Formula weight	1596.10	
Temperature	100.01(10) K	
Wavelength	0.71073 Å	
Crystal system	Triclinic	
Space group	P-1	
Unit cell dimensions	a = 12.6638(3) Å	α = 88.220(2)°
	b = 13.4045(3) Å	β = 75.669(2)°
	c = 20.2237(5) Å	γ = 80.778(2)°
Volume	3283.06(15) Å ³	
Z	2	
Density (calculated)	1.615 Mg/m ³	
Absorption coefficient	2.196 mm ⁻¹	
F(000)	1596	
Crystal size	0.497 x 0.302 x 0.16 mm ³	
Theta range for data collection	2.330 to 26.372°.	
Index ranges	-15 ≤ h ≤ 15, -16 ≤ k ≤ 14, -25 ≤ l ≤ 25	
Reflections collected	41934	
Independent reflections	13411 [R(int) = 0.0440]	
Completeness to theta = 25.242°	99.9 %	
Absorption correction	Gaussian	
Max. and min. transmission	1.000 and 0.350	
Refinement method	Full-matrix least-squares on F ²	
Data / restraints / parameters	13411 / 372 / 959	
Goodness-of-fit on F ²	1.068	
Final R indices [I > 2σ(I)]	R1 = 0.0565, wR2 = 0.1352	
R indices (all data)	R1 = 0.0644, wR2 = 0.1403	
Extinction coefficient	n/a	
Largest diff. peak and hole	3.181 and -1.562 e/Å ⁻³	

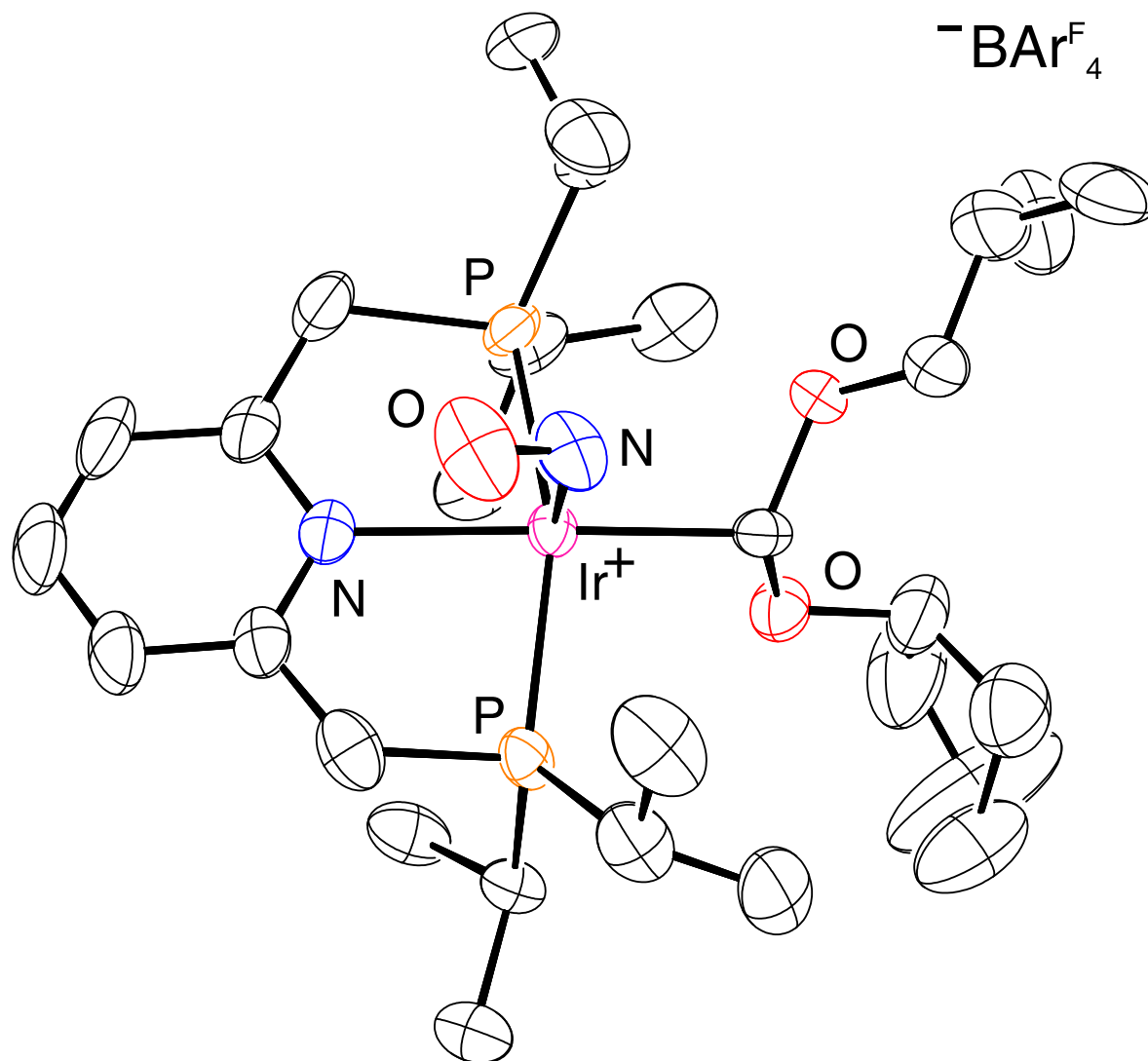


Figure 3.6.9. ORTEP diagram of **10** with ellipsoids shown at 50%. The anion is omitted for clarity.

3.7 References

- (1) Janowicz, A. H.; Bergman, R. G., "Carbon-hydrogen activation in completely saturated hydrocarbons: direct observation of $M + R-H \rightarrow M(R)(H)$." *J. Am. Chem. Soc.* **1982**, *104* (1), 352-354.
- (2) Janowicz, A. H.; Bergman, R. G., "Activation of carbon-hydrogen bonds in saturated hydrocarbons on photolysis of $(\eta^5-C_5Me_5)(PMe_3)IrH_2$. Relative rates of reaction of the intermediate with different types of carbon-hydrogen bonds and functionalization of the metal-bound alkyl groups." *J. Am. Chem. Soc.* **1983**, *105* (12), 3929-3939.
- (3) Crabtree, R. H.; Mihelcic, J. M.; Quirk, J. M., "Iridium Complexes in Alkane Dehydrogenation." *J. Am. Chem. Soc.* **1979**, *101* (26), 7738-7740.

- (4) Crabtree, R. H.; Demou, P. C.; Eden, D.; Mihelcic, J. M.; Parnell, C. A.; Quirk, J. M.; Morris, G. E., "Dihydrido olefin and solvento complexes of iridium and the mechanisms of olefin hydrogenation and alkane dehydrogenation." *J. Am. Chem. Soc.* **1982**, *104* (25), 6994-7001.
- (5) Burk, M. J.; Crabtree, R. H.; Parnell, C. P.; Uriarte, R. J., "Selective stoichiometric and catalytic carbon-hydrogen bond cleavage reactions in hydrocarbons by iridium complexes." *Organometallics* **1984**, *3* (5), 816-817.
- (6) Burk, M. J.; Crabtree, R. H., "Selective Catalytic Dehydrogenation of Alkanes to Alkenes." *J. Am. Chem. Soc.* **1987**, *109* (26), 8025-8032.
- (7) Felkin, H.; Fillebeen-Khan, T.; Gault, Y.; Holmes-Smith, R.; Zakrzewski, J., "Activation of C-H bonds in saturated hydrocarbons. The catalytic functionalisation of cyclooctane by means of some soluble iridium and ruthenium polyhydride systems." *Tetrahedron Lett.* **1984**, *25* (12), 1279-1282.
- (8) Felkin, H.; Fillebeen-khan, T.; Holmes-Smith, R.; Yingrui, L., "Activation of C-H bonds in saturated hydrocarbons. The selective, catalytic functionalisation of methyl groups by means of a soluble iridium polyhydride system." *Tetrahedron Lett.* **1985**, *26* (16), 1999-2000.
- (9) Burk, M. J.; Crabtree, R. H.; McGrath, D. V., "Thermal and photochemical catalytic dehydrogenation of alkanes with $[\text{IrH}_2(\text{CF}_3\text{CO}_2)(\text{PR}_3)_2]$ (R = C₆H₄F-p and cyclohexyl)." *J. Chem. Soc., Chem. Commun.* **1985**, (24), 1829-1830.
- (10) Gupta, M.; Hagen, C.; Flesher, R. J.; Kaska, W. C.; Jensen, C. M., "A highly active alkane dehydrogenation catalyst: stabilization of dihydrido rhodium and iridium complexes by a P-C-P pincer ligand." *Chem. Commun.* **1996**, (17), 2083-2084.
- (11) Gupta, M.; Hagen, C.; Kaska, W. C.; Cramer, R. E.; Jensen, C. M., "Catalytic Dehydrogenation of Cycloalkanes to Arenes by a Dihydrido Iridium P-C-P Pincer Complex." *J. Am. Chem. Soc.* **1997**, *119* (4), 840-841.
- (12) Choi, J.; MacArthur, A. H. R.; Brookhart, M.; Goldman, A. S., "Dehydrogenation and Related Reactions Catalyzed by Iridium Pincer Complexes." *Chem. Rev.* **2011**, *111* (3), 1761-1779.
- (13) Kumar, A.; Goldman, A. S., "Recent Advances in Alkane Dehydrogenation Catalyzed by Pincer Complexes." In *The Privileged Pincer-Metal Platform: Coordination Chemistry & Applications*, van Koten, G.; Gossage, R. A., Eds. Springer International Publishing: Cham, 2016; pp 307-334.
- (14) Kumar, A.; Bhatti, T. M.; Goldman, A. S., "Dehydrogenation of Alkanes and Aliphatic Groups by Pincer-Ligated Metal Complexes." *Chem. Rev.* **2017**, *117* (19), 12357-12384.

- (15) Gupta, M.; Kaska, W.; M. Jensen, C., "Catalytic dehydrogenation of ethylbenzene and tetrahydrofuran by a dihydrido iridium P–C–P pincer complex." *Chem. Commun.* **1997**, (5), 461-462.
- (16) Lu, Y. J.; Zhang, X.; Malakar, S.; Krogh-Jespersen, K.; Hasanayn, F.; Goldman, A. S., "Formation of Enamines via Catalytic Dehydrogenation by Pincer-Iridium Complexes." *J. Org. Chem.* **2020**.
- (17) Zhang, X.; Fried, A.; Knapp, S.; Goldman, A. S., "Novel synthesis of enamines by iridium-catalyzed dehydrogenation of tertiary amines." *Chem. Commun.* **2003**, (16), 2060-2061.
- (18) Lyons, T. W.; Bézier, D.; Brookhart, M., "Iridium Pincer-Catalyzed Dehydrogenation of Ethers Featuring Ethylene as the Hydrogen Acceptor." *Organometallics* **2015**, 34 (16), 4058-4062.
- (19) Yao, W.; Zhang, Y.; Jia, X.; Huang, Z., "Selective Catalytic Transfer Dehydrogenation of Alkanes and Heterocycles by an Iridium Pincer Complex." *Angew. Chem. Int. Ed.* **2014**, 53 (5), 1390-1394.
- (20) Conejero, S.; Paneque, M.; Poveda, M. L.; Santos, L. L.; Carmona, E., "C–H Bond Activation Reactions of Ethers That Generate Iridium Carbenes." *Acc. Chem. Res.* **2010**, 43 (4), 572-580.
- (21) Whited, M. T.; Grubbs, R. H., "Late Metal Carbene Complexes Generated by Multiple C–H Activations: Examining the Continuum of M=C Bond Reactivity." *Acc. Chem. Res.* **2009**, 42 (10), 1607-1616.
- (22) Whited, M. T.; Grubbs, R. H., "Elucidation of Heterocumulene Activation by a Nucleophilic-at-Metal Iridium(I) Carbene." *Organometallics* **2009**, 28 (1), 161-166.
- (23) Meiners, J.; Friedrich, A.; Herdtweck, E.; Schneider, S., "Facile Double C–H Activation of Tetrahydrofuran by an Iridium PNP Pincer Complex." *Organometallics* **2009**, 28 (21), 6331-6338.
- (24) Zhang, Y.; Schley, N. D., "Reversible Alkoxy carbene Formation by C–H Activation of Ethers via Discrete, Isolable Intermediates." *Chem. Commun.* **2017**, 53 (13), 2130-2133.
- (25) Zhang, Y.; Mueller, B. R. J.; Schley, N. D., "Formation of a Delocalized Iridium Benzylidene with Azaquinone Methide Character via Alkoxy carbene Cleavage." *Organometallics* **2018**, 37 (12), 1825-1828.
- (26) Whited, M. T.; Grubbs, R. H., "A Catalytic Cycle for Oxidation of tert-Butyl Methyl Ether by a Double C–H Activation-Group Transfer Process." *J. Am. Chem. Soc.* **2008**, 130 (49), 16476-16477.
- (27) Whited, M. T. Synthetic and Mechanistic Studies of Small-Molecule Activation at Low-Valent Iron, Cobalt, and Iridium Centers. Dissertation (Ph.D.), California Institute of Technology, 2009.

- (28) Álvarez, E.; Paneque, M.; Petronilho, A. G.; Poveda, M. L.; Santos, L. L.; Carmona, E.; Mereiter, K., "Activation of Aliphatic Ethers by TpMe2Ir Compounds: Multiple C–H Bond Activation and C–C Bond Formation." *Organometallics* **2007**, *26* (5), 1231-1240.
- (29) Valpuesta, J. E. V.; Álvarez, E.; López-Serrano, J.; Maya, C.; Carmona, E., "Reversible Double C-H Bond Activation of Linear and Cyclic Ethers To Form Iridium Carbenes." *Chemistry – A European Journal* **2012**, *18* (41), 13149-13159.
- (30) Whited, M. T.; Grubbs, R. H., "Oxygen-Atom Transfer from Carbon Dioxide to a Fischer Carbene at (PNP)Ir." *J. Am. Chem. Soc.* **2008**, *130* (18), 5874-5875.
- (31) Chapp, S. M.; Schley, N. D., "Evidence for Reversible Cyclometalation in Alkane Dehydrogenation and C–O Bond Cleavage at Iridium Bis(phosphine) Complexes." *Organometallics* **2017**, *36* (22), 4355-4358.
- (32) Luecke, H. F.; Arndtsen, B. A.; Burger, P.; Bergman, R. G., "Synthesis of Fischer Carbene Complexes of Iridium by C-H Bond Activation of Methyl and Cyclic Ethers: Evidence for Reversible Alpha-Hydrogen Migration." *J. Am. Chem. Soc.* **1996**, *118* (10), 2517-2518.
- (33) Gunanathan, C.; Milstein, D., "Metal–Ligand Cooperation by Aromatization–Dearomatization: A New Paradigm in Bond Activation and "Green" Catalysis." *Acc. Chem. Res.* **2011**, *44* (8), 588-602.
- (34) Schwartsburd, L.; Iron, M. A.; Konstantinovski, L.; Diskin-Posner, Y.; Leitun, G.; Shimon, L. J. W.; Milstein, D., "Synthesis and Reactivity of an Iridium(I) Acetyl PNP Complex. Experimental and Computational Study of Metal–Ligand Cooperation in H–H and C–H Bond Activation via Reversible Ligand Dearomatization." *Organometallics* **2010**, *29* (17), 3817-3827.
- (35) Ben-Ari, E.; Leitun, G.; Shimon, L. J. W.; Milstein, D., "Metal–Ligand Cooperation in C–H and H₂ Activation by an Electron-Rich PNP Ir(I) System: Facile Ligand Dearomatization–Aromatization as Key Steps." *J. Am. Chem. Soc.* **2006**, *128* (48), 15390-15391.
- (36) Crabtree, R. H., "The organometallic chemistry of alkanes." *Chem. Rev.* **1985**, *85* (4), 245-269.
- (37) Ben-Ari, E.; Cohen, R.; Gandelman, M.; Shimon, L. J. W.; Martin, J. M. L.; Milstein, D., "ortho C–H Activation of Haloarenes and Anisole by an Electron-Rich Iridium(I) Complex: Mechanism and Origin of Regio- and Chemoselectivity. An Experimental and Theoretical Study." *Organometallics* **2006**, *25* (13), 3190-3210.
- (38) Harrold, N. D.; Waterman, R.; Hillhouse, G. L.; Cundari, T. R., "Group-Transfer Reactions of Nickel–Carbene and –Nitrene Complexes with Organoazides and Nitrous Oxide that Form New C=N, C=O, and N=N Bonds." *J. Am. Chem. Soc.* **2009**, *131* (36), 12872-12873.

- (39) Gallop, M. A.; Roper, W. R., "Carbene and Carbyne Complexes of Ruthenium, Osmium, and Iridium." In *Adv. Organomet. Chem.*, Stone, F. G. A.; West, R., Eds. Academic Press: 1986; Vol. 25, pp 121-198.
- (40) Hoffbauer, M. R.; Comanescu, C. C.; Iluc, V. M., "Reactivity of a Pd(II) carbene towards 2,6-dimesitylphenyldiazomethane and 2,6-dimesitylphenylazide." *Polyhedron* **2019**, *158*, 352-356.
- (41) Grotjahn, D. B.; Bikzhanova, G. A.; Collins, L. S. B.; Concolino, T.; Lam, K.-C.; Rheingold, A. L., "Controlled, Reversible Conversion of a Ketene Ligand to Carbene and CO Ligands on a Single Metal Center." *J. Am. Chem. Soc.* **2000**, *122* (21), 5222-5223.
- (42) Urtel, H.; Bikzhanova, G. A.; Grotjahn, D. B.; Hofmann, P., "Reversible Carbon–Carbon Double Bond Cleavage of a Ketene Ligand at a Single Iridium(I) Center: A Theoretical Study." *Organometallics* **2001**, *20* (18), 3938-3949.
- (43) Goll, J. M.; Fillion, E., "Tuning the Reactivity of Palladium Carbenes Derived from Diphenylketene." *Organometallics* **2008**, *27* (14), 3622-3625.
- (44) Staudaher, N. D.; Arif, A. M.; Louie, J., "Synergy between Experimental and Computational Chemistry Reveals the Mechanism of Decomposition of Nickel–Ketene Complexes." *J. Am. Chem. Soc.* **2016**, *138* (42), 14083-14091.
- (45) Al, N.; Stolley, R. M.; Staudaher, N. D.; Vanderlinden, R. T.; Louie, J., "Electronic Effect of Ligands on the Stability of Nickel–Ketene Complexes." *Organometallics* **2018**, *37* (21), 3750-3755.
- (46) The Rh analogue of **9** has been reported, see: Parker, G. L.; Lau, S.; Leforestier, B.; Chaplin, A. B., "Probing the Donor Properties of Pincer Ligands Using Rhodium Carbonyl Fragments: An Experimental and Computational Case Study." *Eur. J. Inorg. Chem.* **2019**, (33), 3791-3798.
- (47) Houk, K. N.; Strozier, R. W.; Hall, J. A., "Heterocumulene molecular orbitals: Ketenes, isocyanates, sulfenes, and sulfonylanines." *Tetrahedron Lett.* **1974**, *15* (11), 897-900.
- (48) Hyatt, J. A.; Reynolds, P. W., "Ketene Cycloadditions." *Organic Reactions* **2004**, 159-646.
- (49) Fermin, M. C.; Bruno, J. W., "Oxygen atom transfer with niobocene ketenes; Baeyer-Villiger chemistry with unusual Regioselectivities." *Tetrahedron Lett.* **1993**, *34* (47), 7545-7548.
- (50) Fermin, M. C.; Hneihen, A. S.; Maas, J. J.; Bruno, J. W., "Activation of niobocene-ketene complexes: ligand-centered syntheses of hydrides and acyls." *Organometallics* **1993**, *12* (5), 1845-1856.

- (51) Grotjahn, D. B.; Collins, L. S. B.; Wolpert, M.; Bikzhanova, G. A.; Lo, H. C.; Combs, D.; Hubbard, J. L., "First Direct Structural Comparison of Complexes of the Same Metal Fragment to Ketenes in Both C,C- and C,O-Bonding Modes." *J. Am. Chem. Soc.* **2001**, *123* (34), 8260-8270.
- (52) Löwe, C.; Huttner, G.; Zsolnai, L.; Berke, H., Acetalisierte Formylmangan-Komplexe / Acetals of Formyl Manganese Complexes. In *Zeitschrift für Naturforschung B*, 1988; Vol. 43, p 25.
- (53) Hattori, T.; Matsukawa, S.; Kuwata, S.; Ishii, Y.; Hidai, M., "Mono(sulfido)-bridged mixed-valence nitrosyl complex: protonation and oxidative addition of iodine across the Ir(II)–Ir(0) bond." *Chem. Commun.* **2003**, (4), 510-511.
- (54) Matsukawa, S.; Kuwata, S.; Hidai, M., "Reactions of iridium and ruthenium arenethiolato complexes with propylene sulfide. X-ray structures of 1-arythio-2-propanethiolato-S,S' iridium and ruthenium complexes." *Inorg. Chem. Commun.* **1998**, *1* (10), 368-371.
- (55) Hodgson, D. J.; Ibers, J. A., "Crystal and molecular structure of iodocarbonylnitrosylbis(triphenylphosphine)iridium(I) tetrafluoroborate-benzene, [IrI(CO)(NO)(P(C₆H₅)₃)₂][BF₄].C₆H₆." *Inorg. Chem.* **1969**, *8* (6), 1282-1287.
- (56) Matsukawa, S.; Kuwata, S.; Hidai, M., "Syntheses, Structures, and Reactivities of Mono- and Dinuclear Iridium Thiolato Complexes Containing Nitrosyl Ligands." *Inorg. Chem.* **2000**, *39* (4), 791-798.
- (57) Hodgson, D. J.; Ibers, J. A., "Crystal and molecular structure of chlorocarbonylnitrosylbis(triphenylphosphine)iridium(II) tetrafluoroborate, [IrCl(CO)(NO)(P(C₆H₅)₃)₂][BF₄]." *Inorg. Chem.* **1968**, *7* (11), 2345-2352.
- (58) Schoonover, M. W.; Baker, E. C.; Eisenberg, R., "Ligand dynamics of nitrosyl(η^3 -allyl)bis(triphenylphosphine)iridium(1+). A facile linear-bent nitrosyl equilibrium." *J. Am. Chem. Soc.* **1979**, *101* (7), 1880-1882.
- (59) Zumeta, I.; Mendicutie-Fierro, C.; Rodríguez-Diéguez, A.; Seco, J. M.; Garralda, M. A., "On the Reactivity of Dihydridoirida- β -diketones with 2-Aminopyridines. Formation of Acylhydrido Complexes with New PCN Terdentate Ligands." *Organometallics* **2015**, *34* (1), 348-354.
- (60) Walsh, J. L.; Bullock, R. M.; Meyer, T. J. Alkyl nitrite complexes of ruthenium prepared by acid-base chemistry at the bound nitrosyl group. *Inorg. Chem.* 1980, *19* (4), 865–869.
- (61) Reed, C. A.; Roper, W. R. Alkoxide-ion attack at the nitrosyl group of [IrCl₃(NO)(PPh₃)₂]⁺ to give alkyl nitrite complexes of iridium(III). *J. Chem. Soc., Dalton Trans.* 1972, No. 12, 1243–1246.

- (62) Andrews, M. A.; Chang, T. C. T.; Cheng, C. W. F.; Emge, T. J.; Kelly, K. P.; Koetzle, T. F. Synthesis, characterization, and equilibria of palladium(II) nitrile, alkene, and heterometallacyclopentane complexes involved in metal nitro catalyzed alkene oxidation reactions. *J. Am. Chem. Soc.* 1984, 106 (20), 5913–5920.
- (63) Neumann, J.; Elangovan, S.; Spannenberg, A.; Junge, K.; Beller, M., "Improved and General Manganese-Catalyzed N-Methylation of Aromatic Amines Using Methanol." *Chemistry – A European Journal* **2017**, 23 (23), 5410-5413.
- (64) Reger, D. L.; Little, C. A.; Lamba, J. J. S.; Brown, K. J., "Sodium Tetrakis(3,5-bis(trifluoromethyl)phenyl)borate, Na[B(3,5-(CF₃)₂C₆H₃)₄]." *Inorg. Synth.* **2004**, 34, 5-8.
- (65) Del Castillo, T. J.; Thompson, N. B.; Peters, J. C., "A Synthetic Single-Site Fe Nitrogenase: High Turnover, Freeze-Quench 57Fe Mössbauer Data, and a Hydride Resting State." *J. Am. Chem. Soc.* **2016**, 138 (16), 5341-5350.
- (66) Crisenza, G. E. M.; McCreanor, N. G.; Bower, J. F., "Branch-Selective, Iridium-Catalyzed Hydroarylation of Monosubstituted Alkenes via a Cooperative Destabilization Strategy." *J. Am. Chem. Soc.* **2014**, 136 (29), 10258-10261.
- (67) Hodous, B. L.; Fu, G. C., "Enantioselective Addition of Amines to Ketenes Catalyzed by a Planar-Chiral Derivative of PPY: Possible Intervention of Chiral Brønsted-Acid Catalysis." *J. Am. Chem. Soc.* **2002**, 124 (34), 10006-10007.
- (68) Baigrie, L. M.; Seiklay, H. R.; Tidwell, T. T., "Stereospecific formation of enolates from reaction of unsymmetrical ketenes and organolithium reagents." *J. Am. Chem. Soc.* **1985**, 107 (19), 5391-5396.
- (69) Ochiai, M.; Yoshimura, A.; Miyamoto, K.; Hayashi, S.; Nakanishi, W., "Hypervalent λ^3 -Bromane Strategy for Baeyer–Villiger Oxidation: Selective Transformation of Primary Aliphatic and Aromatic Aldehydes to Formates, Which is Missing in the Classical Baeyer–Villiger Oxidation." *J. Am. Chem. Soc.* **2010**, 132 (27), 9236-9239.
- (70) Dolomanov, O. V.; Bourhis, L. J.; Gildea, R. J.; Howard, J. A. K.; Puschmann, H., "OLEX2: a complete structure solution, refinement and analysis program." *J. Appl. Crystallogr.* **2009**, 42 (2), 339-341.
- (71) Sheldrick, G., "A short history of SHELX." *Acta Crystallographica Section A* **2008**, 64 (1), 112-122.

Chapter IV

REVERSIBLE C(*sp*³)-Si OXIDATIVE ADDITION OF UNSUPPORTED ORGANOSILANES: EFFECTS OF SILICON SUBSTITUENTS ON KINETICS AND THERMODYNAMICS

Adapted in part from manuscript submitted: Scott M. Chapp and Nathan D. Schley.

4.1 Introduction

Organosilanes are an important and versatile class of compounds which have found diverse applications in materials, fine chemicals, and as building blocks for the synthesis of complex molecules. For instance, alkoxy silanes are prepared and used on industrial scales including in residential plumbing systems where vinylalkoxy silanes are employed in the synthesis of cross-linked polyethylene (PEX) tubing.^{1,2} A variety of organosilane derivatives have found applications as partners in cross-coupling chemistry, with organosilanes bearing electron withdrawing groups (alkoxy, siloxy, fluoro) being favored in Hiyama-type reactions.^{3,4}

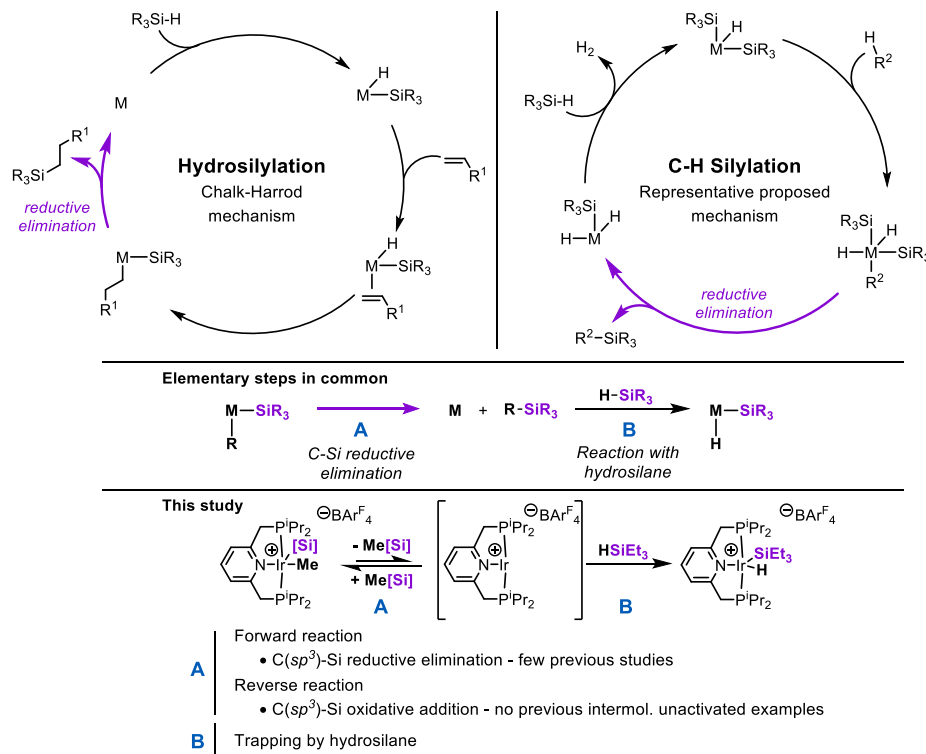


Figure 4.1.1. Proposed mechanisms for olefin hydrosilylation and C-H silylation and relationship to this study.

Although organosilanes can be prepared in stoichiometric fashion from alkyl, aryl, or vinyl halides, their preparation by catalytic methods including olefin hydrosilylation or direct C-H silylation offers the opportunity to avoid the formation of stoichiometric byproducts. Of these two catalytic approaches, olefin hydrosilylation represents the more mature process, with established catalytic systems having been demonstrated for many transition metals.⁵ For instance, Pt and Ir hydrosilylation catalysts are typically highly active and thought to operate through the Chalk-Harrod mechanism (**Figure 4.1.1, top left**) with C-Si bond-formation occurring through a concerted reductive elimination.⁵⁻⁶ Conversely, direct C-H silylation is a challenging process which has been largely limited to a few catalyst systems.⁷ In one example, the Hartwig group proposed that phenanthroline-supported iridium complexes catalyze the C-H silylation of arenes through an Ir(III)/(V) cycle (**Figure 4.1.1, top right**).⁸ $\text{HSi}(\text{OSiMe}_3)_2(\text{CH}_3)$ serves as the silylating reagent with C-Si bond-formation presumably occurring from an iridium(V)disilyldihydrido σ -aryl. In the case of electron deficient arenes, C-Si reductive elimination appears to represent the rate determining step.⁸ Other notable examples of sp^2 C-H silylation include diimine/Ir catalysts examined by Miyaura⁹, a Rh-catalyzed process developed by Hartwig¹⁰, as well as a recent pincer-supported iridium system reported by Esteruelas.¹¹

Although olefin hydrosilylation and alkane/arene C-H silylation are distinct processes, both feature a C-Si reductive elimination step prior to product formation. Despite the importance of this transformation, few reports have examined C-Si reductive elimination in detail. The Ozawa group showed that C-Si reductive elimination occurs from (alkyl)Pt(II) silyl complexes in the presence of π -acidic ligands including olefins and acetylenes, with the rate of reductive elimination showing first order dependence on the alkyne.¹² Further studies examined the effect of the Pt-R (R=Me, Et, Pr, Bu, Ph) on the rate of C-Si reductive elimination and showed Me-Si reductive elimination to be the fastest.¹³ By comparison, to our knowledge only a single example of an isolable Ir silyl complex bearing an unsupported Ir-C bond has been reported. The Tilley group demonstrated that this complex undergoes reductive elimination after rate-limiting phosphine dissociation, precluding an in-depth analysis of other factors that control the rate of C-Si reductive elimination in cases where ligand dissociation is not rate determining.¹⁴

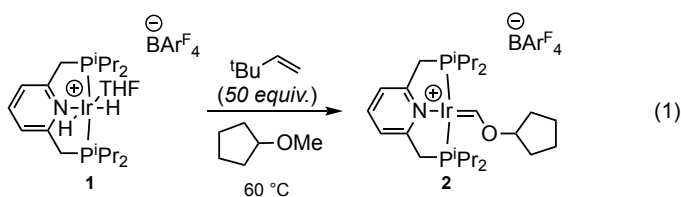


Figure 4.1.2. Dehydrogenation of complex **1** with TBE in CPME to form complex **2**.

Recently our group has been studying the conversion of ethers to alkoxy-carbenes via the α,α -dehydrogenation at cationic iridium complexes.¹⁵⁻¹⁶ We reported the synthesis of a cationic PNP pincer-supported Ir(I) alkoxy-carbene complex **2** derived from cyclopentyl methyl ether (**Figure 4.1.2, eq 1**) and demonstrated its reactivity in atom- and group-transfer reactions.¹⁷

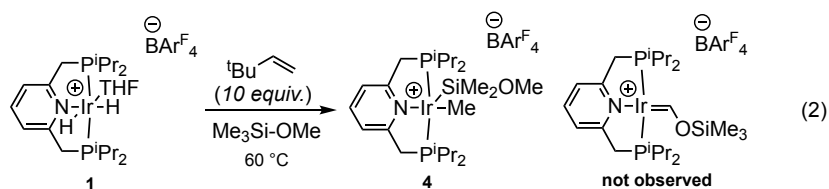


Figure 4.1.3. Dehydrogenation of complex **1** with TBE in methoxytrimethylsilane to form complex **4**.

During the course of our studies, we found that methoxytrimethylsilane does not undergo α,α -dehydrogenation to form a siloxymethylidene, but instead reacts via Si-CH₃ oxidative addition to give the (methyl)Ir(III)silyl complex **4** (**Figure 4.1.3, eq 2**). This outcome is unexpected given the paucity of examples of direct C(*sp*³)-Si oxidative addition. To our knowledge, no examples of an analogous oxidative addition to give an isolable, unsupported alkyl of a metal silyl have been reported except in cases involving strained silicon-containing rings,¹⁸ though this reaction has been explored computationally.¹⁹⁻²¹ The product metal alkyl silyl would be a plausible intermediate in the catalytic *sp*³ C-H silylation of unactivated alkanes, but there are no reports of undirected, intermolecular catalytic *sp*³ C-H silylation^{7,22} except for one that operates through a σ -bond metathesis mechanism.²³ Thus this seemingly simple oxidative addition is apparently exceptionally uncommon.

Furthermore, we have found that this transformation is remarkably general and we now report a kinetic and thermodynamic analysis of a systematic series of organoiridium silyls formed by C(*sp*³)-Si oxidative addition. Kinetic analyses show that C(*sp*³)-Si activation is a facile and reversible process and supplemental studies using DFT suggest a difference in driving force of over 12 kcal/mol across the series of complexes.

4.2 Results and Discussion

Dehydrogenation of complex **1** with excess *tert*-butylethylene (TBE, 10 equiv.) in neat methoxytrimethylsilane yields complex **4**, which gives a ³¹P{¹H} NMR signal at 32.6 ppm and an upfield triplet ¹³C{¹H} resonance at -20.8 ppm corresponding to

Ir-CH₃. Complex **4** was characterized by X-ray diffraction, (Figure 2) confirming its structure as an unprecedented example of a 5-coordinate metal silyl methyl complex resulting from intermolecular C(sp³)-Si activation. Analogous reactivity was found for a large family of methyl organosilanes including tetramethylsilane, dimethoxydimethylsilane, trimethoxymethylsilane, ethoxytrimethylsilane, trifluoromethyltrimethylsilane, hexamethyldisiloxane and octamethyltrisiloxane. In all cases, intermolecular C(sp³)-Si activation was observed, giving complexes **3-10** (Figure 4.2.1, eq 3). These complexes were characterized in solution by ¹H, ¹³C{¹H} and ³¹P{¹H} NMR and in the solid state by single-crystal X-ray diffraction (Figure 4.2.2). Thus we have been able to achieve intermolecular C(sp³)-Si oxidative addition in tetraorganosilanes, as well as mono-, di- and trialkoxysilanes and two siloxysilanes (Table 4.2.1).

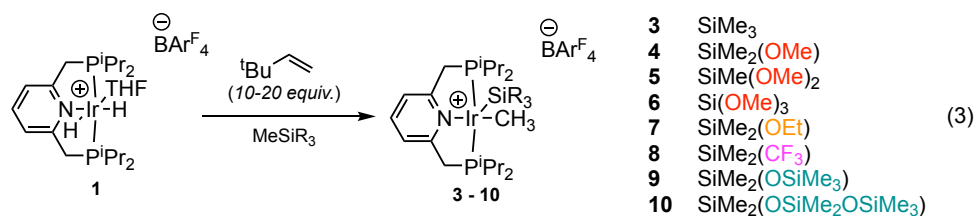


Figure 4.2.1. Dehydrogenation of complex **1** with TBE in various organosilanes to yield complexes **3-10**.

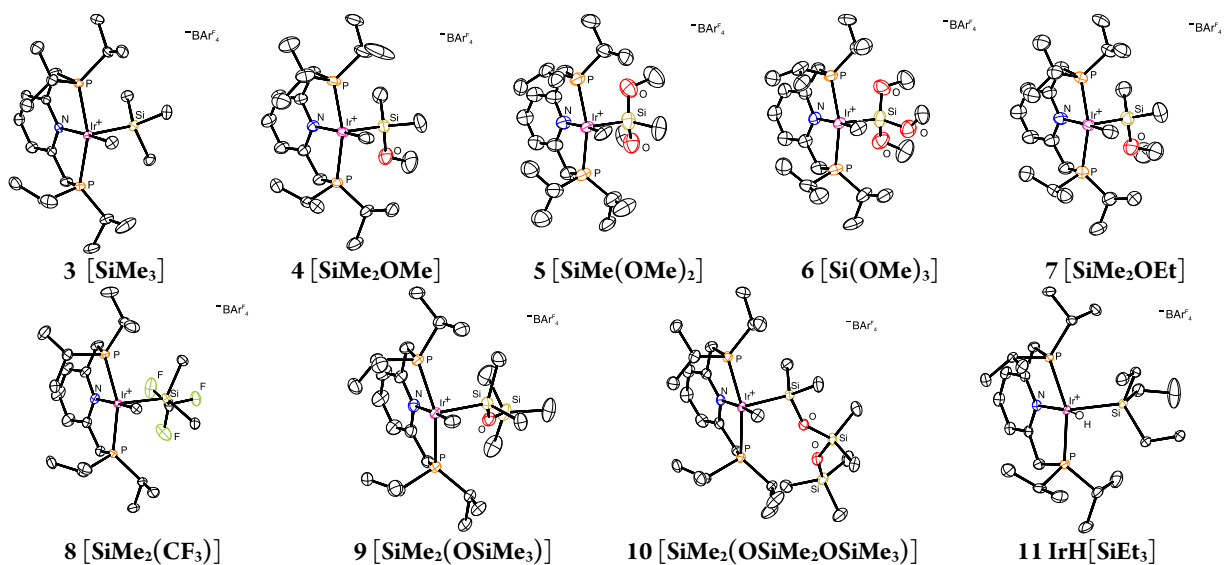


Figure 4.2.2. ORTEP diagrams of Complexes **3-11** shown at 50% probability. Full disorder models and anions are omitted for clarity.

When octamethyltrisiloxane is used, complex **10** is obtained as the major product, however this silane differs from the other members of the family (**3-9**) by virtue of having both internal and terminal methylsilane groups. Although the product

of terminal activation is obtained as the major product (**10**), a minor component can be separated in impure form by crystallization. This minor component is the product of C(*sp*³)-Si activation of an internal methyl group, which would give a silyl complex analogous to that derived from HSi(OSiMe₃)₂(CH₃), the most-common silane reagent employed in C-H silylation catalysis.^{8, 10, 24-31} Unfortunately, unambiguous characterization of this minor isomer has not been successful.

Table 4.2.1. Experimental and Computed Metrics of Ir Complexes

Complex	Si-Ir-C (DFT) ^a	Si-Ir-C (XRD)	Ir-Si (XRD)	³¹ P{ ¹ H} (ppm) ^b	¹³ C{ ¹ H} (ppm) ^b
3	94.9	93.1(1)	2.334(1)	28.8	-21.3
4	96.8	98.2(1)	2.298(1)	32.6	-20.8
5^c	96.9	97.8(3)	2.235(4)	35.1	-20.8
6^c	100.6	94.5(2)	2.247(2)	35.2	-21.6
7^c	96.2	96.9(2)	2.273(2)	32.5	-20.6
8	84.1	84.1(1)	2.290(1)	28.1	-22.4
9	98.3	94.2(1)	2.312(1)	31.6	-20.7
10	96.6	95.1(1)	2.306(1)	31.9	-20.7

^a See § 4.4 Experimental. ^b NMR in CD₂Cl₂. ^c Extensive disorder in the X-ray structure may decrease the accuracy of the experimental structural metrics.

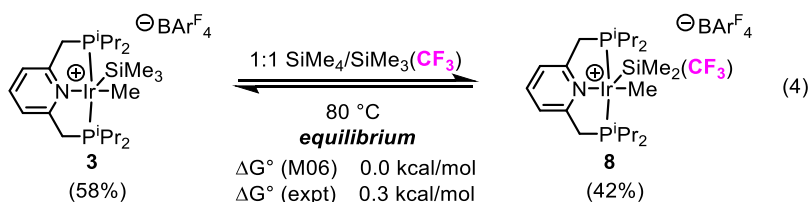
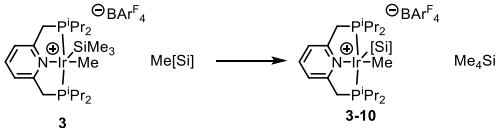


Figure 4.2.3. Equilibration of **3** and **8** in 1:1 equimolar SiMe₄:SiMe₃(CF₃)

Although complexes **3-10** are stable in solution at room temperature, we have found that C(*sp*³)-Si oxidative addition is completely reversible in certain cases. For instance, heating a solution of the tetramethylsilane-derived complex **3** in an equimolar mixture of tetramethylsilane and trifluoromethyltrimethylsilane gives an equilibrium between complexes **3** and **8**. At equilibrium, the observed **3**:**8** ratio is found to be 58:42, corresponding to a ΔG° of *ca.* 0.3 kcal·mol⁻¹. On the other hand, attempts to equilibrate the methoxytrimethylsilane-derived complex **4** with trifluoromethyltrimethylsilane failed to show any reactivity, which inspired us to analyze the relative stability of the silyl complexes by DFT. A summary of computed relative free energies (M06/def2svp/def2tzvp) is given in **Table 4.2.2** and reveals a profound impact of the silicon substituents on the stability of the

resulting silyl complexes. For instance, while the computed ΔG° for the **3**:**8** pair is 0.0 kcal·mol⁻¹ (in good agreement with the experimentally determined value of 0.3 kcal·mol⁻¹), **4** is downhill from both **3** and **8** by more than 6 kcal·mol⁻¹. This finding explains the lack of apparent reversibility of oxidative addition when **4** is heated in trifluoromethyltrimethylsilane solution, as this reaction would be substantially uphill. Indeed the reverse reaction between **8** and methoxytrimethylsilane proceeds to **4** as one would expect given the driving force.

Table 4.2.2. Predicted stability of (methyl)iridium silyl complexes.



Complex	[Si]	$\Delta G^\circ_{\text{calc}}$ (Kcal·mol ⁻¹) ^a
3	SiMe ₃	0
4	SiMe ₂ (OMe)	-6.3
5	SiMe(OMe) ₂	-7.2
6	Si(OMe) ₃	-11.3
7	SiMe ₂ (OEt)	-7.3
8	SiMe ₂ (CF ₃)	0.0
9	SiMe ₂ (OSiMe ₃)	-7.7
10	SiMe ₂ (OSiMe ₂ OSiMe ₃)	-12.3

^a See § 4.4 Experimental.

When considering the computed relative free energies of silyl exchange in complexes **3-10**, we find that formation of alkoxy- and siloxysilyl complexes is predicted to be the most downhill. These computations serve as a readout of the relative Si-CH₃/Ir-Si bond strengths,³² the latter of which is expected to be strongly influenced by the π -accepting ability of the silyl ligand. Previous DFT experiments on a series of Os(SiR₃) complexes showed that the Os-Si bond strength tracks with the π -accepting ability of the Si-X σ^* orbitals.³³ This analysis argues for the π -accepting ability of alkoxy- and siloxysilanes in **4-7**, **9**, and **10** and suggests that the trifluoromethyldimethylsilyl group in **8** is a poor π -acceptor. Formation of complex **10** is predicted to be furthest downhill from **3** or **8**, with a predicted ΔG° of -12.3 kcal·mol⁻¹ being slightly more negative than the value calculated for trimethoxysilyl complex **6** (Table 4.2.2).

Rates of reductive elimination and trapping. While the relative driving forces computed for C(sp³)-Si oxidative addition in **3-10** served to illuminate our experiments demonstrating the reversibility of C(sp³)-Si oxidative addition, our successful isolation of

these complexes provided a unique opportunity to experimentally examine the kinetics of the corresponding C(sp³)-Si reductive elimination process. A previous report has examined the kinetics of C-Si reductive elimination from *cis*-PtMe(SiPh₃)(PMePh₂)₂ in the presence of diphenylacetylene, though in that case the reaction rate was found to be inversely dependent on phosphine, implicating rate-limiting ligand dissociation.¹²⁻¹³ To our knowledge, no analogous study has been conducted for a family of silyl substituents despite the importance of C-Si reductive elimination in both olefin hydrosilylation and C-H silylation catalysis.

Table 4.2.3. Rates of reductive elimination and trapping by HSiEt₃.

Complex	[Si]	Rate: 65 °C	23 °C, (s ⁻¹)
3	SiMe ₃	-	1.90(2) * 10 ⁻⁴
4	SiMe ₂ (OMe)	1.01(9) * 10 ⁻⁴	-
5	SiMe(OMe) ₂	1.7(2) * 10 ⁻⁵	-
7	SiMe ₂ (OEt)	5.4(3) * 10 ⁻⁵	-
8	SiMe ₂ (CF ₃)	1.34(3) * 10 ⁻³	1.55(2) * 10 ⁻⁵
9	SiMe ₂ (OSiMe ₃)	9.7(3) * 10 ⁻⁴	-
10	SiMe ₂ (OSiMe ₂ OSiMe ₃)	1.40(2) * 10 ⁻⁴	-

Seven of the eight complexes (**3-5** and **7-10**) undergo C-Si reductive elimination on treatment with triethylsilane to give the free organosilane and a new iridium complex **11**. NMR analysis of **11** is consistent with a monohydride monosilyl complex, which we were able to confirm by single-crystal X-ray diffraction. With an excess of triethylsilane, all seven complexes undergo reductive elimination following pseudo first-order kinetics when conversion is monitored by ³¹P{¹H} NMR spectroscopy. The use of a hydrosilane as the trapping reagent is highly relevant to both olefin hydrosilylation and C-H silylation mechanisms, since in both cases reaction with a hydrosilane follows the C-Si reductive elimination step.

Our kinetic findings are summarized in **Table 4.2.3**. The alkoxy- and siloxysilyl complexes **4, 5, 7, 9** and **10** undergo reductive elimination over hours at 65 °C, while the triorganosilyl complexes **3** and **8** react rapidly even at 23 °C. The apparent order of reactivity follows SiMe₃ > SiMe₂(CF₃) > SiMe₂OSiMe₃ > SiMe₂OSiMe₂OSiMe₃ > SiMe₂(OMe) > SiMe₂(OEt) > SiMe(OMe)₂. Thus the triorganosilyl complexes undergo reductive elimination more rapidly than the siloxysilyl complexes, which are themselves significantly faster than the alkoxy- versus alkoxy- silyl complexes.

argues that the relative thermodynamic stabilities of the silyl methyl complexes (**Table 4.2.2**) is not the only determinant of the rate of C(*sp*³)-Si reductive elimination in this family of complexes. Instead, we hypothesize that the π -accepting ability of the silyl group contributes to the kinetics of reductive elimination, since the slowest rates are observed for the mono and dialkoxysilyl complexes **4** and **5**. Monomethoxysilyl complex **4** converts to **11** nearly an order of magnitude slower than monosiloxysilyl complex **9**, with the dialkoxysilyl **5** converting nearly two orders of magnitude slower. It may be the case that the success of siloxysilanes in arene C-H silylation stems from the increased stability of the iridium siloxysilyl intermediates relative to trialkylsilyl complexes, which does not appear to incur as significant a penalty to the rate of C(*sp*³)-Si reductive elimination as alkoxy-silyl derivatives.

The decreased rates of reductive elimination of organometal silyls bearing electron-withdrawing substituents contrasts with the behavior observed for Si-H oxidative addition at late transition metals. In many cases, hydrosilanes bearing electron-withdrawing groups are found to react *more* rapidly, with triorganohydrosilanes undergoing Si-H oxidative addition slowly or not at all,³⁴⁻³⁶ though at least one counter-example exists.³⁷ Both the increased rate of Si-H activation for electron-deficient silanes³⁵ and the increased stability of the resulting silyl complexes³⁸⁻⁴⁰ have been attributed to the formation of stronger M-Si bonds with such silanes. Several studies on rhodium complexes show reduced rates of olefin hydrosilylation using electron-deficient silanes, which has also been attributed to the increased stability of the metal silyl intermediates.⁴¹⁻⁴³ By the same reasoning, the more-stable iridium silyl complexes in our study show decreased rates of C(*sp*³)-Si reductive elimination, though the higher rate of reductive elimination of siloxysilyl complexes relative to alkoxy-silyl complexes is not reflected in the calculated metal silyl stabilities and likely stems from purely kinetic factors. This apparent distinction between the reactivity of methoxy and siloxysilyls is important since methoxy groups have been substituted for siloxy groups to simplify computations,⁸ but our experimental findings indicate that this may not be a benign substitution.

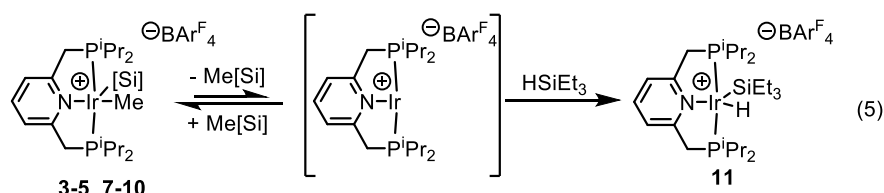


Figure 4.2.4. Proposed mechanism for C(*sp*³)-Si bond reductive elimination

Given our observation that C-Si reductive elimination can occur in the absence of triethylsilane, (**Figure 4.2.3, eq 4**) we propose that reductive elimination in the presence of triethylsilane occurs via the mechanism given in (**Figure 4.2.4, eq 5**) where

pre-equilibrium reductive elimination is followed by irreversible trapping by silane. An alternative mechanism involving triethylsilane-assisted C-Si reductive elimination (either through an Ir(V) complex or a σ -SiH complex) is difficult to rule out, but is not necessary given the evidence that reductive elimination can occur from the 5-coordinate iridium(III) complexes **3** and **8** in the absence of hydrosilane. A comparison of the rate of reductive elimination of **8** and **10** and trapping with HSiEt₃ and DSiEt₃ in separate experiments gives a small H/D isotope effect of 1.2 and 1.1 respectively, a value inconsistent with rate-limiting Si-H oxidative addition, thus the mechanism given in eqn. 5 seems most probable (Table 4.2.4). The overall reaction scheme involving pre-equilibrium reductive elimination followed by trapping is distinct from the C(*sp*³)-Si reductive elimination system studied by Ozawa, which proceeds via pre-equilibrium ligand exchange followed by irreversible reductive elimination.^{13,44}

Table 4.2.4. H/D isotope effect on the rate of reductive elimination and trapping by HSiEt₃.

Complex	Rate: HSiEt ₃	DSiEt ₃ , (s ⁻¹)	H/D
8	1.34(3) * 10 ⁻³	1.09(2) * 10 ⁻³	1.2
10	1.40(2) * 10 ⁻⁴	1.27(6) * 10 ⁻⁴	1.1

4.3 Conclusion

In summary, we report a cationic pincer-supported iridium system capable of intermolecular C(*sp*³)-Si oxidative addition. The generality of this manifold to activate C(*sp*³)-Si bonds is shown for a large family of alkyl, alkoxy, and siloxysilanes. A thermodynamic analysis of these complexes by DFT shows a strong correlation of stability with the presence of electron withdrawing groups on the silyl ligand, providing a quantitative description of trends dating to early studies on olefin hydrosilylation. The predicted stabilities correspond well with experimental rates observed for reversible C(*sp*³)-Si reductive elimination followed by trapping by silane, with an apparent order of reactivity following: SiMe₃ > SiMe₂(CF₃) > SiMe₂OSiMe₃ > SiMe₂OSiMe₂OSiMe₃ > SiMe₂(OMe) > SiMe₂(OEt) > SiMe(OMe)₂. The significantly higher rate of RE/trapping for the siloxysilyl complexes versus the alkoxy-silyl complexes does not correlate with the relative stability of the corresponding silyl complexes, hinting at an important kinetic distinction between these two classes of metal silyls. Given the importance of organometal silyl intermediates in catalytic C-

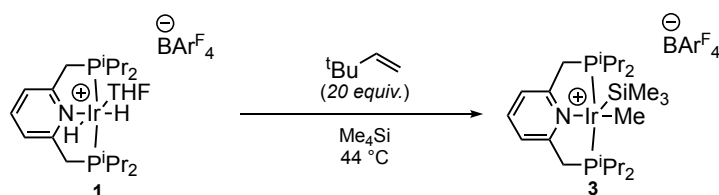
H silylation and olefin hydrosilylation, we believe that our structural, thermodynamic, and kinetic analyses on the diverse family of iridium silyl complexes **3-11** will provide a strong basis for silyl-substituent selection in future catalytic method development.

4.4 Experimental

General Considerations. All manipulations were carried out using standard vacuum, Schlenk, cannula, or glovebox techniques under N₂ unless otherwise specified. Tetrahydrofuran, dichloromethane, pentane, toluene and diethyl ether were degassed with argon and dried over activated alumina using a solvent purification system. Complex **1** was prepared according to a reported procedure.¹ Trimethylsilane was prepared from chlorotrimethylsilane according to a literature procedure.² Commercial silanes were degassed with nitrogen and stored over activated 4 Å molecular sieves for at least seven days prior to use. 3,3-dimethyl-1-butene (*tert*-butylethylene) sourced from a commercial supplier was found to be contaminated with Me₂S, which was removed by stirring over CuBr followed by distillation.

Spectroscopy. ¹H, ¹³C{¹H} and ³¹P{¹H} NMR spectra were recorded on Bruker NMR spectrometers at ambient temperature unless otherwise noted. ¹H and ¹³C{¹H} chemical shifts are referenced to residual solvent signals; ³¹P{¹H} chemical shifts are referenced to an external H₃PO₄ standard.

Elemental Analysis. Elemental analyses of complexes **3 – 11** are of the bulk samples for which yields are reported. No additional purification operations are carried out prior to packaging for analysis. Elemental analyses were performed at the University of Rochester CENTC Elemental Analysis Facility.



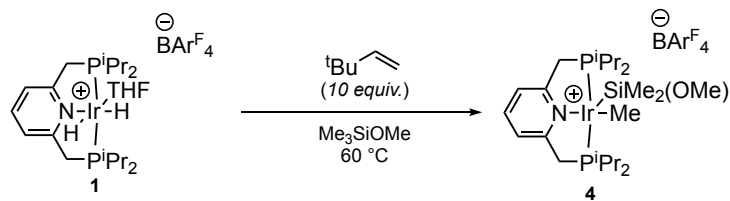
Preparation of [(PNP(ⁱPr)₄)IrMe(SiMe₃)]BAr^F₄ (3**).** A 20 mL scintillation vial was charged with **1** (0.1003 g, 0.068 mmol), tetramethylsilane (3 mL), a stir bar, and *tert*-butylethylene (176 μL, 1.4 mmol) and was sealed with a PTFE-lined septum cap. The suspension was heated at 44 °C for 80 hours. The mixture was then allowed to cool to room temperature, the solvent was decanted,

and the red precipitate was dried under vacuum. The resulting solid was then extracted with two, 1 mL portions of diethyl ether which were filtered through a 0.45 μm PTFE syringe filter. The resulting red solution was dried under vacuum to give a red solid. The red solid was then dissolved in 1.0 mL of diethyl ether which was carefully layered with 0.3 mL of pentane. Additional pentane was layered on top in four, 0.3 mL portions followed by two, 0.2 mL portions for a total of 1.9 mL of pentane. On standing, red crystals deposited from the red, viscous bottom layer. The red bottom layer was carefully removed using a pipette, followed by the pale orange top layer to yield red crystals alongside a red residue. The crystals were separated from the residue with a spatula and transferred to a 20 mL scintillation vial. The crystals were then ground with a spatula and dried under vacuum to give complex **3** as an orange solid. Yield: 0.0378 g (37%). Crystals of **3** suitable for X-ray diffraction were obtained by layering a saturated solution of diethyl ether with pentane at room temperature. Anal. Calcd. for $\text{C}_{55}\text{H}_{59}\text{B}_1\text{F}_{24}\text{Ir}_1\text{N}_1\text{P}_2\text{Si}_1$: C, 44.54; H, 4.01; N, 0.94. Found: C, 44.456; H, 3.847; N, 0.879.

^1H NMR (500 MHz, CD_2Cl_2): δ 0.16 (s, 9H, $\text{Si}(\text{CH}_3)_3$), 1.01 (apparent q, 6H, $\text{PCH}(\text{CH}_3)$, $J_{\text{H-H}} = 7.1$ Hz), 1.23 (apparent q, 6H, $\text{PCH}(\text{CH}_3)$, $J_{\text{H-H}} = 7.7$ Hz), 1.35 (apparent q, 6H, $\text{PCH}(\text{CH}_3)$, $J_{\text{H-H}} = 6.9$ Hz), 1.54 (apparent q, 6H, $\text{PCH}(\text{CH}_3)$, $J_{\text{H-H}} = 8.0$ Hz), 1.88 (t, 3H, Ir-CH_3 , $J_{\text{H-P}} = 5.5$ Hz), 2.61-2.68 (m, 4H, PCH), 3.39 (dot, 2H, PCH_2 , $^2J_{\text{H-H}} = 17.8$ Hz, $^2J_{\text{H-P}} = 4.0$ Hz), 3.89 (dot, 2H, PCH_2 , $^2J_{\text{H-H}} = 17.9$ Hz, $^2J_{\text{H-P}} = 4.1$ Hz), 7.50 (d, 2H, py-H3,5 , $^3J_{\text{H-H}} = 7.7$ Hz), 7.55 (br s, 4H, CH of BAr^{F}_4), 7.73 (br s, 8H, CH of BAr^{F}_4), 7.86 (t, 1H, py-H4 , $^3J_{\text{H-H}} = 7.7$ Hz)

$^{31}\text{P}\{^1\text{H}\}$ NMR (202 MHz, CD_2Cl_2): δ 28.78 (s)

$^{13}\text{C}\{^1\text{H}\}$ NMR (125 MHz, CD_2Cl_2): δ -21.32 (t, Ir-CH_3 , $^2J_{\text{C-P}} = 5.8$ Hz), 6.43 (s, $\text{Si}(\text{CH}_3)_3$), 18.47 (s, $\text{PCH}(\text{CH}_3)_2$), 19.31 (s, $\text{PCH}(\text{CH}_3)_2$), 20.48 (s, $\text{PCH}(\text{CH}_3)_2$), 20.61 (s, $\text{PCH}(\text{CH}_3)_2$), 25.40 (t, $\text{PCH}(\text{CH}_3)_2$, $^1J_{\text{C-P}} = 13.0$ Hz), 28.25 (t, $\text{PCH}(\text{CH}_3)_2$, $^1J_{\text{C-P}} = 13.8$ Hz), 42.66 (t, PCH_2 , $^1J_{\text{C-P}} = 13.8$ Hz), 117.88 (m, CH of BAr^{F}_4), 122.43 (apparent t, py-C3,5 , $^3J_{\text{C-P}} = 4.6$ Hz), 125.01 (q, CF_3 of BAr^{F}_4 , $^1J_{\text{C-F}} = 272.4$ Hz), 129.30 (q, C of BAr^{F}_4 , $^2J_{\text{C-F}} = 31.3$ Hz), 135.21 (s, CH of BAr^{F}_4), 138.38 (s, py-C4), 162.17 (q, B-C, $^1J_{\text{C-B}} = 49.9$ Hz), 162.76 (s, py-C2,6 and B-C)

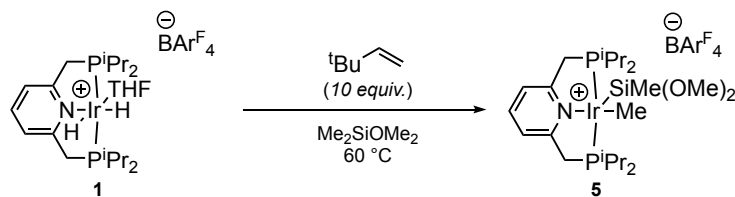


Preparation of [(PNP(^{*t*}Pr)₄)IrMe(SiMe₂(OMe))]BAr^F₄ (4**).** A 20 mL scintillation vial was charged with **1** (0.1004 g, 0.068 mmol), methoxytrimethylsilane (2 mL) and *tert*-butylethylene (88 μL, 0.68 mmol) and was sealed with a PTFE-lined septum cap. The solution was heated at 60 °C for 1 hr. The reaction was then allowed to cool to room temperature and the solvent was removed under vacuum to give a yellow residue. The residue was washed with three, 5 mL portions of pentane and dried under vacuum. The residue was then dissolved in 2 mL diethyl ether and carefully layered with 3 mL of pentane. Crystals deposited on standing for a few hours, which were separated from the supernatant by decanting the oily solution with a pipette. The crystals were then washed with three, 5 mL portions of pentane and dried under vacuum. The crystals were then ground with a spatula and dried under vacuum to give complex **4** as a yellow solid. Yield: 0.0555 g (54%). Crystals of **4** suitable for X-ray diffraction were obtained by layering a saturated solution of diethyl ether with pentane at room temperature. Anal. Calcd. For C₅₅H₅₉B₁F₂₄Ir₁N₁O₁P₂Si₁: C, 44.07; H, 3.97; N, 0.93. Found: C, 44.079; H, 3.704; N, 0.830.

¹H NMR (500 MHz, CD₂Cl₂): δ 0.19 (s, 6H, Si(CH₃)₂), 0.99 (apparent q, 6H, PCH(CH₃), J_{H-H} = 7.1 Hz), 1.19 (apparent q, 6H, PCH(CH₃), J_{H-H} = 7.7 Hz), 1.34 (apparent q, 6H, PCH(CH₃), J_{H-H} = 7.1 Hz), 1.51 (apparent q, 6H, PCH(CH₃), J_{H-H} = 8.1 Hz), 1.79 (t, 3H, Ir-CH₃, J_{H-P} = 5.5 Hz), 2.65-2.77 (m, 4H, PCH), 3.28 (s, Si(OCH₃)), 3.58 (dot, 2H, PCH₂, ²J_{H-H} = 17.6 Hz, ²J_{H-P} = 4.9 Hz), 3.83 (dot, 2H, PCH₂, ²J_{H-H} = 17.7 Hz, ²J_{H-P} = 4.0 Hz), 7.47 (d, 2H, py-H3,5, ³J_{H-H} = 7.8 Hz), 7.55 (br s, 4H, CH of BAr^F₄), 7.71 (br s, 8H, CH of BAr^F₄), 7.84 (t, 1H, py-H4, ³J_{H-H} = 7.8 Hz)

³¹P{¹H} NMR (202 MHz, CD₂Cl₂): δ 32.62 (s)

¹³C{¹H} NMR (125 MHz, CD₂Cl₂): δ -20.77 (t, Ir-CH₃, ²J_{C-P} = 5.8 Hz), 3.27 (s, Si(CH₃)₂), 18.51 (s, PCH(CH₃)₂), 19.30 (s, PCH(CH₃)₂), 20.07 (s, PCH(CH₃)₂), 20.34 (s, PCH(CH₃)₂), 25.98 (t, PCH(CH₃)₂, ¹J_{C-P} = 12.7 Hz), 28.27 (t, PCH(CH₃)₂, ¹J_{C-P} = 14.5 Hz), 42.46 (t, PCH₂, ¹J_{C-P} = 14.0 Hz), 50.58 (s, Si(OCH₃)), 117.88 (apparent t, CH of BAr^F₄, ³J_{C-F} = 3.7 Hz), 122.14 (apparent t, py-C3,5, ³J_{C-P} = 4.7 Hz), 125.01 (q, CF₃ of BAr^F₄, ¹J_{C-F} = 271.7 Hz), 129.30 (q, C of BAr^F₄, ²J_{C-F} = 31.5 Hz), 135.21 (s, CH of BAr^F₄), 138.33 (s, py-C4), 162.17 (q, B-C, ¹J_{C-B} = 49.8 Hz), 163.55 (apparent t, py-C2,6, J_{C-P} = 3.6 Hz)



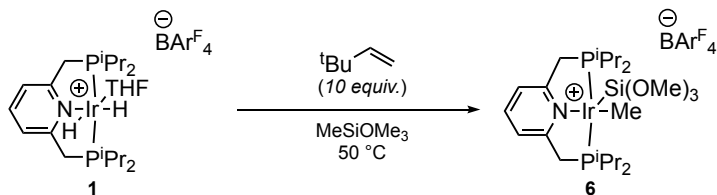
Preparation of [(PNP(^tPr)₄)IrMe(SiMe(OMe)₂)]BAr^F₄ (5**).** A 20 mL scintillation vial was charged with **1** (0.0999 g, 0.068 mmol), dimethoxydimethylsilane (1 mL), and *tert*-butylethylene (88 μ L, 0.68 mmol) and was sealed with a PTFE-lined septum cap. The solution was heated at 30 °C for 30 min followed by 60 °C for 60 min. The reaction was then allowed to cool to room temperature and 3 mL of pentane was added to give a precipitate. The supernatant was then removed using a pipette. The resulting green/brown solid was washed with three, 1 mL portions of pentane. The solid was then dissolved in 2.0 mL of diethyl ether and carefully layered with 0.90 mL of pentane. Yellow crystals began to form on standing. The solution was then layered with an additional 0.90 mL pentane in three, 0.30 mL portions for a total of 1.80 mL of pentane, leading to the precipitation of additional yellow crystals. The dark green supernatant was removed using a pipette and the resulting yellow crystals were washed with three, 1 mL portions of pentane and dried under vacuum. The crystals were then ground with a spatula and dried under vacuum to give complex **5** as a yellow solid. Yield: 0.0205 g (20%). Crystals of **5** suitable for X-ray diffraction were obtained by layering a saturated solution of ether with pentane at room temperature. Anal. Calcd. For C₅₃H₅₉B₁F₂₄Ir₁N₁O₂P₂Si₁: C, 43.60; H, 3.93; N, 0.92. Found: C, 43.590; H, 3.735; N, 0.809.

¹H NMR (500 MHz, CD₂Cl₂): δ 0.50 (s, 3H, Si(CH₃)), 0.98 (apparent q, 6H, PCH(CH₃), J_{H-H} = 7.3 Hz), 1.18 (apparent q, 6H, PCH(CH₃), J_{H-H} = 7.6 Hz), 1.34 (apparent q, 6H, PCH(CH₃), J_{H-H} = 7.3 Hz), 1.50 (apparent q, 6H, PCH(CH₃), J_{H-H} = 8.0 Hz), 1.69 (t, 3H, Ir-CH₃, J_{H-P} = 5.6 Hz), 2.72-2.79 (m, 4H, PCH), 3.22 (s, 6H, Si(OCH₃)₂), 3.71 (dot, 2H, PCH₂, ²J_{H-H} = 17.3 Hz, ²J_{H-P} = 5.7 Hz), 3.80 (dot, 2H, PCH₂, ²J_{H-H} = 17.3 Hz, ²J_{H-P} = 4.0 Hz), 7.45 (d, 2H, py-H3,5, ³J_{H-H} = 7.8 Hz), 7.55 (br s, 4H, CH of BAr^F₄), 7.71 (br s, 8H, CH of BAr^F₄), 7.82 (t, 1H, py-H4, ³J_{H-H} = 7.8 Hz)

³¹P{¹H} NMR (202 MHz, CD₂Cl₂): δ 35.10 (s)

¹³C{¹H} NMR (125 MHz, CD₂Cl₂): δ -20.80 (t, Ir-CH₃, ²J_{C-P} = 6.0 Hz), 1.13 (s, Si(CH₃)), 18.36 (s, PCH(CH₃)₂), 19.25 (s, PCH(CH₃)₂), 19.81 (s, PCH(CH₃)₂), 20.38 (s, PCH(CH₃)₂), 26.32 (t, PCH(CH₃)₂, ¹J_{C-P} = 12.9 Hz), 27.90 (t, PCH(CH₃)₂, ¹J_{C-P} = 15.3 Hz), 42.49 (t, PCH₂, ¹J_{C-P} = 14.5 Hz), 50.81 (s, Si(OCH₃)₂), 117.88 (m, CH of BAr^F₄), 121.73 (apparent t, py-C3,5, ³J_{C-P} = 4.6

Hz), 125.01 (q, CF_3 of $BARF_4$, $^1J_{C-F} = 271.4$ Hz), 129.30 (q, C of $BARF_4$, $^2J_{C-F} = 31.7$ Hz), 135.21 (s, CH of $BARF_4$), 138.38 (s, py-C4), 162.17 (q, B-C, $^1J_{C-B} = 49.8$ Hz), 164.32 (br s, py-C2,6)



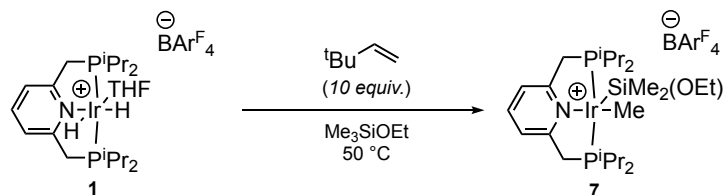
Preparation of $[(PNP(^iPr)_4)IrMe(Si(OMe)_3)]BARF_4$ (6**).** A 20 mL scintillation vial was charged with **1** (0.0997 g, 0.068 mmol), trimethoxymethylsilane (1 mL), and *tert*-butylethylene (88 μ L, 0.68 mmol) and was sealed with a PTFE-lined septum cap. The solution was heated at 50 °C for 120 min. The reaction was then allowed to cool to room temperature and was carefully layered with 2 mL pentane. Crystals deposited on standing which were separated by decanting the supernatant using a pipette. The crystals were washed with three, 1 mL portions of pentane, then were dissolved in 1 mL diethyl ether. The ether solution was carefully layered with 0.40 mL pentane in two, 0.20 mL portions. On standing yellow crystals deposited which were separated by decanting the supernatant using a pipette. The crystals were washed with three, 1 mL portions of pentane and were dried under vacuum. The crystals were then ground with a spatula and dried under vacuum to give complex **6** as a yellow solid. Yield: 0.0169 g (16%). Single crystals of **6** were obtained by layering a saturated solution of ether with pentane at room temperature. Anal. Calcd. For $C_{55}H_{59}B_1F_{24}Ir_1N_1O_3P_2Si_1$: C, 43.15; H, 3.88; N, 0.91. Found: C, 43.163; H, 3.701; N, 0.871.

1H NMR (500 MHz, CD_2Cl_2): δ 0.98 (apparent q, 6H, $PCH(CH_3)$, $J_{H-H} = 7.3$ Hz), 1.18 (apparent q, 6H, $PCH(CH_3)$, $J_{H-H} = 7.5$ Hz), 1.33 (apparent q, 6H, $PCH(CH_3)$, $J_{H-H} = 7.2$ Hz), 1.52 (apparent q, 6H, $PCH(CH_3)$, $J_{H-H} = 8.1$ Hz), 1.86 (t, 3H, Ir- CH_3 , $J_{H-P} = 5.5$ Hz), 2.74-2.84 (m, 4H, PCH), 3.41 (s, 9H, $Si(OCH_3)_3$), 3.69 (dot, 2H, PCH_2 , $^2J_{H-H} = 17.3$ Hz, $^2J_{H-P} = 5.2$ Hz), 3.80 (dot, 2H, PCH_2 , $^2J_{H-H} = 17.3$ Hz, $^2J_{H-P} = 3.8$ Hz), 7.45 (d, 2H, py-H3,5, $^3J_{H-H} = 7.7$ Hz), 7.55 (br s, 4H, CH of $BARF_4$), 7.71 (br s, 8H, CH of $BARF_4$), 7.81 (t, 1H, py-H4, $^3J_{H-H} = 7.7$ Hz)

$^{31}P\{^1H\}$ NMR (202 MHz, CD_2Cl_2): δ 35.16 (s)

$^{13}C\{^1H\}$ NMR (125 MHz, CD_2Cl_2): δ -21.61 (Ir- CH_3 , $^2J_{C-P} = 6.0$ Hz), 18.22 (s, $PCH(CH_3)_2$), 19.10 (s, $PCH(CH_3)_2$), 19.69 (s, $PCH(CH_3)_2$), 20.42 (s, $PCH(CH_3)_2$), 26.40 (t, $PCH(CH_3)_2$, $^1J_{C-P} = 12.6$ Hz), 28.08 (t, $PCH(CH_3)_2$, $^1J_{C-P} = 15.2$ Hz), 42.68 (t, PCH_2 , $^1J_{C-P} = 14.6$ Hz), 51.50 (s, $Si(OCH_3)_3$), 117.88 (m, CH of $BARF_4$, $^3J_{C-F} = 3.7$ Hz), 121.74 (m, py-C3,5), 125.02 (q, CF_3 of $BARF_4$, $^1J_{C-F}$

= 272.5 Hz), 129.30 (q, C of BAr^{F_4} , $^2\text{J}_{\text{C-F}}$ 31.3 Hz), 135.21 (s, CH of BAr^{F_4}), 138.59 (s, py-C4), 162.18 (q, B-C, $^1\text{J}_{\text{C-B}}$ = 49.7 Hz), 164.27 (s, py-C2,6)

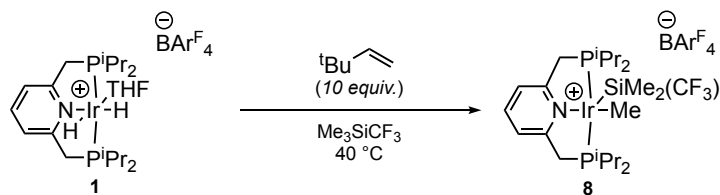


Preparation of $[(\text{PNP}(\text{tPr})_4)\text{IrMe}(\text{SiMe}_2(\text{OEt}))]\text{BAr}^{\text{F}_4}$ (7). A 20 mL scintillation vial was charged with **1** (0.0998 g, 0.068 mmol), ethoxytrimethylsilane (1 mL), and *tert*-butylethylene (88 μL , 0.68 mmol) and was sealed with a PTFE-lined septum cap. The solution was heated at 50 °C for 120 min with periodic agitation. The crude mixture was then allowed to cool to room temperature. The supernatant was decanted using a pipette to give an orange solid. The orange solid was then washed with three, 2 mL portions of pentane and dried under vacuum to give complex **7** as an orange solid. Yield: 0.0879 g (85%). Crystals of **7** suitable for X-ray diffraction were obtained by layering a saturated solution of ethoxytrimethylsilane with pentane at room temperature. Anal. Calcd. For $\text{C}_{56}\text{H}_{61}\text{B}_1\text{F}_{24}\text{IrN}_1\text{O}_1\text{P}_2\text{Si}_1$: C, 44.45; H, 4.06; N, 0.93. Found: C, 44.668; H, 3.795; N, 0.884.

^1H NMR (500 MHz, CD_2Cl_2): δ 0.19 (s, 6H, $\text{Si}(\text{CH}_3)_2$), 1.00 (apparent q, 6H, $\text{PCH}(\text{CH}_3)$, $\text{J}_{\text{H-H}} = 7.2$ Hz), 1.05 (t, 3H, OCH_2CH_3 , $^3\text{J}_{\text{H-H}} = 7.0$ Hz), 1.19 (apparent q, 6H, $\text{PCH}(\text{CH}_3)$, $\text{J}_{\text{H-H}} = 7.7$ Hz), 1.34 (apparent q, 6H, $\text{PCH}(\text{CH}_3)$, $\text{J}_{\text{H-H}} = 7.2$ Hz), 1.52 (apparent q, 6H, $\text{PCH}(\text{CH}_3)$, $\text{J}_{\text{H-H}} = 8.1$ Hz), 1.79 (t, 3H, Ir-CH_3 , $\text{J}_{\text{H-P}} = 5.5$ Hz), 2.66-2.70 (m, 2H, PCH), 2.80-2.86 (m, 2H, PCH), 3.47 (q, $\text{Si}(\text{OCH}_2\text{CH}_3)$, $^3\text{J}_{\text{H-H}} = 7.0$ Hz), 3.64 (dot, 2H, PCH_2 , $^2\text{J}_{\text{H-H}} = 17.6$ Hz, $^2\text{J}_{\text{H-P}} = 4.0$ Hz), 3.83 (dot, 2H, PCH_2 , $^2\text{J}_{\text{H-H}} = 17.7$ Hz, $^2\text{J}_{\text{H-P}} = 4.0$ Hz), 7.47 (d, 2H, py-H3,5, $^3\text{J}_{\text{H-H}} = 7.8$ Hz), 7.55 (br s, 4H, CH of BAr^{F_4}), 7.72 (br s, 8H, CH of BAr^{F_4}), 7.83 (t, 1H, py-H4, $^3\text{J}_{\text{H-H}} = 7.8$ Hz)

$^31\text{P}\{^1\text{H}\}$ NMR (202 MHz, CD_2Cl_2): δ 32.50 (s)

$^{13}\text{C}\{^1\text{H}\}$ NMR (125 MHz, CD_2Cl_2): δ -20.62 (Ir-CH_3 , $^2\text{J}_{\text{C-P}} = 6.0$ Hz), 3.95 (s, $\text{Si}(\text{CH}_3)_2$), 18.35 (s, OCH_2CH_3), 18.43 (s, $\text{PCH}(\text{CH}_3)_2$), 19.28 (s, $\text{PCH}(\text{CH}_3)_2$), 20.20 (s, $\text{PCH}(\text{CH}_3)_2$), 20.39 (s, $\text{PCH}(\text{CH}_3)_2$), 25.87 (t, $\text{PCH}(\text{CH}_3)_2$, $^1\text{J}_{\text{C-P}} = 12.7$ Hz), 28.13 (t, $\text{PCH}(\text{CH}_3)_2$, $^1\text{J}_{\text{C-P}} = 14.3$ Hz), 42.42 (t, PCH_2 , $^1\text{J}_{\text{C-P}} = 14.2$ Hz), 59.29 (s, $\text{Si}(\text{OCH}_2\text{CH}_3)$), 117.90 (m, CH of BAr^{F_4} , $^3\text{J}_{\text{C-F}} = 3.7$ Hz), 122.11 (apparent t, py-C3,5, $^3\text{J}_{\text{C-P}} = 4.8$ Hz), 125.03 (q, CF_3 of BAr^{F_4} , $^1\text{J}_{\text{C-F}} = 272.9$ Hz), 129.33 (q, C of BAr^{F_4} , $^2\text{J}_{\text{C-F}} = 32.0$ Hz), 135.23 (s, CH of BAr^{F_4}), 138.30 (s, py-C4), 162.20 (q, B-C, $^1\text{J}_{\text{C-B}} = 49.9$ Hz), 162.79 (s, py-C2,6)

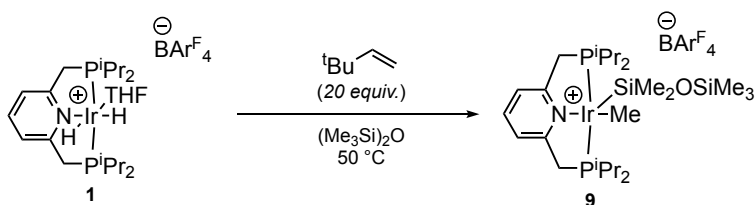


Preparation of [(PNP(^tPr)₄)IrMe(SiMe₂(CF₃))]BAr^F₄ (8**).** A 20 mL scintillation vial was charged with **1** (0.0998 g, 0.068 mmol), (trifluoromethyl)trimethylsilane (0.50 mL), and *tert*-butylethylene (88 μ L, 0.68 mmol) and was sealed with a PTFE-lined septum cap. The solution was heated at 40 °C for 60 min. The mixture was then allowed to cool to room temperature. Pentane (3.0 mL) was added at once to give a precipitate which was separated by decanting the supernatant. The resulting orange solid was dissolved in 1.0 mL of diethyl ether which was carefully layered with 1.00 mL of pentane in two, 0.40 mL portions followed by one 0.20 mL portion. On standing, red/orange crystals deposited which were separated by removal of the supernatant using a pipet. The crystals were washed with three, 1 mL portions of pentane and dried under vacuum. The crystals were then ground with a spatula and dried under vacuum to give complex **8** as an orange solid. Yield: 0.0626 g (60%). Crystals of **8** suitable for X-ray diffraction were obtained by layering a saturated solution of trifluoromethyltrimethylsilane with pentane at room temperature. Anal. Calcd. For C₄₉H₄₂B₁F₂₇IrN₁P₂Si₁: C, 42.98; H, 3.67; N, 0.91. Found: C, 43.142; H, 3.446; N, 0.832.

¹H NMR (500 MHz, CD₂Cl₂): δ 0.51 (s, 6H, Si(CH₃)₂), 1.06 (apparent q, 6H, PCH(CH₃), J_{H-H} = 7.1 Hz), 1.21 (apparent q, 6H, PCH(CH₃), J_{H-H} = 7.4 Hz), 1.36 (apparent q, 6H, PCH(CH₃), J_{H-H} = 7.1 Hz), 1.52 (apparent q, 6H, PCH(CH₃), J_{H-H} = 8.2 Hz), 1.94 (t, 3H, Ir-CH₃, J_{H-P} = 5.2 Hz), 2.58-2.71 (m, 4H, PCH), 3.52 (dot, 2H, PCH₂, ²J_{H-H} = 17.9 Hz, ²J_{H-P} = 3.9 Hz), 3.97 (dot, 2H, PCH₂, ²J_{H-H} = 17.9 Hz, ²J_{H-P} = 3.9 Hz), 7.55 (br s, 4H, CH of BAr^F₄), 7.58 (d, 2H, py-H3,5 ³J_{H-H} = 7.8 Hz) 7.72 (br s, 8H, CH of BAr^F₄), 7.91 (t, 1H, py-H4, ³J_{H-H} = 7.8 Hz)

³¹P{¹H} NMR (202 MHz, CD₂Cl₂): δ 28.06 (s)

¹³C{¹H} NMR (125 MHz, CD₂Cl₂): δ -22.40 (t, Ir-CH₃, ²J_{C-P} = 4.5 Hz), 2.75 (s, Si(CH₃)₂), 18.66 (s, PCH(CH₃)₂), 19.08 (s, PCH(CH₃)₂), 20.45 (s, PCH(CH₃)₂), 20.69 (s, PCH(CH₃)₂), 25.30 (t, PCH(CH₃)₂, ¹J_{C-P} = 12.7 Hz), 27.96 (t, PCH(CH₃)₂, ¹J_{C-P} = 13.8 Hz), 41.66 (t, PCH₂, ¹J_{C-P} = 13.8 Hz), 117.89 (br m, CH of BAr^F₄), 122.56 (apparent t, py-C3,5, ³J_{C-P} = 4.5 Hz), 125.02 (q, CF₃ of BAr^F₄, ¹J_{C-F} = 271.9 Hz), 129.30 (q, C of BAr^F₄, ²J_{C-F} 31.4 Hz), 135.22 (s, CH of BAr^F₄), 139.61 (s, py-C4), 162.18 (q, B-C, ¹J_{C-B} = 50.0 Hz), 163.13 (s, py-C2,6)



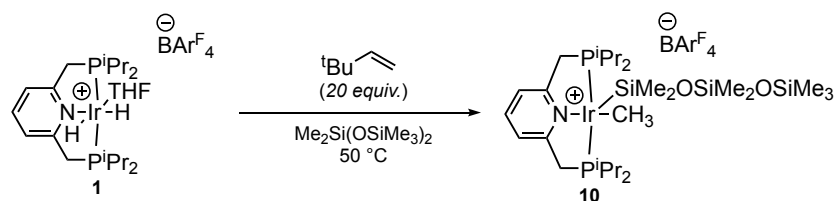
Preparation of [of [(PNP(ⁱPr)₄)IrMe(SiMe₂OSiMe₃)]BAr^F₄ (9**).** A 20 mL scintillation vial was charged with **1** (0.0999 g, 0.068 mmol), hexamethyldisiloxane (4 mL), a stir bar, and *tert*-butylethylene (176 μ L, 1.4 mmol) and was sealed with a PTFE-lined septum cap. The suspension was heated at 50 °C for 120 hours. The mixture was allowed to cool to room temperature and the solvent was removed using a pipette. The resulting orange residue was then washed with three, 3 mL portions of pentane and was dried under vacuum. The resulting solid was then extracted with two, 1 mL portions of diethyl ether and filtered through a 0.45 μ m PTFE syringe filter. The resulting orange solution was dried under vacuum to give an orange solid. The solid was taken up in 0.80 mL of diethyl ether and carefully layered with two, 0.40 mL portions of pentane. Orange crystals deposited on standing overnight. The supernatant and residual orange oil were removed using a pipette and the orange crystals were dried under vacuum. The crystals were ground with a spatula and further dried under vacuum to give **9** as an orange solid. Yield: 0.0520 g (49%). Crystals of **9** suitable for X-ray diffraction were obtained by layering a saturated solution of diethyl ether with pentane at room temperature. Anal. Calcd. For C₅₉H₇₁B₁F₂₄IrN₁O₂P₂Si₃: C, 43.96; H, 4.21; N, 0.90. Found: C, 43.942; H, 4.039; N, 0.843.

¹H NMR (500 MHz, CD₂Cl₂): δ -0.012 (s, SiCH₃), 0.26 (s, SiCH₃), 1.00 (apparent q, 6H, PCH(CH₃), J_{H-H} = 7.2 Hz), 1.21 (apparent q, 6H, PCH(CH₃), J_{H-H} = 7.7 Hz), 1.34 (apparent q, 6H, PCH(CH₃), J_{H-H} = 7.0 Hz), 1.53 (apparent q, 6H, PCH(CH₃), J_{H-H} = 8.0 Hz), 1.80 (t, 3H, Ir-CH₃, J_{H-P} = 5.6 Hz), 2.68-2.78 (m, 4H, PCH), 3.53 (dot, 2H, PCH₂, ²J_{H-H} = 17.7 Hz, ²J_{H-P} = 4.7 Hz), 3.86 (dot, 2H, PCH₂, ²J_{H-H} = 17.8 Hz, ²J_{H-P} = 4.1 Hz), 7.50 (d, 2H, py-H3, ³J_{H-H} = 7.8 Hz), 7.55 (br s, 4H, CH of BAr^F₄), 7.71 (br s, 8H, CH of BAr^F₄), 7.86 (t, 1H, py-H4, ³J_{H-H} = 7.8 Hz)

³¹P{¹H} NMR (202 MHz, CD₂Cl₂): δ 31.63 (s)

¹³C{¹H} NMR (125 MHz, CD₂Cl₂): δ -20.72 (t, Ir-CH₃, ²J_{C-P} = 5.9 Hz), 2.01 (s, Si(CH₃)₃), 7.87 (s, Si(CH₃)₂), 18.41 (s, PCH(CH₃)₂), 19.26 (s, PCH(CH₃)₂), 20.34 (s, PCH(CH₃)₂), 20.42 (s, PCH(CH₃)₂), 25.70 (t, PCH(CH₃)₂, ¹J_{C-P} = 12.8 Hz), 27.96 (t, PCH(CH₃)₂, ¹J_{C-P} = 13.9 Hz), 42.46 (t, PCH₂, ¹J_{C-P} = 14.2 Hz), 117.88 (br m, CH of BAr^F₄), 122.22 (apparent t, py-C3, ³J_{C-P} = 4.9 Hz), 125.01 (q, CF₃ of BAr^F₄, ¹J_{C-F} = 272.4 Hz), 129.28 (q, C of BAr^F₄, ²J_{C-F} 31.3 Hz), 135.21 (s, CH of BAr^F₄), 138.34 (s, py-C4),

162.17 (q, B-C, $^1J_{C-B} = 49.8$ Hz), 163.27 (s, py-C2,6)



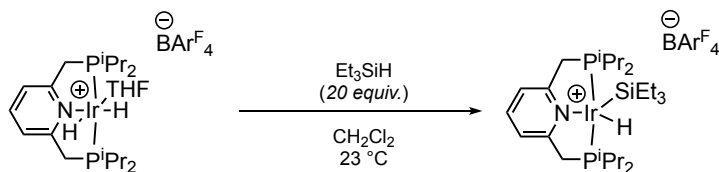
Preparation of [(PNP(^{*i*}Pr)₄)IrMe(SiMe₂OSiMe₂OSiMe₃)]BARF₄ (10**).** A 20 mL scintillation vial was charged with **1** (0.1004 g, 0.068 mmol), octamethyltrisiloxane (3 mL), a stir bar, and *tert*-butylethylene (176 μL , 1.4 mmol) and was sealed with a PTFE-lined septum cap. The solution was heated at 50 °C for 7 days. The mixture was then allowed to cool to room temperature and the solution was decanted using a pipette. The resulting yellow residue was dried under vacuum and then ground with a spatula to give a yellow solid. This solid was washed with three, 3 mL portions of pentane and dried under vacuum. The solid was then extracted with two, 1 mL portions of diethyl ether and the extracts filtered through a 0.45 μm PTFE syringe filter. The resulting yellow/orange solution was dried under vacuum and washed with three, 3 mL portions of pentane to give a yellow solid. The solid was ground with a spatula and dried under vacuum. The solid was then taken up in 1 mL diethyl ether and 0.20 mL pentane was carefully layered on top. Additional pentane was added in four, 0.30 mL portions followed by one, 0.20 mL portion for a total of 1.6 mL. Yellow crystals deposited on standing from the viscous orange bottom layer. The bottom layer was removed using a pipette, followed by the pale-yellow top layer to give yellow crystals and an orange residue. The crystals were transferred away from the residue into a 20 mL scintillation vial using a spatula. The crystals were then ground with a spatula and dried under vacuum. The yellow solid was then extracted with two, 1 mL portions of diethyl ether which were filtered through a 0.45 μm PTFE syringe filter and dried under vacuum to give a yellow solid. The solid was dissolved in 0.50 mL diethyl ether and carefully layered with 0.20 mL pentane. Additional pentane was added in two, 0.20 mL portions, leading to the deposition of yellow crystals on standing. The supernatant was decanted using a pipette and the yellow crystals washed with three, 1.0 mL portions of pentane. The crystals were then ground with a spatula and dried under vacuum to give complex **10** as a yellow solid. Yield: 0.0361 g (33%). Crystals of **10** suitable for X-ray diffraction were obtained by layering a saturated solution of diethyl ether with pentane at room temperature. Anal. Calcd. For C₅₉H₇₁B₁F₂₄IrN₁O₂P₂Si₃: C, 43.44; H, 4.39; N, 0.86. Found: C, 43.276; H, 4.251; N, 0.955.

$^1\text{H NMR}$ (500 MHz, CD₂Cl₂): δ -0.05 (s, SiCH₃), 0.04 (s, SiCH₃), 0.28 (s, SiCH₃), 0.99 (apparent q, 6H, PCH(CH₃), $J_{\text{H-H}} = 7.3$

Hz), 1.21 (apparent q, 6H, PCH(CH₃), J_{H-H} = 7.8 Hz), 1.33 (apparent q, 6H, PCH(CH₃), J_{H-H} = 7.0 Hz), 1.53 (apparent q, 6H, PCH(CH₃), J_{H-H} = 8.1 Hz), 1.80 (t, 3H, Ir-CH₃, J_{H-P} = 5.5 Hz), 2.66-2.82 (m, 4H, PCH), 3.62 (dot, 2H, PCH₂, ²J_{H-H} = 17.7 Hz, ²J_{H-P} = 4.7 Hz), 3.84 (dot, 2H, PCH₂, ²J_{H-H} = 17.8 Hz, ²J_{H-P} = 4.1 Hz), 7.48 (d, 2H, py-H3,5 ³J_{H-H} = 7.7 Hz), 7.56 (br s, 4H, CH of BAR^F₄), 7.72 (br s, 8H, CH of BAR^F₄), 7.84 (t, 1H, py-H4, ³J_{H-H} = 7.8 Hz)

³¹P{¹H} NMR (202 MHz, CD₂Cl₂): δ 31.86 (s)

¹³C{¹H} NMR (125 MHz, CD₂Cl₂): δ -20.65 (t, Ir-CH₃, ²J_{C-P} = 5.9 Hz), 1.63 (s, SiCH₃), 1.78 (s, SiCH₃), 7.68 (s, SiCH₃), 18.50 (s, PCH(CH₃)₂), 19.33 (s, PCH(CH₃)₂), 20.28 (s, PCH(CH₃)₂), 20.41 (s, PCH(CH₃)₂), 25.80 (t, PCH(CH₃)₂, ¹J_{C-P} = 12.8 Hz), 27.93 (t, PCH(CH₃)₂, ¹J_{C-P} = 14.4 Hz), 42.42 (t, PCH₂, ¹J_{C-P} = 14.1 Hz), 117.88 (br m, CH of BAR^F₄), 122.16 (apparent t, py-C3,5, ³J_{C-P} = 4.7 Hz), 125.02 (q, CF₃ of BAR^F₄, ¹J_{C-F} = 271.7 Hz), 129.31 (q, C of BAR^F₄, ²J_{C-F} = 31.7 Hz), 135.22 (s, CH of BAR^F₄), 138.21 (s, py-C4), 162.18 (q, B-C, ¹J_{C-B} = 49.8 Hz), 163.44 (s, py-C2,6)



Preparation of [(PNP(ⁱPr)₄)IrH(SiEt₃)]BAR^F₄ (11**).** A 20 mL scintillation vial was charged with **1** (0.1002 g, 0.068 mmol), dichloromethane (1 mL), and triethylsilane (217 μL, 1.4 mmol) and was sealed with a PTFE-lined septum cap. The solution was allowed to stand at room temperature for 1 hour. The mixture was then dried under vacuum to give an orange solid. The solid was dissolved in 0.80 mL diethyl ether and pentane was carefully layered on top in two, 0.50 mL portions. Once orange crystals began to deposit, an additional 0.20 mL portion of pentane was layered on top. After standing overnight, the supernatant was decanted using a pipette. The crystals were washed with three, 1 mL portions of pentane and dried under vacuum. The crystals were then ground with a spatula and further dried under vacuum to give complex **11** as an orange solid. Yield: 0.0875 g (85%). Crystals of **11** suitable for X-ray diffraction were obtained by layering a saturated solution of diethyl ether with pentane at room temperature. Anal. Calcd. For C₅₉H₇₁B₁F₂₄IrN₁O₂P₂Si₃: C, 45.30; H, 4.20; N, 0.93. Found: C, 45.353; H, 3.846; N, 0.875.

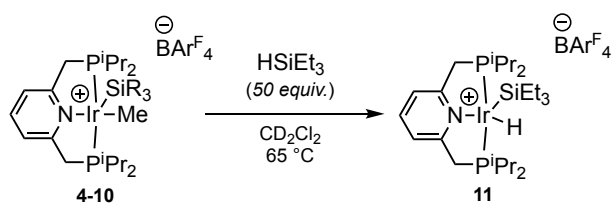
¹H NMR (500 MHz, CD₂Cl₂): δ -15.84 (t, 1H, Ir-H, ²J_{H-P} = 11.0 Hz), 0.72 (q, 6H, Si(CH₂CH₃)₃, ³J_{H-H} = 7.4 Hz), 0.82 (t, 9H, Si(CH₂CH₃)₃, ³J_{H-H} = 7.4 Hz), 0.99 (apparent q, 6H, PCH(CH₃), J_{H-H} = 7.4 Hz), 1.18-1.25 (m, 12H, PCH(CH₃)), 1.38 (apparent q, 6H, PCH(CH₃), J_{H-H} = 7.7 Hz), 2.38-2.50 (br m, 4H, PCH(CH₃)), 3.62 (br m, 2H, PCH₂), 3.84 (br m, 2H, PCH₂), 7.55 (br s, 4H,

CH of BAR^{F}_4), 7.62 (d, 2H, py-H3, $^3J_{\text{H-H}} = 7.7$ Hz), 7.72 (br s, 8H, CH of BAR^{F}_4), 7.96 (t, 1H, py-H4, $^3J_{\text{H-H}} = 7.7$ Hz)

$^{31}\text{P}\{^1\text{H}\}$ NMR (202 MHz, CD_2Cl_2): δ 52.36 (d, $^2J_{\text{P-H}} = 5.0$ Hz)

$^{13}\text{C}\{^1\text{H}\}$ NMR (125 MHz, CD_2Cl_2): δ 9.17 (s, SiEt_3), 11.83 (s, SiEt_3), 17.76 (s, $\text{PCH}(\text{CH}_3)_2$), 18.63 (s, $\text{PCH}(\text{CH}_3)_2$), 20.77 (s, $\text{PCH}(\text{CH}_3)_2$), 21.89 (s, $\text{PCH}(\text{CH}_3)_2$), 25.96 (t, $\text{PCH}(\text{CH}_3)_2$, $^1J_{\text{C-P}} = 13.8$ Hz), 26.17 (t, $\text{PCH}(\text{CH}_3)_2$, $^1J_{\text{C-P}} = 13.8$ Hz), 40.32 (t, PCH_2 , $^1J_{\text{C-P}} = 12.0$ Hz), 117.88 (br m, CH of BAR^{F}_4), 121.90 (apparent t, py-C3,5, $^3J_{\text{C-P}} = 4.0$ Hz), 125.00 (q, CF_3 of BAR^{F}_4 , $^1J_{\text{C-F}} = 272.5$ Hz), 129.29 (q, C of BAR^{F}_4 , $^2J_{\text{C-F}} = 31.4$ Hz), 135.21 (s, CH of BAR^{F}_4), 140.95 (s, py-C4), 162.17 (q, B-C, $^1J_{\text{C-B}} = 50.0$ Hz), 164.34 (t, py-C2,6 $^2J_{\text{C-P}} = 3.0$ Hz)

Procedure for the equilibration of 3 in an equimolar solution of trifluoromethyltrimethylsilane and tetramethylsilane (eqn. 4). A 4 mL vial was charged with 3 (0.0122 g, 0.0082 mmol) and trifluoromethyltrimethylsilane (104 μL , 0.70 mmol). The solution was transferred to a thick walled J. Young tube and tetramethylsilane was added (96 μL , 0.70 mmol). The J. Young tube was sealed and inverted. The reaction was then heated at 80 $^\circ\text{C}$ and monitored by $^{31}\text{P}\{^1\text{H}\}$ until the ratio of 3 to 8 became constant. The computed ΔG° is based on the relative intensities of the $^{31}\text{P}\{^1\text{H}\}$ signals after cooling to 23 $^\circ\text{C}$.



General procedure for the reaction of 4-7 and 9-10 with triethylsilane at 65 $^\circ\text{C}$ (Figure 4.4.1). A 20 mL scintillation vial was charged with the iridium complex (0.012 mmol), 1.20 mL CD_2Cl_2 , and triethylsilane (96 μL , 0.60 mmol). Two 0.50 mL aliquots were then removed and transferred to separate J. Young NMR tubes. Reactions were monitored by $^{31}\text{P}\{^1\text{H}\}$ NMR at 65 $^\circ\text{C}$ in duplicate to observe the rate of conversion to complex 11.

General procedure for the reaction of 8 with triethylsilane at 65 $^\circ\text{C}$ (Figure 4.4.1). A 20 mL scintillation vial was charged with 8 (0.012 mmol) and 1.20 mL of CD_2Cl_2 . Two 0.50 mL aliquots was then removed and transferred to separate J. Young NMR tubes. The samples in the NMR tubes were frozen in a liquid nitrogen-cooled cold well. Once frozen, triethylsilane (40 μL , 0.25 mmol)

was added to each NMR tube. The NMR tubes were then sealed, removed from the glove box and handled in a -78 °C bath. Prior to kinetic analysis, the J. Young NMR tube was removed from the cold bath, inverted to mix the reagents and then was monitored by $^{31}\text{P}\{^1\text{H}\}$ NMR at 65 °C to observe the rate of conversion to complex **11**.

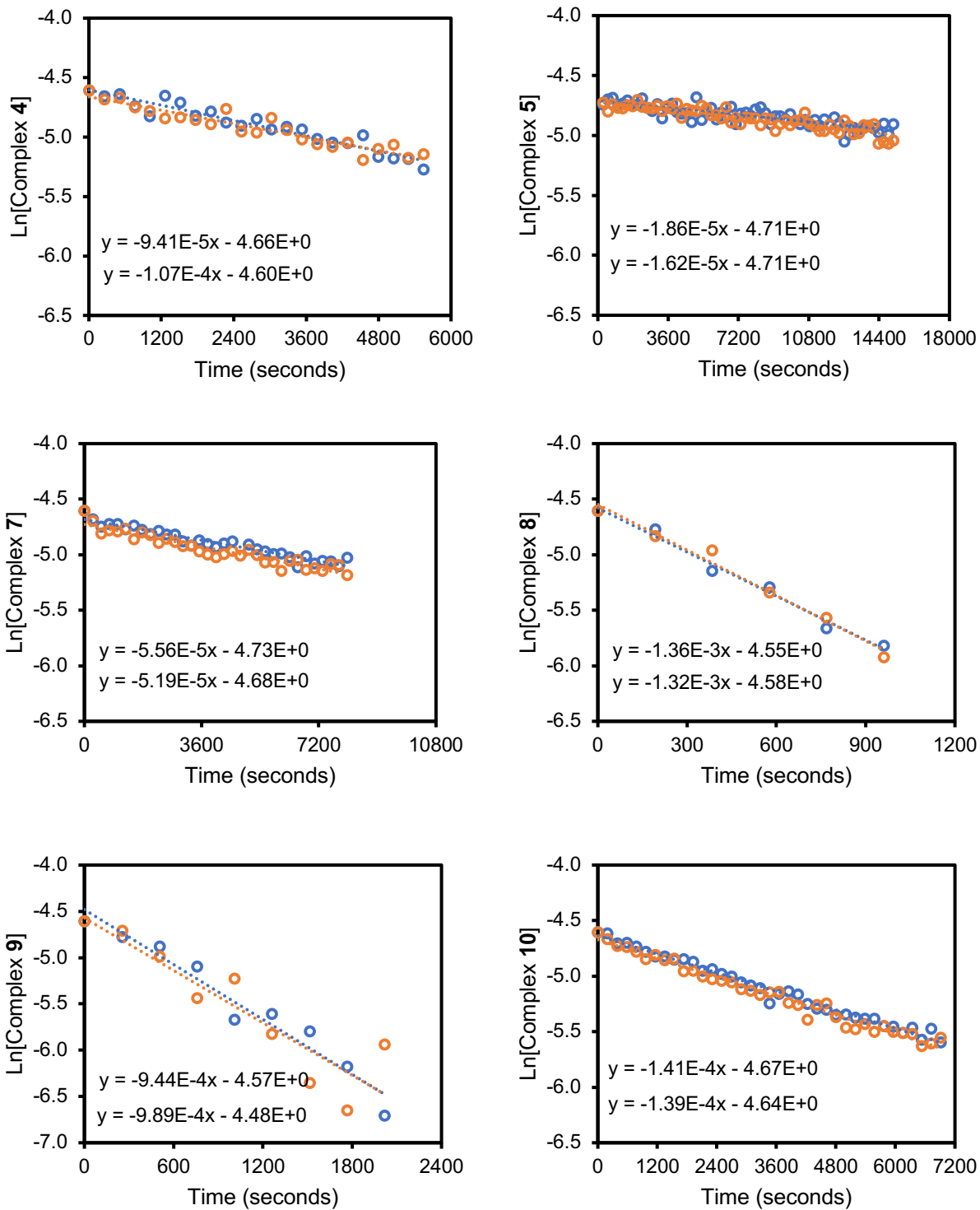
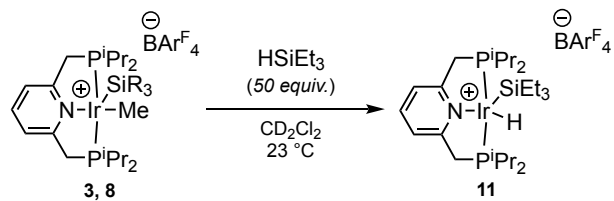


Figure 4.4.1. Kinetics of reductive elimination at 65 °C with HSiEt₃; Ln[Ir] versus time. Experiments shown in duplicate.



General procedure for the reaction of 3 and 8 with triethylsilane at 23 °C (Figure 4.4.2). A 20 mL scintillation vial was charged with 3 or 8 (0.012 mmol) and 1.20 mL of CD₂Cl₂. Two 0.50 mL aliquots was then removed and transferred to separate J. Young NMR tubes. The samples in the NMR tubes were frozen in a liquid nitrogen-cooled cold well. Once frozen, triethylsilane (40 μL, 0.25 mmol) was added to each NMR tube. The NMR tubes were then sealed, removed from the glove box and handled in a -78 °C bath. Prior to kinetic analysis, the J. Young NMR tube was removed from the cold bath, inverted to mix the reagents and then was monitored by ³¹P{¹H} NMR at 23 °C to observe the rate of conversion to complex 11.

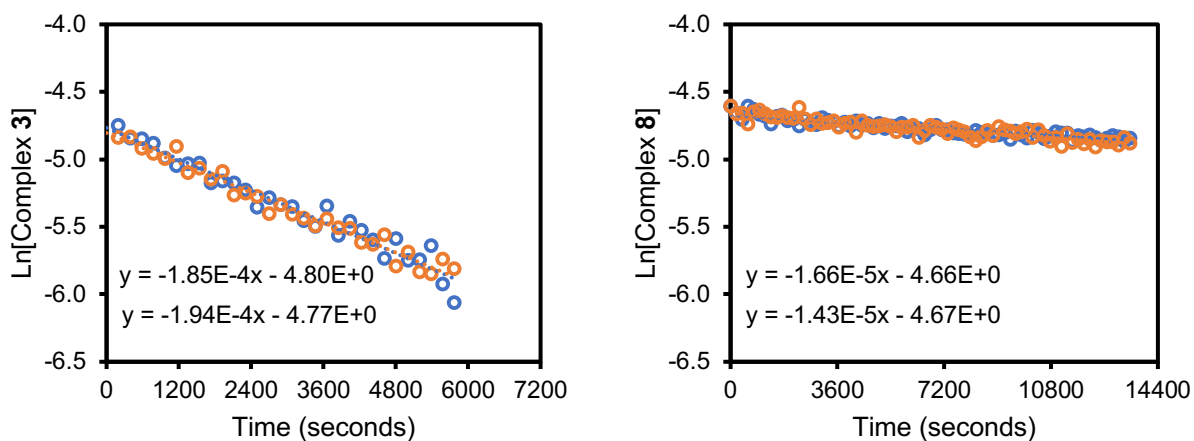
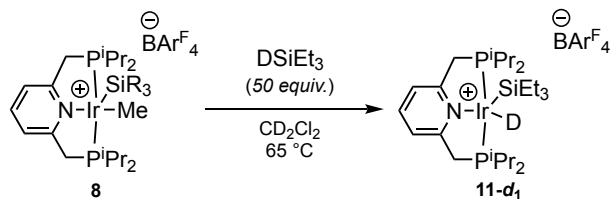
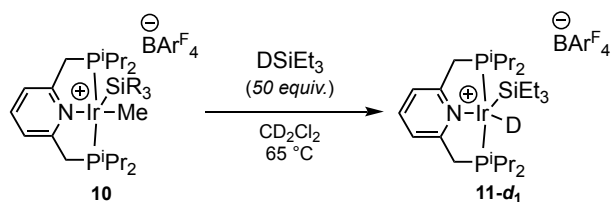


Figure 4.4.2. Kinetics of reductive elimination at 23 °C with HSiEt₃: Ln[Ir] versus time. Experiments shown in duplicate



General procedure for the reaction of 8 with triethylsilane- d_1 at 65 °C (Figure 4.4.3). A 20 mL scintillation vial was charged with **8** (0.012 mmol) and 1.20 mL of CD_2Cl_2 . Two 0.50 mL aliquots was then removed and transferred to separate J. Young NMR tubes. The samples in the NMR tubes were frozen in a liquid nitrogen-cooled cold well. Once frozen, triethylsilane- d_1 (40 μL , 0.25 mmol) was added to each NMR tube. The NMR tubes were then sealed, removed from the glove box and handled in a -78 °C bath. Prior to kinetic analysis, the J. Young NMR tube was removed from the cold bath, inverted to mix the reagents and then was monitored by $^{31}\text{P}\{^1\text{H}\}$ NMR at 65 °C to observe the rate of conversion to complex **11-d₁**.



General procedure for the reaction of 10 with triethylsilane- d_1 at 65 °C (Figure 4.4.3). A 20 mL scintillation vial was charged with the iridium complex (0.012 mmol), 1.20 mL CD_2Cl_2 , and triethylsilane- d_1 (96 μL , 0.60 mmol). Two 0.50 mL aliquots were then removed and transferred to separate J. Young NMR tubes. Reactions were monitored by $^{31}\text{P}\{^1\text{H}\}$ NMR at 65 °C in duplicate to observe the rate of conversion to complex **11-d₁**.

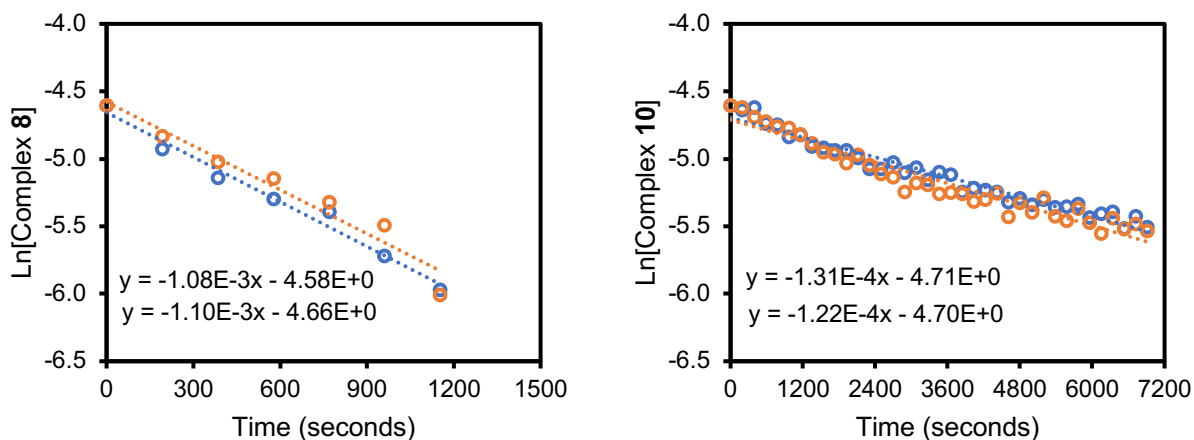


Figure 4.4.3. Kinetics of reductive elimination at 65 °C with DSiEt_3 : $\text{Ln}[\text{Ir}]$ versus time. Experiments shown in duplicate

General procedure for catalytic hydrosilylation of *tert*-butylethylene with pentamethyldisiloxane at 80 °C (Figure 4.4.4, right). A 20 mL scintillation vial was charged with **1** (0.0176 g, 0.012 mmol), 0.92 mL of CD₂Cl₂, *tert*-butylethylene (0.23 mL, 1.8 mmol) followed by pentamethyldisiloxane (47 μL, 0.24 mmol). Two 0.50 mL aliquots were removed and transferred to separate J. Young NMR tubes. The rate of hydrosilylation was monitored by heating the sealed tubes in an oil bath at 80 °C for 10 minute intervals. After each interval, the samples were rapidly cooled to 23 °C and analyzed by ¹H NMR spectroscopy. Product formation was monitored by comparison to reported characterization data.³

General procedure for catalytic hydrosilylation of *tert*-butylethylene with trimethylsilane at 80 °C (Figure 4.4.4, left). A 20 mL scintillation vial was charged with **1** (0.0176 g, 0.012 mmol), 0.72 mL of CD₂Cl₂ followed by *tert*-butylethylene (0.23 mL, 1.8 mmol) and cooled to -35 °C. A 0.25 mL aliquot of a 970 mM solution of trimethylsilane (0.24 mmol) in CH₂Cl₂ was added. Two 0.50 mL aliquots were removed and transferred to separate J. Young NMR tubes. The rate of hydrosilylation was monitored by heating the sealed tubes in an oil bath at 80 °C for 10 minute intervals. After each interval, the samples were rapidly cooled to 23 °C and analyzed by ¹H NMR spectroscopy. Product formation was monitored by comparison to reported characterization data.⁴

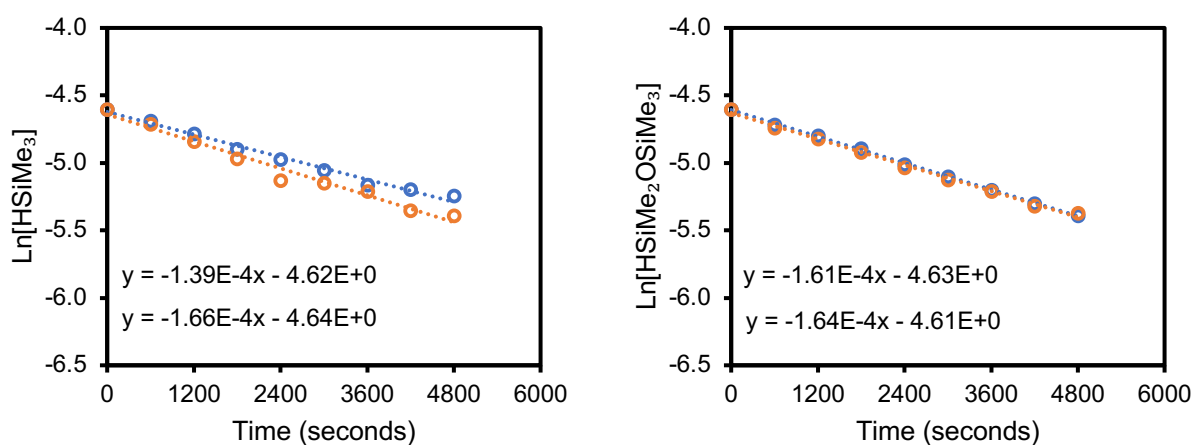


Figure 4.4.4. Kinetics of catalytic hydrosilylation of *tert*-butylethylene by **1** at 80 °C: Ln[Silane] versus time. Experiments shown in duplicate.

General Methods. Density functional theory (DFT) calculations were performed using Gaussian 09.⁵

Computational treatment of reductive elimination/oxidative addition thermodynamics (Figure 4.4.5 and Figure 4.4.6).

X-ray crystallographic data provided initial atomic coordinates for each iridium complex. Initial coordinates for organic compounds were generated using Gaussview. A DFT optimization and frequency calculation was performed to compute the free energy of each complex and compound using the M06⁶ functional with the following basis sets: (CHNOF: def2SVP, IrPSi: def2TZVP).⁷ The ECP for Ir was retrieved from the EMSL basis set exchange (<http://bse.pnl.gov/>).⁸ The tabulated free energies were used to calculate ΔG° values for the transformations shown in Figure 4.4.5 and Figure 4.4.6.

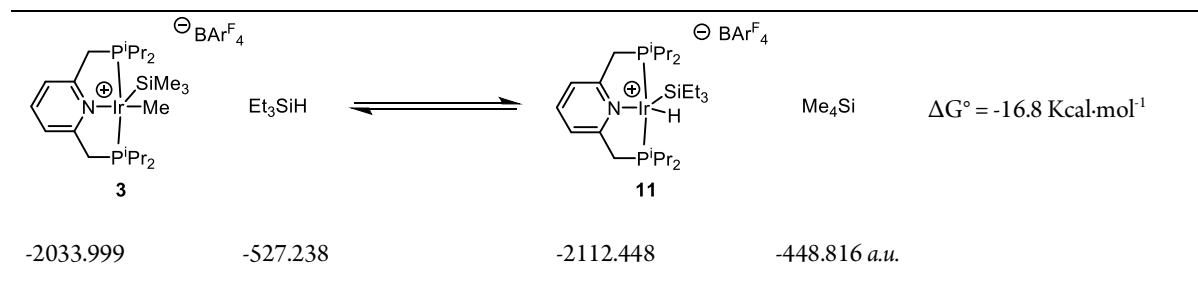
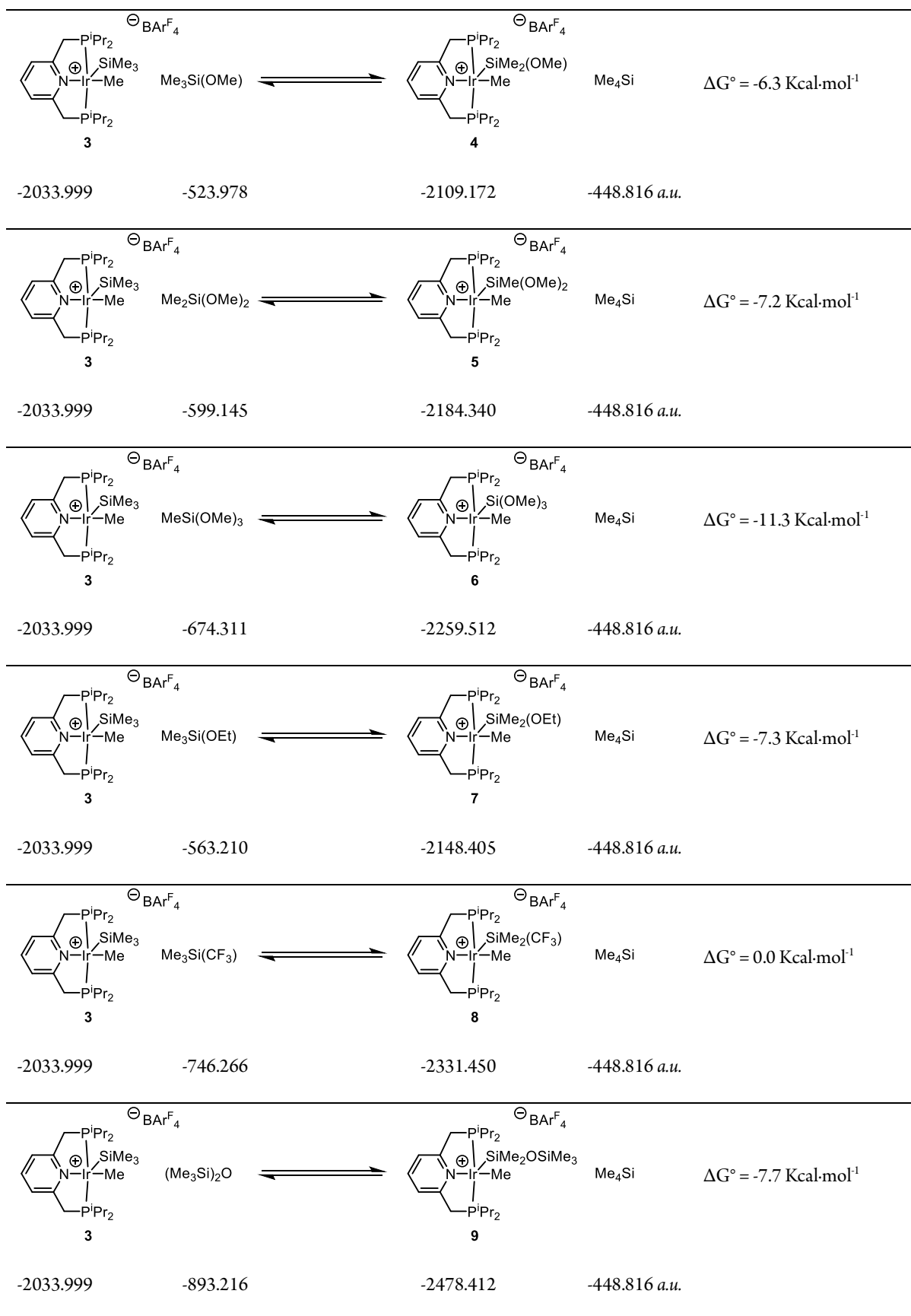


Figure 4.4.5. Computed thermodynamics of conversion of **3** to **11**.



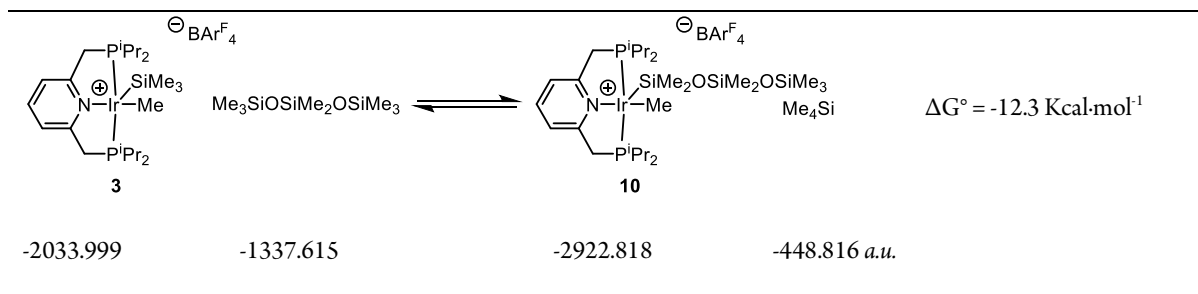


Figure 4.4.6. Computed relative stabilities of silyl complexes **3-10**.

4.5 Additional Figures

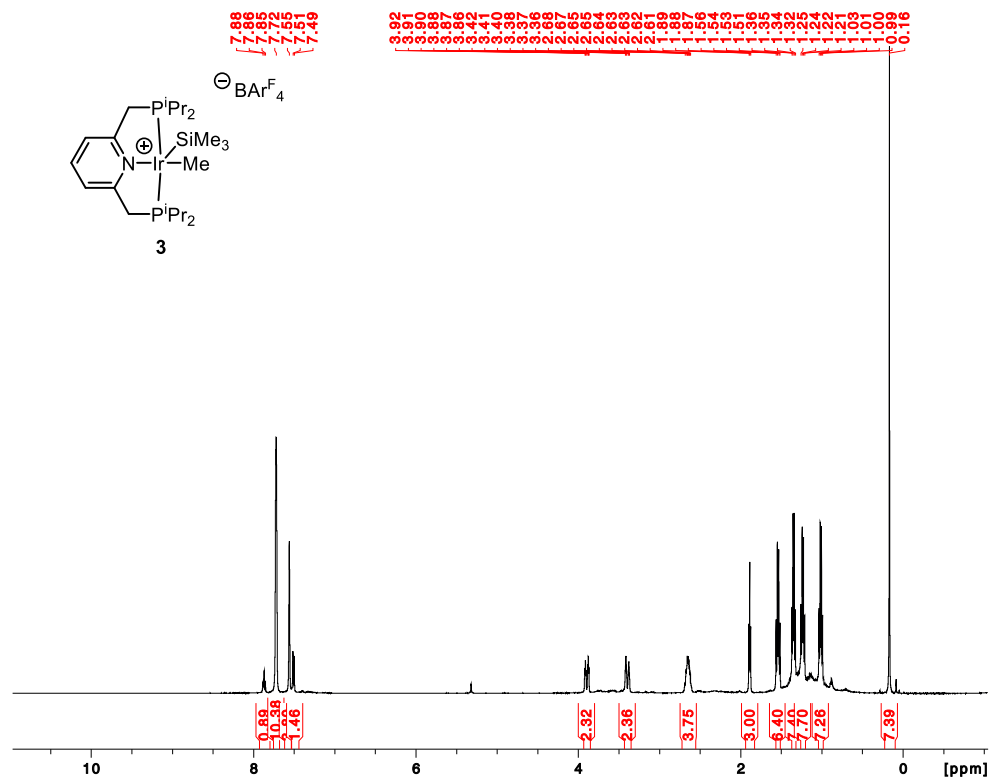


Figure 4.5.1. ^1H NMR Spectrum of $[(\text{PNP}(\text{iPr})_4)\text{IrMe}(\text{SiMe}_3)]\text{BARf}_4$ (**3**) (500 MHz, CD_2Cl_2).

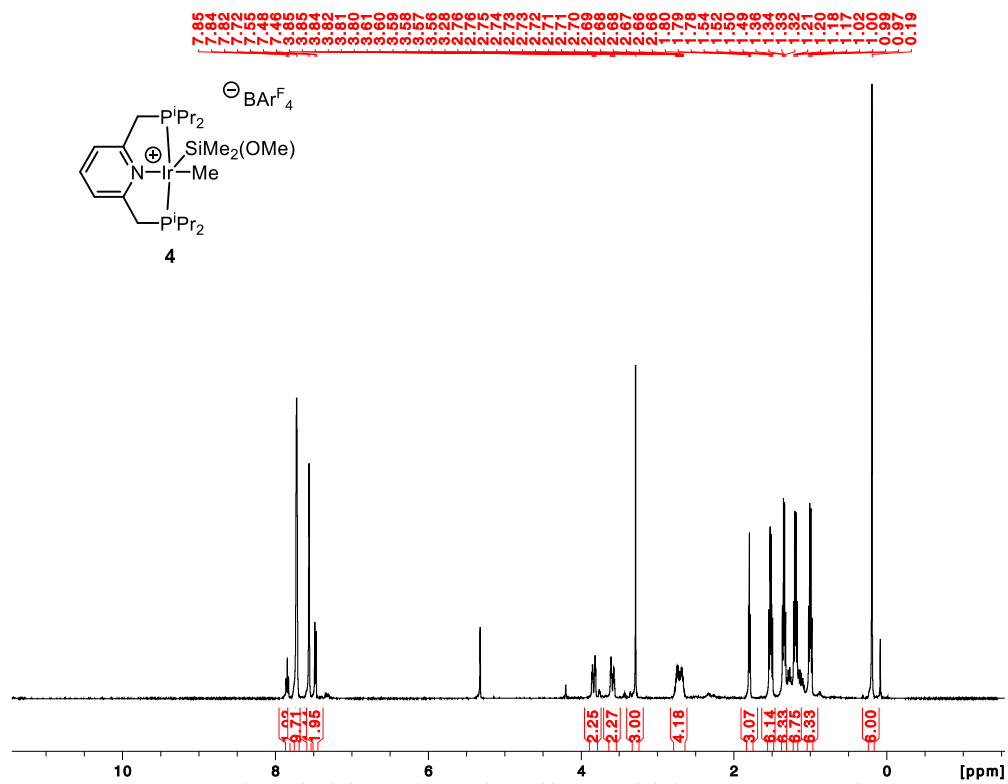


Figure 4.5.4. ^1H NMR Spectrum of $[(\text{PNP}(\text{iPr})_4)\text{IrMe}(\text{SiMe}_2(\text{OMe}))]\text{BAR}^{\text{F}_4}$ (**4**) (500 MHz, CD_2Cl_2).

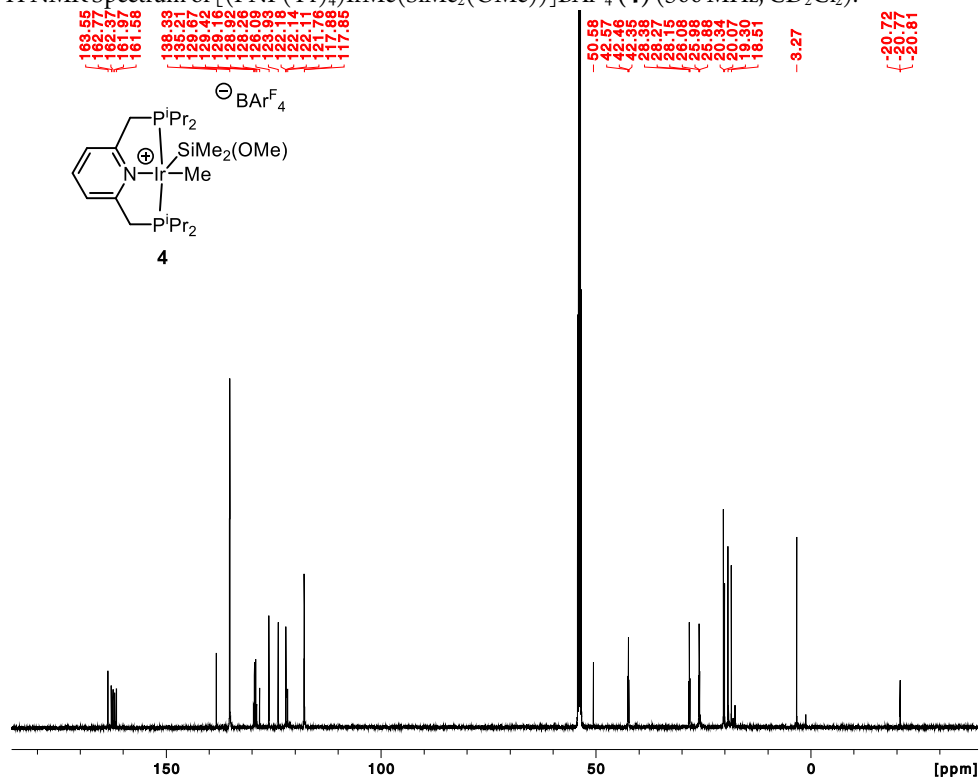


Figure 4.5.5. $^{13}\text{C}\{^1\text{H}\}$ NMR Spectrum of $[(\text{PNP}(\text{iPr})_4)\text{IrMe}(\text{SiMe}_2(\text{OMe}))]\text{BAR}^{\text{F}_4}$ (**4**) (126 MHz, CD_2Cl_2).

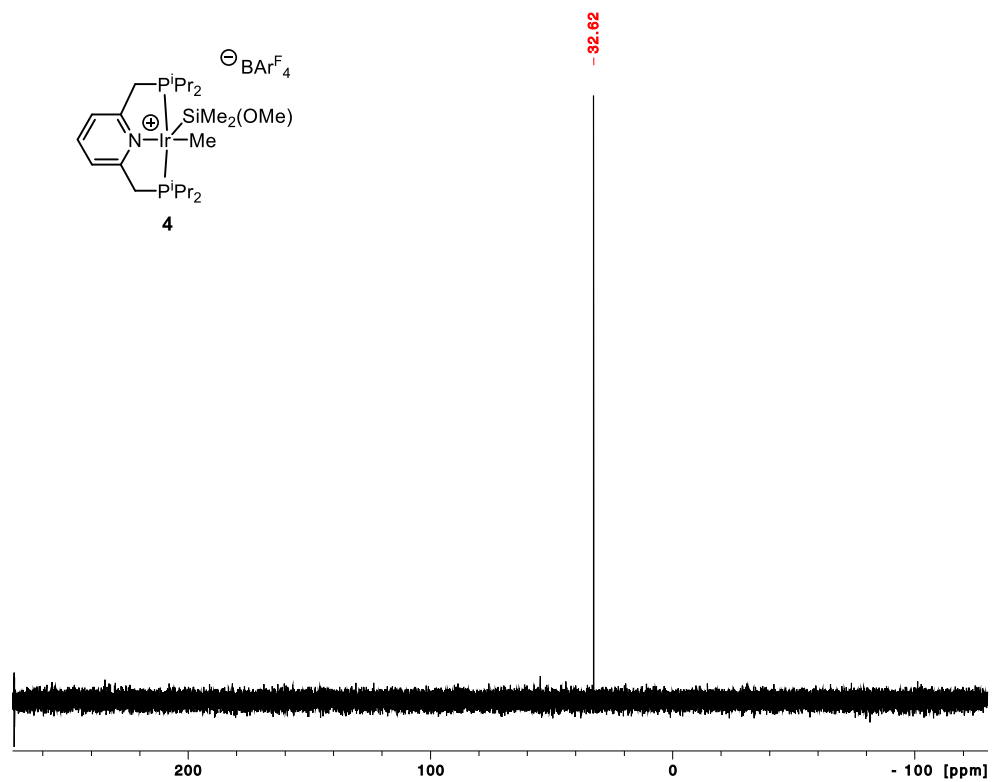


Figure 4.5.6. $^{31}\text{P}\{^1\text{H}\}$ NMR Spectrum of $[(\text{PNP}(\text{iPr})_4)\text{IrMe}(\text{SiMe}_2(\text{OMe}))]\text{BArF}_4$ (**4**) (202 MHz, CD_2Cl_2).

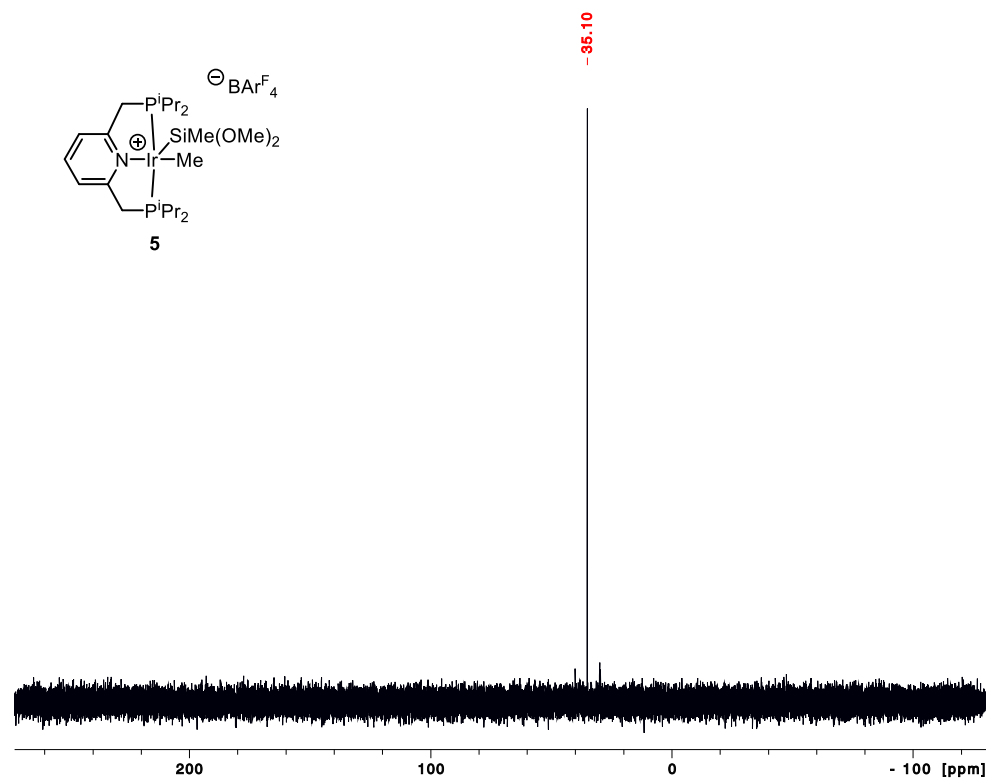


Figure 4.5.9. $^{31}\text{P}\{^1\text{H}\}$ NMR Spectrum of $[(\text{PNP}(\text{iPr})_4)\text{IrMe}(\text{SiMe}(\text{OMe})_2)]\text{BArF}_4$ (**5**) (202 MHz, CD_2Cl_2).

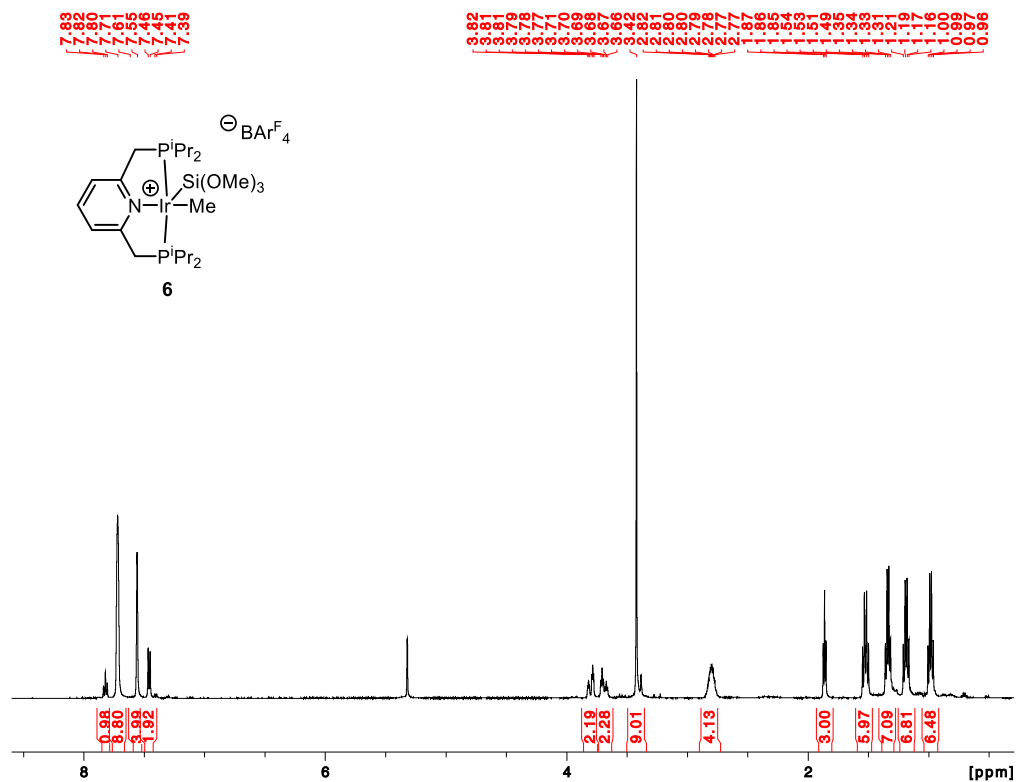
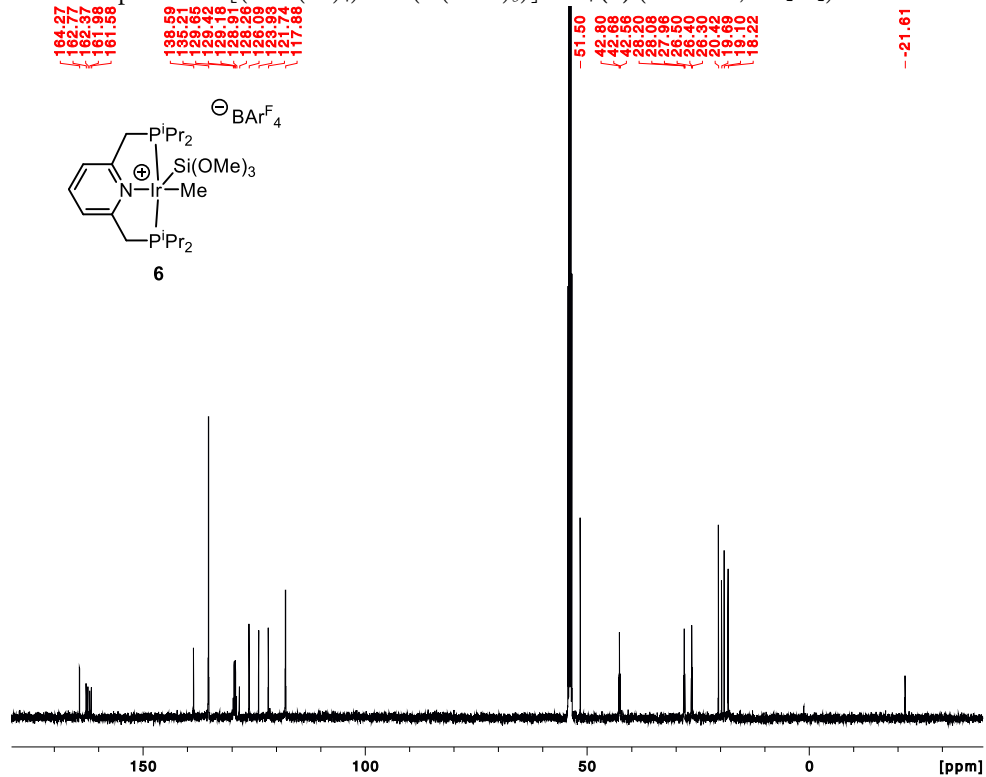


Figure 4.5.10. 1H NMR Spectrum of $[(PNP(iPr)_4)IrMe(Si(OMe)_3)]BARF_4$ (**6**) (500 MHz, CD_2Cl_2).



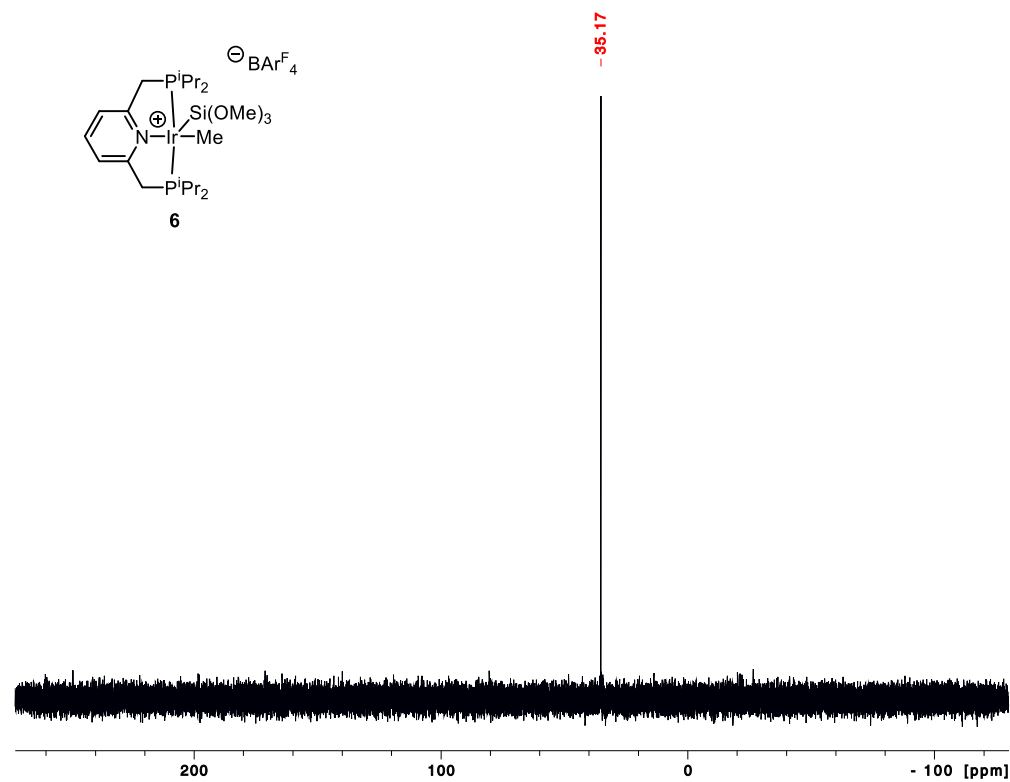


Figure 4.5.12. $^{31}\text{P}\{^1\text{H}\}$ NMR Spectrum of $[(\text{PNP}(\text{iPr})_4)\text{IrMe}(\text{Si}(\text{OMe})_3)]\text{BArF}_4$ (**6**) (202 MHz, CD_2Cl_2).

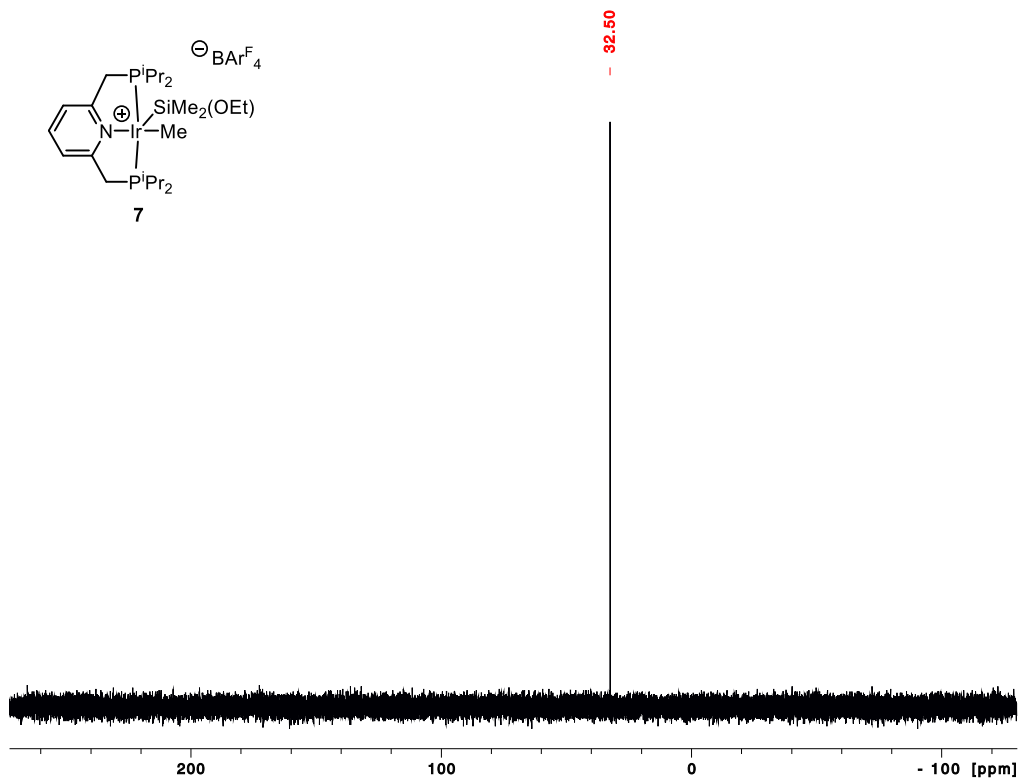


Figure 4.5.15. $^{31}\text{P}\{^1\text{H}\}$ NMR Spectrum of $[(\text{PNP}(\text{iPr})_4)\text{IrMe}(\text{SiMe}_2(\text{OEt}))]\text{BARF}_4^-$ (7) (202 MHz, CD_2Cl_2).

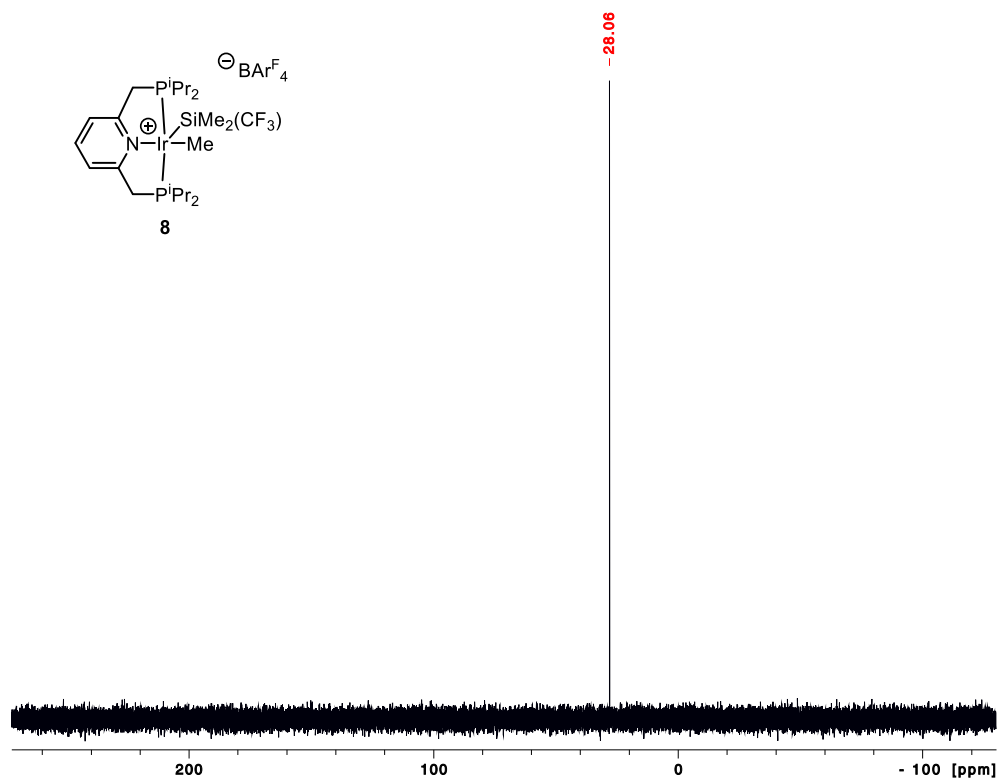


Figure 4.5.18. $^{31}\text{P}\{^1\text{H}\}$ NMR Spectrum of $[(\text{PNP}(\text{iPr})_4)\text{IrMe}(\text{SiMe}_2(\text{CF}_3))]\text{BAR}_4^{\ominus}$ (**8**) (202 MHz, CD_2Cl_2).

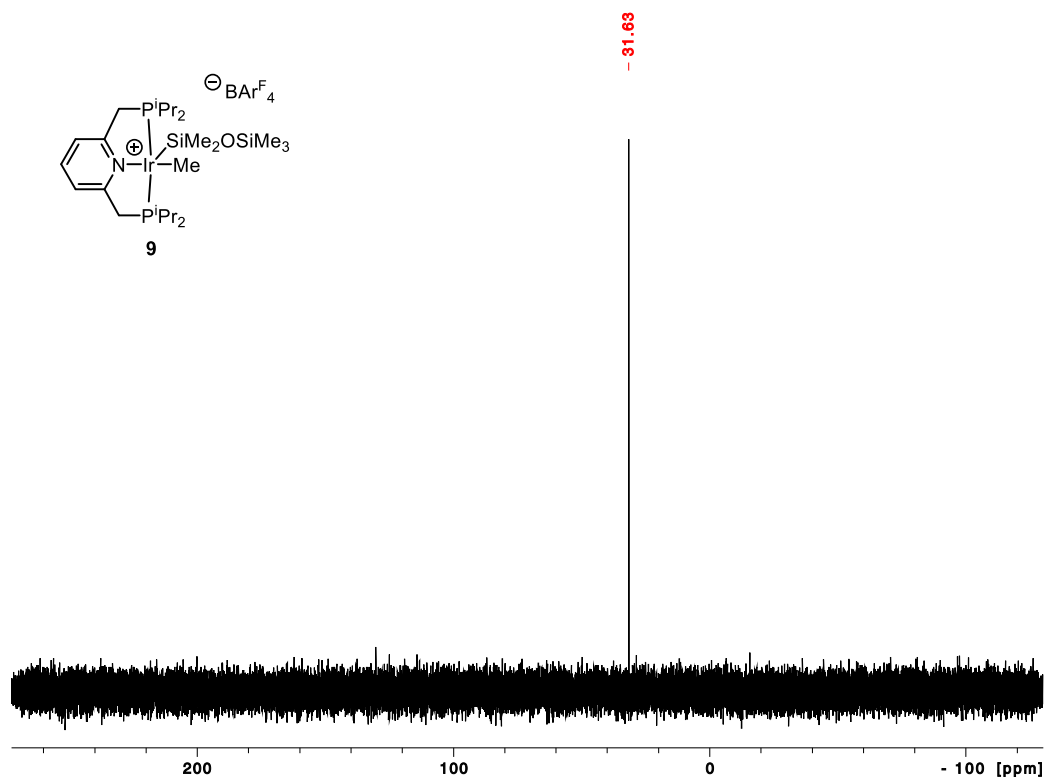
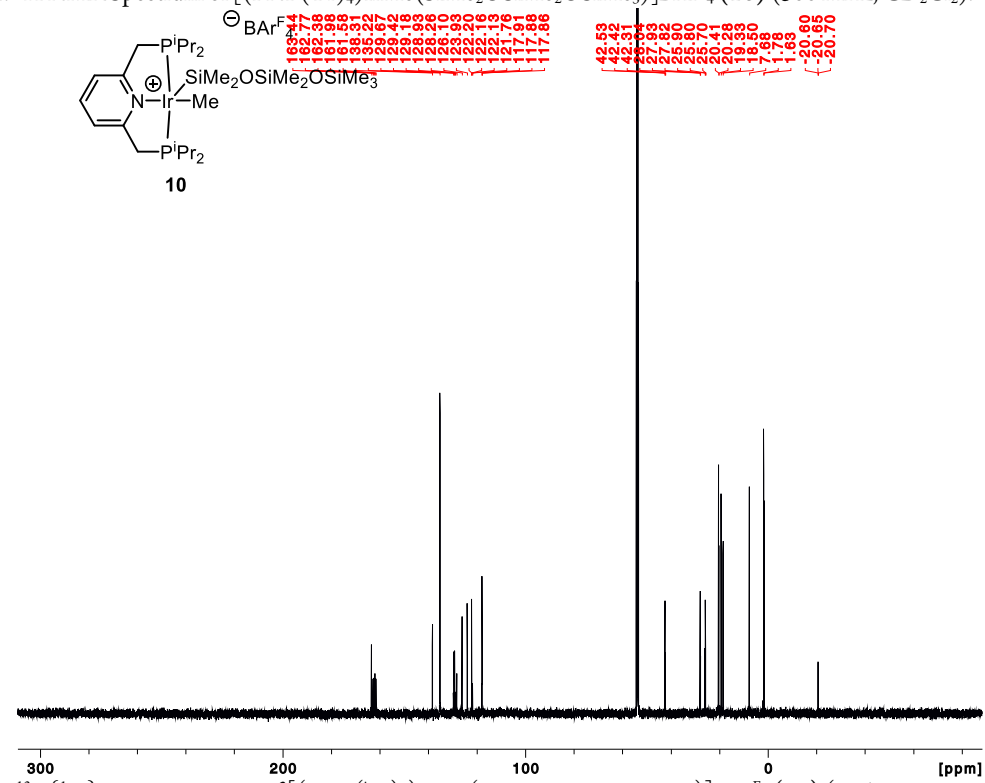
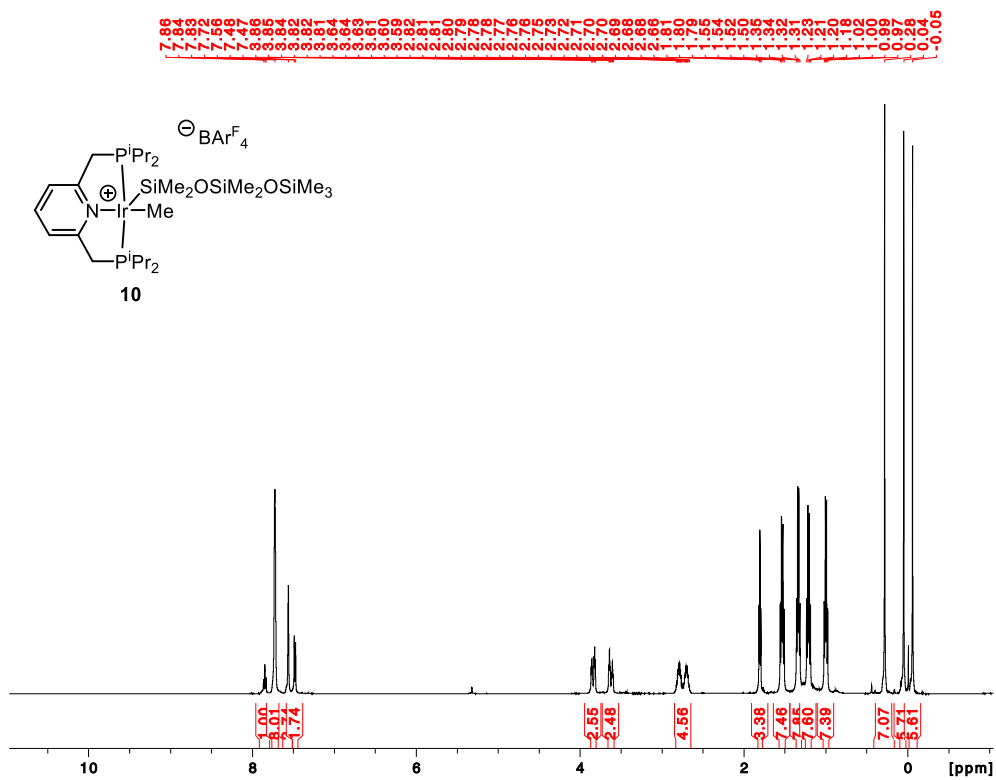


Figure 4.5.21. $^{31}\text{P}\{^1\text{H}\}$ NMR Spectrum of $[(\text{PNP}(\text{iPr})_4)\text{IrMe}(\text{SiMe}_2\text{OSiMe}_3)]\text{BArF}_4$ (**9**) (202 MHz, CD_2Cl_2).



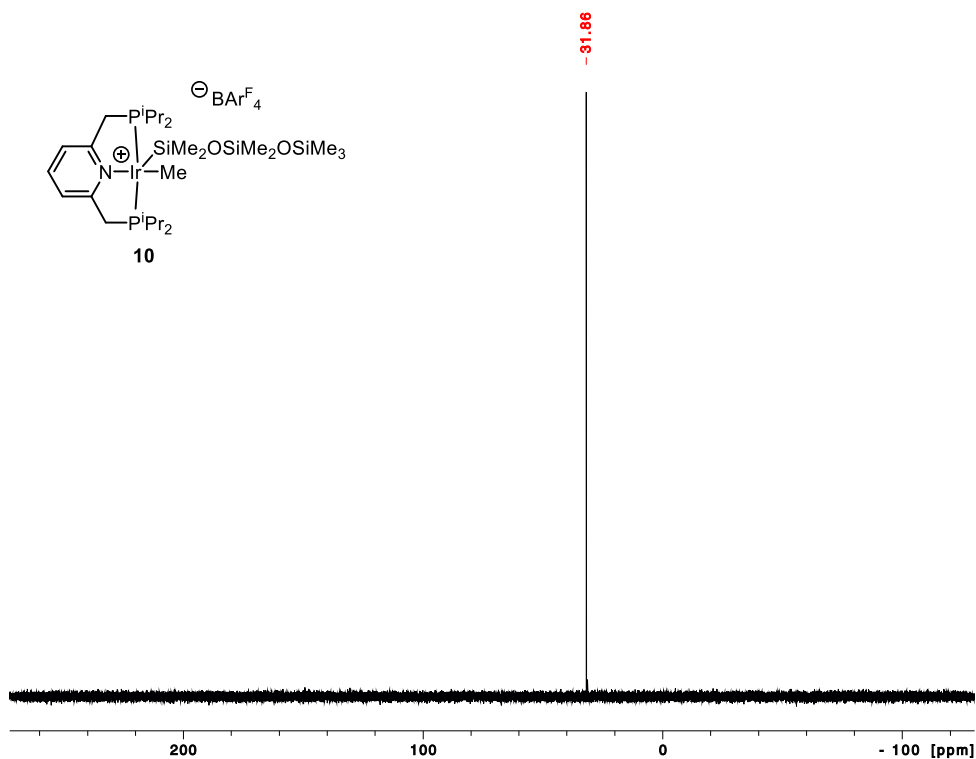


Figure 4.5.24. $^{31}\text{P}\{^1\text{H}\}$ NMR Spectrum of $[(\text{PNP}(^i\text{Pr})_4)\text{IrMe}(\text{SiMe}_2\text{OSiMe}_2\text{OSiMe}_3)]\text{BArF}_4$ (**10**) (202 MHz, CD_2Cl_2).

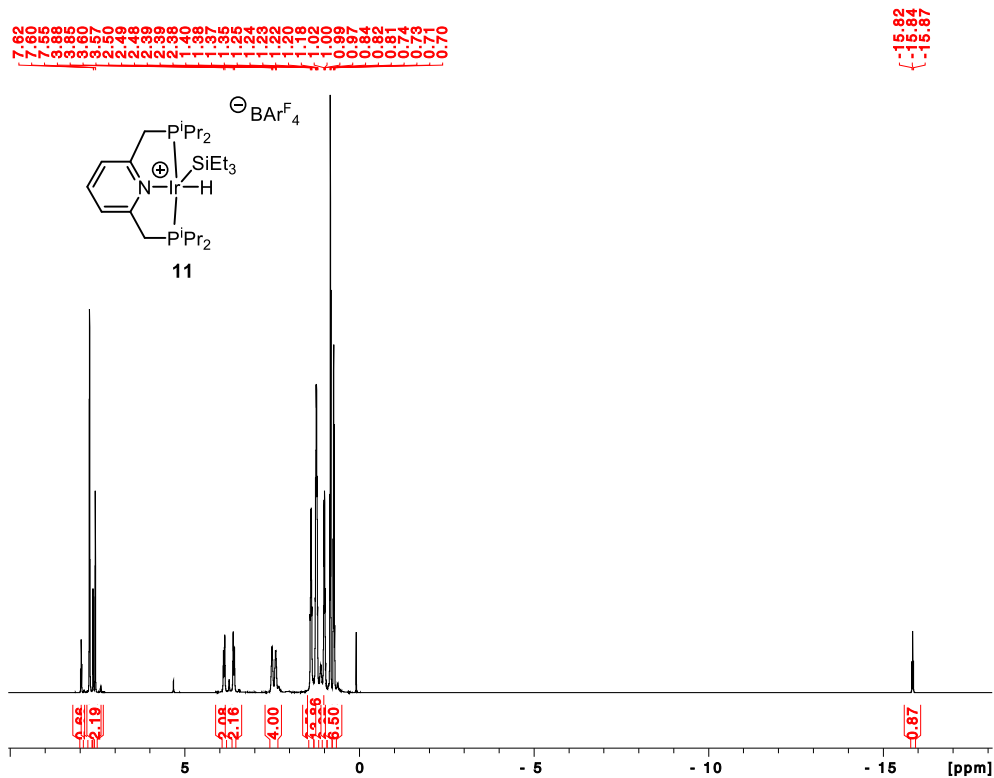


Figure 4.5.25. ^1H NMR Spectrum of $[(\text{PNP}(\text{iPr})_4)\text{IrH}(\text{SiEt}_3)]\text{BAr}^{\text{F}_4}$ (**11**) (500 MHz, CD_2Cl_2).

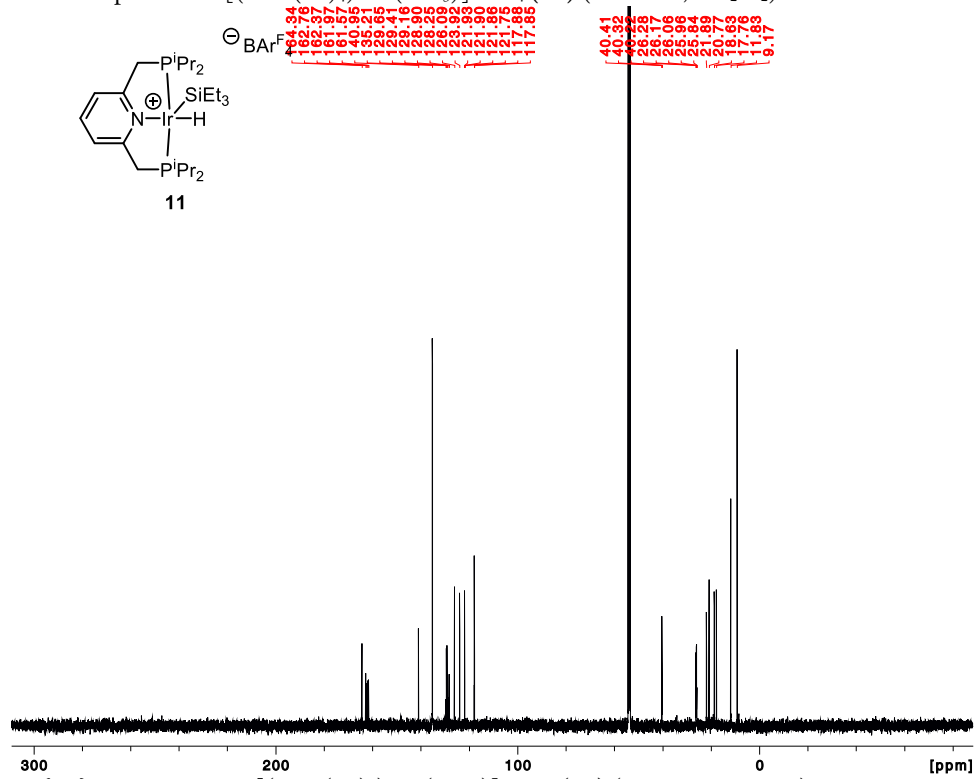


Figure 4.5.26. $^{13}\text{C}\{^1\text{H}\}$ NMR Spectrum $[(\text{PNP}(\text{iPr})_4)\text{IrH}(\text{SiEt}_3)]\text{BAr}^{\text{F}_4}$ (**11**) (126 MHz, CD_2Cl_2).

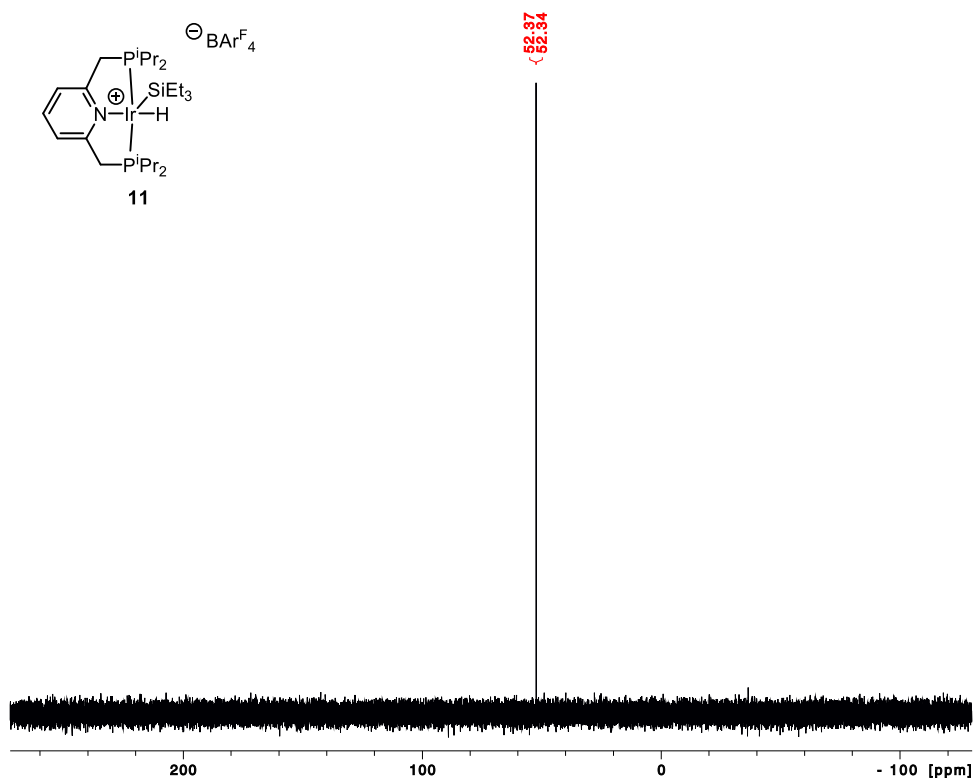


Figure 4.5.27. $^{31}\text{P}\{^1\text{H}\}$ NMR Spectrum $[(\text{PNP}(\text{iPr})_4)\text{IrH}(\text{SiEt}_3)]\text{BAr}^{\text{F}}_4$ (**11**) (202 MHz, CD_2Cl_2).

4.6 X-Ray Crystallography

Details of crystallographic refinement

General Methods. A suitable crystal of each sample was selected for analysis and mounted in a polyimide loop. Crystal samples were handled under immersion oil and quickly transferred to a cold nitrogen stream. All measurements were made on a Rigaku Oxford Diffraction Supernova Eos CCD with filtered Mo-K α or Cu-K α radiation at a temperature of 100 K. Using Olex2,⁹ the structure was solved with the ShelXT structure solution program using Direct Methods and refined with the ShelXL refinement package¹⁰ using Least Squares minimization.

Compound 3

Disorder in one trifluoromethyl group was modeled over two positions with similarity restraints placed on atomic thermal parameters and C-F bond distances.

Compound 4

A disordered trifluoromethyl group was modeled over two positions with similarity restraints placed on the C-F bond distances and atom thermal parameters.

Compound 5

Extensive two-site disorder of the iridium cation was modeled over two positions with similarity restraints placed on atomic bond distances and thermal parameters. Disorder in trifluoromethyl groups on the anion were modeled similarly.

Compound 6

The crystal was a non-merohedral twin with two components in a 56:44 ratio. Both components were integrated and refinement was done against a two-component hklf5 file. Disorder in a trifluoromethyl group of the anion was modeled over two positions with similarity restraints placed on the C-F bond distances and atom thermal parameters. 2-site disorder in the (SiOMe₃)IrMe fragment of the cation was modeled over two positions with similarity restraints placed on the bond distances and atom thermal parameters. The iridium thermal parameters were constrained to be identical. Two anti-bumping restraints were added to keep the low-occupancy OMe groups in a chemically-sensible position.

Compound 7

Disorder in the cation was modeled over two positions with similarity restraints placed on atomic bond distances and thermal parameters. Disorder in several trifluoromethyl groups on the anion was modeled in a similar fashion.

Compound 8

Disorder in trifluoromethyl groups was modeled over two positions with similarity restraints placed on C-F bond distances and atomic thermal parameters.

Compound 9

Disorder in trifluoromethyl groups was modeled over two positions with similarity restraints placed on atomic thermal parameters and C-F bond distances.

Compound 10

Disorder in trifluoromethyl groups was modeled over two positions with similarity restraints placed on atomic thermal parameters and C-F bond distances.

Compound 11

Disorder in trifluoromethyl groups was modeled over two positions with similarity restraints placed on C-F bond distances and atomic thermal parameters. The metal hydride was located in the difference map and refined without restraint.

Table 4.6.1. Crystal data and structure refinement for **3**.

Empirical formula	$C_{55}H_{59}BF_{24}IrNP_2Si$	
Formula weight	1483.07	
Temperature	100.00(10) K	
Wavelength	0.71073 Å	
Crystal system	Monoclinic	
Space group	P 1 21/n 1	
Unit cell dimensions	$a = 17.0144(2)$ Å	$\alpha = 90^\circ$
	$b = 14.30758(19)$ Å	$\beta = 103.3935(15)^\circ$
	$c = 24.9845(4)$ Å	$\gamma = 90^\circ$
Volume	$5916.68(15)$ Å ³	
Z	4	
Density (calculated)	1.665 Mg/m ³	
Absorption coefficient	2.445 mm ⁻¹	
F(000)	2952	
Crystal size	0.339 x 0.245 x 0.182 mm ³	
Theta range for data collection	2.322 to 29.472°.	
Index ranges	-23 ≤ h ≤ 22, -19 ≤ k ≤ 19, -32 ≤ l ≤ 32	
Reflections collected	66888	
Independent reflections	14691 [R(int) = 0.0392]	
Completeness to theta = 25.242°	99.9 %	
Absorption correction	Gaussian	
Max. and min. transmission	1.000 and 0.458	
Refinement method	Full-matrix least-squares on F ²	
Data / restraints / parameters	14691 / 124 / 815	
Goodness-of-fit on F ²	1.038	
Final R indices [I > 2σ(I)]	R1 = 0.0307, wR2 = 0.0669	
R indices (all data)	R1 = 0.0386, wR2 = 0.0705	
Largest diff. peak and hole	1.751 and -1.311 e/Å ⁻³	

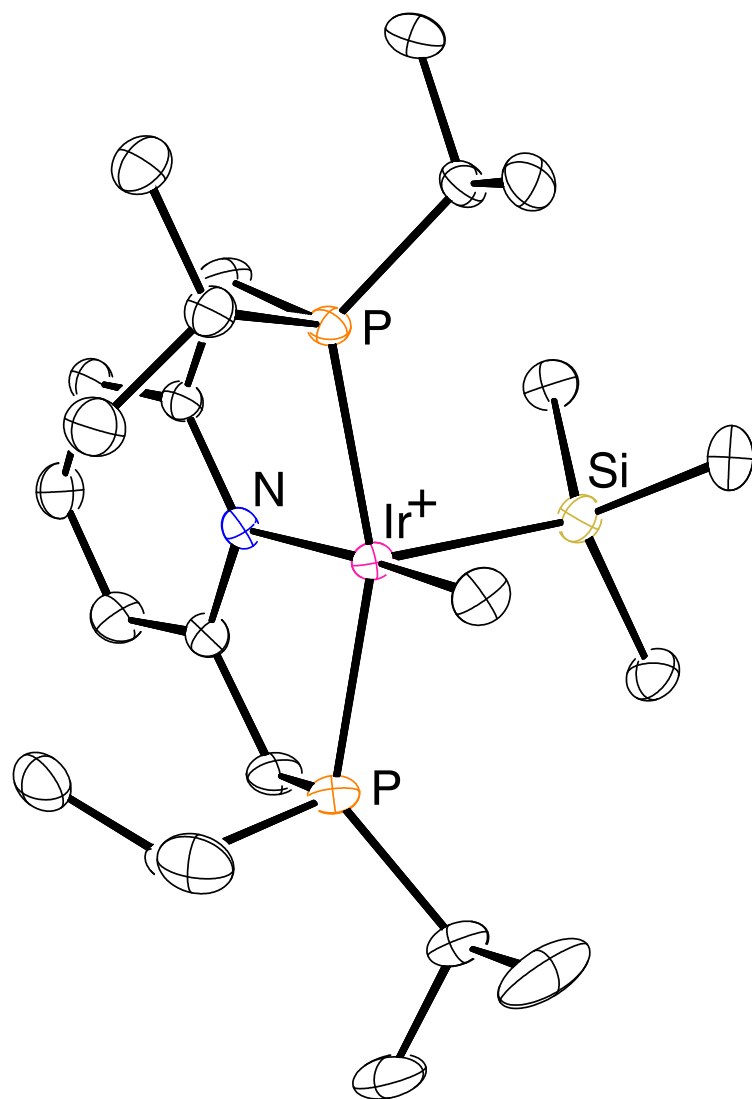


Figure 4.6.1. ORTEP diagram of 3 with ellipsoids shown at 50%. The anion is omitted for clarity.

Table 4.6.2. Crystal data and structure refinement for 4.

Empirical formula	$C_{53}H_{59}BF_{24}IrNOP_2Si$	
Formula weight	1499.07	
Temperature	100.01(10) K	
Wavelength	1.54184 Å	
Crystal system	Monoclinic	
Space group	P 1 21/c 1	
Unit cell dimensions	$a = 12.16585(9)$ Å	$\alpha = 90^\circ$
	$b = 12.79696(11)$ Å	$\beta = 97.7046(7)^\circ$
	$c = 39.1793(3)$ Å	$\gamma = 90^\circ$
Volume	$6044.60(8)$ Å ³	
Z	4	
Density (calculated)	1.647 Mg/m ³	
Absorption coefficient	5.994 mm ⁻¹	
F(000)	2984	
Crystal size	0.192 x 0.121 x 0.041 mm ³	
Theta range for data collection	3.637 to 73.507°.	
Index ranges	-15 <= h <= 14, -15 <= k <= 13, -48 <= l <= 48	
Reflections collected	70861	
Independent reflections	12044 [R(int) = 0.0280]	
Completeness to theta = 67.684°	100.0 %	
Absorption correction	Gaussian	
Max. and min. transmission	0.918 and 0.447	
Refinement method	Full-matrix least-squares on F ²	
Data / restraints / parameters	12044 / 46 / 824	
Goodness-of-fit on F ²	1.051	
Final R indices [I > 2sigma(I)]	R1 = 0.0433, wR2 = 0.1110	
R indices (all data)	R1 = 0.0456, wR2 = 0.1129	
Largest diff. peak and hole	2.139 and -1.085 e/Å ⁻³	

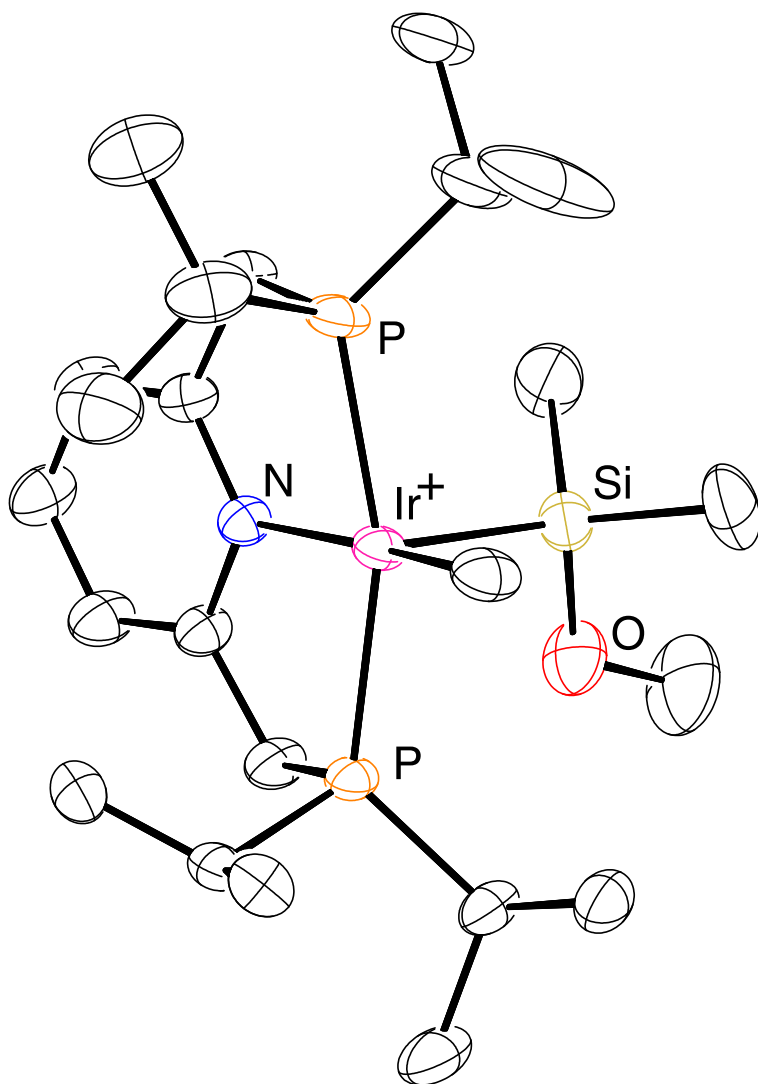


Figure 4.6.2. ORTEP diagram of 4 with ellipsoids shown at 50%. The anion is omitted for clarity.

Table 4.6.3. Crystal data and structure refinement for **5**.

Empirical formula	$C_{55}H_{59}BF_{24}IrNO_2P_2Si$	
Formula weight	1515.07	
Temperature	99.98(10) K	
Wavelength	1.54184 Å	
Crystal system	Monoclinic	
Space group	$P 1 21/c 1$	
Unit cell dimensions	$a = 12.2722(4)$ Å	$\alpha = 90^\circ$
	$b = 12.8166(3)$ Å	$\beta = 97.402(3)^\circ$
	$c = 39.0118(10)$ Å	$\gamma = 90^\circ$
Volume	$6084.9(3)$ Å ³	
Z	4	
Density (calculated)	1.654 Mg/m ³	
Absorption coefficient	5.975 mm ⁻¹	
F(000)	3016	
Crystal size	$0.081 \times 0.058 \times 0.022$ mm ³	
Theta range for data collection	3.632 to 72.082° .	
Index ranges	$-14 < h < 14$, $-11 < k < 15$, $-46 < l < 47$	
Reflections collected	45532	
Independent reflections	11767 [R(int) = 0.0722]	
Completeness to theta = 67.684°	99.9 %	
Absorption correction	Gaussian	
Max. and min. transmission	0.912 and 0.712	
Refinement method	Full-matrix least-squares on F ²	
Data / restraints / parameters	11767 / 1289 / 1189	
Goodness-of-fit on F2	1.056	
Final R indices [I > 2sigma(I)]	R1 = 0.0713, wR2 = 0.1846	
R indices (all data)	R1 = 0.0913, wR2 = 0.2010	
Largest diff. peak and hole	2.063 and -1.085 e/Å ⁻³	

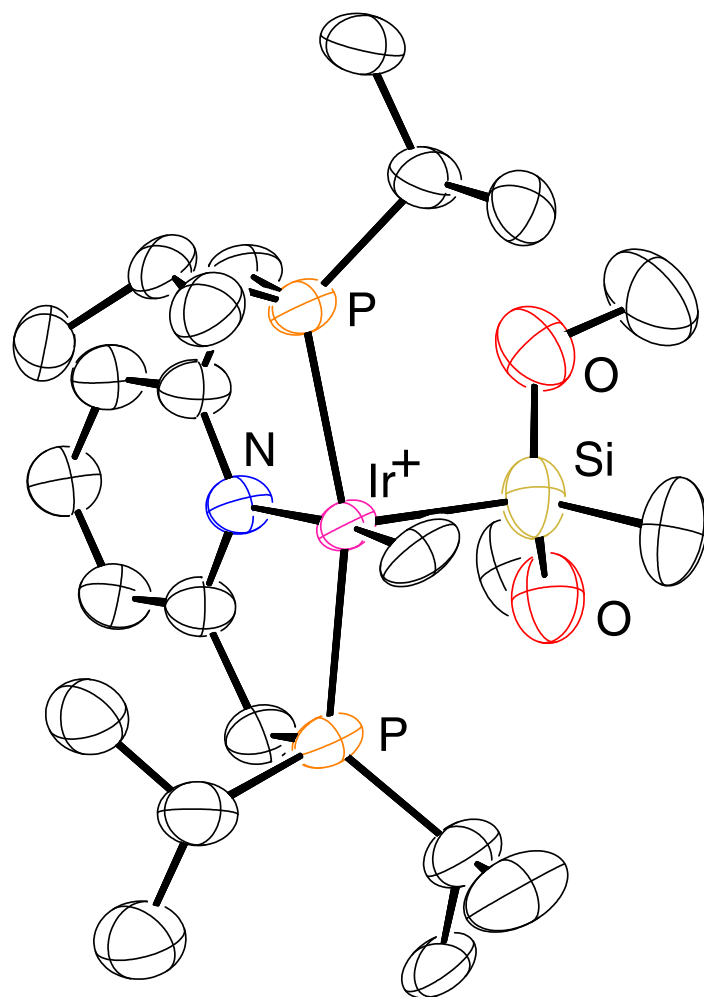


Figure 4.6.3. ORTEP diagram of **5** with ellipsoids shown at 50%. The anion and the full disorder model of the cation is omitted for clarity.

Table 4.6.4. Crystal data and structure refinement for **6**.

Empirical formula	$C_{55}H_{59}BF_{24}IrNO_3P_2Si$	
Formula weight	1531.07	
Temperature	99.97(15) K	
Wavelength	1.54184 Å	
Crystal system	Triclinic	
Space group	P-1	
Unit cell dimensions	$a = 13.1917(8) \text{ \AA}$	$\alpha = 106.129(5)^\circ$
	$b = 13.2106(8) \text{ \AA}$	$\beta = 98.354(5)^\circ$
	$c = 18.5480(12) \text{ \AA}$	$\gamma = 95.022(5)^\circ$
Volume	$3044.2(3) \text{ \AA}^3$	
Z	2	
Density (calculated)	1.670 Mg/m^3	
Absorption coefficient	5.991 mm^{-1}	
F(000)	1524	
Crystal size	$0.102 \times 0.083 \times 0.059 \text{ mm}^3$	
Theta range for data collection	2.520 to 73.708° .	
Index ranges	$-16 \leq h \leq 16, -16 \leq k \leq 16, -22 \leq l \leq 23$	
Reflections collected	18884	
Completeness to $\theta = 67.684^\circ$	100.0 %	
Absorption correction	Gaussian	
Max. and min. transmission	0.892 and 0.620	
Refinement method	Full-matrix least-squares on F^2	
Data / restraints / parameters	18884 / 362 / 916	
Goodness-of-fit on F^2	1.053	
Final R indices [$I > 2\sigma(I)$]	R1 = 0.0553, wR2 = 0.1502	
R indices (all data)	R1 = 0.0596, wR2 = 0.1535	
Largest diff. peak and hole	2.475 and $-1.485 \text{ e/\AA}^{-3}$	

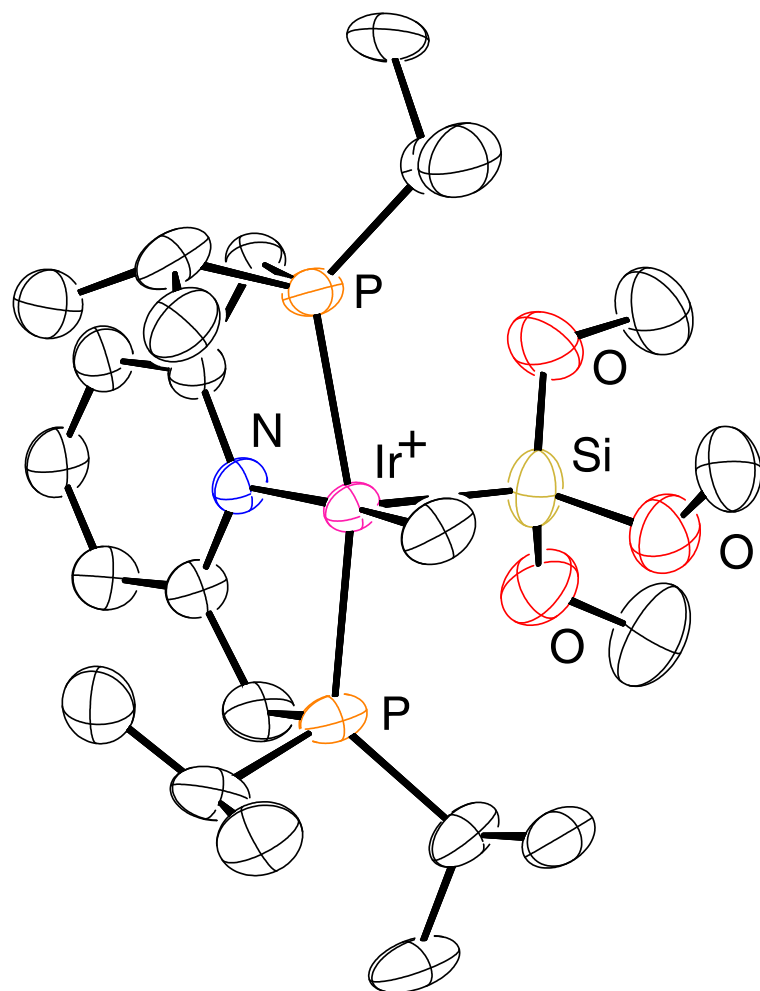


Figure 4.6.4. ORTEP diagram of **6** with ellipsoids shown at 50%. The anion and the full disorder model of the cation is omitted for clarity.

Table 4.6.5. Crystal data and structure refinement for 7.

Empirical formula	$C_{56}H_{61}BF_{24}IrNOP_2Si$	
Formula weight	1513.09	
Temperature	100.01(10) K	
Wavelength	1.54184 Å	
Crystal system	Monoclinic	
Space group	P 1 21/c 1	
Unit cell dimensions	a = 12.35830(10) Å	$\alpha = 90^\circ$
	b = 12.84960(10) Å	$\beta = 98.5490(10)^\circ$
	c = 39.0336(3) Å	$\gamma = 90^\circ$
Volume	6129.63(8) Å ³	
Z	4	
Density (calculated)	1.640 Mg/m ³	
Absorption coefficient	5.917 mm ⁻¹	
F(000)	3016	
Crystal size	0.179 x 0.094 x 0.013 mm ³	
Theta range for data collection	3.617 to 71.841°.	
Index ranges	-15 < h <= 15, -15 <= k <= 13, -47 <= l <= 47	
Reflections collected	88001	
Independent reflections	11960 [R(int) = 0.0503]	
Completeness to theta = 67.684°	100.0 %	
Absorption correction	Gaussian	
Max. and min. transmission	1.000 and 0.522	
Refinement method	Full-matrix least-squares on F ²	
Data / restraints / parameters	11960 / 1190 / 1178	
Goodness-of-fit on F ²	1.078	
Final R indices [I > 2sigma(I)]	R1 = 0.0630, wR2 = 0.1653	
R indices (all data)	R1 = 0.0719, wR2 = 0.1723	
Largest diff. peak and hole	2.059 and -1.151 e/Å ⁻³	

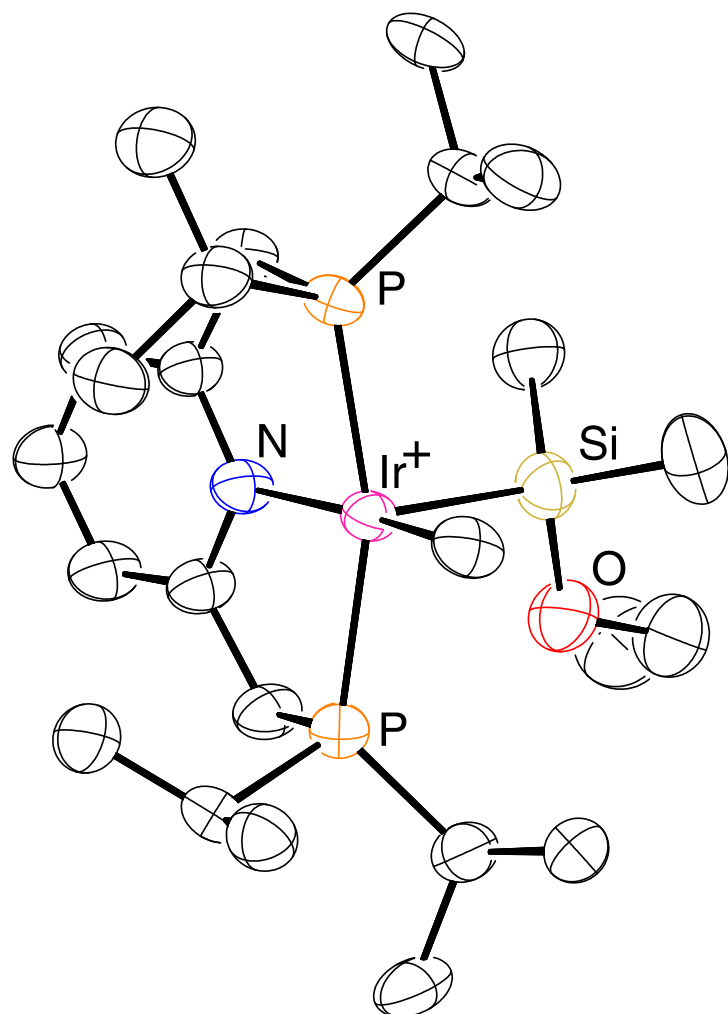


Figure 4.6.5. ORTEP diagram of 7 with ellipsoids shown at 50%. The anion and the full disorder model of the cation is omitted for clarity.

Table 4.6.6. Crystal data and structure refinement for **8**.

Empirical formula	$C_{53}H_{36}BF_{27}IrNP_2Si$	
Formula weight	1537.04	
Temperature	100(1) K	
Wavelength	1.54184 Å	
Crystal system	Monoclinic	
Space group	P 1 21/c 1	
Unit cell dimensions	$a = 12.34370(10)$ Å	$\alpha = 90^\circ$
	$b = 17.54890(10)$ Å	$\beta = 90.3000(10)^\circ$
	$c = 28.67270(10)$ Å	$\gamma = 90^\circ$
Volume	$6210.95(7)$ Å ³	
Z	4	
Density (calculated)	1.644 Mg/m ³	
Absorption coefficient	5.910 mm ⁻¹	
F(000)	3048	
Crystal size	0.214 x 0.107 x 0.062 mm ³	
Theta range for data collection	2.952 to 73.105°.	
Index ranges	-14 <= h <= 15, -21 <= k <= 21, -35 <= l <= 34	
Reflections collected	46503	
Independent reflections	12219 [R(int) = 0.0282]	
Completeness to theta = 67.684°	100.0 %	
Absorption correction	Gaussian	
Max. and min. transmission	0.810 and 0.467	
Refinement method	Full-matrix least-squares on F ²	
Data / restraints / parameters	12219 / 199 / 869	
Goodness-of-fit on F2	1.051	
Final R indices [I > 2sigma(I)]	R1 = 0.0238, wR2 = 0.0543	
R indices (all data)	R1 = 0.0255, wR2 = 0.0552	
Largest diff. peak and hole	0.586 and -0.520 e/Å ⁻³	

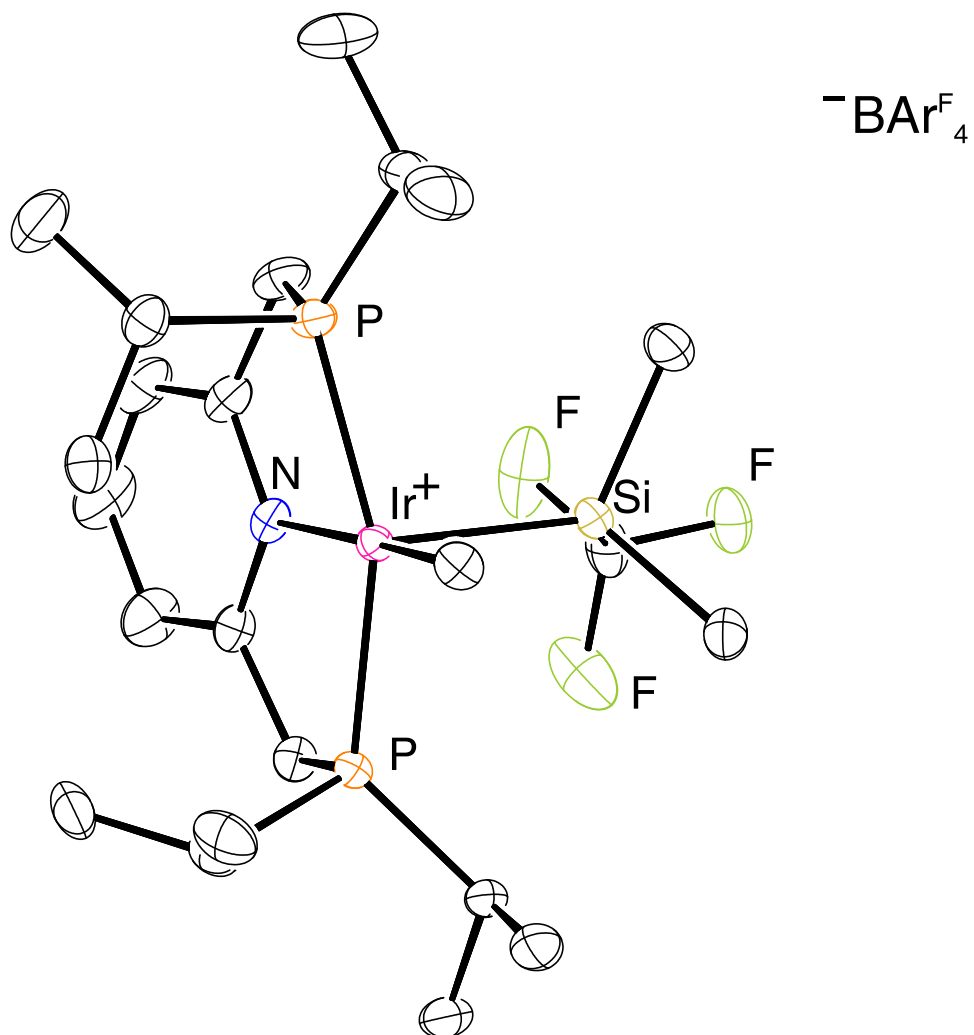


Figure 4.6.6. ORTEP diagram of **8** with ellipsoids shown at 50%. The anion is omitted for clarity.

Table 4.6.7. Crystal data and structure refinement for **9**.

Empirical formula	$C_{57}H_{65}BF_{24}IrNOP_2Si_2$	
Formula weight	1557.23	
Temperature	99.98(10) K	
Wavelength	1.54184 Å	
Crystal system	Monoclinic	
Space group	P 1 21/n 1	
Unit cell dimensions	$a = 18.46133(13)$ Å	$\alpha = 90^\circ$
	$b = 18.58127(12)$ Å	$\beta = 101.4003(7)^\circ$
	$c = 19.29978(15)$ Å	$\gamma = 90^\circ$
Volume	6489.88(8) Å ³	
Z	4	
Density (calculated)	1.594 Mg/m ³	
Absorption coefficient	5.777 mm ⁻¹	
F(000)	3112	
Crystal size	0.208 x 0.062 x 0.021 mm ³	
Theta range for data collection	3.027 to 71.861°.	
Index ranges	-22 <= h <= 22, -14 <= k <= 22, -23 <= l <= 23	
Reflections collected	49527	
Independent reflections	12569 [R(int) = 0.0423]	
Completeness to theta = 67.684°	99.9 %	
Absorption correction	Gaussian	
Max. and min. transmission	1.000 and 0.397	
Refinement method	Full-matrix least-squares on F ²	
Data / restraints / parameters	12569 / 274 / 909	
Goodness-of-fit on F2	1.043	
Final R indices [I > 2sigma(I)]	R1 = 0.0394, wR2 = 0.0929	
R indices (all data)	R1 = 0.0452, wR2 = 0.0966	
Largest diff. peak and hole	2.380 and -1.607 e/Å ⁻³	

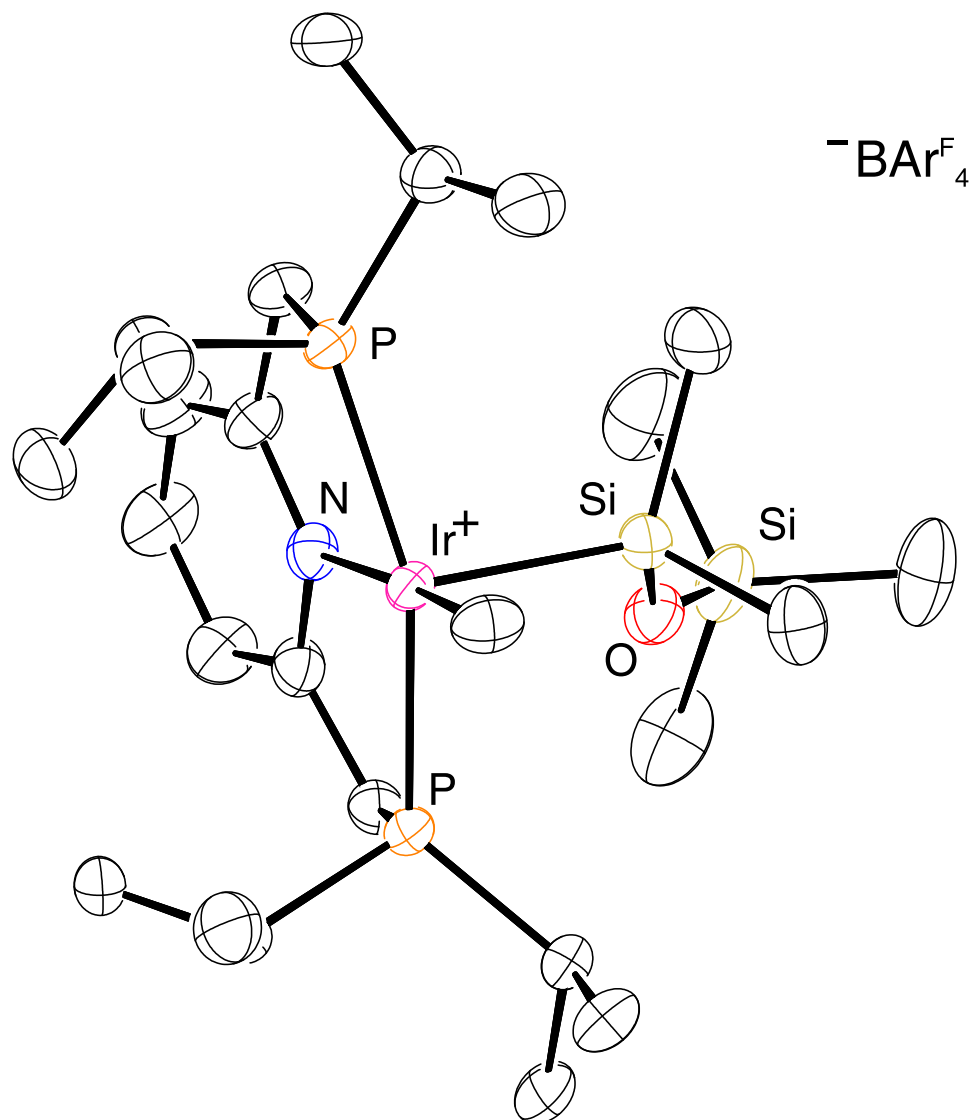


Figure 4.6.7. ORTEP diagram of **9** with ellipsoids shown at 50%. The anion is omitted for clarity.

Table 4.6.8. Crystal data and structure refinement for **10**.

Empirical formula	$C_{59}H_{71}BF_{24}IrNO_2P_2Si_3$	
Formula weight	1631.38	
Temperature	99.98(10) K	
Wavelength	0.71073 Å	
Crystal system	Monoclinic	
Space group	P 1 21/n 1	
Unit cell dimensions	a = 15.5274(3) Å	$\alpha = 90^\circ$
	b = 25.4071(7) Å	$\beta = 92.4951(17)^\circ$
	c = 17.3544(4) Å	$\gamma = 90^\circ$
Volume	6839.9(3) Å ³	
Z	4	
Density (calculated)	1.584 Mg/m ³	
Absorption coefficient	2.158 mm ⁻¹	
F(000)	3272	
Crystal size	0.291 x 0.288 x 0.172 mm ³	
Theta range for data collection	2.349 to 29.446°.	
Index ranges	-17 <= h <= 20, -26 <= k <= 35, -21 <= l <= 23	
Reflections collected	63373	
Independent reflections	16436 [R(int) = 0.0497]	
Completeness to theta = 25.242°	99.9 %	
Absorption correction	Gaussian	
Max. and min. transmission	1.000 and 0.386	
Refinement method	Full-matrix least-squares on F ²	
Data / restraints / parameters	16436 / 150 / 910	
Goodness-of-fit on F2	1.029	
Final R indices [I > 2sigma(I)]	R1 = 0.0397, wR2 = 0.0777	
R indices (all data)	R1 = 0.0543, wR2 = 0.0842	
Largest diff. peak and hole	1.808 and -0.984 e/Å ⁻³	

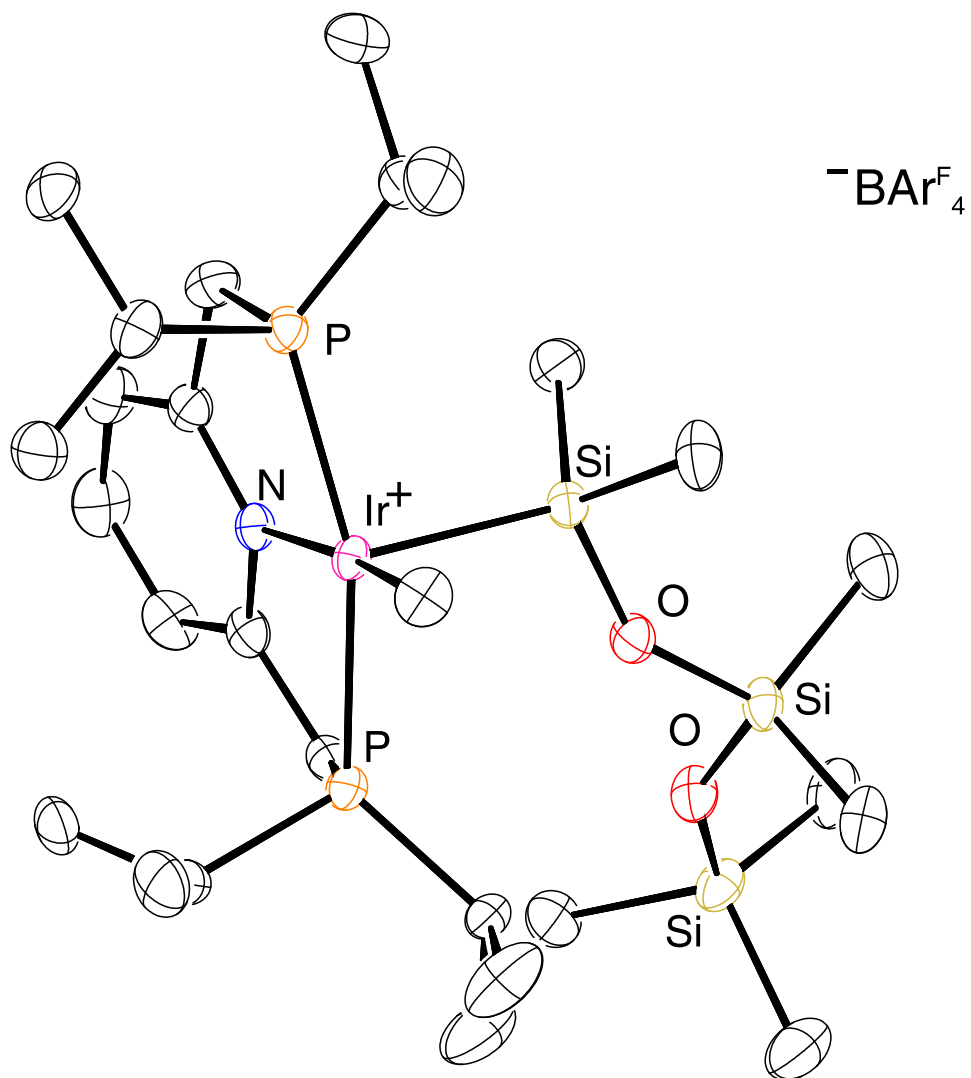


Figure 4.6.8. ORTEP diagram of **10** with ellipsoids shown at 50%. The anion is omitted for clarity.

Table 4.6.9. Crystal data and structure refinement for **11**.

Empirical formula	$C_{57}H_{63}BF_{24}IrNP_2Si$	
Formula weight	1511.12	
Temperature	100.0(4) K	
Wavelength	1.54184 Å	
Crystal system	Monoclinic	
Space group	I 1 2/a 1	
Unit cell dimensions	$a = 25.63408(16)$ Å	$\alpha = 90^\circ$
	$b = 13.82077(7)$ Å	$\beta = 103.0837(6)^\circ$
	$c = 35.5938(2)$ Å	$\gamma = 90^\circ$
Volume	12282.89(13) Å ³	
Z	8	
Density (calculated)	1.634 Mg/m ³	
Absorption coefficient	5.892 mm ⁻¹	
F(000)	6032	
Crystal size	0.459 x 0.306 x 0.123 mm ³	
Theta range for data collection	2.549 to 71.831°.	
Index ranges	-31 < h <= 30, -16 <= k <= 16, -43 <= l <= 42	
Reflections collected	50142	
Independent reflections	11874 [R(int) = 0.0277]	
Completeness to theta = 67.684°	100.0 %	
Absorption correction	Gaussian	
Max. and min. transmission	1.000 and 0.148	
Refinement method	Full-matrix least-squares on F ²	
Data / restraints / parameters	11874 / 156 / 855	
Goodness-of-fit on F ²	1.096	
Final R indices [I > 2sigma(I)]	R1 = 0.0283, wR2 = 0.0700	
R indices (all data)	R1 = 0.0286, wR2 = 0.0703	
Largest diff. peak and hole	2.229 and -1.005 e/Å ⁻³	

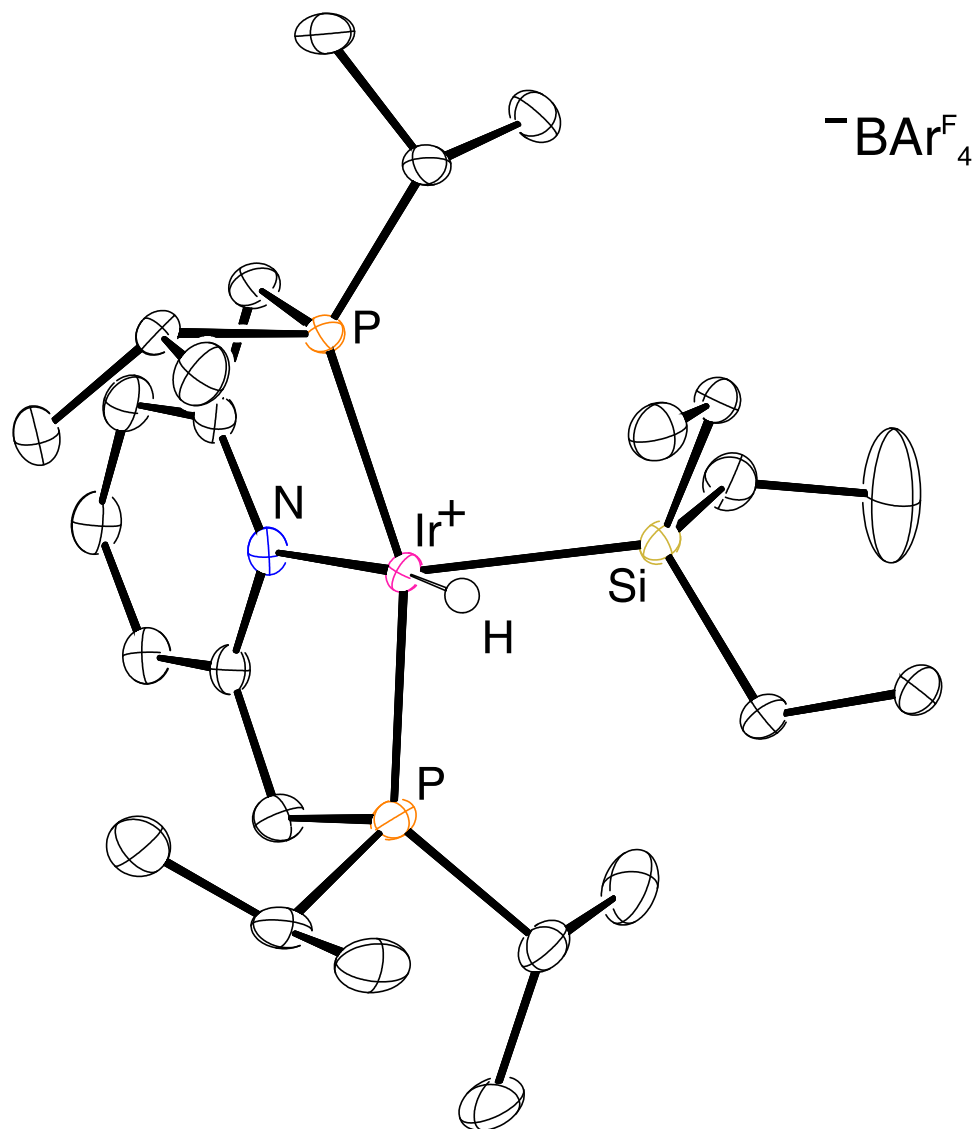


Figure 4.6.9. ORTEP diagram of **11** with ellipsoids shown at 50%. The anion is omitted for clarity.

4.7 References

- (1) Scott, H. G. Crosslinking of olefinic polymers and copolymers. GB1286460A, 1972.
- (2) Narkis, M.; Tzur, A.; Vaxman, A.; Fritz, H. G., Some properties of silane-grafted moisture-crosslinked polyethylene. *Polymer Engineering & Science* **1985**, *25*, 857-862.
- (3) Sore, H. F.; Galloway, W. R. J. D.; Spring, D. R., Palladium-catalysed cross-coupling of organosilicon reagents. *Chem. Soc. Rev.* **2012**, *41*, 1845-1866.
- (4) Nakao, Y.; Hiyama, T., Silicon-based cross-coupling reaction: an environmentally benign version. *Chem. Soc. Rev.* **2011**, *40*, 4893-4901.

- (5) Troegel, D.; Stohrer, J., Recent advances and actual challenges in late transition metal catalyzed hydrosilylation of olefins from an industrial point of view. *Coord. Chem. Rev.* **2011**, *255*, 1440-1459.
- (6) Gao, W.; Ding, S., Progress on Iridium-Catalyzed Hydrosilylation of Alkenes and Alkynes. *Synthesis* **2020**, *52*, 3549-3563.
- (7) Cheng, C.; Hartwig, J. F., Catalytic Silylation of Unactivated C–H Bonds. *Chem. Rev.* **2015**, *115*, 8946-8975.
- (8) Karmel, C.; Hartwig, J. F., Mechanism of the Iridium-Catalyzed Silylation of Aromatic C–H Bonds. *J. Am. Chem. Soc.* **2020**, *142*, 10494-10505.
- (9) Ishiyama, T.; Sato, K.; Nishio, Y.; Miyaura, N., Direct Synthesis of Aryl Halosilanes through Iridium(I)-Catalyzed Aromatic C–H Silylation by Disilanes. *Angew. Chem. Int. Ed.* **2003**, *42*, 5346-5348.
- (10) Cheng, C.; Hartwig, J. F., Rhodium-Catalyzed Intermolecular C–H Silylation of Arenes with High Steric Regiocontrol. *Science* **2014**, *343*, 853-857.
- (11) Esteruelas, M. A.; Martínez, A.; Oliván, M.; Oñate, E., Kinetic Analysis and Sequencing of Si–H and C–H Bond Activation Reactions: Direct Silylation of Arenes Catalyzed by an Iridium-Polyhydride. *J. Am. Chem. Soc.* **2020**, *142*, 19119-19131.
- (12) Ozawa, F.; Hikida, T.; Hayashi, T., Reductive Elimination of *cis*-PtMe(SiPh₃)(PMePh₂)₂. *J. Am. Chem. Soc.* **1994**, *116*, 2844-2849.
- (13) Hasebe, K.; Kamite, J.; Mori, T.; Katayama, H.; Ozawa, F., Thermolysis Reactions of *cis*-PtR(SiPh₃)(PMe₂Ph)₂ in Solution. *Organometallics* **2000**, *19*, 2022-2030.
- (14) McBee, J. L.; Tilley, T. D., Synthesis and Reactivity of Iridium and Rhodium Silyl Complexes Supported by a Bipyridine Ligand. *Organometallics* **2009**, *28*, 5072-5081.
- (15) Zhang, Y.; Schley, N. D., Reversible Alkoxycarbene Formation by C–H Activation of Ethers via Discrete, Isolable Intermediates. *Chem. Commun.* **2017**, *53*, 2130-2133.
- (16) Zhang, Y.; Mueller, B. R. J.; Schley, N. D., Formation of a Delocalized Iridium Benzylidene with Azaquinone Methide Character via Alkoxycarbene Cleavage. *Organometallics* **2018**, *37*, 1825-1828.
- (17) Chapp, S. M.; Schley, N. D., Group-Transfer Reactions of a Cationic Iridium Alkoxycarbene Generated by Ether Dehydrogenation. *Inorg. Chem.* **2020**, *59*, 7143-7149.
- (18) Tanaka, Y.; Yamashita, H.; Shimada, S.; Tanaka, M., The First Alkyl(silyl)palladium Complexes: Formation by Oxidative Addition of Silacyclobutanes to Palladium Complexes, Reductive Elimination, and Other Reactivities Relevant to Catalysis. *Organometallics* **1997**, *16*, 3246-3248.

- (19) Sakaki, S.; Ieki, M., Oxidative addition reactions of saturated Si-X bonds (X = H, F, C, or Si) to Pt(PH₃)₂. An ab initio MO/MP4 study. *J. Am. Chem. Soc.* **1993**, *115*, 2373-2381.
- (20) Bärsch, S.; Böhme, T.; Schröder, D.; Schwarz, H., Theoretical and experimental studies on the activation of ethylsilane by bare Co⁺ cations. *Int. J. Mass spectrom.* **2000**, *199*, 107-125.
- (21) Algarra, A. G.; Macgregor, S. A.; Panetier, J. A., Mechanistic Studies of CX Bond Activation at Transition-Metal Centers. In *Comprehensive Inorganic Chemistry II (Second Edition)*, Reedijk, J.; Poeppelmeier, K., Eds. Elsevier: Amsterdam, 2013; pp 635-694.
- (22) Hartwig, J. F.; Romero, E. A., Iridium-catalyzed silylation of unactivated C–H bonds. *Tetrahedron* **2019**, *75*, 4059-4070.
- (23) Sadow, A. D.; Tilley, T. D., Catalytic Functionalization of Hydrocarbons by σ -Bond-Metathesis Chemistry: Dehydrosilylation of Methane with a Scandium Catalyst. *Angew. Chem. Int. Ed.* **2003**, *42*, 803-805.
- (24) Sakurai, T.; Matsuoka, Y.; Hanataka, T.; Fukuyama, N.; Namikoshi, T.; Watanabe, S.; Murata, M., Ruthenium-catalyzed Ortho-selective Aromatic C–H Silylation: Acceptorless Dehydrogenative Coupling of Hydrosilanes. *Chem. Lett.* **2012**, *41*, 374-376.
- (25) Miki, M.; Naoaki, F.; Jun-ichi, W.; Shinji, W.; Yuzuru, M., Platinum-catalyzed Aromatic C–H Silylation of Arenes with 1,1,1,3,5,5,5-Heptamethyltrisiloxane. *Chem. Lett.* **2007**, *36*, 910-911.
- (26) Cheng, C.; Hartwig, J. F., Iridium-Catalyzed Silylation of Aryl C–H Bonds. *J. Am. Chem. Soc.* **2015**, *137*, 592-595.
- (27) Cheng, C.; Hartwig, J. F., Mechanism of the Rhodium-Catalyzed Silylation of Arene C–H Bonds. *J. Am. Chem. Soc.* **2014**, *136*, 12064-12072.
- (28) Karmel, C.; Rubel, C. Z.; Kharitonova, E. V.; Hartwig, J. F., Iridium-Catalyzed Silylation of Five-Membered Heteroarenes: High Sterically Derived Selectivity from a Pyridyl-Imidazoline Ligand. *Angew. Chem. Int. Ed.* **2020**, *59*, 6074-6081.
- (29) Karmel, C.; Chen, Z.; Hartwig, J. F., Iridium-Catalyzed Silylation of C–H Bonds in Unactivated Arenes: A Sterically Encumbered Phenanthroline Ligand Accelerates Catalysis. *J. Am. Chem. Soc.* **2019**, *141*, 7063-7072.
- (30) Takada, K.; Hanataka, T.; Namikoshi, T.; Watanabe, S.; Murata, M., Ruthenium-Catalyzed Dehydrogenative Aromatic C–H Silylation of Benzamides with Hydrosilanes. *Adv. Synth. Catal.* **2015**, *357*, 2229-2232.
- (31) Kon, K.; Suzuki, H.; Takada, K.; Kohari, Y.; Namikoshi, T.; Watanabe, S.; Murata, M., Site-Selective Aliphatic C–H Silylation of 2-Alkyloxazolines Catalyzed by Ruthenium Complexes. *ChemCatChem* **2016**, *8*, 2202-2205.
- (32) Sakaki, S.; Mizoe, N.; Sugimoto, M., Theoretical Study of Platinum(0)-Catalyzed Hydrosilylation of Ethylene. Chalk–Harrod

- Mechanism or Modified Chalk–Harrod Mechanism. *Organometallics* **1998**, *17*, 2510-2523.
- (33) Hübler, K.; Hunt, P. A.; Maddock, S. M.; Rickard, C. E. F.; Roper, W. R.; Salter, D. M.; Schwerdtfeger, P.; Wright, L. J., Examination of Metal–Silicon Bonding through Structural and Theoretical Studies of an Isostructural Set of Five-Coordinate Silyl Complexes, $\text{Os}(\text{SiR}_3)\text{Cl}(\text{CO})(\text{PPh}_3)_2$ (R = F, Cl, OH, Me). *Organometallics* **1997**, *16*, 5076-5083.
- (34) Lemke, F. R.; Simons, R. S.; Youngs, W. J., (η^1 -Pentamethylcyclopentadienyl)silyl Complexes of Ruthenium. Preparation, Reactivity, and X-ray Crystal Structure of $\text{Cp}(\text{PMe}_3)_2\text{RuSiCl}_2(\eta^1\text{-Cp}^*)$. *Organometallics* **1996**, *15*, 216-221.
- (35) Lemke, F. R.; Chaitheerapapkul, C., Silyl and bis(silyl)hydride complexes of ruthenium: Effect of ancillary groups on the oxidative addition of Si-H bonds. *Polyhedron* **1996**, *15*, 2559-2565.
- (36) Corey, J. Y.; Braddock-Wilking, J., Reactions of Hydrosilanes with Transition-Metal Complexes: Formation of Stable Transition-Metal Silyl Compounds. *Chem. Rev.* **1999**, *99*, 175-292.
- (37) Wanandi, P. W.; Tilley, T. D., Osmium Alkyl and Silyl Derivatives with Cyclopentadienyl(phosphine) and Pentamethylcyclopentadienyl(phosphine) Ligand Sets. *Organometallics* **1997**, *16*, 4299-4313.
- (38) de Charentenay, F.; Osborn, J. A.; Wilkinson, G., Interaction of silanes with tris(triphenylphosphine)chlororhodium(I) and other rhodium complexes; hydrosilation of hex-1-ene by use of trichlorosilane. *Journal of the Chemical Society A: Inorganic, Physical, Theoretical* **1968**, 787-790.
- (39) Haszeldine, R. N.; Parish, R. V.; Taylor, R. J., Organosilicon chemistry. Part XII. Stability and catalytic activity of some chlorohydridobis(phosphine)(silyl)rhodium(III) complexes. *J. Chem. Soc., Dalton Trans.* **1974**, 2311-2315.
- (40) Chalk, A. J.; Harrod, J. F., Homogeneous Catalysis. II. The Mechanism of the Hydrosilation of Olefins Catalyzed by Group VIII Metal Complexes. *J. Am. Chem. Soc.* **1965**, *87*, 16-21.
- (41) Rejhon, J.; Hetflejš, J., Catalytic Activity of Rhodium(I) Complexes in Hydrosilylation of Alkenes. *Collect. Czech. Chem. Commun.* **1975**, *40*, 3680-3687.
- (42) Haszeldine, R. N.; Parish, R. V.; Parry, D. J., Organosilicon chemistry. Part V. Rhodium(III)–silyl complexes and the hydrosilation of hex-1-ene. *Journal of the Chemical Society A: Inorganic, Physical, Theoretical* **1969**, 683-690.
- (43) Duczmal, W.; Śliwińska, E.; Maciejewska, B.; Marciniak, B.; Maciejewski, H., Stereoelectronic effects of substituents at silicon on the hydrosilylation of 1-hexene catalysed by $[\text{RhCl}(\text{cod})(1\text{-hexene})]$. *Transition Met. Chem.* **1995**, *20*, 435-439.
- (44) Ozawa, F., The chemistry of organo(silyl)platinum(II) complexes relevant to catalysis. *Journal of Organometallic Chemistry* **2000**, *611*, 332-342.

Chapter V

PROGRESS TOWARDS TANDEM OLIGOMERIZATION/HYDROGENATION OF SIMPLE OLEFINS TO BRANCHED ALKANES

5.1 Introduction

With the earth's population ever increasing, the demand for energy is expected to rise by 56% by 2040 compared to 2010.¹ As of 2019, 28% of the total energy consumption of the United States was for transportation purposes and 91% of that energy was derived from petroleum products.² With more than a quarter of energy being used with combustion engines, the need for reducing CO₂ levels has never been more dire. While long term solutions to the energy crisis lies with renewable energy sources like hydroelectric, solar, and wind, an immediate impact can be made by utilizing motor fuels with higher octane ratings which allow for higher engine compression ratios and more efficient combustion. The octane scale is referenced from 0 to 100, with 0 being n-heptane and 100 being 2,2,4-trimethylpentane (isooctane).

In the 1920's tetraethyl lead became a major fuel additive for increasing engine compression ratios, however due to environmental and neurotoxicity concerns it was phased out and replaced with methyl *tert*-butyl ether (MTBE).³ MTBE is synthesized commercially from isobutene and methanol using several different catalysts.⁴ Worldwide, the demand for MTBE grew dramatically until it peaked in 1995 at 30 million tons and then dropped precipitously in the 2000's when the U.S. and Canada banned its use in gasoline due to concerns of leaching into the groundwater. Despite the ban, the U.S. continues to have a large infrastructure to synthesize MTBE as it is still exported to countries like Mexico, Chile and Venezuela.⁵

Since the infrastructure for isobutene production and use is already in place, converting isobutene to isooctane would be a valuable endeavor. The current process for isooctane production involves the dimerization of isobutene in a fixed bed reactor with a heterogenous acid catalyst followed by catalytic hydrogenation in a stirred tank reactor, with most processes operating at low conversion (20-60%).⁶ Thus a catalyst that could reduce the number of steps and operate at higher conversions would be ideal.

Recently our group has been exploring cationic bis(phosphine) iridium complexes to generate alkoxycarbenes derived from α,α -dehydrogenation of ethers and have shown this process to be facile and reversible.⁷ Utilizing a Lewis base directing group, complex **1** could be dehydrogenated with *tert*-butylethylene (TBE) to give alkoxycarbene complex **2** via the putative 14 e⁻ Ir(I) fragment **A** (**Figure 5.1.1**).⁸ While traditional Fischer carbenes are electrophilic at carbon, our group examined the reactivity **2** with CD₃OD and found no conversion to **B** (**Figure 5.1.1**). This data suggests that **2** may be insufficiently electrophilic at carbon as a

result of stronger metal d_{π} backbonding into the empty p-orbital of the alkoxy carbene. The results from these experiments prompted the exploration of the less electron-releasing phosphine, tris(3,5-bis(trifluoromethyl)phenyl)phosphine (PAr^{F_3}) with the aim of generating a more electrophilic alkoxy carbene. During the course of these studies, we found no evidence for alkoxy carbene formation, however we found that many PAr^{F_3} -supported iridium complexes were highly acidic. We now report the synthesis of electron poor, cationic iridium bis(phosphine) complexes and their ability to catalyze the tandem process of olefin oligomerization and hydrogenation in a one-pot reaction.

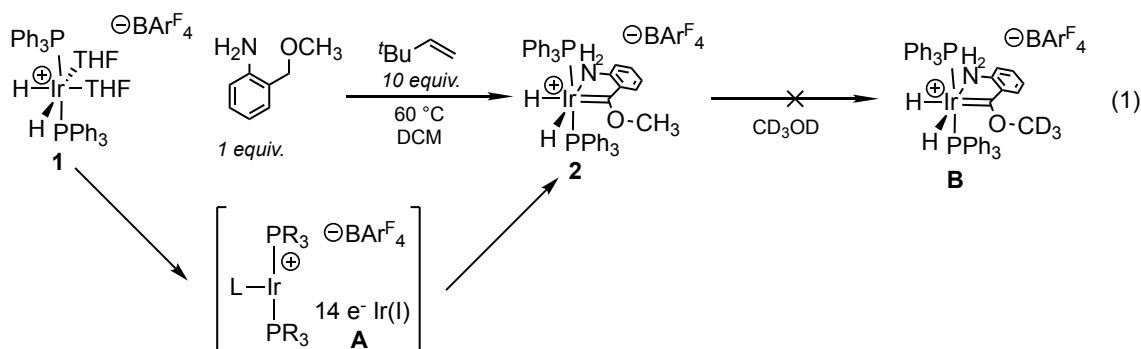


Figure S.1.1. Lewis base directed α, α -dehydrogenation resulting in **2** and unsuccessful attempts at nucleophilic displacement with CD_3OD to form **B**.

5.2 Results and Discussion

Treatment of commercially-available $[(\text{cod})\text{IrCl}]_2$ with sodium tetrakis[3,5-bis(trifluoromethyl)phenyl]borate and PAr^{F_3} resulted in large red crystals of **3** upon standing overnight (Figure 5.2.1, eq 2). Complex **3** is extremely insoluble in the majority of solvents tested including dichloromethane, chloroform, diisopropyl ether, diethyl ether, benzene and bromobenzene. While it is only sparsely soluble in fluorobenzene, complex **3** was found to be extremely soluble in 1,2-difluorobenzene and hexafluorobenzene. Hydrogenation of **3** in 1,2-difluorobenzene with 20 equiv. of water led to the isolation of $[(\text{PAr}^{\text{F}_3})_2\text{IrH}_2(\text{H}_2\text{O})_2]\text{BAR}^{\text{F}_4}$ **4** (Figure 5.2.2, eq 3), which we have characterized in the solid state using X-ray crystallography (Figure 5.2.3, left).

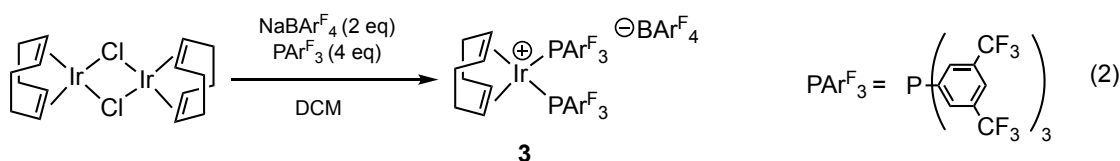


Figure 5.2.1. Reaction of $[(\text{cod})\text{IrCl}]_2$ with PAr^{F_3} , $\text{NaBAR}^{\text{F}_4}$ in DCM

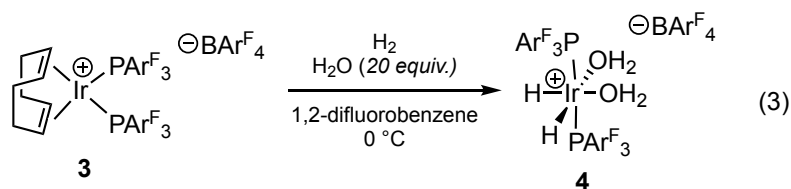


Figure 5.2.2. Hydrogenation of **3** in the presence of trace H₂O in 1,2-difluorobenzene

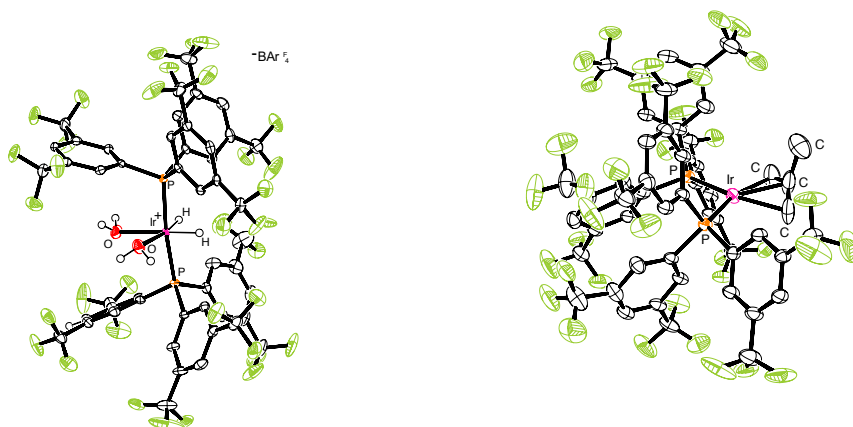


Figure 5.2.3. ORTEPs of **4** (left) and **5** (right). Anions, solvent of crystallization and full disorder models omitted for clarity

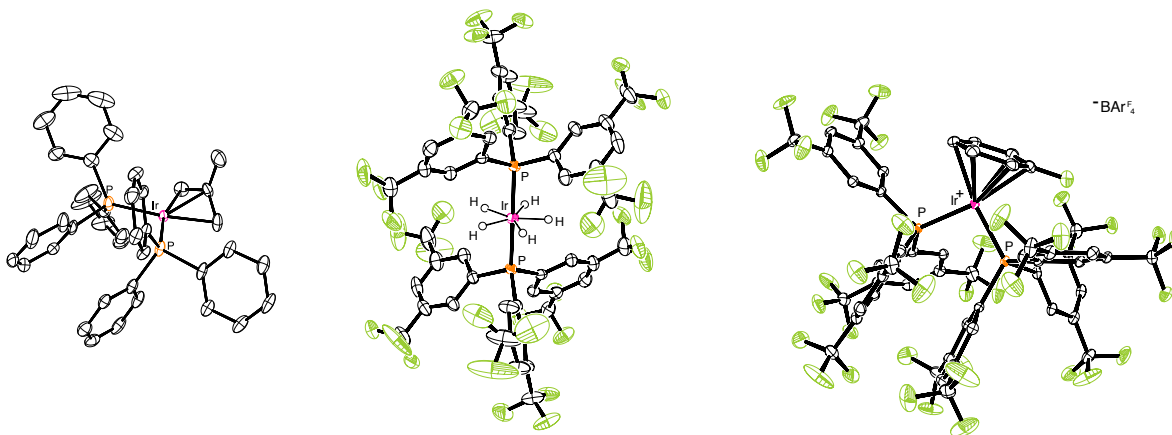


Figure 5.2.4. ORTEPs of **8** (left), **10** (center) and **11** (right). Anions, solvent of crystallization and full disorder models omitted for clarity

Attempts to form alkoxycarbene complexes via dehydrogenation of **4** with TBE in the presence of several ethers was unsuccessful. However, when **4** was treated with TBE in MTBE, the formation of a neutral Ir(I) methallyl complex **5** derived from

C-O bond cleavage was observed (**Figure 5.2.5, eq 4**). Complex **5** has been characterized in the solid state via X-ray crystallography (**Figure 5.2.3, right**). The isolation of a neutral complex was perplexing when considering a similar complex, $[(PPh_3)_2IrH_2(THF)_2]PF_6$, supported by a more electron-releasing phosphine was demonstrated to form a cationic Ir(III) methallyl complex (**7**) under similar conditions (**Figure 5.2.6, eq 5**) (see chapter 2).⁹ Indeed, cationic complex **7** could be deprotonated using triethylamine to give the neutral Ir(I) methallyl complex **8**, (**Figure 5.2.7, eq 6**) which has been fully characterized in solution and in the solid state by X-ray crystallography (**Figure 5.2.4, left**). However, in the case of complex **4**, no apparent base had been added.

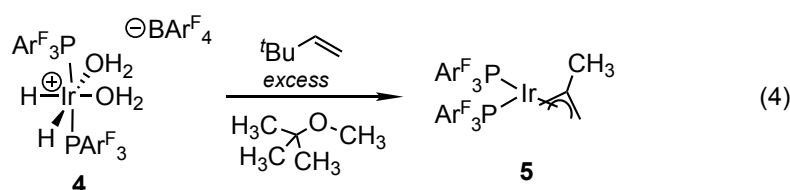


Figure 5.2.5. Dehydrogenation of **4** with TBE in MTBE

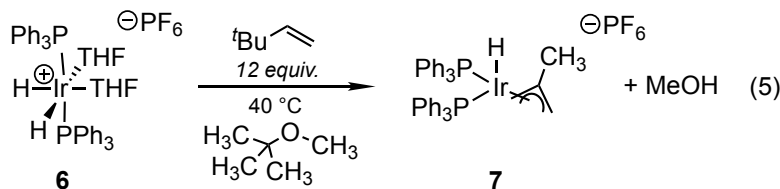


Figure 5.2.6. Dehydrogenation of **6** with TBE in MTBE

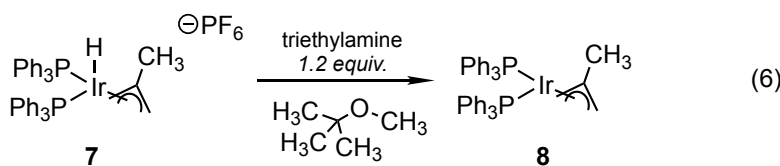


Figure 5.2.7. Reaction of **7** upon addition of triethylamine in MTBE

Extensive work by the Roddick group however, has demonstrated that (fluoroalkyl)phosphine-supported iridium complexes give highly acidic metal hydrides which can be easily deprotonated with weak bases including diethyl ether and acetone.¹⁰ To investigate whether the formation of **5** is proceeding via the deprotonation of a cationic hydridoallyl by ether solvent, we attempted to independently prepare the cationic Ir(III) methallyl complex **9** with excess isobutene in 1,2-difluorobenzene (**Figure 5.2.8, eq 7**). These conditions omit any apparent Brønsted base and would be expected to allow for the observation of even an exceedingly acidic iridium complex. Under these conditions a new $^{31}P\{^1H\}$ resonance is observed at 18.18 ppm alongside the

presence of an Ir-H at -31.67 ppm in the ^1H NMR spectrum. While the structure has not been confirmed via X-ray crystallography, we have tentatively assigned these resonances to the cationic hydridoiridium methallyl complex **9**. To test whether the metal hydride generated from **eq 7** could be deprotonated with a weakly basic alkyl ether, the material obtained by evaporation of the crude reaction was dissolved in either diisopropyl ether or diethyl ether. These solutions eventually deposited orange crystals suitable for X-ray diffraction which confirmed the formation of **5**. Additional evidence that cationic bis(PAr^{F})Ir hydride complexes are sufficiently acidic to be deprotonated by alkyl ethers was found through the hydrogenation of **3** in diisopropyl ether, which gives the neutral pentahydride **10** (Figure 5.2.9, eq 8). Our group has characterized **10** in solution by ^1H , $^{13}\text{C}\{^1\text{H}\}$, $^{31}\text{P}\{^1\text{H}\}$ and in the solid state by X-ray diffraction (Figure 5.2.4, center).¹¹ An additional stable cationic bis(PAr^{F}) iridium complex includes an iridium (η^6 -fluorobenzene) complex **11** synthesized from the dehydrogenation of **4** with excess TBE (Figure 5.2.10, eq 9). Complex **11** has been characterized in the solid state by X-ray diffraction (Figure 5.2.4, right), however the lability of the fluoroarene with other deuterated and aromatic solvents has precluded characterization in solution by NMR.

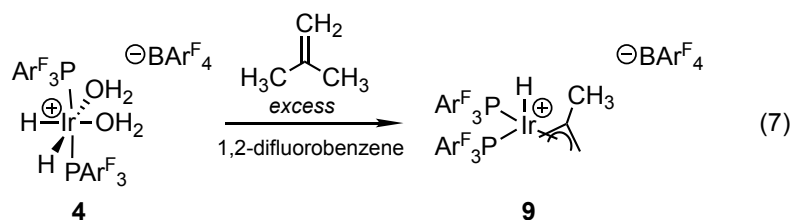


Figure 5.2.8. Dehydrogenation of **4** with isobutene in 1,2-difluorobenzene

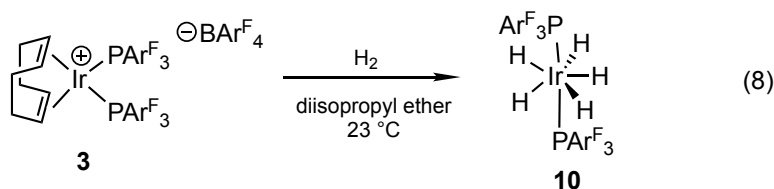


Figure 5.2.9. Hydrogenation of **3** in diisopropyl ether

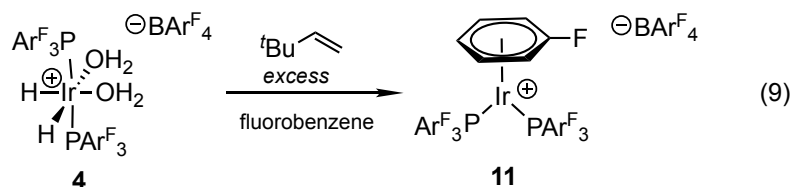


Figure 5.2.10. Dehydrogenation of **4** with TBE in fluorobenzene

When **4** is treated with excess isobutene, organic products resulting from the dimerization (diisobutylene) and oligomerization of isobutene are observed by ^1H NMR and confirmed by GC/MS. As cationic iridium phosphine complexes are known for being famously excellent olefin hydrogenation catalysts, this system showed potential promise for a tandem oligomerization/hydrogenation catalyst. We initially surveyed **3** as a precatalyst for the oligomerization/hydrogenation of isobutene to form isooctane. A selection of experiments at various pressures of isobutene:hydrogen with precatalyst **3** is shown in **Table 5.2.1**. Our preliminary experiments show that our one-pot tandem dimerization/hydrogenation of isobutene gives isooctane yields as high as 31% (**Table 5.2.1, rxn 2**). The production of isooctane was analyzed using GC/FID against a standard of isooctane purchased from a commercial vendor. These preliminary studies suggest that complex **3** is a competent precatalyst for the tandem dimerization/hydrogenation of isobutene to form isooctane. A proposed mechanism for this reaction is shown in **Figure 5.2.11**. Further work is needed to optimize this transformation to minimize undesired byproducts (isobutane, trimers, tetramers and pentamers). Future experiments should be designed around varying the ratio of H_2 :isobutene, as well as the catalyst loading. Additional avenues to pursue include exploration of other more or less π -acidic phosphines/ligands as well as potential cross-dimerization/hydrogenation of other 1,1-disubstituted olefins.

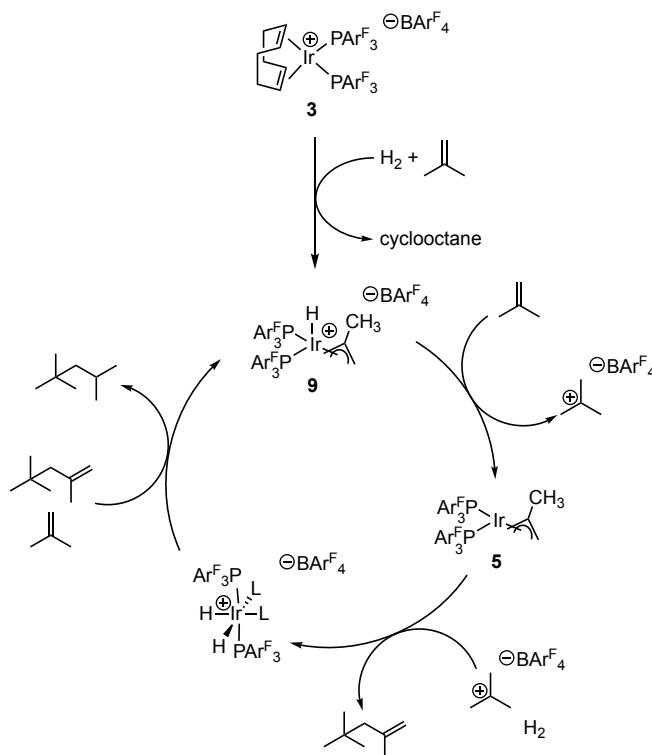


Figure 5.2.11. Proposed mechanism for ionic oligomerization/hydrogenation of isobutene to isooctane.

Table S.2.1. Preliminary pressure optimization of H₂:Isobutene for dimerization/hydrogenation of isobutene.

Reaction ^a	H ₂ (atm)	Isobutene (atm)	Ratio H ₂ :isobutene	Isobutene (mmol)	Isooctane Produced (mmol)	Turnovers	Yield ^b Isooctane (%)
1	3.0	2.4	1.2:1.0	0.25	0.025	10.4	20
2	3.0	1.7	1.8:1.0	0.18	0.028	11.7	31
3	2.4	2.4	1.0:1.0	0.25	0.031	12.9	25

^a 0.0024 mmol of **3** was used. ^b yield was determined by GC-FID

5.3 Conclusion

In summary, we report preliminary studies examining the formation of highly acidic metal bis(phosphine) iridium complexes utilizing an electron-poor phosphine. The formation of an acidic metal hydride is observed by ¹H NMR and is shown to be easily deprotonated using an ethereal base such as diethyl ether or diisopropyl ether. The efficacy of alkyl ethers as weak bases allows us to estimate a minimum pK_a of ~ -3.8 (protonated dimethyl ether).¹² The acidic nature of this metal complex is demonstrated in the dimerization and oligomerization of isobutene. Further experiments show the potential for this system to catalyze the tandem oligomerization/hydrogenation of isobutene to branched alkanes. Despite these initial results further work is needed to determine the efficiency of this catalytic system for the one-pot production of isooctane.

5.4 Experimental

General Considerations. All manipulations were carried out using standard vacuum, Schlenk, cannula, or glovebox techniques under N₂ unless otherwise specified. Tetrahydrofuran, dichloromethane, pentane, and diethyl ether were degassed with argon and dried over activated alumina using a solvent purification system. 1,2-difluorobenzene, diisopropyl ether and methyl *tert*-butyl ether were degassed with nitrogen and stored over activated 4Å molecular sieves. Complexes **3,6,7,10** were prepared by our group in previous reports.^{9,11}

Spectroscopy. ^1H , ^{13}C and ^{31}P NMR spectra were recorded on Bruker NMR spectrometers at ambient temperature unless otherwise noted. ^1H and ^{13}C chemical shifts are referenced to residual solvent signals; ^{31}P chemical shifts are referenced to an external H_3PO_4 standard.

X-ray Crystallography. X-ray crystallographic data were collected on a Rigaku Oxford Diffraction Supernova diffractometer. Crystal samples were handled under immersion oil and quickly transferred to a cold nitrogen stream.

Elemental Analysis. Elemental analyses of complexes **8** are of the bulk sample for which yields are reported. No additional purification operations are carried out prior to packaging for analysis. Elemental analyses were performed at the University of Rochester CENTC Elemental Analysis Facility.

Crude preparation of $[(\text{PAr}^{\text{F}}_3)_2\text{IrH}_2(\text{H}_2\text{O})_2]\text{BAr}^{\text{F}}_4$ (4**).** A 20 mL scintillation vial was charged with complex **3** (0.1999 g, 0.080 mmol) and 2.0 mL of 1,2-difluorobenzene and sealed with a PTFE-lined septum cap. The solution was cooled to 0°C and H_2O (30.0 μL , 1.7 mmol) was added. H_2 was then bubbled through the solution for 15 minutes while swirling the vial. After 15 minutes, 12 mL of dry pentane was added and the yellow solution changed to cloudy white. The reaction was kept at 0°C and H_2 was bubbled for an additional 20 minutes. At this time a white solid precipitated. The vial was then pressurized with 1.1 atm of H_2 and returned to the glovebox. The supernatant was then decanted with a pipette and saved in separate vial. The resulting white solid was washed with 3 x 2.0 mL of pentane and the pentane washes were combined with the saved supernatant. The saved supernatant was swirled for a few minutes and additional white solid precipitated. The supernatant was then removed and the 2nd crop of white precipitate was combined with the first crop and dried under vacuum to yield 0.1741 g (90%) of complex **4** as a white solid. Single crystals of **4** were grown from a saturated solution in 1,2-difluorobenzene layered with pentane. *Note-crude NMR peaks are listed below with corresponding ^1H and $^{31}\text{P}\{^1\text{H}\}$ NMR included in §5.5 Additional Figures

^1H NMR (500 MHz, CD_2Cl_2): δ -27.59 (br s, 2H, $\text{Ir}(\text{H})_2$), 2.53 (br s, 4H, $\text{Ir}(\text{H}_2\text{O})_2$), 7.56 (br s, 4H, CH of BAr^{F}_4), 7.74 (br s, 8H, CH of BAr^{F}_4), 7.92 (t, 12 H, Ar-H2,6, $^3J_{\text{H-P}} = 5.4$ Hz), 8.29 (br s, 6H, Ar-H4)

$^{31}\text{P}\{^1\text{H}\}$ NMR (202 MHz, CD_2Cl_2): δ 27.84 (br)

Preparation of [(PPh₃)₂Ir(C₄H₇)] (8). To a 20 mL scintillation vial was charged with complex 7 (0.0991 g, 0.11 mmol), 1.5 mL of methyl *tert*-butyl ether, triethylamine (18 μ L, 0.13 mmol) and a stir bar and sealed with a PTFE-lined septum cap. The solution was stirred for 3 h at room temperature and resulted in a tan solid and a color change from pale yellow to orange. The reaction was filtered and the vial washed with 4x2mL portions of pentane and filtered. The orange filtrate was then dried in vacuo. 2 mL of pentane was added followed by drying in vacuo and was repeated twice more to yield complex 8 (0.0613 g, 74%) as an orange solid. Single crystals of 3 were obtained by slow evaporation from a saturated pentane solution at room temperature. Anal. Calcd. For C₄₀H₃₇IrP₂: C, 62.24; H, 4.83. Found: C, 62.315; H, 4.777

¹H NMR (500 MHz, C₆D₆): δ 1.86(s, 3H, CH₃), 2.52(d, 2H, CH_{anti}), 2.85(broad s, 2H, CH_{syn}), 6.90-6.98(m, 18H, Ar), 7.57-7.69(m, 12H, Ar)

¹³C{¹H} NMR (125 MHz, C₆D₆): δ 25.87(s, CH₃), 54.59(d, 2.7 Hz, CH₂), 54.81(d, 2.7 Hz, CH₂), 113.18(s, C(CH₂)₂CH₃), 127.48(d, 9.6Hz, CH_{Ar}), 128.69(s, CH_{Ar}), 134.4(d, 12.4Hz CH_{Ar}), 139.2(d, 45.1Hz, C_{Ar})

³¹P{¹H} NMR (202 MHz, C₆D₆): δ 30.94(s)

Crude preparation of [(PAr^F₃)₂IrH(C₄H₇)]BAR^F₄ (9). To a 20 mL scintillation vial was charged with complex 4 (0.0991 g, 0.041 mmol), 1.5 mL of 1,2-difluorobenzene and sealed with a PTFE-lined septum cap. Isobutene was bubbled through the solution for 5 minutes and the color changed to a vibrant yellow. The reaction was then dried under vacuum resulting in a sticky yellow solid. Afterwards, the sticky yellow solid was washed with 2 x 8 mL of pentane and dried under vacuum to yield a yellow powder. *Note- crude NMR peaks are listed below with corresponding ¹H and ³¹P{¹H} NMR included in §5.5 Additional Figures

¹H NMR (500 MHz, C₆D₆): δ -31.67(br s, IrH)

³¹P{¹H} NMR (202 MHz, C₆D₆): δ 18.18(s)

Crude preparation of [(PAr^F₃)₂Ir(η ⁶-fluorobenzene)]BAR^F₄ (11). A 20 mL scintillation vial was charged with complex 4 (0.0490 g, 0.021 mmol), 2.0 mL of fluorobenzene, *tert*-butylethylene (20.0 μ L, 0.16 mmol) and sealed with a PTFE-lined septum cap. The color changed to orange and the solution was allowed to stand for 2 hours. Afterwards, the solution was filtered through a syringe filter and layered with 2.0 mL of pentane. Crystals grew and the supernatant was removed from the crystals with a pipette

to yield **11** as an orange solid. Single crystals of **11** were grown by layering a saturated solution of fluorobenzene with pentane. Only X-ray diffraction was used to confirm this product owing to the lability of the fluorobenzene to dissociate in common deuterated solvents and replaced by other aromatic solvents.

5.5 Additional Figures

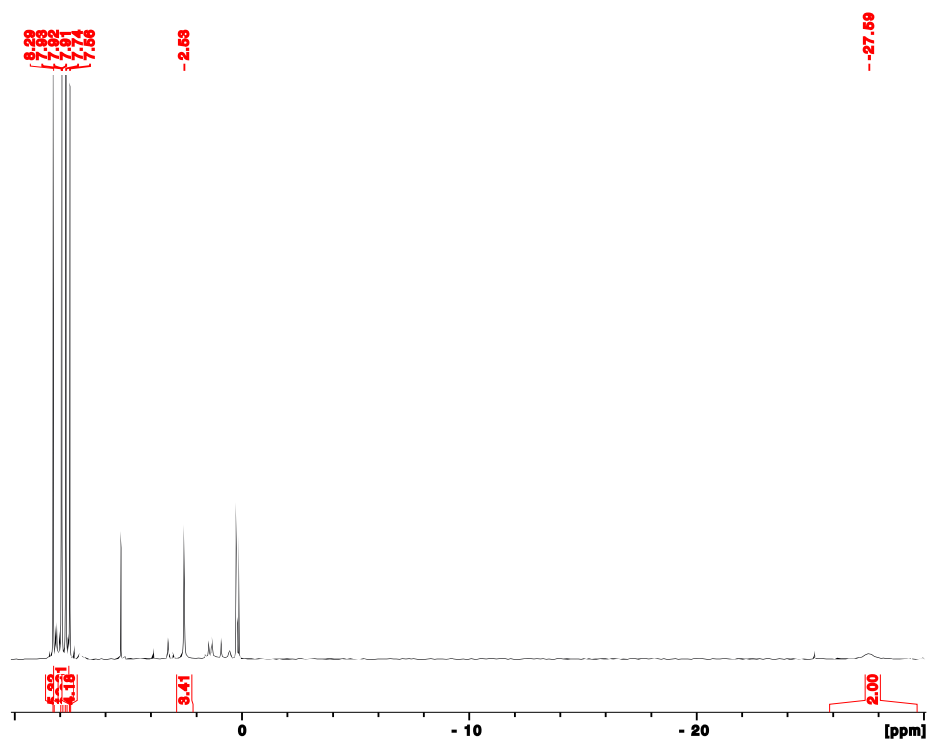


Figure S.5.1. ¹H NMR Spectrum of crude [(PAr^F₃)₂IrH₂(H₂O)₂]BAr^F₄ (**4**) (500 MHz, CD₂Cl₂)

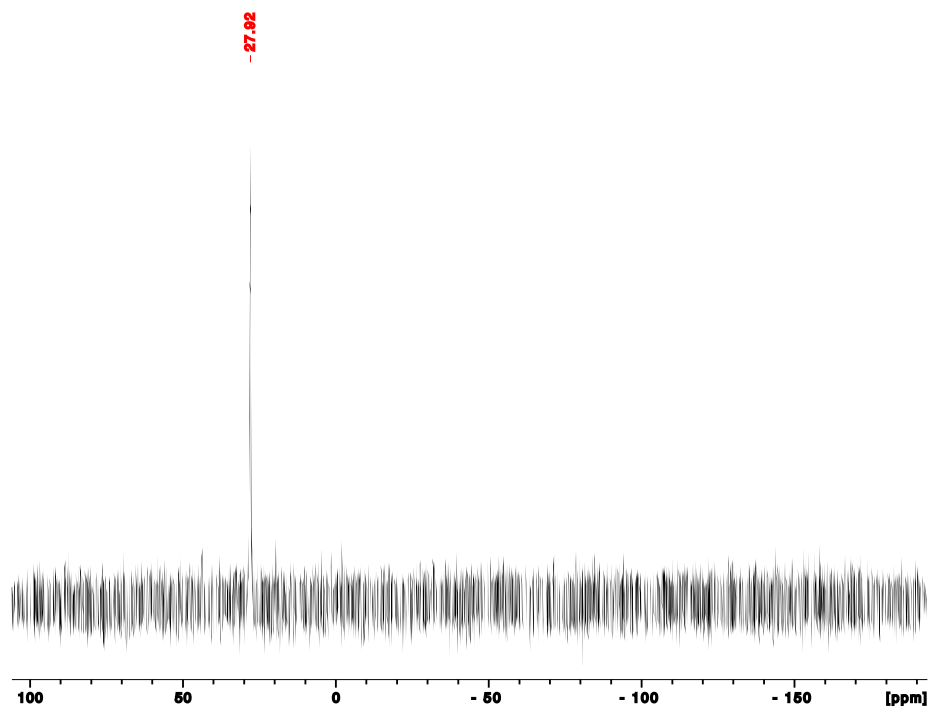


Figure 5.5.2. $^{31}\text{P}\{^1\text{H}\}$ NMR Spectrum of crude $[(\text{PAR}^{\text{F}_3})_2\text{IrH}_2(\text{H}_2\text{O})_2]\text{BAR}^{\text{F}_4}$ (**4**) (202 MHz, CD_2Cl_2)

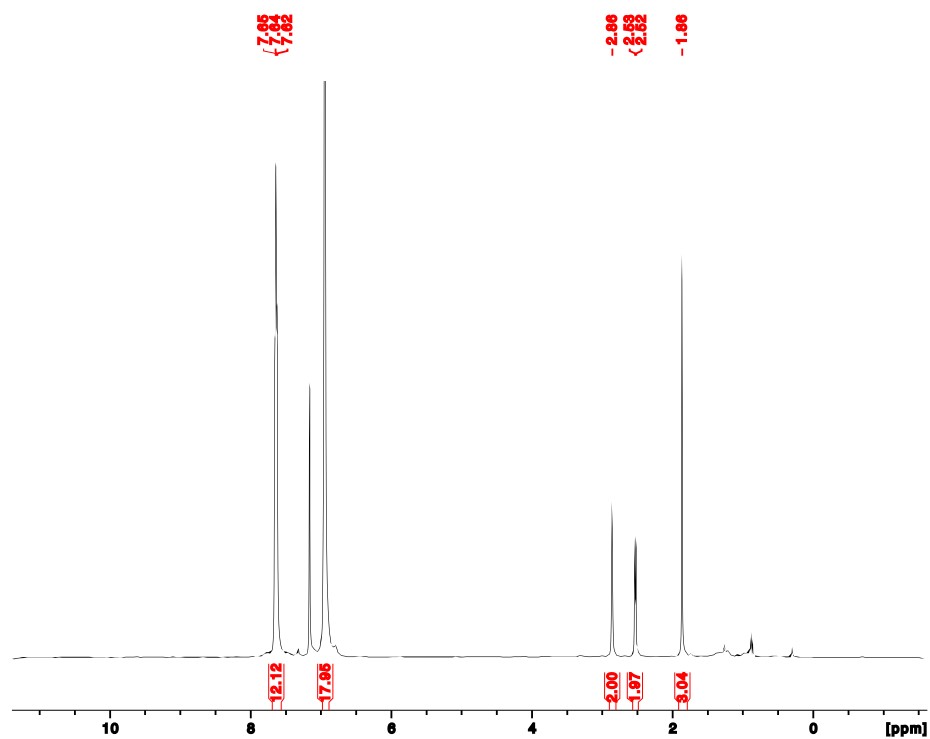


Figure 5.5.3. ^1H NMR Spectrum of $[(\text{PPh}_3)_2\text{Ir}(\text{C}_4\text{H}_7)]$ (**8**) (500 MHz, C_6D_6)

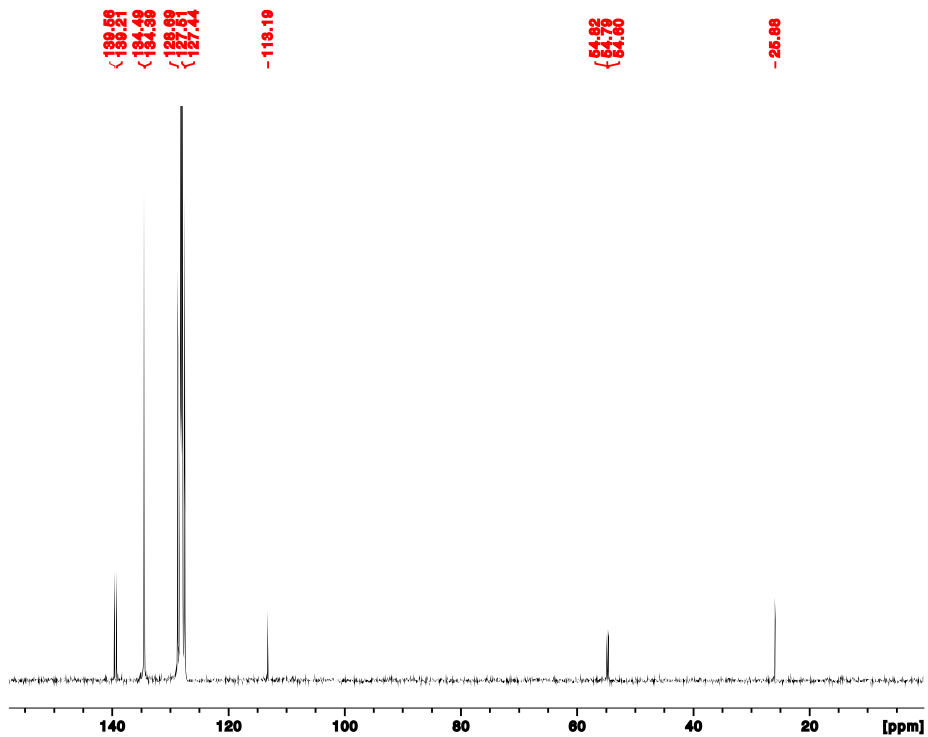


Figure S.5.4. ^{13}C NMR Spectrum of $[(\text{PPh}_3)_2\text{Ir}(\text{C}_4\text{H}_7)]$ (8) (126 MHz, C_6D_6)

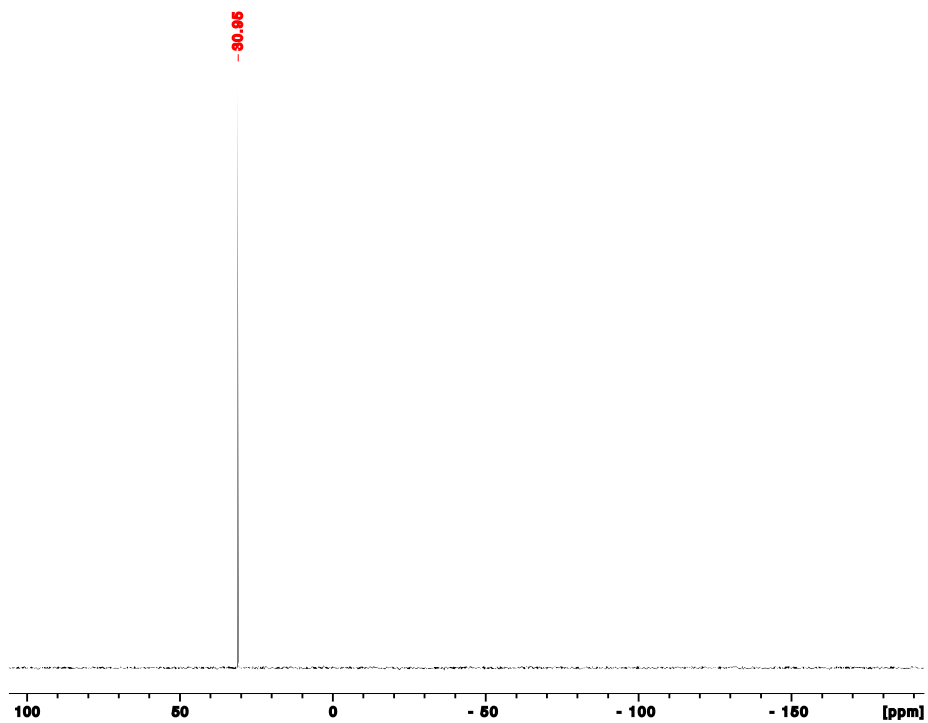


Figure S.5.5. $^{31}\text{P}\{^1\text{H}\}$ NMR Spectrum of $[(\text{PPh}_3)_2\text{Ir}(\text{C}_4\text{H}_7)]$ (8) (202 MHz, C_6D_6)

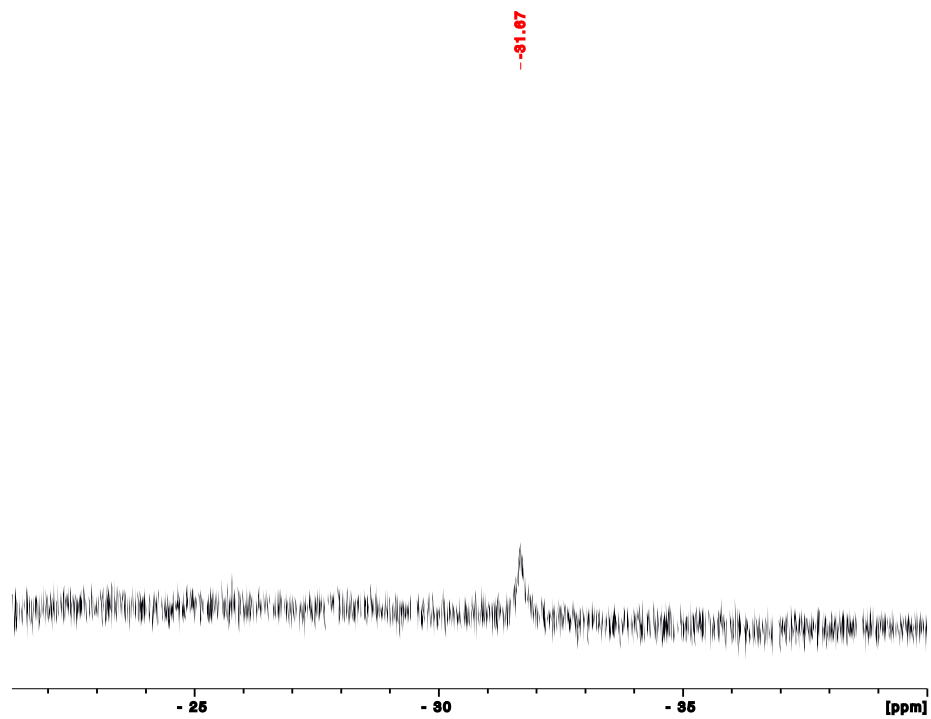


Figure 5.5.6. ^1H NMR Spectrum (hydride region) of speculated crude $[(\text{PAr}^{\text{F}_3})_2\text{IrH}(\text{C}_4\text{H}_7)]\text{BAr}^{\text{F}_4}$ (**9**) (500 MHz, CD_2Cl_2)

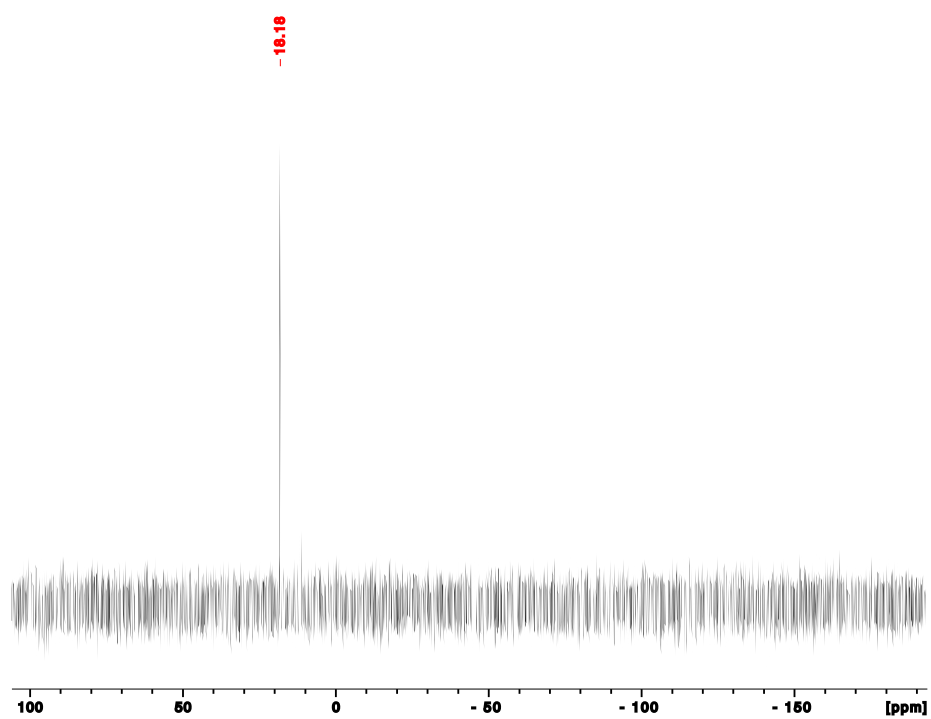


Figure 5.5.7. $^{31}\text{P}\{^1\text{H}\}$ NMR Spectrum of crude $[(\text{PAr}^{\text{F}_3})_2\text{IrH}(\text{C}_4\text{H}_7)]\text{BAr}^{\text{F}_4}$ (**9**) (202 MHz, CD_2Cl_2)

5.6 X-Ray Crystallography

Table S.6.1. Crystal data and structure refinement for **4**.

Identification code	4	
Empirical formula	C ₈₀ H ₄₀ B F ₆₀ Ir O ₄ P ₂	
Formula weight	2470.07	
Temperature	100.0(3) K	
Wavelength	0.71073 Å	
Crystal system	Orthorhombic	
Space group	P2 ₁ 2 ₁ 2 ₁	
Unit cell dimensions	a = 13.3559(3) Å	α = 90°
	b = 24.3275(6) Å	β = 90°
	c = 27.2126(6) Å	γ = 90°
Volume	8841.8(4) Å ³	
Z	4	
Density (calculated)	1.856 Mg/m ³	
Absorption coefficient	1.723 mm ⁻¹	
F(000)	4816	
Crystal size	0.303 x 0.275 x 0.15 mm ³	
Theta range for data collection	3.033 to 30.291°.	
Index ranges	-18 ≤ h ≤ 18, -33 ≤ k ≤ 32, -38 ≤ l ≤ 20	
Reflections collected	72060	
Independent reflections	23200 [R(int) = 0.0459]	
Completeness to theta = 25.242°	99.7 %	
Absorption correction	Gaussian	
Max. and min. transmission	1.000 and 0.436	
Refinement method	Full-matrix least-squares on F ²	
Data / restraints / parameters	23200 / 158 / 1461	
Goodness-of-fit on F ²	1.047	
Final R indices [I > 2σ(I)]	R1 = 0.0367, wR2 = 0.0669	
R indices (all data)	R1 = 0.0433, wR2 = 0.0693	
Absolute structure parameter	-0.0118(17)	
Extinction coefficient	n/a	
Largest diff. peak and hole	0.799 and -1.251 e/Å ⁻³	

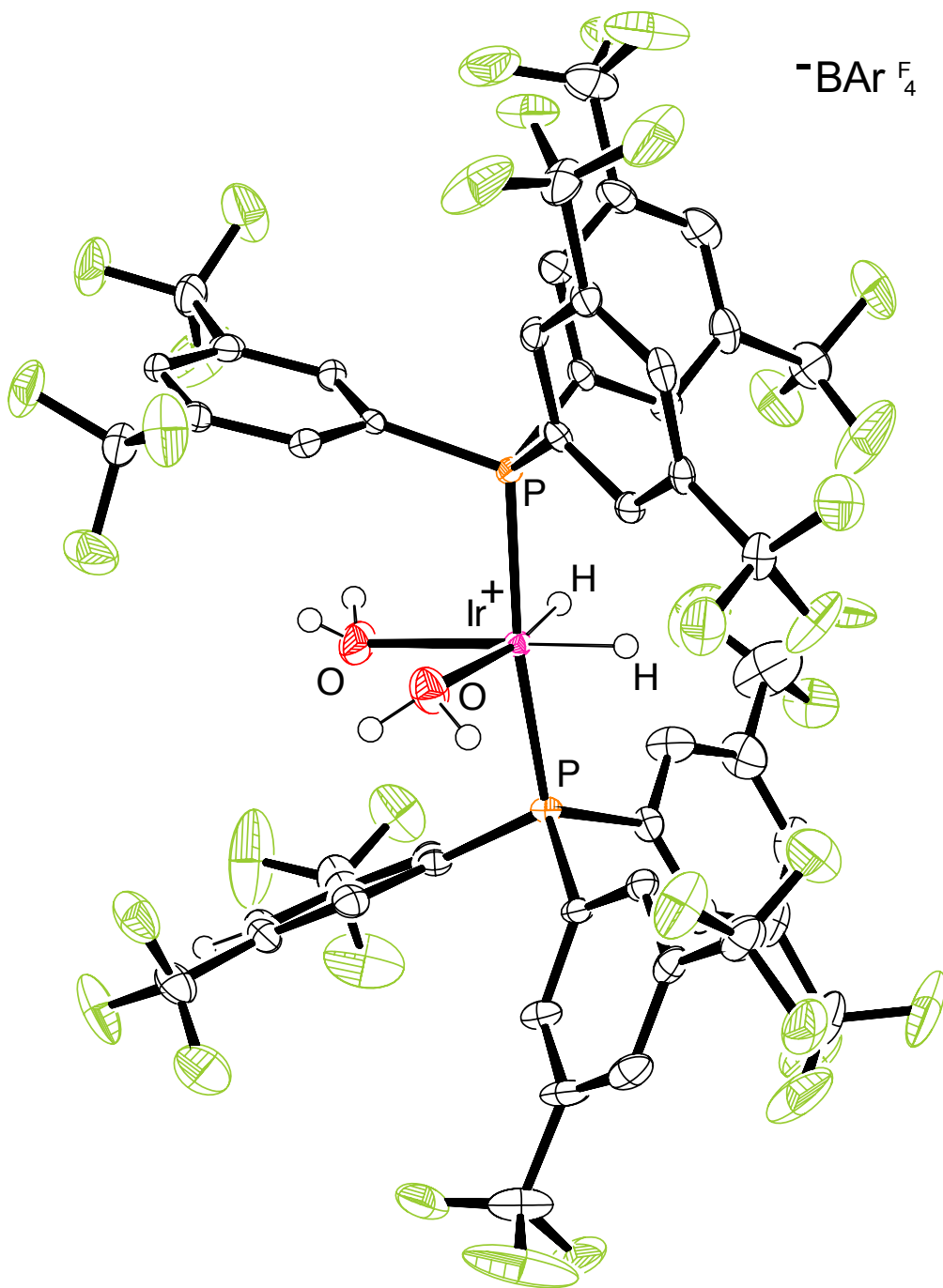


Figure S.6.1. ORTEP diagram of 4 with ellipsoids shown at 50%. The anion is omitted for clarity.

Table S.6.2. Crystal data and structure refinement for **5**.

Identification code	5	
Empirical formula	C ₅₂ H ₂₅ F ₃₆ Ir P ₂	
Formula weight	1587.86	
Temperature	99.9(4) K	
Wavelength	1.54184 Å	
Crystal system	Triclinic	
Space group	P-1	
Unit cell dimensions	a = 10.2914(3) Å	α = 80.5152(11)°
	b = 12.91883(17) Å	β = 89.5788(17)°
	c = 20.5956(3) Å	γ = 88.2886(17)°
Volume	2699.60(9) Å ³	
Z	2	
Density (calculated)	1.953 Mg/m ³	
Absorption coefficient	6.874 mm ⁻¹	
F(000)	1536	
Crystal size	0.107 x 0.063 x 0.011 mm ³	
Theta range for data collection	3.470 to 73.573°.	
Index ranges	-12 ≤ h ≤ 12, -16 ≤ k ≤ 15, -17 ≤ l ≤ 24	
Reflections collected	38958	
Independent reflections	10529 [R(int) = 0.0463]	
Completeness to theta = 67.684°	98.8 %	
Absorption correction	Gaussian	
Max. and min. transmission	0.979 and 0.613	
Refinement method	Full-matrix least-squares on F ²	
Data / restraints / parameters	10529 / 168 / 877	
Goodness-of-fit on F ²	1.041	
Final R indices [I > 2σ(I)]	R1 = 0.0496, wR2 = 0.1199	
R indices (all data)	R1 = 0.0550, wR2 = 0.1234	
Extinction coefficient	n/a	
Largest diff. peak and hole	2.160 and -1.727 e/Å ⁻³	

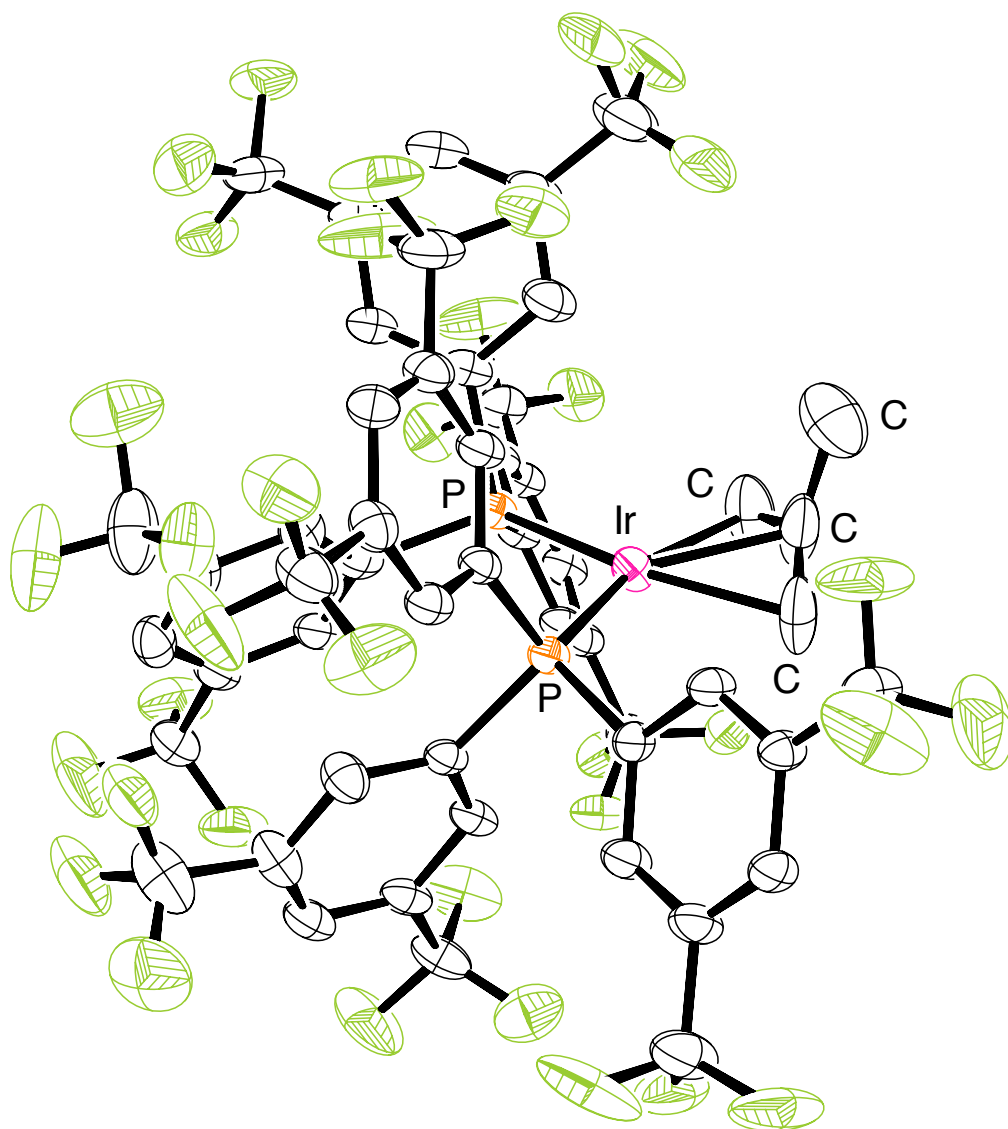


Figure S.6.2. ORTEP diagram of **5** with ellipsoids shown at 50%.

Table S.6.3. Crystal data and structure refinement for **8**.

Identification code	8	
Empirical formula	C ₄₀ H ₃₇ IrP ₂	
Formula weight	771.83	
Temperature	100 K	
Wavelength	0.71073 Å	
Crystal system	Triclinic	
Space group	P-1	
Unit cell dimensions	a = 8.8051(2) Å	α = 89.0973(18)°
	b = 10.4885(2) Å	β = 81.116(2)°
	c = 17.9977(4) Å	γ = 84.717(2)°
Volume	1635.21(7) Å ³	
Z	2	
Density (calculated)	1.568 Mg/m ³	
Absorption coefficient	4.208 mm ⁻¹	
F(000)	768	
Crystal size	0.074 x 0.063 x 0.036 mm ³	
Theta range for data collection	3.007 to 30.194°.	
Index ranges	-12 ≤ h ≤ 12, -14 ≤ k ≤ 13, -24 ≤ l ≤ 24	
Reflections collected	39705	
Independent reflections	8780 [R(int) = 0.0363]	
Completeness to theta = 25.242°	99.8 %	
Absorption correction	Gaussian	
Max. and min. transmission	0.932 and 0.778	
Refinement method	Full-matrix least-squares on F ²	
Data / restraints / parameters	8780 / 0 / 436	
Goodness-of-fit on F ²	1.325	
Final R indices [I > 2σ(I)]	R1 = 0.0419, wR2 = 0.0677	
R indices (all data)	R1 = 0.0541, wR2 = 0.0702	
Extinction coefficient	n/a	
Largest diff. peak and hole	0.747 and -1.215 e/Å ⁻³	

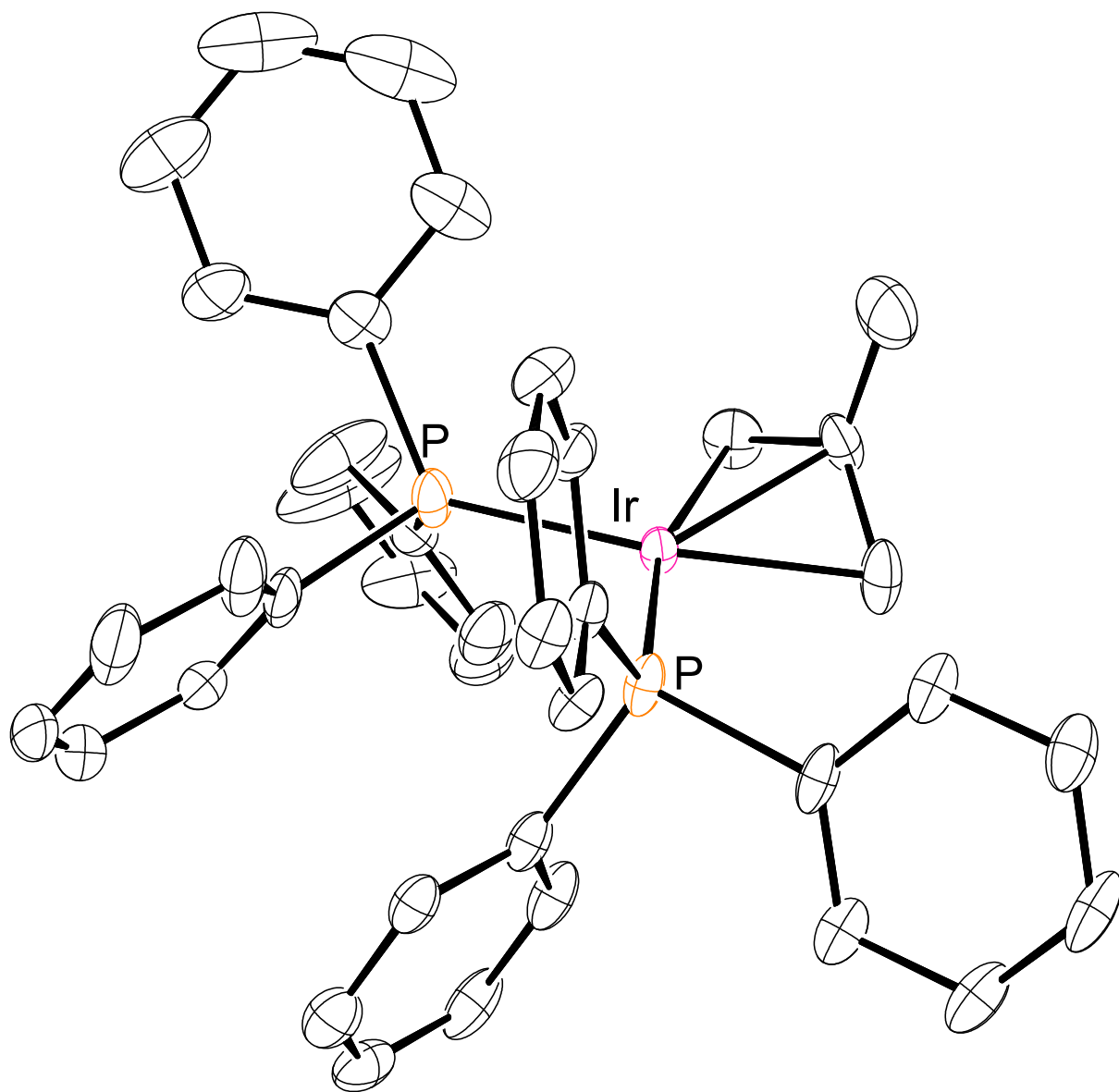


Figure S.6.3. ORTEP diagram of **8** with ellipsoids shown at 50%.

Table S.6.4. Crystal data and structure refinement for complex **10**.

Identification code	10	
Empirical formula	C ₄₈ H ₂₃ F ₃₆ IrP ₂	
Formula weight	1537.80	
Temperature	100.1(6) K	
Wavelength	1.54184 Å	
Crystal system	Triclinic	
Space group	P-1	
Unit cell dimensions	a = 12.3828(3) Å	α = 64.281(3)°
	b = 15.2107(5) Å	β = 83.752(2)°
	c = 16.6665(5) Å	γ = 70.114(3)°
Volume	2656.74(16) Å ³	
Z	2	
Density (calculated)	1.922 Mg/m ³	
Absorption coefficient	6.957 mm ⁻¹	
F(000)	1484	
Crystal size	0.058 x 0.05 x 0.006 mm ³	
Theta range for data collection	3.413 to 73.388°.	
Index ranges	-15 ≤ h ≤ 12, -17 ≤ k ≤ 18, -20 ≤ l ≤ 20	
Reflections collected	31423	
Independent reflections	10332 [R(int) = 0.0567]	
Completeness to theta = 67.684°	98.8 %	
Absorption correction	Gaussian	
Max. and min. transmission	0.983 and 0.706	
Refinement method	Full-matrix least-squares on F ²	
Data / restraints / parameters	10332 / 114 / 929	
Goodness-of-fit on F ²	1.027	
Final R indices [I > 2σ(I)]	R1 = 0.0433, wR2 = 0.1008	
R indices (all data)	R1 = 0.0605, wR2 = 0.1119	
Extinction coefficient	n/a	
Largest diff. peak and hole	1.733 and -1.212 e/Å ⁻³	

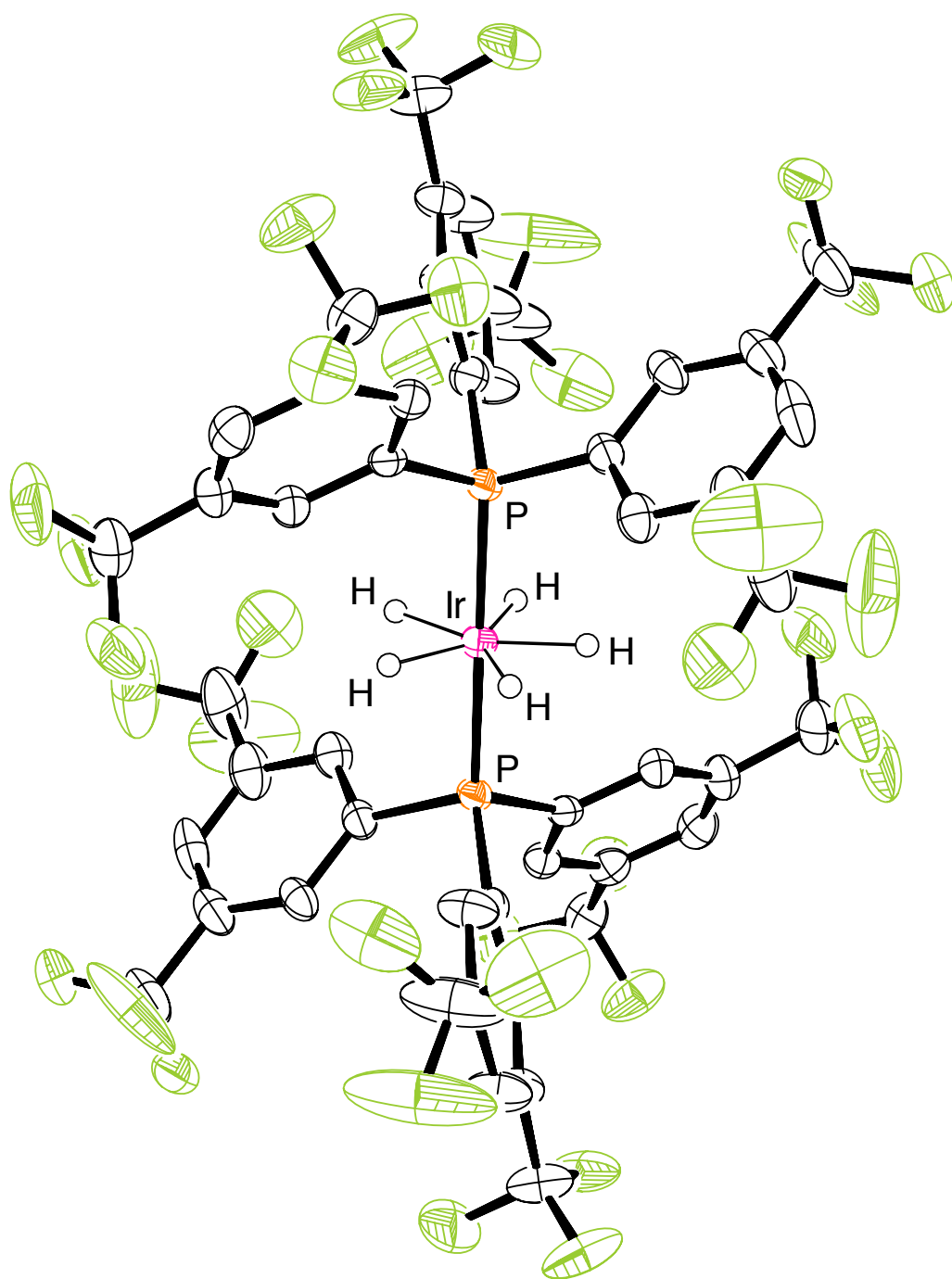


Figure S.6.4. ORTEP diagram of **10** with ellipsoids shown at 50%.

Table S.6.5. Crystal data and structure refinement for **11**.

Identification code	11	
Empirical formula	C _{100.50} H ₅₁ B ₆₃ IrP ₂	
Formula weight	2720.36	
Temperature	100.0(4) K	
Wavelength	0.71073 Å	
Crystal system	Triclinic	
Space group	P-1	
Unit cell dimensions	a = 12.72177(14) Å	α = 94.4575(11)°
	b = 17.5799(2) Å	β = 99.3783(10)°
	c = 22.8862(3) Å	γ = 93.4932(10)°
Volume	5020.62(11) Å ³	
Z	2	
Density (calculated)	1.799 Mg/m ³	
Absorption coefficient	1.528 mm ⁻¹	
F(000)	2666	
Crystal size	0.352 x 0.159 x 0.07 mm ³	
Theta range for data collection	1.991 to 30.255°	
Index ranges	-17 ≤ h ≤ 17, -24 ≤ k ≤ 24, -32 ≤ l ≤ 32	
Reflections collected	124939	
Independent reflections	27184 [R(int) = 0.0385]	
Completeness to theta = 25.242°	99.9 %	
Absorption correction	Gaussian	
Max. and min. transmission	1.000 and 0.390	
Refinement method	Full-matrix least-squares on F ²	
Data / restraints / parameters	27184 / 30 / 1533	
Goodness-of-fit on F ²	1.055	
Final R indices [I > 2σ(I)]	R1 = 0.0343, wR2 = 0.0808	
R indices (all data)	R1 = 0.0394, wR2 = 0.0832	
Extinction coefficient	n/a	
Largest diff. peak and hole	1.664 and -0.976 e/Å ⁻³	

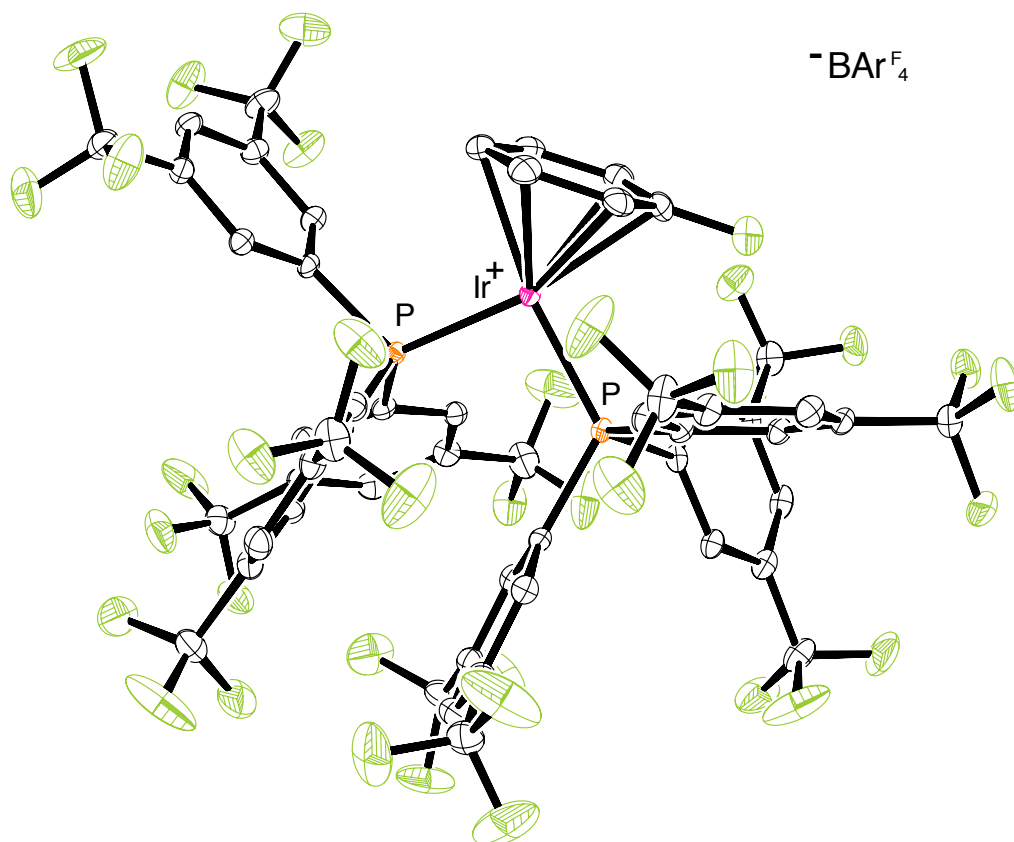


Figure S.6.5. ORTEP diagram of **11** with ellipsoids shown at 50%. The anion is omitted for clarity.

5.7 References

- (1) U.S. Energy Information Administration, International Energy Outlook. **2019**.
- (2) U.S. Energy Information Administration, Monthly Energy Review, Table 2.1, May **2020**.
- (3) Octane Enhancers. *Ullmann's Encyclopedia of Industrial Chemistry*, Weinheim, Germany, **2017**; 1-19.
- (4) Mahdi, H. I.; Muraza, O. Conversion of Isobutylene to Octane-Booster Compounds after Methyl *tert*-butyl Ether Phaseout: The Role of Heterogeneous Catalysis. *Ind. Eng. Chem. Res.* **2016**, 55, 11193-11210.
- (5) U.S. Energy Information Administration, Petroleum Supply Monthly
- (6) Goortani, B. M.; Gaurav, A.; Deshpande, A.; Ng, F. T. T.; Rempel, G. L. Production of Isooctane from Isobutene: Energy Integration and Carbon Dioxide Abatement via Catalytic Distillation. *Ind. Eng. Chem. Res.* **2015**, 3570-3581.

- (7) Zhang, Y.; Schley, N. D. Reversible Alkoxycarbene Formation by C-H Activation of Ethers via Discrete, Isolable Intermediates. *Chem. Commun.* **2017**, 53, 2130-2133.
- (8) Zhang, Y.; Mueller, B. R. J.; Schley, N. D. Formation of a Delocalized Iridium Benzylidene with Azaquinone Methide Character via Alkoxycarbene Cleavage. *Organometallics*. **2018**, 37, 12, 1825-1828.
- (9) Chapp, S. M.; Schley, N. D. Evidence for Reversible Cyclometalation in Alkane Dehydrogenation and C-O Bond Cleavage at Iridium Bis(phosphine) Complexes. *Organometallics*. **2017**, 36, 4355-4358.
- (10) Schnabel, C. R.; Roddick, D. M. (Fluoroalkyl)phosphine Hydride Complexes of Iridium. Synthesis and structures of $(dfep)_2IrH$ and $(dfep)_2Ir_2(H)(\mu-H)_2(\mu-O_3SCF_3)$. *Organometallics*. **1993**, 12, 704-711.
- (11) Fast, C. D.; Jones, C. A. H.; Schley, N. D. Selectivity and Mechanism of Iridium-Catalyzed Cyclohexyl Methyl Ether Cleavage. *ACS Catal.* **2020**, 10, 11, 6450-6456.
- (12) See document reported by Ripin, D. H.; Evans, D. A. pKa's of Inorganic and Oxo-Acids. Chem 206.